TESIS DE LA UNIVERSIDAD DE ZARAGOZA

2021 189

Jorge Calvo Ibar

Dynamics and spectrum of a molecule coupled to a vibrational mode.

Director/es

Zueco Lainez, David

Martín Moreno, Luis

ISSN 2254-7606

Prensas de la Universidad Universidad Zaragoza

ISSN 2254-7606

Universidad Zaragoza
1542

Tesis Doctoral

DYNAMICS AND SPECTRUM OF A MOLECULE COUPLED TO A VIBRATIONAL MODE.

Autor

Jorge Calvo Ibar

Director/es

Zueco Lainez, David
Martín Moreno, Luis

UNIVERSIDAD DE ZARAGOZA
Escuela de Doctorado

2021

Dynamics and spectrum of a molecule coupled to a vibrational mode

Colección de Estudios de Física
Vol. 31

Esta colección recoge las tesis presentadas en el Departamento de Física de la Materia Condensada de la Universidad de Zaragoza desde su constitución en 1987.

Colección de Estudios de Física Vol. 31

Dynamics and spectrum of a molecule coupled to a vibrational mode

Jorge Calvo Ibar

Prensas de la Universidad
Universidad Zaragoza

Aqui va la hoja de creditos.... asi que habra que sustituir esta pagina en el pdf final por la que nos den

A mis padres y mi hermano

Contents

Abstract

The studies in the field of cavity Quantum Electrodynamics (cavity-QED) during the last century [1] has allowed us to obtain a coherent interaction (Rabi oscillations) between the light and matter, reaching the regime known as strong coupling.

There is a plethora of experimental platforms in order to study the light-matter interaction; from nano-mechanical oscillators [2] to systems of artificial atoms composed of Josephson junctions. The latter setups have allowed the construction of the first quantum computer by Google in 2019 [3].

In this work, we have focused on a two-level system constituted by an organic molecule [4]. This system has a characteristic feature: its vibrational modes. Thus, we have studied an organic molecule with a vibrational mode embedded in an electromagnetic cavity.

First, we study the energy spectrum of the system (chapter 2) and the ultratrong effects found in it. In other words, the effect of the terms of the Rabi Hamiltonian [5] which do not conserve the number of excitations. In order to do that we use several techniques such as the Polaron transformation and the perturbation theory; or numerical techniques such us the exact diagonalization.

Then, we continue with the study of the dynamics of the system (chapter 3). Thus, we modelize the energy losses using the formalism of the master equation [6]. In this formalism, we study the Rabi oscillations and the decay of the system and their dependence with the coupling with the vibrational mode. Furthermore, we analyze the spectrum of the Lindbladian in order to obtain the most relevant transitions of the dynamics.

Next, we calculate the noise spectrum [7] of the system (chapter 4) which, as we show, also presents some ultrastrong effects. At the end, we consider the molecule placed in a waveguide (chapter 5) and study the bound states [8] which appear around the emitter.

Resumen

El estudio en el campo de la *electrodinámica cuántica de cavidad* (*cavity Quantum Electrodynamics* (*QED*)) durante el último siglo [1] ha permitido la interacción coherente (oscilaciones *Rabi*) de la luz con la materia, alcanzándose así, el régimen conocido como *acoplamiento fuerte* o *strong coupling*.

Existen multitud de plataformas experimentales para el estudio de la interacción luz-materia; desde *osciladores nano-mecánicos* (*nano-mechanical oscillators*) [2] a sistemas de átomos artificiales formados a partir de *uniones Josephson*. Estos últimos sistemas han permitido la construcción del primer ordenador cuántico por Google en 2019 [3].

En este trabajo, nos hemos centrado en un sistema de dos niveles constituído por una molécula orgánica [4]. Un sistema como este, presenta una característica diferenciadora, los modos de vibración. Estos son parametrizados a través del denominado como factor de *Huang-Rhys* [9] (1950). Así, hemos estudiado una molécula (sistema de dos niveles) con un modo de vibración, embebida en una cavidad electromagnética. En primer lugar, estudiamos el espectro de energías del sistema (capítulo 2) y los efectos *ultrastrong* en el mismo. Es decir, el efecto en el sistema de los términos que no conservan el número de excitaciones en el modelo de *Rabi* [5]. Para ello, usamos técnicas tales como la transformación de *Polarón* y la teoría de perturbaciones; o técnicas numéricas como la diagonalización exacta.

Seguidamente, continuamos estudiando la dinámica del sistema (capítulo 3). Así, modelizamos las pérdidas energéticas usando el formalismo de la *ecuación maestra* [6]. Con ello, estudiamos la dependencia de la frecuencia *Rabi* del sistema y el decaimiento con el acoplo de la molécula con su modo de vibración. Además, analizamos el espectro del *Lindbladiano* para obtener las transiciones más relevantes en la dinámica.

A continuación, calculamos el *espectro de ruido* (*noise spectrum*) [7] del sistema (capítulo 4), estudiando de nuevo los efectos *ultrastrong* en el mismo. Por último, insertamos nuestro sistema en una guía de ondas (capítulo 5) y estudiamos los *estados ligados* (*bound states*) [8] que se forman entorno al emisor.

Chapter 1

Introduction

The interaction between the light and matter has been intensively studied during the last century. Here, our interest is the study of the interaction of molecules with light and the influence of vibrations in their energy spectrum and their dynamics. This is an important question that we are going to answer through this thesis. But, how did this story begin?

1.1 Cavity Quantum Electrodynamics, How does matter interact with light?

The emission of a photon by an excited atom (or a molecule) in free space is an irreversible process known as spontaneous emission. The photon propagates away and the atom does not reabsorb it. One reason for that is the value of the light-matter interaction strength: It is proportional to the fine structure constant[1] $\alpha = 1/137$, whose smallness makes it possible to treat this phenomenon perturbatively [10]. Thus, at first sight, we cannot obtain coherent light-matter interactions. In other words, it is hard to obtain a periodic energy exchange between light and matter. So, how could we get such a coherent interaction?

The solution is to confine the light in a "photon box" in a similar fashion as Einstein and Bohr thought in one of their Gedanken-Experiments [11]. In our case, this "photon box" consists of a cavity whose walls are highly reflecting mirrors. So, the photons will "bounce" against the walls over and over again, enabling the atom to reabsorb the photons. Thus, we will obtain the desired periodic coupling.

[1] Remember: $\alpha = e^2/(4\pi\epsilon_0\hbar c)$, where e is the elementary charge, c the speed of light in vacuum, $\hbar = h/2\pi$ the reduced Planck constant and ϵ_0 is the electric permittivity of vacuum.

However, this is a long story which did not start from this stage. First, the light-matter interaction was studied by *Rabi* [5, 12] in 1936, using a semiclassical model. He described the simplest case, the interaction between a classical light mode of frequency ω_c and a dipole. The *Rabi* model is the main model in the field in order to describe the light-matter interaction. Its quantum version [13] has been used in a large number of systems from quantum optics to solid-state platforms. This field is known as *cavity Quantum Electrodynamics* (*cavity QED*). It studies the interaction between a two-level system and an electromagnetic mode of an optical or microwave cavity.

Afterwards, in the context of magnetic resonance, Purcell [14] showed in 1946 that the spontaneous emission rate of a quantum system could be enhanced by its environment. This enhancement occurs when we embed the atom to a resonant cavity with a magnitude given by the *Purcell factor* F_{cav}:

$$F_{cav} = \frac{3}{4\pi^2}\frac{\lambda^3 Q}{V} \tag{1.1}$$

where λ is the light wavelength within the cavity, V the cavity mode volume and Q the quality factor which is related to the cavity losses. So, we can engineer our environment in order to enhance the spontaneous emission. For instance, modifying the volume or the quality factor of our cavity reducing the losses.

Then, in 1963, Jaynes and Cummings developed a simplified model of the semiclasical *Rabi* model, the *Jaynes-Cummings* model [15] which neglects some rapid oscillating terms whose average is negligible when the light-matter interaction is weak. This is the *Rotating Wave Approximation* which we will see in detail in the following sections.

Afterwards, in the decade of 1970's, many groups were interested in Rydberg atoms for their *Cavity Quantum Electrodynamics* experiments. In these atoms one of the electrons is excited to a state of very high principal quantum number. The usual example are excited valence electrons of the alkali atoms [16].

In particular, some of these atoms have states whose classical limit is described by an electron in a circular orbit. These are the *circular Rydberg atoms*. They have very attractive properties such as: (i) they act as a "two-level" atoms, (ii) the dipole moments of the allowed trasitions are large, which enable high light-matter couplings, and (iii) they have states with long lifetimes [17].

Using Rydberg atoms in a cavity made of copper mirrors in 1983, Goy, Haroche *et al.* [18] showed the *Purcell effect* in the context of microwave cavities. They showed that the spontaneous emission of Rydberg atoms was enhanced when they crossed a resonant cavity with a high Q, as we can see in the figure 1.1.

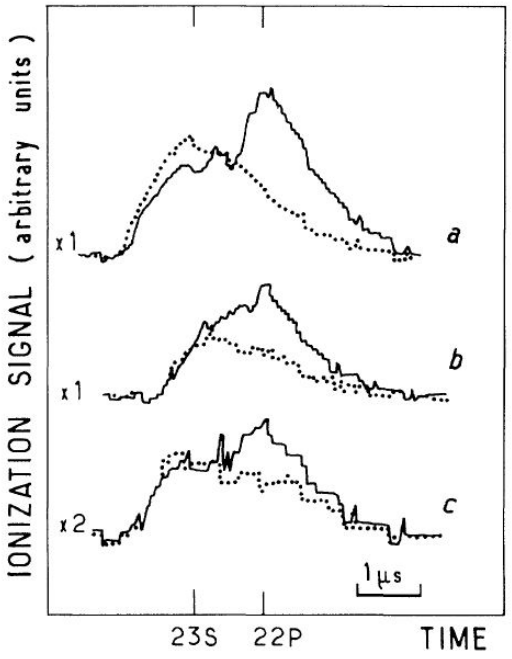

Figure 1.1: Cavity-enhanced spontaneous emission signals. The dotted lines are off-resonant cavity and the continuous lines the resonant cavity. The different letters (a, b and c) correspond to different cases. The figure was obtained from [18], see that reference for more details.

However, the coherent dynamic behaviour was still to be observed. This periodic exchange of energy between light and matter had been predicted before in the context of the Jaynes-Cummings model by Eberly *et al.* [19] in 1980. They predicted an oscillations with a frequency known as *vacumm Rabi frequency*. This regime is known as the *strong coupling* regime. But, in order to reach it, we need to confine the photon for a sufficiently long time by reducing the losses of the cavity [16].

Thus, the objective was to increase the quality factor Q and reach the *Holy Grail*, the *strong coupling*, using the words of the Nobel laureate Haroche [1]. Nevertheless, it was Meschede *et al.* [20] who achieved this "holy cup" in 1985, Munich. The key was to replace the open cavities by a closed cylinder. Thus, they increased the lifetime of the photons several orders of magnitude. But, they could not yet directly observe the Rabi oscillations.

Moreover, this closed cavity had some problems. The Rydberg atoms had to pass through small metallic holes which produced stray electrical fields when the atoms crossed. This perturbed the sensitive Rydberg atoms. The solution was to come back to the open cavities avoiding these "annoying holes". In 1996, using superconducting copper mirrors with sputtered Niobium in an open cavity, Haroche *et al.* [21] reached the strong coupling regime. In the same year, using another type of experiment, Wineland *et al.* [22] also reached the *strong coupling* regime. Haroche and Wineland were awarded with the *Nobel prize* in 2012 by these contributions in the field of *Cavitiy Quantum Electrodynamics*.

On the one hand, the Haroche's experiment in the Ecole Normale Supérieure (ENS) in Paris, consisted of trapping photons in a cavity with highly reflecting mirrors. They used a beam of excited Rydberg atoms to study their dynamics, see figure 1.2a. Thus, they obtained the *Rabi oscillations* in the probability to find the Rydberg atoms in the ground state, see figure 1.2b.

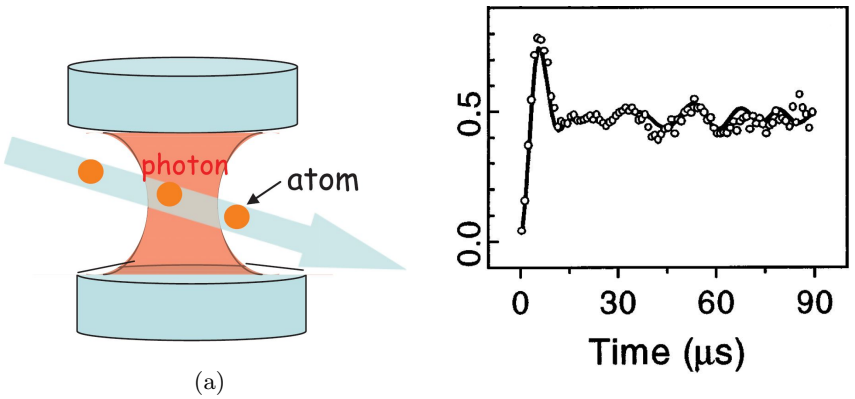

(a) (b)

Figure 1.2: (a) Schematic figure of the Haroche's *et al.* [21] experiment where they reached the strong coupling regime. Figure obtained from Haroche's Nobel Lecture [1]. (b) Rabi oscillations, probability to find the Rydberg atom in the ground state versus time. Figure obtained from Haroche's *et al.* article [21]

On the other hand, the Wineland's experiment in the National Institute of Standards and Technology (NIST) in Boulder, consisted of trapping Beryllium ions with a configuration of fields produced by electrodes. They also used laser beams to detect and manipulate photons and study the dynamics of the system, see figure 1.3a. Thus, they obtained the *Rabi oscillations* in the ground state probability of the ions, see figure 1.3b.

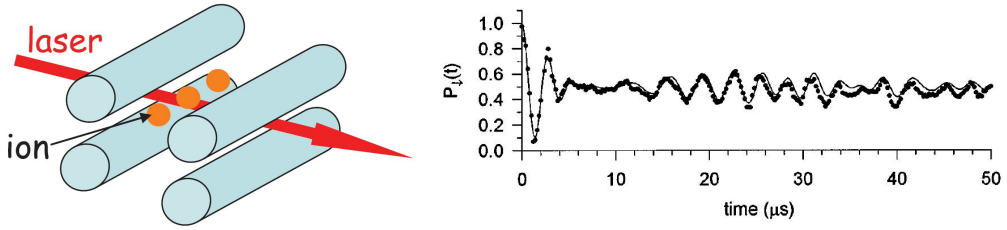

(a) (b)

Figure 1.3: (a) Schematic figure of the Wineland's *et al.* [22] experiment where they reached the strong coupling regime. Figure obtained from Haroche's Nobel Lecture [1]. (b) Rabi oscillations, probability to find the Berylium ions in the ground state versus time. Figure obtained from Wineland's *et al.* article [22]

Here, we have just reviewed the main milestones of *cavity Quantum Electrodynamics* field history. A very good and more detailed review of the topic can be found in Haroche's Nobel Lecture [1] or in the reviews by Forn-Diaz and Frisk [23, 10]. The next section 1.2 is devoted to present the main models used in the field.

1.2 Light-matter interaction models

In this section, we describe the main models used in *cavity QED*. First, we are going to start with the *Rabi* and *Jaynes-Cummings* models. We just provide a brief glance of them; their first principles derivation can be consulted in the appendices A and B. The Hamiltonian[2] of the *Rabi* model is:

$$\hat{\mathcal{H}}_{Rabi} = \hbar\Delta\hat{\sigma}^{+}\hat{\sigma}^{-} + \hbar\omega_c\hat{a}^{\dagger}\hat{a} + \hbar g\hat{\sigma}_x(\hat{a}^{\dagger} + \hat{a}) \tag{1.2}$$

where $\hat{a}^{\dagger}$ and $\hat{a}$ are bosonic creation annihilation operators $[\hat{a}, \hat{a}^{\dagger}] = 1$, ω_c is the cavity frequency, and the Pauli matrices $\hat{\sigma}^{+}$ and $\hat{\sigma}^{-}$ create and annihilate an exciton of energy Δ respectively. Finally, the last term ($\hat{H}_{int}$), represents the light-matter coupling whose strength is measured by the parameter g. Recalling that $\hat{\sigma}_x = \hat{\sigma}^{+} + \hat{\sigma}^{-}$, we can rewrite the last term or interaction Hamiltonian:

$$\hat{H}_{int} = g(\hat{\sigma}^{+} + \hat{\sigma}^{-})(\hat{a}^{\dagger} + \hat{a}) = g(\hat{\sigma}^{-}\hat{a}^{\dagger} + \sigma^{+}\hat{a}) + \underbrace{g(\hat{\sigma}^{+}\hat{a}^{\dagger} + \hat{\sigma}^{-}\hat{a})}_{\text{conterrotating terms}} \tag{1.3}$$

[2]Hereafter, we will take $\hbar = 1$ in order to simplify the expressions.

The first terms of (1.3) conserve the number of excitations ($\hat{N}_{ext} = \hat{\sigma}^+\hat{\sigma}^- + \hat{a}^\dagger\hat{a}$) as they are compose of one operator that creates one excitation (electron excitation or photon) and one that anihilates the other one. On the contrary, the last two terms (known as counterrotating terms) either create or destroy two excitations at the same time.

Up to 2004 [24, 23] the experiments had a very small light-matter coupling g [see figure 1.10], when compared with a characteristic energy of the system such as the cavity frequency ω_c ($g/\omega_c \ll 1$). In this case, the counterrotating terms can be neglected leading to what is known as the *Rotating Wave Approximation* (RWA). In order to justify this approximation, we are going to change to the *Interaction picture* an take as the exactly solvable part $\hat{H}_0$ of the *Rabi Hamiltonian* (1.2):

$$\hat{H}_0 = \omega_c\hat{a}^\dagger\hat{a} + \Delta\hat{\sigma}^+\hat{\sigma}^- \tag{1.4}$$

So, in the *Interaction picture*, a state reads:

$$|\psi(t)\rangle = \exp[-i\hat{H}_0]\,|\psi^{(I)}(t)\rangle \tag{1.5}$$

Besides, we know the form Schrödinger equation in the *Schrödinger picture*. Thus, using equation (1.5), we can easily get its *Interaction picture* counterpart:

$$i\frac{d\,|\psi^{(I)}(t)\rangle}{dt} = \hat{H}^I_{int}\,|\psi^{(I)}(t)\rangle \tag{1.6}$$

where $\hat{H}^{(I)}_{int}$ is:

$$\hat{H}^{(I)}_{int} = \exp[i\hat{H}_0]\hat{H}_{int}\exp[-i\hat{H}_0] \tag{1.7}$$

So, it can be easily shown [cf. [25]] that the *Interaction picture* version of the interaction Hamiltonian $\hat{H}_{int}$ takes the form of:

$$\hat{H}^{(I)}_{int} = g(\hat{\sigma}^-\hat{a}^\dagger e^{i(\omega_c-\Delta)t} + \hat{\sigma}^+\hat{a}e^{-i(\omega_c-\Delta)t} + \hat{\sigma}^-\hat{a}e^{i(\omega_c+\Delta)t} + \hat{\sigma}^+\hat{a}^\dagger e^{-i(\omega_c+\Delta)t}) \tag{1.8}$$

As we have just noticed the Schrödinger equation (1.6) is a first order differential equation in time. Hence, the time integration will bring us factors proportional to $\propto g/(\omega_c - \Delta)$ in some terms and proportional to $\propto g/(\omega_c + \Delta)$ in other terms. When $g \lll \omega_c$, Δ and $\omega_c \sim \Delta$, we will get that $g/(\omega_c + \Delta) \lll g/(\omega_c - \Delta)$. Therefore, we can neglect the rapidly oscillating terms (the counterrotating terms $\hat{\sigma}^-\hat{a}$ and $\hat{\sigma}^+\hat{a}^\dagger$), see [25] for more details. This approximation is known as ***Rotating Wave Approximation***. Thus, coming back to Schrödinger picture, we have:

$$\hat{H}_{int} \approx g(\hat{\sigma}^-\hat{a}^\dagger + \hat{\sigma}^+\hat{a}) \tag{1.9}$$

The model, (1.2) with the interaction term approximated by $\hat{H}_{int}$ in (1.9), is known as *Jaynes-Paul-Cummings* (JC) the model [15] (1963):

$$\hat{\mathcal{H}}_{JC} = \hbar\Delta\hat{\sigma}^{+}\hat{\sigma}^{-} + \hbar\omega_c\hat{a}^{\dagger}\hat{a} + \hbar g(\hat{\sigma}^{-}\hat{a}^{\dagger} + \sigma^{+}\hat{a}) \tag{1.10}$$

Both *Rabi* (1.2) and the *Jaynes-Cummings* models represent the interaction of a two-level atom or molecule coupled to single electromagnetic field mode. Then, in section 1.6, we will add energy losses using the master equation formalism. See figure 1.4 for a schematic view.

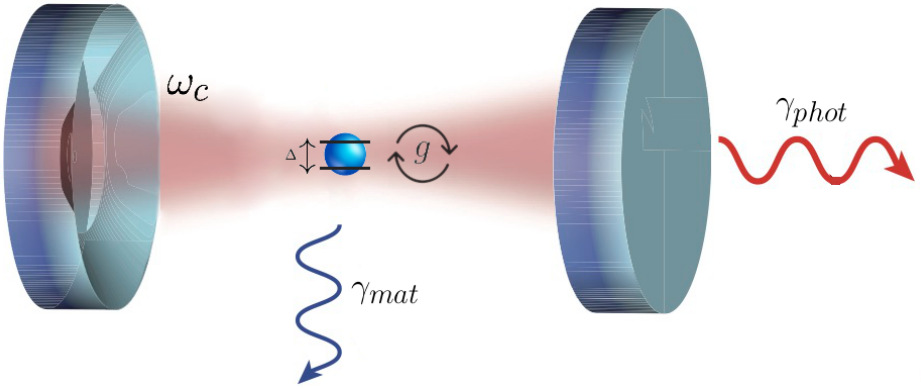

Figure 1.4: Cavity with a two-level system with an energy splitting Δ, a cavity frequency ω_c and a light-matter coupling g. There are tow main losses channels, the photon leakage through the mirrors γ_{phot} and the matter losses γ_{matt}.

Due to the fact that the *Jaynes-Cummings* Hamiltonian (1.10) conserves the number of excitations $\hat{N}_{ext}$, its energy spectrum is well known. This diagonalization is done in subspaces with a fixed number of excitations. Its eigenstates and eigenenergies, known as the *polaritons*[3] are given by:

$$|P_{\pm}^{(n)}\rangle \frac{1}{\sqrt{\tau_{\pm n}^2 + 1}}(\tau_{\pm n}\,|\uparrow\ n-1\rangle + |\downarrow\ n\rangle) \qquad \epsilon_{\pm n} = n\omega_c + \tau_{\pm n}g\sqrt{n} \tag{1.11}$$

where n is the number of photons, $\uparrow$ / $\downarrow$ the excited/ground state of matter and:

$$\tau_{\pm n} = \frac{\delta \pm \sqrt{4g^2 n + \delta^2}}{2g\sqrt{n}}, \qquad \delta = \Delta - \omega_c \tag{1.12}$$

Thus, we have classified the states by their number of total excitations. However, this does not happen with the *Rabi* model (1.2). It only conserves the parity operator $\hat{P} = \exp(i\pi\hat{N}_{ext})$. This allows us to classify the spectrum in

[3] States formed by the mixing of light and matter excitations.

states with positive and negative parity. Fortunately, an analytical solution was found in 2011 [13]. However, this solution is quite complicated. It requires to solve transcedental equations. In any case, we can also obtain numerically the eigenstates and eigenenergies of the Rabi model (1.2) using diagonalization in a truncated (but sufficiently large) Fock space of excitations. Figure 1.5 shows the comparison between the energy spectrum of the Jaynes-Cummings (1.10) and the Rabi model (1.2) as a function of the light-matter coupling g at the resonant condition $\Delta = \omega_c$:

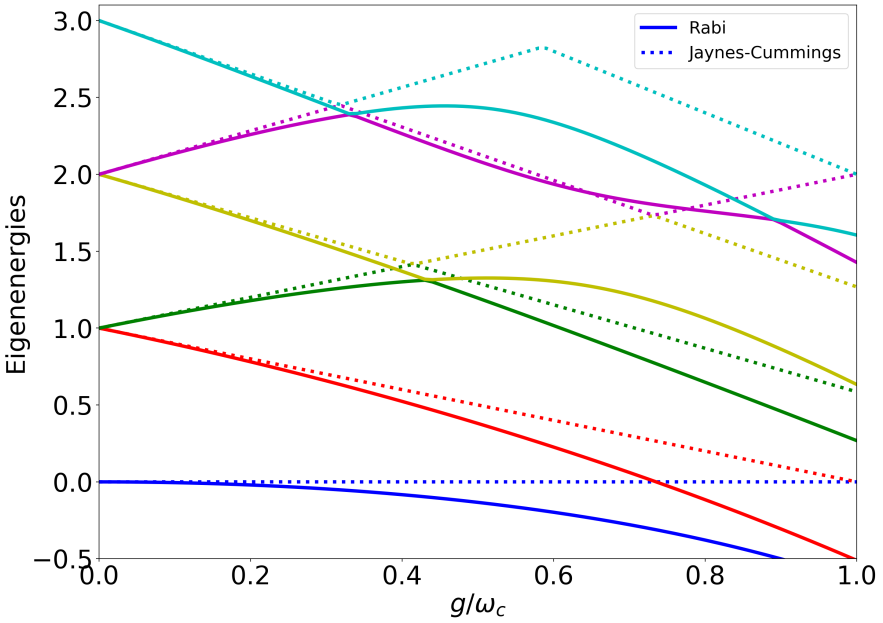

Figure 1.5: Energy spectrum of the *Rabi* model (1.2) (continuous lines) and of the *Jaynes-Cummings* model (1.10) (dotted lines) versus the normalized light-matter coupling g/ω_c. We have set the resonance condition $\Delta = \omega_c$.

In the figure 1.5, we can see that, for $g/\omega_c \ll 1$, the energies of *Rabi* (1.2) and *Jaynes-Cummings* (1.10) models are virtually equal. Confirming the validity of the *Rotating Wave Approximation* (RWA) in this regime.

There are two generalizations to the *Rabi* (1.2) and *Jaynes-Cummings* (1.10) Hamiltonians when many molecules couple to light. The first one is the *Dicke* model [26] (1954), a generalization of the *Rabi* model (1.2). Its Hamiltonian is (see [27]):

$$\hat{H}_{Dicke} = \hbar\Delta \sum_j^N \hat{\sigma}_j^+ \hat{\sigma}_j^- + \hbar\omega_c \hat{a}^\dagger \hat{a} + \frac{\hbar 2g}{\sqrt{N}} \sum_j^N (\hat{\sigma}_j^+ + \hat{\sigma}_j^-)(\hat{a}^\dagger + \hat{a}) \qquad (1.13)$$

where $\hat{\sigma}_j^+$ and $\hat{\sigma}_j^-$ are the Pauli matrices which create an exciton in the j-molecule. This model describes the light-matter coupling of N two-level

molecules or atoms in a cavity of frequency ω_c. Again, as the *Rabi* model (1.2), it has counterrotating terms. When we perform the *Rotating Wave Approximation* over the *Dicke* model, we obtain the *Tavis-Cummings* model [28] (1968). It is the equivalent of the *Jaynes-Cummings* model (1.10), but with N molecules coupled to light. Its Hamiltonian is (see [27]):

$$\hat{H}_{TC} = \hbar\Delta \sum_j^N \hat{\sigma}_j^+ + \hbar\omega_c \hat{a}^\dagger \hat{a} + \frac{\hbar g}{\sqrt{N}} \sum_j^N (\hat{\sigma}_j^- \hat{a}^\dagger + \hat{\sigma}_j^+ \hat{a}) \tag{1.14}$$

We can see an schematic view of these models in figure 1.6.

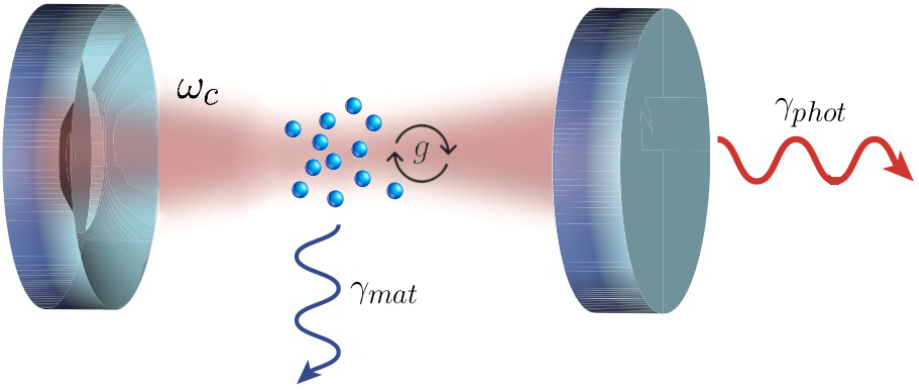

Figure 1.6: Cavity with a N two-level systems with an energy splitting Δ, a cavity frequency ω_c, a light-matter coupling g, a leakage rate through the mirrors γ_{phot} and the exciton decay rate γ_{matt}.

For completeness of this section, we have added at the end of the document some appendices, the quantization of the electromagnetic field can be found appendix A. Then, we explore how to modelize the light-matter coupling and we get the *Rabi* Hamiltonian (1.2) [cf. appendix B]. There are many books [29, 30, 31, 32, 33] where these developments are developed in a more comprehensire way. Here, as main references, we mainly use the book by Schleich [25], chapters 10, 14 and 15, the book by Nolting [34] and Zueco's review [24].

1.3 Light-matter Coupling Regimes

In this section, we are going to explore the different types of regimes in *Cavity Quantum Electrodynamics*. First, we are going to see the difference between *weak* and *strong coupling* regimes (see Zuecos' review [24] for a detailed explanation which we have followed here). Imagine that your atom is in the excited state, $|\psi(0)\rangle = |\uparrow, 0_{phot}\rangle$ and it is embedded in a cavity at resonance with the atom ($\delta = \omega_c - \Delta = 0$). Thus, using the *Jaynes-Cummings* model (see equations [1.10-1.11]), we can calculate the evolution of our state $|\psi(t)\rangle$ and the probability $P_\uparrow$ to find the atom in an excited state as a function of time:

$$P_\uparrow = \mathrm{Tr}_c[|\uparrow\rangle\langle\uparrow| \, |\psi(t)\rangle\langle\psi(t)|] = \cos(2gt) \tag{1.15}$$

These are the so called *Rabi oscillations*: the coherent exchange of energy between light and matter. However, as we said in our historical introduction, *Rabi ocillations* are not easy to see. The reason is that systems have losses, coming from two main channels: The photon leakage through the mirrors of the cavity (the radiative losses γ_{phot}) and the decay of the atom to other channels apart from the cavity photons (the non-radiative losses γ_{matt}). We can include the losses through the master equation formalism which we will see in the section 1.6. A simplied master equation for this system is:

$$\dot{\rho} = -i[\hat{\mathcal{H}}_{JC}, \rho] - \gamma_{phot}(\hat{a}\rho\hat{a}^\dagger - \frac{1}{2}\{\hat{a}^\dagger\hat{a}, \rho\}) - \gamma_{matt}(\hat{\sigma}^-\rho\hat{\sigma}^+ - \frac{1}{2}\{\hat{\sigma}^+\hat{\sigma}^-, \rho\}) \tag{1.16}$$

where ρ is the density matrix of the system. Solving this equation we obtain the damped *Rabi oscillations*:

$$P_\uparrow = e^{-(\gamma_{phot}+\gamma_{matt})t}\cos(2\sqrt{g^2 - (\gamma_{matt}+\gamma_{phot})^2/4}\ t) \tag{1.17}$$

So, in order to resolve coherent exhange of light and matter: $g^2 - (\gamma_{matt} + \gamma_{phot})^2/4 > 0$. Therefore, it has to be fullfilled the condition $g > (\gamma_{matt} + \gamma_{phot})/2$. This is known as the *strong coupling* regime. In other words, it is the regime where the losses are small enough to allow a coherent dynamics. On the contrary, we are in the *weak coupling* regime (an overdamped regime).

After Haroche's and Wineland's experiments [21, 22, 35], the *strong coupling* was reached for a single atom in microwave [20] and optical [36] cavities. Furthermore, it was reached by systems whose two-level systems are "artificial atoms", such us quantum dots [37] or superconducting circuits [38].

We have just compared the coupling strength g with the dissipation rates of the system, giving rise to the *weak* and *strong coupling*. Hereafter, we are going to compare it with a characteristic energy of the system such as cavity or photon frequency ω_c. We call this parameter $\eta \equiv g/\omega_c$. Its value can be estimated [23] using typical values of common experimental setups as Fabry-Perot cavities:

$$\eta \equiv g/\omega_c = -\frac{\vec{d}\cdot\vec{E}}{\hbar\omega_c} = |\vec{d}|\sqrt{\frac{2\pi c\alpha}{e^2\omega_c V_m}} \tag{1.18}$$

where $\vec{d}$ is the transition dipole moment, $\vec{E}$ the electric field, c the speed of light, e the electron charge, α the fine-structure constant and V_m the cavity mode volume. The typical value of the mode volume in a Fabry-Perot optical cavity [39] is $V_m \sim 10^{-15}\ m^3$. It is also typical to use an alkali element, such as Cesium or Rubidium, that have dipole moments of the order of $|\vec{d}| \sim 10^{-29}\ Cm$. Hence, for a cavity with $\omega_c = 351.7$ THz (resonant with a Cesium atom), we get a value of $g/\omega_c \sim 10^{-7}$. Therefore, the counter-rotating terms can be safely neglected and thus be within the domain of *Jaynes-Cummings* (1.10) model, using the already mentioned RWA.

Henceforward, the efforts were focussed on raising this parameter η in order to study the physics of the Rabi model (1.2). This regime, where we have to take into account the counterrotating terms, is known as *Ultrastrong Coupling*[4]. These terms hybridize states with different number of excitations. An accepted rule of thumb is that *Ultrastrong coupling* effects require $\eta > 0.1$. Although this is not a well defined boundary. In figure 1.5, we saw the effect of the *Ultrastrong coupling* in the deviation between the eigenvalues of the RWA (1.10) and those of the quantum *Rabi* model (1.2). We highlight some aspects to take into account in the *Ultrastrong coupling* regime:

- **Ground state properties:** When the relative coupling $g/\omega_c \ll 0.1$, we are in the domain of the *Jaynes-Cummings model* (1.10). The ground state of the system in that regime is the vacuum. In other words, there is not any photon in the cavity and the atom is in its ground state. Nonetheless, in the *Ultrastrong coupling*, the picture changes dramatically. The ground state of the system populates with both atomic and photonic excitations [40, 41].

  These ground state photons are strongly bound to the atom [42]. So, these are considered as "virtual photons" [10]. They cannot be detected with a photoabsorver inside the cavity. Although, there are some alternative proposals in order to detect them [10, 43, 44].

[4] We recommend the reviews [23, 10] to inquire as to the topic

- **Diamagnetic term:** We have to notice that even the *Rabi* model (1.2) is a simplified model of the light-matter interaction. As we can see in detail in appendix B, the light-matter coupling is introduced through the minimal coupling substitution:

$$\hat{p} \longrightarrow \hat{p} + \hat{A} \tag{1.19}$$

  where $\hat{A}$ is the magnetic vector potential operator proportional to $\propto (\hat{a}+\hat{a}^\dagger)$ and $\hat{p}$ the momentum. We perform this substitution in the kinetic Hamiltonian $H_{kin} = \hat{p}^2/2\mu$, where μ is the reduced mass of the system proton-electron, which it is the simplest atom. So, using the minimal coupling substitution, we get a term proportional to $\propto \hat{p}\hat{A}$ which we will give us the light-matter interaction of the *Rabi* model $g(\hat{\sigma}^+ + \hat{\sigma}^-)(\hat{a}^\dagger + \hat{a})$.

  Besides of this term, we obtain another term proportional to $\hat{A}^2 \propto g^2(\hat{a}+\hat{a}^\dagger)^2$. This is known as the diamagnetic term, which give us quadratic terms such as $g^2\hat{a}^\dagger\hat{a}$. So being of order g^2, it is usually neglected in the context of *Jaynes-Cummings* regime. However, this term has to be taken into account in the *Ultrastrong* regime and it is unavoidable in the *Deep-strong coupling* regime, where $g/\omega_c > 1$.

  Due to its importance in the *Ultrastrong* and *Deep-strong* regimes, we will include this term in our model using a Bogoliubov transformation at the expense of renormalizing the photon frequency $\omega_c \to \sqrt{\omega_c^2 + 4\omega_c D}$ (where D is a measure of the diamagnetic term) [10, 45].

There are many other *Ultrastrong* effects. For instance, the thermally emitted photons are emitted bunched (in groups of photons) in a cavity; and the atomic emission is anti-bunched (each photon is emitted one by one). However, in the *Ultrastrong coupling* regime, it is the other way round. The thermally emitted photons are emitted anti-bunched in a cavity; and the atomic emission is bunched. [46, 47].

In order to reach the *Ultrastrong coupling* regime, there are many strategies to enhance η. For instance, it can be increased by coupling N dipoles to the same cavity mode (the *Dicke* model predicts an effective g proportional to $\propto \sqrt{N}$). Furthermore, we can increase the value of the dipole moment (for example the Rydberg atoms have a very large value of $\vec{d}$) or we can reduce the volume of our cavities.

The *Ultrastrong coupling* was reached in 2005 using intersubband polaritons [48]. Next, a microwave cavity embedded in a quantum well reached *Ultrastrong coupling* [49] in 2009. They got a value of $\eta = 0.11$. Then using superconducting circuits as "artificial atoms" also reached *Ultrastrong* coupling in 2010 [50]. They obtained values of $\eta = 0.10 - 0.12$.

We stress that the *Ultrastrong coupling* regime is not a strong coupling one with greater g. On the one hand, in the *strong coupling*, we are in a situation where the energy losses are much smaller than the coupling g, and the *Rabi oscillations* can be resolved. On the other hand, the *Ultrastrong coupling* compares the coupling g with the cavity frequency ω_c. Thus, we can be in the *Ultrastrong coupling* and the *weak coupling* at the same time, the *weak Ultrastrong coupling* regime, see figure 1.7.

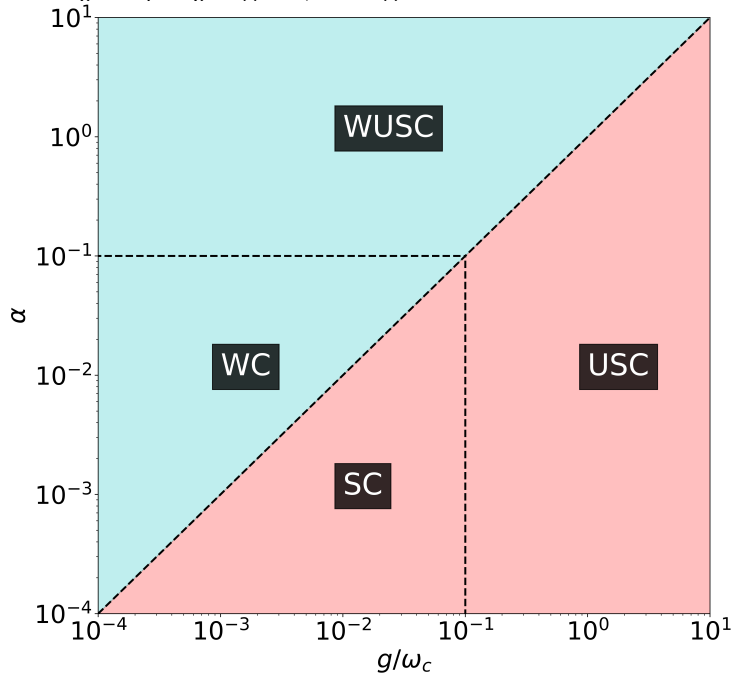

Figure 1.7: Scheme of the main regimes of *Cavity Quantum Electrodynamics*. The red region marks where the *Rabi oscillations* occur, the *strong coupling* region (SC and USC). The blue region marks where the system is overdamped and there are not *Rabi oscillations*. The *weak Ultrastrong coupling* (WUSC) and the *Ultrastrong coupling* (USC) mark the regions where the counterrotating terms are relevant. The parameter α is a proportionality constant of the matter losses γ_{matter}. Figure obtained from [51].

Inside the *Ultrastrong coupling* regime, we distinguish two regions: a pertubative region ($0.1 \lesssim g/\omega_c \lesssim 0.3$) and a nonperturbative one ($0.3 \lesssim g/\omega_c \lesssim 1$) [52], depending on whether the counterrotating terms can be treated as a perturbation or not. When $g/\omega_c > 1$ the system is said to be in the *Deep strong coupling* regime. This regime is characterised by high-order-perturbative processes. It was theoretically predicted in 2010 by Casanova *et al.* [53] and experimentally explored in 2017 by Bayer *et al.* [54], reaching the record with $\eta = 1.43$. However, in general, these limits between regimes are sharply defined, see for example the figure 1.8 for a schematic view of these regimes for the energy spectrum of *Rabi* model (1.2) as a function of g/ω_c, (see [52, 23] for more details).

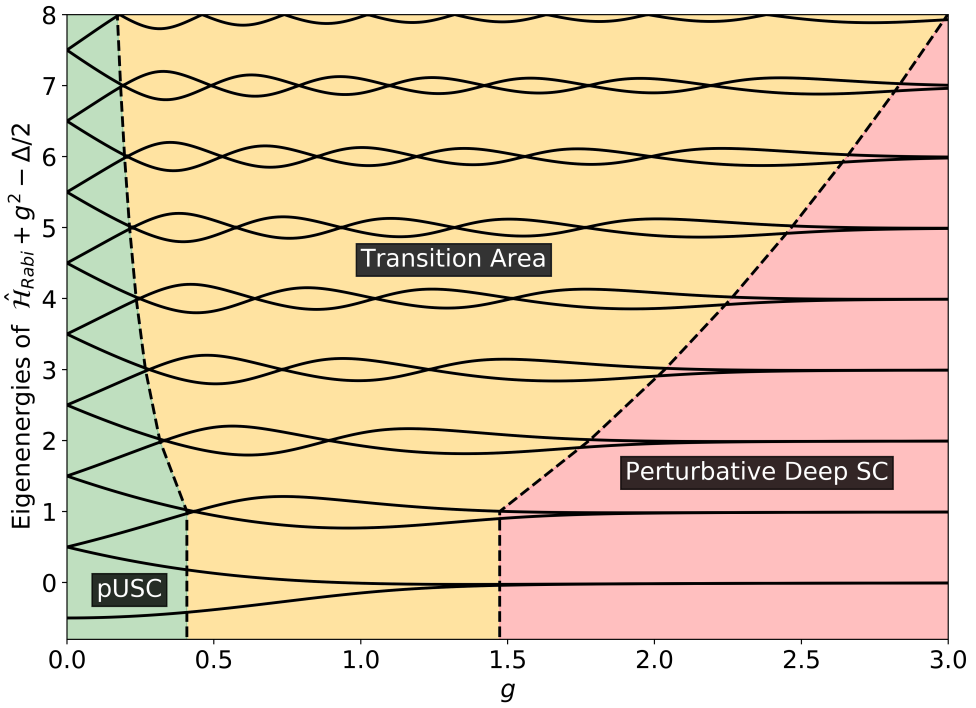

Figure 1.8: Classification of the different regimes of the *Rabi model* (1.2). The parameters ω and g_0 correspond to ω_c and g. The green area belongs to the *perturbative Ultrastrong coupling* (pUSC), the yellow to the transition area *nonperturbative Deep-strong coupling* (Deep SC); and the red area to the *perturbative Deep strong coupling*. Figure obtained from [52].

1.4 Experimental setups

Until now, we have seen the origin of *cavity QED* and its main models and regimes (*Weak*, *Strong*, *Ultrastrong* etc.). Now, we will discuss the plethora of realizations of the *Cavity Quantum Electrodynamics*. Then, we will center our attention in the study of the coupling between a molecule and a cavity mode and the vibrations (phonons). So, the most important experimental setups are:

- **Superconducting circuits:** In this experimental realization (called *circuit Quantum Electrodynamics*). The atoms have been substituted by superconducting circuits with Josephson junctions. These have an energy level structure similar to the natural atoms, playing the role of two-level systems. Thus, they are usually called "artificial atoms". They are coupled to photons in resonators composed by an inductance and a capacitance. This coupling between the artificial atom and the resonator can also be modelized by the *Jaynes-Cummings* (1.10) or the *Rabi* (1.2) Hamiltonians. See figure 1.9 for a schematical representation of these systems, and [23] for a review of *circuit Quantum Electrodynamics*.

  These systems were used firstly in 2004 [55]. Wallraff *et al.* used a superconducting coplanar waveguide and a charge qubit as an "atom". They reached the *strong coupling* regime with a coupling of $g/\omega_c \sim 10^{-3}$ (clearly, not in the *Ultrastong coupling* regime yet).

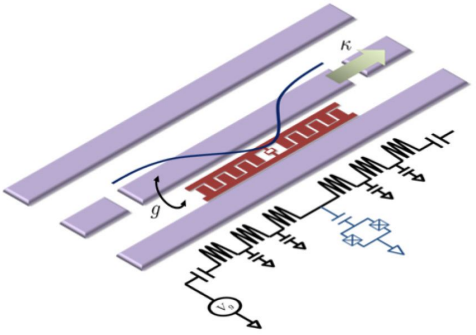

Figure 1.9: A scheme of a realization of circuit QED (the qubit, in red, is not in scale). Figure obtained from [24].

  The *Ultrastrong coupling* regime was achieved in 2010, in the Walter Meissner Institute, by Niemczyk *et al.* [50]. They obtained a coupling of $g/\omega_c \approx 0.1$. Besides, *Ultrastrong coupling* was also reached the same year in Delf by Forn-Diaz *et al.* [56] using an LC-resonator. Eventually, *Deep-Strong coupling* was reached in 2017 by Yoshihara *et al.* [57].

Thanks to the lithographic methods, these circuits are a great candidate for quantum information applications. Thus, they have been used in quantum information processing such as the engineering of quantum gates. In this way; in 2019, in Google labs, John Martinis' group [3] were able to build an quantum computer of 53-qubits. They generated a quantum state of 53-qubits and measured the bit distribution.

- **Organic molecules**: Recently, organic molecules has been considered as candidates for two-level systems in *cavity Quantum Electrodynamics*. These systems consist of thin films of organic molecules with enormous dipole moments sandwiched between metallics mirrors. Thanks to those large dipole moments, these systems are able to achieve *Ultrastrong coupling* regime, with couplings in the order of $\eta \sim 0.3$ [4].

  There have also been experimental realizations with a small number of organic molecules in cavities [58], even reaching the single molecule limit in the case of plasmonic cavities [59, 60].

  Moreover, when a bunch of these molecules is set in an extended cavitiy, it has been reported that their chemical reaction rates [61], the exciton transport [62, 63] or the electronic conductivity [64] are modified.

  It is also easy to think that these molecules present peculiarities associated to their manifold of vibrational excitations. In this thesis, we are going to study the coupling of a molecule to light and the *Ultrastrong coupling* effects. So, we will take into account these vibrations in our model. This will be done in section 1.5, where we introduce the *Holstein model*. This model describes an organic molecule with intramolecular vibrations. To this we will add the *quantum Rabi model (1.2)* which give us the light-matter interaction.

  Organic molecules have also been also considered as two-level systems in 1D waveguides in the optical [65] and microwave [66] regimes, with interesting applications in the field of quantum information.

- **Optomechanics:** This field consists of nano-mechanical oscillators coupled to atomic systems or electromagnetic field resonators [2, 67]. These systems have recently also achieved the *Ultrastrong coupling regime*, reaching a coupling of $\eta \sim 0.3$, using a setup of a plasmonic cavity coupled to the vibrational degrees of freedom of individual molecules [68].

Benz *et al.* [68] showed that single molecules can be trapped inside the gap of a plasmonic nanoassembly. There, the light is localized in a volume below 1 nm^3, known as a "picocavity". Thanks to that, it was obtained an great enhancement of the light-matter coupling between the picocavity and vibrations of individual molecular bonds.

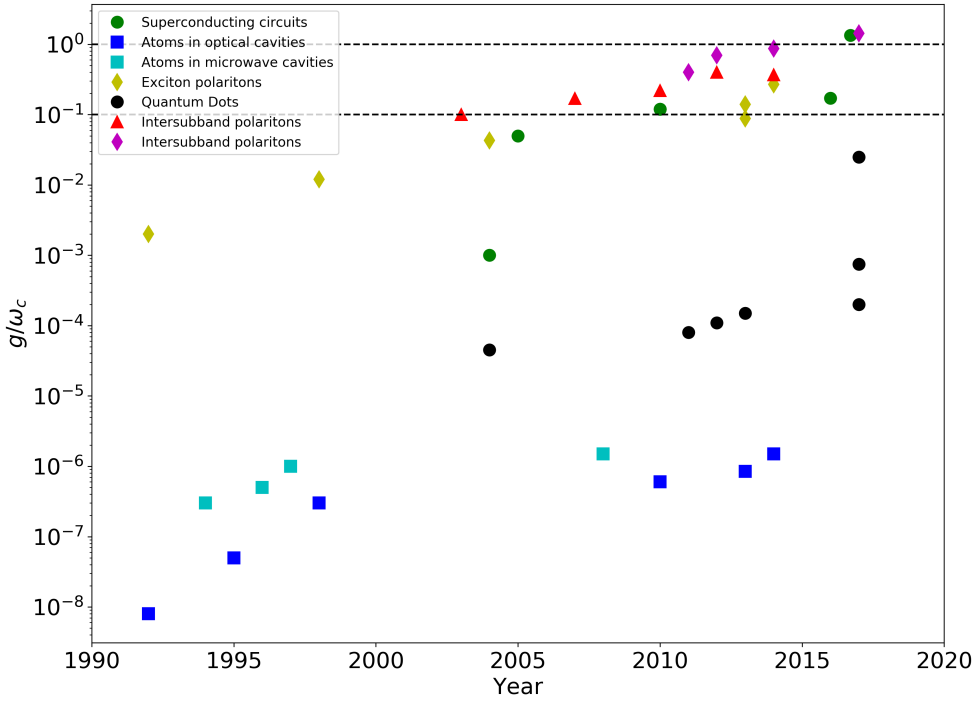

Figure 1.10: Evolution of the coupling g/ω_c for different experimental setups. Figure obtained from the data of [23].

- **Other systems:** We have already introduced the experiments with Rydberg atoms in microwave cavities of Haroche *et al.* [21] or the ion trap experiments of Wineland *et al.* [22] above. But, there are many other setups which we have not mentioned yet. We can also highlight: the *optical cavities* studies [69], the *Microcavity exciton polaritons* [4, 70], *Magnons in microwave cavities* [71, 72], *Quantum Dots* [73, 74], *NV-centers in diamond* [75] among others. The plethora of different realizations is immense. The figure 1.10 shows how the different setups have been enhancing the light-matter coupling g/ω_c, reaching the *Ultrastrong coupling* in the last years.

1.5 Vibrations and Holstein model

The goal of this work is the study of the light-matter interaction of a molecule with light in an electromagnetic cavity. We will consider the molecule as a two-level system with an energy splitting Δ. However, even considering the simplest case of diatomic molecules, these systems are more complex than just two energy levels. They have energy replicas separated by a frequency ω_v, each one of them with a differet number of vibrational quanta. Vibrations can be modelised using a harmonic oscillator:

$$H = \Delta\hat{\sigma}^{+}\hat{\sigma}^{-} + \omega_v\hat{b}^{\dagger}\hat{b} \tag{1.20}$$

where $\hat{b}^{\dagger}$ y $\hat{b}$ are the bosonic operators ($[\hat{b}, \hat{b}^{\dagger}] = 1$) which create a phonon of frequency ω_v. Besides, the molecules have rotational degrees of freedom. For simplicity, we will not take them into account in this work.

However, this is not the end of the story. Consider the simplest molecule, a diatomic molecule. The equilibrium distance between its two atoms R_g is given by a potential energy surface $U_g(r)$, where r is the relative distance between atoms. When the molecule is electronically excited (for example, by absorbing a photon) the equilibrium distance R_e change and it is given by a new potential energy surface $U_e(r)$. This new potential energy surface is displaced with respect to the previous one with an extra energy Δ (usually the new equilibrium distance is bigger than the previous one $R_e > R_g$) [76].

It is also considered that this electronic transition takes place on a time scale which is faster than the relative motion of the nuclei. Thus, we can consider the nuclei as being static during the process of electronic excitation. This is known as *Franck-Condon principle*. It implies that the transition is "vertical" as we can see in the figure 1.11. This principle is very similar to the *Born-Oppenheimer approximation* which exploits the great difference between the mass of the nucleus and the electrons.

Each potential energy surface has a set of discrete vibrational replicas and photon absorption will happen if the photon energy $\hbar\omega$ coincides with the energy difference between the initial and final energy levels. Furthermore, it has to have an overlap between the initial $|\chi_i\rangle$ and final $|\chi_f\rangle$ vibrational wave functions, see figure 1.11. These overlaps $\langle\chi_f|\chi_i\rangle$ are known as *Franck-Condon factors*.

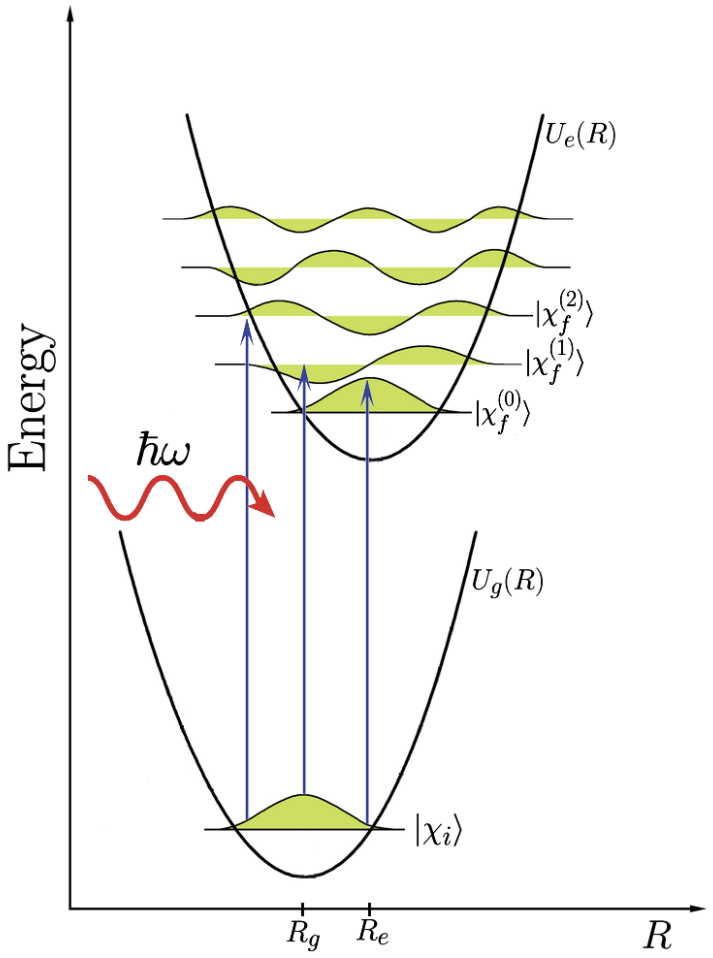

Figure 1.11: Potential energy surfaces of the ground state $U_g(r)$ and the excited state $U_e(g)$ versus the relative distance of the atoms of a diatomic molecule. Different vertical transitions are shown (Fanck-Condon principle). The transition strength is determined by the *Franck-Condon factors*, the overlaps of the vibrational wave functions.

How can we include this effect to the Hamiltonian? In the case of a diatomic molecule in its ground state, including vibrations is easy. We consider a molecule with two atoms A and B interacting through a harmonic oscillator potential $V(r)$ which depends on the relative distance r between atoms:

$$H = \frac{p_A^2}{2m_A} + \frac{p_B^2}{2m_B} + V(r) \approx \frac{p_R^2}{2M} + \frac{p}{2\mu} + \frac{1}{2}\mu\omega_v^2 r^2 \tag{1.21}$$

where p_A, m_A and p_B, m_B are the momentum and mass of each atom. We have performed the certer-of-mass transformation where $\mu = m_A m_B/(m_A + m_B)$ is the the reduced mass, $M = m_A + m_B$; and p_R and p are the momentum of the center of mass and the momentum of the relative motion.

Thus, neglecting the center-of-mass kinetic energy $p_R^2/2M$; changing the variables for operators and defining the bosonic operators ($[\hat{b}, \hat{b}^\dagger] = 1$):

$$\begin{aligned} \hat{r} &= \sqrt{\frac{\hbar}{\mu\omega_v}}\frac{1}{\sqrt{2}}(\hat{b}^\dagger + \hat{b}) \\ \hat{p} &= \sqrt{\mu\hbar\omega_v}\frac{1}{\sqrt{2}}i(\hat{b}^\dagger - \hat{b}) \end{aligned} \tag{1.22}$$

where $\hat{b}$ ($\hat{b}^\dagger$) annihilates (creates) a phonon. We obtain quantum harmonic oscillator of frequency ω_v:

$$H = \hbar\omega_v \hat{b}^\dagger \hat{b} \tag{1.23}$$

where we have neglected the constant term. Now, in the case of a molecule electronically excited , we have to include an energy Δ and a shift $\lambda\sqrt{2\hbar/\mu\omega_v}$ in the equilibrium position in the potential:

$$H \approx \Delta + \frac{p}{2\mu} + \frac{1}{2}\mu\omega_v^2(r + \lambda\sqrt{2\hbar/\mu\omega_v})^2 \tag{1.24}$$

Again, changing variables to operators and using (1.22), we obtain:

$$H = \Delta + \hbar\omega_v \hat{b}^\dagger \hat{b} + \hbar\omega_v \lambda(\hat{b}^\dagger + \hat{b}) \tag{1.25}$$

where we have neglected the constant terms. Thus, we have obtained a quantum harmonic oscillator with a displacement λ. So, putting all these ideas together, the Hamiltonian which we will use to model the intramolecular vibrations is (in units of $\hbar$):

$$H_{Holstein} = \Delta\hat{\sigma}^+\hat{\sigma}^- + \omega_v \hat{b}^\dagger \hat{b} + \omega_v \lambda \hat{\sigma}^+\hat{\sigma}^-(\hat{b}^\dagger + \hat{b} + \lambda) \tag{1.26}$$

By including the operator $\hat{\sigma}^+\hat{\sigma}^-$, the shift in the potential is only considered when the molecule is in its excited state, see figure 1.11. The last term ($\omega_v\lambda^2\hat{\sigma}^+\hat{\sigma}^-$) is justified below. This Hamiltonian is known as the *Holstein Hamiltonian*. The name comes from Holstein [77, 78] (1959) who suggested to include intramolecular vibrations (or optical phonons) in the context of charge-carrier transport in organic molecular crystals.

The squared of the parameter λ is known as the Huang-Rhys factor [9] (1950) and quantifies the strength of vibronic coupling. This parameters governs the relative shift of the two nuclear potentials [79]. From a classical perspective, λ produces a shift in the nuclear potential minimum. In the quantum counterpart, λ produces a displaced harmonic oscillator only when the molecule is excited.

The Holstein Hamiltonian (1.26) can be diagonalized using the *Polaron transformation*. This is a general method to treat a Hamiltonian with a linear coupling [80]. It consists of applying a unitary transformation, the displacement operator:

$$U = \exp\left(\xi(\hat{b}^\dagger - \hat{b})\right) \tag{1.27}$$

when U is applied over an bosonic operator $\hat{b}$, it gives a displaced one:

$$U^\dagger \hat{b} U = \hat{b} + \xi \tag{1.28}$$

In our case, we have to apply the unitary transformation:

$$U = \exp\left(\xi \hat{\sigma}^+ \hat{\sigma}^- (\hat{b}^\dagger - \hat{b})\right) \tag{1.29}$$

$$U^\dagger \hat{b} U = \hat{b} + \xi \hat{\sigma}^+ \hat{\sigma}^- \tag{1.30}$$

Obtaining:

$$\begin{aligned} U^\dagger H_{Holstein} U =& \Delta \hat{\sigma}^+ \hat{\sigma}^- + \omega_v (\hat{b}^\dagger + \xi \hat{\sigma}^+ \hat{\sigma}^-)(\hat{b} + \xi \hat{\sigma}^+ \hat{\sigma}^-) \\ &+ \omega_v \lambda \hat{\sigma}^+ \hat{\sigma}^- (\hat{b}^\dagger + \hat{b} + 2\xi \hat{\sigma}^+ \hat{\sigma}^- + \lambda) \end{aligned} \tag{1.31}$$

Finally, setting $\xi = -\lambda$, we get:

$$U^\dagger H_{Holstein} U = \Delta \hat{\sigma}^+ \hat{\sigma}^- + \omega_v \hat{b}^\dagger \hat{b} \tag{1.32}$$

Besides, we can justify the additional term in (1.26) without it the extra term $-\omega_v \lambda^2 \hat{\sigma}^+ \hat{\sigma}^-$ would have implied negative energies for a high enough λ and the renormalization of the term $\Delta \hat{\sigma}^+ \hat{\sigma}^-$.

Therefore, the eigenvalues and eigenvectors of the *Holstein Hamiltonian* (1.26) are $|\psi_{\uparrow n}\rangle = |\uparrow, \tilde{n}_{phon}\rangle$, $\epsilon_{\uparrow n} = \Delta + \omega_v \tilde{n}_{phon}$ and $|\psi_{\downarrow n}\rangle = |\downarrow, \tilde{n}_{phon}\rangle$, $\epsilon_{\downarrow n} = \omega_v \tilde{n}_{phon}$, where $\uparrow\downarrow$ indicate the excited/ground state of the molecule and $\tilde{n}_{phon}$ the number of phonons after the Polaron transformation, this is, the number of "displaced phonons". The natural basis, in which (1.26) can be represented, is $\{|\uparrow, n_{phon}\rangle\,,\ |\downarrow, n_{phon}\rangle\}$, and, the basis which diagonalize it is $\{|\uparrow, \tilde{n}_{phon}\rangle\,,\ |\downarrow, \tilde{n}_{phon}\rangle\}$. Both basis are related via a Polaron transformation:

$$\{|\uparrow, \tilde{n}_{phon}\rangle\,,\ |\downarrow, \tilde{n}_{phon}\rangle\} = \{\exp\left(-\lambda(\hat{b}^\dagger - \hat{b})\right)|\uparrow, n_{phon}\rangle\,,\ |\downarrow, n_{phon}\rangle\} \tag{1.33}$$

Notice that the number of displaced phonons in the case of the ground state coincides with the number of non-displaced phonons i.e. $|\downarrow, \tilde{n}_{phon}\rangle = |\downarrow, n_{phon}\rangle$.

As we have already said, the electronic transitions are weighted by the *Franck-Condon factors* which are the overlap between the vibrational wave functions involved in the transition i.e.:

$$D_{n\tilde{n}} \equiv \langle n|\tilde{n}\rangle = \langle n|D(-\lambda)|n\rangle \tag{1.34}$$

where $D(-\lambda) = \exp\left[-\lambda(\hat{b}^\dagger - \hat{b})\right]$ is the displacement operator. This overlap (1.34) can be analytically calculated, see Tobias Brandes' notes [80] or appendix E for more details.

The interaction of a set of molecules with a cavity mode has been deeply studied in the last years. Many recent works [81, 79, 82, 45, 83, 84, 85, 86, 87] have used a combination of the *Tavis-Cummings model* (used to describe many molecules coupled to a electromagnetic mode cf. section 1.2) and the *Holstein model* (1.26). This model is known as *Holstein-Tavis-Cummings*. In our case, we want to include the ultrastrong effects and study a single molecule in a cavity. For this, we will use a model which combines the *Rabi model* (1.2) and the *Holstein model* (1.26). We call it the *Holstein-Quantum-Rabi* model[5]. In other words:

$$H = \omega_c \hat{a}^\dagger \hat{a} + \Delta \hat{\sigma}^+ \hat{\sigma}^- + g(\hat{\sigma}^+ + \hat{\sigma}^-)(\hat{a}^\dagger + \hat{a}) + \underbrace{\omega_v(\hat{b}^\dagger \hat{b} + \lambda \hat{\sigma}^+ \hat{\sigma}^-(\hat{b}^\dagger + \hat{b} + \lambda))}_{\text{Phonon mode}} \tag{1.35}$$

The study of its energy spectrum and the *Ultrastrong effects* will be the topic of the next chapter. To summarize, we have obtained a model to describe the intramolecular vibrations. More information about this topic is provided by the excellent papers [80, 76, 88, 89] . Futhermore, we have already seen a brief introduction to the topic of *cavity QED* [cf. section 1.1], and, we have studied the main models and regimes used and studied in the field [cf. sections 1.2-1.3].

[5]This model without the counterrotating terms will be named as *Holstein-Jaynes-Cummings* model.

1.6 Dissipation and Master equation

As we are going to study the influence of energy dissipation in the system, and before we dip into the *Holstein-Quantum-Rabi* model (1.35) in the next chapter, we present the *master equation formalism* in this section. This is one of the most important approaches to the study of the dynamics of an open quantum system.

Here, we are mainly going to use the Breuer-Petruccione's book [6] and Rivas' notes [90] for this section. However, there are many other excellent references, see e.g. [24, 76, 91].

The time evolution of a closed system is governed by the *Schrödinger equation*, for the pure states $|\psi\rangle$, and the *Liouvillian - von Neumann equation*, when we have a mixed state described by a density matrix ρ. But, when we want to study a quantum system, we rarely have a completely isolated system.

In the most of the times, there is a coupling with its surroundings. However, it is not practical to take into account all the degrees of freedom of the environment, and normally, we are only interested in doing calculations resticting ourselfs to the system of interest, a "corner of the Universe" [24].

Thus, it would be great to have a differential equation, equivalent to the *von Neumann equation*, which gives us the evolution of our system: a *quantum master equation*. In other words, we need a linear *dynamical map* $\mathcal{E}_{(t,t_0)}$ which connects the state of the system $\rho_S(t_0)$ at some initial time to the state in another time t:

$$\mathcal{E}_{(t,t_0)} : \rho_S(t_0) \longrightarrow \rho_S(t) \tag{1.36}$$

We will impose that this *dynamical map* will not depend on the state of the system $\rho_S(t_0)$ at initial time t_0. In other words, we will impose that it will be a *Universal dynamical map*. Thus, we will need that the coupling of the system and the environment will be weak. Then, the initial state of the system will be a tensor product of the states of the system and the environment, neglecting the correlations ρ_{corr} [cf. [90]]:

$$\rho(t) = \rho_S(t) \otimes \rho_B(t) + \rho_{corr} \approx \rho_S(t) \otimes \rho_B(t) \tag{1.37}$$

The objective of this section is to obtain the *master equation* which governs the dynamics of the reduced density matrix $\rho_S(t)$ in the presence of energy dissipation. In order to do that we are going to consider that our system S is embedded or surrounded by a reservoir or bath B which S is going to dissipate and exchange energy with it.

First, we are going to start with the full Hamiltonian H of the composite system $S + B$:

$$H = H_S + H_B + \varepsilon H_I \tag{1.38}$$

where H_S is the Hamiltonian of our system, the *Holstein-Quantum-Rabi* model (1.35), H_B the reservoir Hamiltonian, H_I the interaction Hamiltonian between the system S and the environment B and ε gives us the strength of that interaction. In order to take into account the dissipation of light, matter and phonons; we can write H_B as the sum of the normal modes of three different reservoirs:

$$H_B = \sum_k \omega_k^{(phot)} \hat{c}_k^\dagger \hat{c}_k + \sum_k \omega_k^{(matt)} \hat{d}_k^\dagger \hat{d}_k + \sum_k \omega_k^{(phon)} \hat{q}_k^\dagger \hat{q}_k \tag{1.39}$$

where $\hat{c}_k$, $\hat{d}_k$ and $\hat{q}_k$ are the bosonic creation/annihilation operators of the photon, matter and phonon reservoir respectively; and $\omega_k^{(n)}$ is the normal mode frequency of each reservoir. The system and environment are coupled via the usual term:

$$H_I = (\hat{a}^\dagger + \hat{a}) \sum_k g_k (\hat{c}_k^\dagger + \hat{c}_k) + (\hat{\sigma}^+ + \hat{\sigma}^-) \sum_k h_k (\hat{d}_k^\dagger + \hat{d}_k) + (\hat{b}^\dagger + \hat{b}) \sum_k f_k (\hat{q}_k^\dagger + \hat{q}_k) \tag{1.40}$$

where g_k, h_k and f_k are the system-reservoir coupling constants. Thus, we are considering three main sources of energy dissipation. The first term of the equation (1.39) represents the bath on which the cavity losses photons, for example because the mirrors of the cavity are not perfect reflectors, see the losses γ_{phot} in figure 1.4. The second term of (1.39) takes into account all other electromagnetic modes different from the cavity electromagnetic mode which the atom also couples. They contribute to the exciton decay, see the losses γ_{matt} in figure 1.4. Finally, we have also added that the vibrations can dissipate to other modes, different from the coupling to our two-level system (see our model (1.35)). Here, we have supposed the same sort of coupling between the system and the environment for each dissipation channel.

Onece H_S, H_B and H_I are defined, the *master equation* can be found [cf. [6, 90] for more details of the following discussion]. This is better derived in the interaction picture. Therefore, the evolution of the total density matrix[6] $\tilde{\rho}(t)$ of the system $S + B$ is governed by the *von Neumann equation*:

$$\frac{d}{dt}\tilde{\rho}(t) = -i\varepsilon[H_I(t), \tilde{\rho}(t)] \tag{1.41}$$

[6]Where the tilde indicates the Interaction Picture, in other words: $\tilde{\rho}(t) = \exp(i(H_S + H_B)t)\rho(t)\exp(-i(H_S + H_B)t)$.

where we have used an arbitrary interaction Hamiltonian H_I which can depend on time in general. The formal solution of the last equation (1.41) is:

$$\tilde{\rho}(t) = \tilde{\rho}(0) - i\varepsilon \int_0^t ds\ [H_I, \tilde{\rho}(s)] \tag{1.42}$$

Inserting this equation into (1.41) and taking the trace over environment (notice: $\tilde{\rho}_S = \mathrm{tr}_B(\tilde{\rho})$), we get:

$$\frac{d}{dt}\tilde{\rho}_S(t) = -\varepsilon^2 \int_0^t ds\ \mathrm{tr}_B([H_I(t), [H_I(s), \tilde{\rho}(s)]]) \tag{1.43}$$

Here, we have assumed that $\mathrm{tr}_B([H_I(t), \tilde{\rho}(0)]) = 0$. We will derive the master equation up to second order in the coupling system-environment, which is an excellent approximation in the situations discussed here. This will allow us to make several simplifications. Since the integrand in (1.43) is already of second order in the system-environment coupling we can write:

$$\tilde{\rho}(t) \approx \tilde{\rho}_S(t) \otimes \tilde{\rho}_B \tag{1.44}$$

where $\tilde{\rho}_B$ is the reduced density matrix of the environment B in the *Interaction Picture*. We assume the environment in thermal equilibrium:

$$\rho_B = \frac{e^{-\beta H_B}}{\mathrm{tr}(e^{-\beta H_B})} \tag{1.45}$$

where $\beta = 1/k_B T$, the inverse of temperature T. Thus, we are assuming that the environment is a large system, whose state is unaffected by coupling to the system S. So, we substitute equation (1.44) into (1.43).

We can simplify equation (1.43) even more if the time relaxation scale τ_R (over which the state of the reduced density matrix ρ_S varies appreciably) is large compared to the time scale τ_B (over which the reservoir decays). This condition, $\tau_R \gg \tau_B$, justifies the approximation known as *Markov approximation*. This approximation consists in substituting the integrand $\tilde{\rho}_S(s)$ by the reduced density matrix $\tilde{\rho}_S(t)$ at the present time t. So, the system is memoryless of its past states. Also, we perform a change of the time variable s by $t - s$. Thus, after the *Born* and *Markov approximations*, we get:

$$\frac{d}{dt}\tilde{\rho}_S(t) \approx -\varepsilon^2 \int_0^t ds\ \mathrm{tr}_B([H_I(t), [H_I(t-s), \tilde{\rho}_S(t) \otimes \rho_B]]) \tag{1.46}$$

Now, we are going to write the interaction Hamiltonian H_I in the Schrödinger picture, as the following tensor product:

$$H_I = \sum_\alpha \hat{A}_\alpha \otimes \hat{B}_\alpha \tag{1.47}$$

where $\hat{A}_\alpha$ and $\hat{B}_\alpha$ are unitary operators[7] of the system and the environment, respectively (the same mathematical form proposed for H_I in the equation (1.40)). Assuming that the spectrum of H_S is discrete, with eigenvectors $|\epsilon\rangle$ and eigenvalues ϵ, we can define the following operators:

$$\hat{A}_\alpha(\omega) = \sum_{\epsilon'-\epsilon=\omega} |\epsilon\rangle \langle\epsilon| \hat{A}_\alpha |\epsilon'\rangle \langle\epsilon'| \tag{1.48}$$

where $\omega = \epsilon' - \epsilon$ are the energy differences. Besides, using the completeness relation $\mathbb{1} = \sum_\epsilon |\epsilon\rangle \langle\epsilon|$, we notice that:

$$\hat{A}_\alpha = \sum_\omega \hat{A}_\alpha(\omega) \tag{1.49}$$

where we have decomposed the operators $\hat{A}_\alpha$ in terms of every transition associated with the energy spectrum of H_S. Changing to the interaction picture the product $\hat{A}_\alpha \otimes \hat{B}_\alpha$, we obtain:

$$H_I(t) = \sum_{\alpha,\ \omega} e^{-i\omega t} \hat{A}_\alpha(\omega) \otimes \hat{B}_\alpha(t) \tag{1.50}$$

where $\hat{B}_\alpha(t) = e^{iH_B t} \hat{B}_\alpha e^{-iH_B t}$. Substituting (1.50) into the equation (1.46), and after some algebra [cf. [6]], we finally obtain:

$$\frac{d}{dt}\tilde{\rho}_S(t) = \varepsilon^2 \sum_{\omega,\ \omega'} \sum_{\alpha,\ \beta} e^{i(\omega'-\omega)t} \Gamma^{(t)}_{\alpha\beta}(\omega) (\hat{A}_\beta(\omega)\tilde{\rho}_S(t)\hat{A}^\dagger_\alpha(\omega') - \hat{A}^\dagger_\alpha(\omega')\hat{A}_\beta(\omega)\tilde{\rho}_S(t)) + \text{h. c.} \tag{1.51}$$

where $\Gamma^{(t)}_{\alpha\beta}(\omega)$ are integrals of *reservoir correlation functions* $\langle \hat{B}^\dagger_\alpha(t)\hat{B}_\beta(t-s)\rangle \equiv \mathrm{tr}_B\{\hat{B}^\dagger_\alpha(t)\hat{B}_\beta(t-s)\rho_B\}$:

$$\Gamma^{(t)}_{\alpha\beta}(\omega) \equiv \int_0^t ds\ e^{i\omega s} \langle \hat{B}^\dagger_\alpha(s)\hat{B}_\beta(0)\rangle \tag{1.52}$$

Futher progress can be made using the *secular approximation*. For that, we denote by τ_S the typical time scale of the intrinsic evolution of the system S, defined typically by $\tau_S \sim |\omega' - \omega|^{-1}$, when $\omega' \neq \omega$. Thus, if τ_S is much bigger than the relaxation time scale τ_R of the open system, we can neglect the terms $\omega' \neq \omega$ because these terms oscillate rapidly during the time τ_R over which ρ_S changes appreciably. This is the *Rotating Wave Approximation* which we

[7] $\hat{A}^\dagger_\alpha = \hat{A}_\alpha$ and $\hat{B}^\dagger_\alpha = \hat{B}_\alpha$

have seen in section 1.2. Explicitly, we can perform this approximation by changing to the formal solution of equation (1.51):

$$\tilde{\rho}_S(t) = \tilde{\rho}_S(0) + \varepsilon^2 \int_0^t du \sum_{\omega,\ \omega'} \sum_{\alpha,\ \beta} e^{i(\omega'-\omega)u} \Gamma^{(u)}_{\alpha\beta}(\omega)(\hat{A}_\beta(\omega)\tilde{\rho}_S(u)\hat{A}^\dagger_\alpha(\omega') - \hat{A}^\dagger_\alpha(\omega')\hat{A}_\beta(\omega)\tilde{\rho}_S(u)) \ + \ \text{h. c.} \tag{1.53}$$

and (i) making a change of variables $v = \varepsilon^2 u$, and (ii) imposing the limit of weak coupling $\varepsilon \to 0$, cf. appendix C.1 and [90] for more details. In the end, we get:

$$\frac{d}{dt}\tilde{\rho}_S(t) = \varepsilon^2 \sum_{\omega} \sum_{\alpha,\ \beta} \Gamma^{(\infty)}_{\alpha\beta}(\omega)(\hat{A}_\beta(\omega)\tilde{\rho}_S(t)\hat{A}^\dagger_\alpha(\omega) - \hat{A}^\dagger_\alpha(\omega)\hat{A}_\beta(\omega)\tilde{\rho}_S(t)) \ + \ \text{h. c.} \tag{1.54}$$

where $\Gamma^{(\infty)}_{\alpha\beta}(\omega)$ are the *Fourier transforms* of the *reservoir correlation functions* [see equation (C.7)]. Now, we are going to define the real and imaginary parts of the Fourier transforms $\Gamma^{(\infty)}_{\alpha\beta}(\omega)$:

$$\Gamma^{(\infty)}_{\alpha\beta}(\omega) = \frac{1}{2}\gamma_{\alpha\beta}(\omega) + iS_{\alpha\beta}(\omega) \tag{1.55}$$

where $S_{\alpha\beta}(\omega)$ is the imaginary part and $\gamma_{\alpha\beta}(\omega)$ the real part. So, with these definitions and changing to the Schrödinger picture equation (1.54), we obtain [cf. [6]]:

$$\frac{d}{dt}\rho_S(t) = -i[H_S + \varepsilon^2 H_{LS}, \rho_S(t)] + \mathcal{D}(\rho_S(t)) \tag{1.56}$$

where the Hermitian operator H_{LS}:

$$H_{LS} = \sum_{\omega} \sum_{\alpha\beta} S_{\alpha\beta}(\omega)\hat{A}^\dagger_\alpha(\omega)\hat{A}_\beta(\omega) \tag{1.57}$$

is known as the *Lamb-Shift* Hamiltonian. Equation (1.56) is known as the *Lindblad Markovian master equation*, and was given by Linbland in 1976 [92]. It is also easy to show that [6, 90]:

$$[H_S, \hat{A}^\dagger_\alpha(\omega)\hat{A}_\beta(\omega)] = 0 \tag{1.58}$$

and using (1.58) it can be shown that the *Lamb-Shift* Hamiltonian commutes with the system Hamiltonian $[H_S, H_{LS}] = 0$. This H_{LS} simply renormalizes some coefficients in H_S. In the following, we will always work with the renormalized H_S. We also have the dissipator superoperator:

$$\mathcal{D}(\rho_S(t)) = \varepsilon^2 \sum_{\omega} \sum_{\alpha,\ \beta} \gamma_{\alpha\beta}(\omega)\left(\hat{A}_\beta(\omega)\rho_S(t)\hat{A}^\dagger_\alpha(\omega) - \frac{1}{2}\{\hat{A}^\dagger_\alpha(\omega)\hat{A}_\beta(\omega), \rho_S(t)\}\right) \tag{1.59}$$

where we have introduced the anticonmutator $\{\hat{A},\ \hat{B}\} = \hat{A}\hat{B} + \hat{B}\hat{A}$. As we can see in the appendix C.2, the matrix $\gamma_{\alpha\beta}$ is a diagonal matrix in our case. So, it has the form [see equation (C.22)]:

$$\mathcal{D}(\rho_S(t)) = \sum_{\omega}\sum_{k}\gamma_k\omega\ \xi_k(\omega)\left(\hat{A}_k(\omega)\rho_S(t)\hat{A}_k^\dagger(\omega) - \frac{1}{2}\{\hat{A}_k^\dagger(\omega)\hat{A}_k(\omega), \rho_S(t)\}\right) \tag{1.60}$$

where we have assumed an *Ohmic spectral density function* $\gamma_{k\beta} = \gamma_k\omega\delta_{k\beta}$, where γ_k is a dimensionless parameter which accounts for the intensity of the dissipation into matter, light or phonon reservoirs (γ_{matt}, γ_{phot} and γ_{phon}) and:

$$\xi_k(\omega) = \begin{cases} 1 + \bar{n}_k(\omega) & \text{for} \quad \omega > 0 \\ \bar{n}_k(\omega) & \text{for} \quad \omega < 0 \end{cases} \tag{1.61}$$

where $\bar{n}_k(\omega)$ is the mean number of bosons in the thermal state ρ_{th} [see equation (1.45)] in the k reservoir (matter, light or phonon):

$$\bar{n}_k(\omega) = \frac{1}{e^{\omega/k_BT_k} - 1} \tag{1.62}$$

In other words, $\bar{n}_k(\omega)$ gives the expected number of particles satisfying the Bose-Einstein statistics. In this thesis, we are going to study the case of zero temperature $T = 0$. Thus, finally, the *master equation* which we are going to use in the numerical calulations is:

$$\frac{d}{dt}\rho_S(t) \approx -i[H_S, \rho_S(t)] + \mathcal{D}(\rho_S(t)) \tag{1.63}$$

where, the dissipator is given by:

$$\mathcal{D}(\rho_S(t)) = \sum_{\omega>0}\sum_{k}\gamma_k\omega\left(\hat{A}_k(\omega)\rho_S(t)\hat{A}_k^\dagger(\omega) - \frac{1}{2}\{\hat{A}_k^\dagger(\omega)\hat{A}_k(\omega), \rho_S(t)\}\right) \tag{1.64}$$

where $\hat{A}_1 = \hat{a}^\dagger + \hat{a}$, $\hat{A}_2 = \hat{\sigma}^+ + \hat{\sigma}^-$, and $\hat{A}_3 = \hat{b}^\dagger + \hat{b}$, are the coupling operators of light, matter and phonon with their respective reservoirs [see H_I equation (1.40)]. In conclusion, we have our model and the master equation to account for the energy losses in our system. Therefore, we have all the main tools to study the *Holstein-Quantum-Rabi model* (1.35) in the following chapters.

Chapter 2

The model and its energy spectrum

In this chapter we discuss the energy spectrum of the *Holstein-Quantum-Rabi* model (1.35) [see an schematic vision of this model in the figure 2.1].

2.1 The model and its spectrum

As we have said in the last chapter, our model (1.35) is a combination of the *Rabi* model (1.2) and the *Holstein* model (1.26). Nonetheless, we are going to repeat two main aspects of the *Holstein-Quantum-Rabi* Hamiltonian: (i) The *Holstein* exciton-phonon interaction takes into account that the molecule vibrates differently on the ground and the excited states. This is characterised by the Huang-Rhys factor λ^2 [76], as we have seen in the section 1.5. (ii) The *Quantum Rabi* model contains the counterrotating terms $H_{CR} = g(\hat{\sigma}^+\hat{a}^\dagger + \hat{\sigma}^-\hat{a})$ where parameter g sets the exciton-photon interaction strength.

As, we have already said in section 1.3 generally that reaching the *Ultrastrong coupling regime* in the *Quantum Rabi* model requires $g \gtrsim 0.1\Delta$ [10, 23, 49, 50]. However, we will show in this thesis that this condition is modified in Molecular-Cavity Quantum Electrodynamics, due to the additional vibrational mode of our molecule.

Though, the main motivation of the *Holstein-Quantum-Rabi* Hamiltonian (1.35) is the interaction of a molecule with an electromagnetic mode inside of a cavity, we stress that it could more generally apply to other cases where our two-level system can be coupled to both a photon and to another bosonic degree of freedom. This is a situation that could be achieved in, for instance, circuit-Quantum Electrodynamics [93].

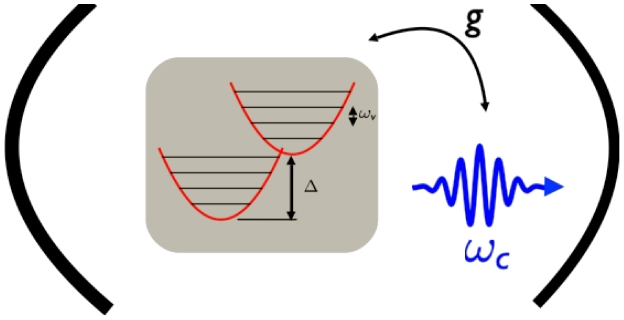

Figure 2.1: Schematic representation of the energy scales in the problem of a molecule inside a cavity.

Hereafter, we are going to study the energy spectrum of our model as a function of the matter-phonon coupling λ. The model is defined by a large number of parameters. The study of the model in all circunstances is outside the scape of this thesis. Instead, we take characteristic values for some parameters:

- We consider the cavity to be at resonance with the zero-phonon excitonic transition ($\omega_c = \Delta$). We denominate this condition as ***nominal*** or ***bare resonance***.
- We fix Δ to have typical values for J-aggregates of organic molecules such as $\pi-$conjugated oligo-mers (oligoacenes, olithiophes): $\Delta \simeq 2\ eV$ [83].
- In these organic molecules, typical vibrational frequencies are $\omega_v = 0.15 - 0.2\ eV$[83, 94, 79].
- The light-matter coupling g ranges from $g = 0.05$ to $\gtrsim 0.5\ eV$, taking representative values of ultrasmall plasmonic cavities or other systems [83, 60, 59].
- Finally, we will present results in a wide range of Huang-Rhys factors (λ^2). For example, $\pi-$conjugated oligomers have values from $\lambda = 0$ to 0.81 [95]. In the case of $J-$aggregates, with $\omega_v = 0.17\ eV$, $\lambda \simeq 1$ [83, 94, 79]. Following the practice of other studies [96, 86] we will extend our analysis to even larger values of λ.

Parameters	Non-normalized ($\omega_c \neq 1$)	Normalized ($\omega_c = 1$)
$\omega_c = \Delta$	$2\ eV$	1
g	$0.05 - 0.5\ eV$	$0.025 - 0.25$
ω_v	$0.15 - 0.2\ eV$	$0.075 - 0.1$

Table 2.1: Characteristic values of the parameters for organic molecules and their normalized ones, see [83, 94, 79, 60, 59].

In what follows, we normalize all energies with respect to ω_c (which is this the unit of energy). In the table 2.1, we have introduced the typical values of the parameters of (1.35) and their normalized equivalent ones. In this thesis, we will choose the following normalized parameters: $\Delta = \omega_c = 1$ (*bare resonance*), $g = 0.05$, $\omega_v = 0.1$ and values from $\lambda = 0$ to $\lambda \sim 3.5$, to study the energy spectrum of the *Holstein-Quantum-Rabi* model (1.35).

First, we perform a numerical study of the energy spectrum of (1.35). Using exact diagonalization[1], we can plot the eigenenergies for the chosen parameters versus the phonon-matter coupling $\lambda = 0.0 - 2.5$, see figure 2.2. Thus, we distinguish two types of eigenenergies or subspaces [cf. figure 2.2]: (i) The ones represented in red correspond to a ladder of energy levels which are multiples of the intramolecular vibration frequency $\omega_v = 0.1$. (ii) The ones represented in black are a set of energy levels, which reminds us the energy spectrum of the typical *Rabi* model (1.2), see figures 1.5 and 1.8. Notice however that in figures 1.5 and 1.8 the spectrum was represented versus light-matter coupling g, while here it is shown as a function of λ!

Before we qualitatively describe the energy spectrum in detail, we present a different (but equivalent) representation of the Hamiltonian (1.35). In (1.35) the Hamiltonian is represented in the basis $\{|\downarrow, n_{phot}, n\rangle\ ,\ |\uparrow, n_{phot}, n\rangle\}$, where n_{phot} is the number of photons, $|\downarrow\rangle\ ,\ |\uparrow\rangle$ are the ground and excited states of the molecule, and n the number of vibrations.

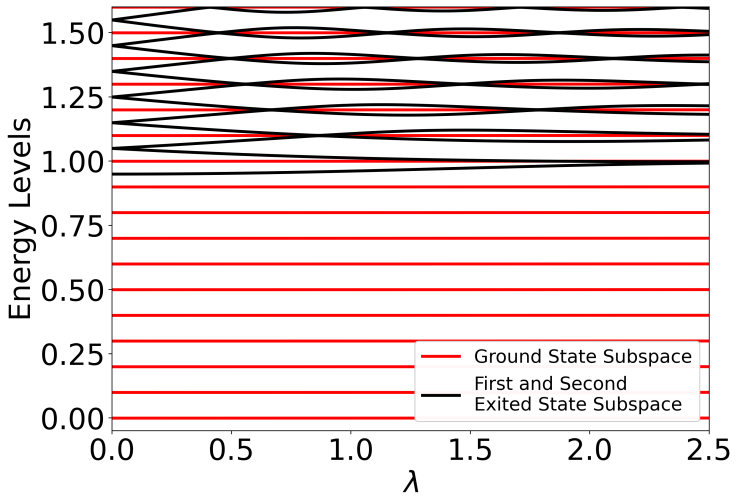

Figure 2.2: At ***bare resonance***, the Lowest eigenenergies as a function of the Huang-Rhys factor. Red lines correspond to the vibrational ladder of the photon-exciton ground-state, while black lines correspond to 1 excitation light-matter (polariton) subspace. Parameters: $\omega_c = \Delta = 1$, $\omega_v = 0.1$ and $g = 0.05$.

[1]All the numerical calculations will be done with *QuTip*, a tool based on *Python*, specialised on *Quantum optics* calculations.

This basis is the eigenstate basis in the case of $\lambda = g = 0$. However, we can go into a representation where vibrations in the electronic ground state are expressed in the original base $\{n\}$, while the vibrations in the exciton subspace are expressed in their own eigenfunctions: the displaced oscillators $\{\tilde{n}\}$. This is done by means of the Polaron transformation which shifts $\hat{b} \to \hat{b} - \lambda\hat{\sigma}^+\hat{\sigma}^-$, using the unitary:

$$U_P^{(0)} = \exp\left(-\lambda\hat{\sigma}^+\hat{\sigma}^-(\hat{b}^\dagger - \hat{b})\right) \tag{2.1}$$

After some algebra, we arrive to:

$$H_P = {U_P^{(0)}}^\dagger H U_P^{(0)} = \omega_c\hat{a}^\dagger\hat{a} + \Delta\hat{\sigma}^+\hat{\sigma}^- + \omega_v\hat{b}^\dagger\hat{b} + g\Big(D(\lambda)\hat{\sigma}^+ + D^\dagger(\lambda)\hat{\sigma}^-\Big)(\hat{a}^\dagger + \hat{a}) \tag{2.2}$$

where $D(\lambda)$ is the displacement operator:

$$D(\lambda) = e^{\lambda(\hat{b}^\dagger - \hat{b})} \tag{2.3}$$

Therefore, in this representation, the vibrations "*dress*" the exciton-photon coupling through the *Franck-Condon factors*: $\langle n|D(\lambda)|\tilde{m}\rangle = \langle n|e^{\lambda(\hat{b}^\dagger - \hat{b})}|\tilde{m}\rangle$ [80]. Using the picture H_P we can better understand the energy spectrum shown in figure 2.2. For that we take two approximations. First, we truncate the Hilbert space to the first three levels of the quantum-Rabi model (1.2). Second, we take the RWA. Therefore, we consider the ground state ($|\downarrow,\ 0_{phot}\rangle$) and the two polaritons ($|P_\pm\rangle = 2^{-1/2}(|\downarrow, 1_{phot}\rangle + |\uparrow, 0_{phot}\rangle)$) of the *Jaynes-Cummings* (JC) model (1.10). Thus, we can approximately describe the ladder, E_n (red curves, figure 2.2) as the phonon replicas of the *Jaynes-Cummings* ground state. In other words:

$$|E_n\rangle \approx |\downarrow\ 0_{phot}\ n_{phon}\rangle\,, \qquad E_n = n_{phon}\omega_v \tag{2.4}$$

On the other side, the *Rabi*-like spectrum (black curves, figure 2.2) can be approximately described at $\lambda = 0$, where the "displaced vibrations" $|\tilde{m}\rangle$ are equal to the "ground state vibrations" $|m\rangle$, as the phonon replicas of the *Jaynes-Cummings* polaritons:

$$|P_\pm^{(m)}\rangle \approx |P_\pm\rangle \otimes |m\rangle = 2^{-1/2}\{|\downarrow, 1_{phot}\rangle \pm |\uparrow, 0_{phot}\rangle\} \otimes |m\rangle \tag{2.5}$$

We denote the first subspace as the *ground state subspace* and the second one as the *polariton subspace* (or *first and second excited state subspace*). So far, this has been a qualitative description. In the next section, we are going to justify it analytically and we will obtain the first *ultrastrong effects*.

2.1.1 Analytical approach (effective model)

As $g \ll \omega_c, \Delta$, we can perform the *Rotating Wave Approximation* in the *Rabi* light-matter coupling in equation (1.35) of the *Holstein-Quantum-Rabi* model (HQR) $g\hat{\sigma}^+\hat{\sigma}^-(\hat{a}^\dagger + \hat{a}) \approx g(\hat{a}^\dagger\hat{\sigma}^- + \hat{a}\hat{\sigma}^+)$. Obatining the Hamiltonian which we name as *Holstein-Quantum-Jaynes-Cummings* Hamiltonian (HQJC):

$$H_{HJC} = \omega_c\hat{a}^\dagger\hat{a} + \Delta\hat{\sigma}^+\hat{\sigma}^- + g(\hat{a}^\dagger\hat{\sigma}^- + \hat{a}\hat{\sigma}^+) + \omega_v(\hat{b}^\dagger\hat{b} + \lambda\hat{\sigma}^+\hat{\sigma}^-(\hat{b}^\dagger + \hat{b} + \lambda)) \quad (2.6)$$

Thus, the ground state and exciton-photon polaritons of the *Jaynes-Cummings* (JC) model and their energies are:

$$|\epsilon_{JC}\rangle = |\downarrow 0_{phot}\rangle\,, \qquad \epsilon_{JC} = 0 \quad (2.7)$$

$$|P_\pm^{(n)}\rangle = \frac{1}{\sqrt{\tau_{\pm n}^2 + 1}}(\tau_{\pm n}\,|\uparrow\ n-1\rangle + |\downarrow\ n\rangle) \qquad \epsilon_{\pm n} = n\omega_c + \tau_{\pm n}g\sqrt{n} \quad (2.8)$$

where n is the number of photons and:

$$\tau_{\pm n} = \frac{\delta \pm \sqrt{4g^2n + \delta^2}}{2g\sqrt{n}}, \qquad \delta = \Delta - \omega_c \quad (2.9)$$

We can project our Hamiltonian H_P (2.2) on the *Jaynes-Cummings* polaritons $|P_\pm^{(1)}\rangle$ $(n = 1)$ and on the ground state $|\epsilon_{JC}\rangle$. Notice that the Hamiltonian (2.2) has been obtained after applying the Polaron transformation $U_P^{(0)} = \exp(-\lambda\hat{\sigma}^+\hat{\sigma}^-(\hat{b}^\dagger - \hat{b}))$ over the initial model (1.35). So, we must apply the same transformation over our eigenstates $|\tilde{\epsilon}_{JC}\rangle = U_P^{(0)^\dagger}|\epsilon_{JC}\rangle$ and $|\tilde{P}_\pm^{(1)}\rangle = U_P^{(0)^\dagger}|P_\pm^{(1)}\rangle$ before the projection. Thus, we obtain:

$$|\tilde{\epsilon}_{JC}\rangle = U_P^{(0)^\dagger}|\epsilon_{JC}\rangle = |\downarrow 0_{phot}\rangle \quad (2.10)$$

$$|\tilde{P}_\pm^{(1)}\rangle = \frac{1}{\sqrt{\tau_{\pm1}^2 + 1}}(\tau_{\pm1}D(\lambda)\,|\uparrow\ 0_{phot}\rangle + |\downarrow\ 1_{phot}\rangle) \quad (2.11)$$

where $D(\lambda) = e^{\lambda(\hat{b}^\dagger - \hat{b})}$ is the displacement operator. Now, we project our Hamiltonian (2.2) over the Hilbert space spanned by transformed ground state (2.10) and the polaritons (2.11). Notably, the ground and polariton subspaces decouple into an effective Hamiltonians for the *ground state subspace* and another one for the *polariton subspace*.

The Hamiltonian and the energies of the electronic ground state subspace are:

$$H_0 \approx \omega_v\hat{b}^\dagger\hat{b} \qquad \longrightarrow \quad E_n \approx n_{phon}\omega_v, \ \text{ where: } n_{phon} = 0,\ 1,\ 2,\ ... \quad (2.12)$$

This explains the set of states represented by the red curves in figure 2.2.

From the projection of the model (2.2) over the polariton subspace $\{|\tilde{P}_+^{(1)}\rangle, |\tilde{P}_-^{(1)}\rangle\}$ we obtain:

$$H_{pol} = \begin{pmatrix} \epsilon_{+,1} & 0 \\ 0 & \epsilon_{-,1} \end{pmatrix} + \omega_v \left(\hat{b}^\dagger \hat{b} + \lambda \begin{pmatrix} \lambda_+ & \Lambda \\ \Lambda & \lambda_- \end{pmatrix} (\hat{b}^\dagger + \hat{b} + \lambda) \right) \tag{2.13}$$

where the parameters $\lambda_\pm$ and Λ are:

$$\begin{aligned} \lambda_\pm &= \langle \tilde{P}_\pm^{(1)} | \hat{\sigma}^+ \hat{\sigma}^- | \tilde{P}_\pm^{(1)} \rangle = \frac{\tau_{\pm 1}^2}{\tau_{\pm 1}^2 + 1} \\ \Lambda &= \langle \tilde{P}_\mp^{(1)} | \hat{\sigma}^+ \hat{\sigma}^- | \tilde{P}_\pm^{(1)} \rangle = -\frac{\tau_{+1}\tau_{-1}}{\sqrt{(\tau_{+1}^2 + 1)(\tau_{-1}^2 + 1)}} \end{aligned} \tag{2.14}$$

At *bare resonance* ($\delta = 0$), we can simplify the Hamiltonian (2.13) using another Polaron transformation $U_P^{(1)} = \exp(-\lambda(\hat{b}^\dagger - \hat{b})/2)$:

$$H_{\text{eff}} = \hat{\Delta} \hat{\sigma}_P^+ \hat{\sigma}_P^- + \omega_v \hat{b}^\dagger \hat{b} + \hat{g}(\lambda)(\hat{\sigma}_P^+ + \hat{\sigma}_P^-)(\hat{b}^\dagger + \hat{b}) + \epsilon \tag{2.15}$$

where $\hat{\sigma}_P$ operators work in the two-level subspace spanned by the exciton-photon polaritons of the JC, $\hat{\Delta} = 2g$, $\hat{g} = \lambda\omega_v/2$ and $\epsilon = \omega_c + \omega_v\lambda^2/4 - g$ is an energy shift of all energies of this subspace. Thus, we have obtained an *effective Rabi* Hamiltonian (2.15) which governs the *polaritonic subspace* [cf. figure 2.2, black lines].

We stress that the name *effective Rabi* refers to the fact that the Hamiltonian is a *Rabi*-like model. However, we have done a RWA and this model comes from a *Jaynes-Cummings*-like model [recall the HQJC model (2.6)]. In the following sections, we will see the effect of the counterrotating terms. To sum up, in order to obtain this *effective Rabi* model (2.15) we have projected the HQR model into the subspace of the lowest polaritons of the *Jaynes-Cummings* model [cf. equation (2.8), with $n = 1$] and we have applied the polaron transformation $U_P^{(1)} = \exp(-\lambda(\hat{b}^\dagger - \hat{b})/2)$. The validity of this model respect to the *Holstein-Quantum-Rabi* Hamiltonian (1.35) (or (2.2)) can be seen in figure 2.3.

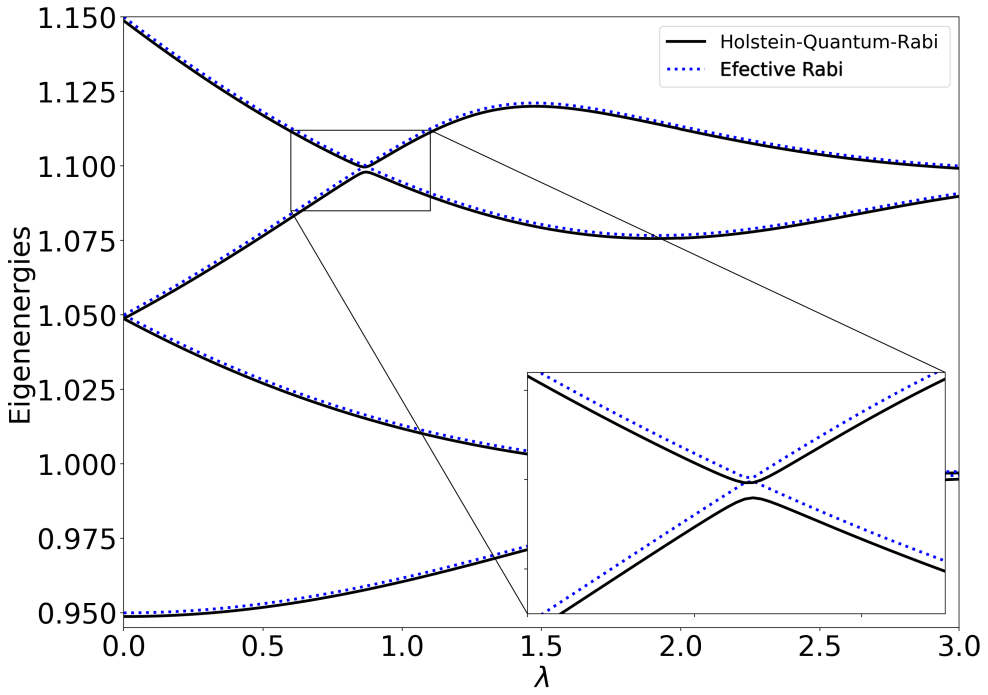

Figure 2.3: At ***bare resonance***, comparison between the *Holstein-Quantum-Rabi* (1.35) energy spectrum [black lines, cf. Hamiltonian (1.35) or (2.2)] and the *effective Rabi* model for the *polariton subspace* energy spectrum [dotted blue lines, cf. Hamiltonian (2.15)]. Parameters: $\Delta = \omega_c = 1$, $g = 0.05$ and $\omega_v = 0.1$.

Therefore, the spectrum of the *effective Rabi* model (2.15) for the *polariton subspace* is quite close to that obtained with the full *Holstein-Quantum-Rabi* (HQR) model (1.35). It thus can be already anticipated that the dynamics in the *polaritonics subspace* will mimic the *Cavity Quantum Electrodynamics* dynamics of a *Rabi* model (1.2), where the exciton-photon polaritons (2.8) will play the role of a two-level system and the phonons the role of the cavity photons (we will treat this point in more detail later on).

2.2 Parity of energy spectrum

However, there is a qualitative difference between the exact diagonalization of the *Holstein-Quantum-Rabi* (1.35) (or (2.2)) and the *effective Rabi* model (2.15) in the *polariton subspace*. In the full model (1.35) energy levels anticross [see inset of the figure 2.3], while they cross in the *effective Rabi* model (2.15).

We can explain this fact invoking the concept of parity. It is represented by an operator $\hat{P} = \exp(i\pi\hat{N})$, where $\hat{N}$ gives us the number of excitations of our eigenstate. Thus, for an even number of excitations the parity is $+1$ and for an odd number -1. Notice that the parity depends on the representation of our model. For example, in the case of H_{JC}, the *Jaynes-Cummings* (1.10) or H_{Rabi}, the *Rabi* (1.2) models, the number of excitations is $\hat{N} = \hat{\sigma}^+\hat{\sigma}^- + \hat{a}^\dagger\hat{a}$. In both models $[H_{JC}, \hat{P}] = [H_{Rabi}, \hat{P}] = 0$, the parity is conserved and we have crossings of the energy levels. In this thesis, using the representation of H_{eff}, the effective model (2.15), we define the parity operator $\hat{P}$ as follows:

$$\hat{P} = \exp(i\pi\hat{N}), \qquad \hat{N} = \hat{\sigma}_P^+\hat{\sigma}_P^- + \hat{b}^\dagger\hat{b} \tag{2.16}$$

where $\hat{N}$ is the operator the number of excitations in the representation of the *effective Rabi* model (2.15). The operators $\hat{\sigma}_P^\pm$ are defined as: $\hat{\sigma}_P^\pm = |\tilde{P}_\pm^{(1)}\rangle\langle\tilde{P}_\mp^{(1)}|$. Thus, $\hat{\sigma}_P^+\hat{\sigma}_P^-$ is the number operator in the two-level system spanned by the JC polaritons. So, the parity operator can be rewritten as:

$$\hat{P} = -\hat{\sigma}_z e^{i\pi\hat{b}^\dagger\hat{b}} \tag{2.17}$$

where $\hat{\sigma}_z$ is the z-Pauli matrix (working in the polariton two-level representation). Formally, the *effective Rabi* model (2.15) is a *Rabi* model. So, it can be shown that $[H_{\text{eff}}, \hat{P}] = 0$. Firstly, it is trivial to see that:

$$[\hat{\Delta}\sigma_P^+\sigma_P^- + \omega_v\hat{b}^\dagger\hat{b},\ \hat{P}] = 0 \tag{2.18}$$

Notice that $[\hat{\sigma}_P^+\hat{\sigma}_P^-, \hat{\sigma}_z] = 0$. Thus, we only have to show that the polariton-phonon coupling term (third term of (2.15)) commutes with the parity operator. In other words, we have to show that:

$$[(\hat{\sigma}_P^+ + \hat{\sigma}_P^-)(\hat{b}^\dagger + \hat{b}), \hat{\sigma}_z e^{i\pi\hat{b}^\dagger\hat{b}}] = 0 \tag{2.19}$$

After some algebra, applying some general commutator properties and $[\hat{\sigma}_P^+ + \hat{\sigma}_P^-, \hat{\sigma}_z] = 2(\hat{\sigma}_P^- - \hat{\sigma}_P^+)$, we arrive to the equivalent expression:

$$(\hat{\sigma}_P^- - \hat{\sigma}_P^+)((\hat{b}^\dagger + \hat{b})e^{i\pi\hat{b}^\dagger\hat{b}} + e^{i\pi\hat{b}^\dagger\hat{b}}(\hat{b}^\dagger + \hat{b})) = 0 \tag{2.20}$$

We know $\hat{b}e^{i\pi\hat{b}^\dagger\hat{b}}|n\rangle = e^{i\pi n}\hat{b}|n\rangle$. Thus, we find trivialy that:

$$e^{i\pi\hat{b}^\dagger\hat{b}}\hat{b}|n\rangle = e^{-i\pi}e^{i\pi n}\hat{b} = -\hat{b}e^{i\pi\hat{b}^\dagger\hat{b}}|n\rangle \tag{2.21}$$

Therefore, $[H_{\text{eff}}, \hat{P}] = 0$ and the *effective Rabi* model (2.15) conserves the parity of our eigenvectors. Thus, we can assign to each eigenstate[2] a value of the parity. This can be done calculating their energy at $\lambda = 0$. For instance the first four eigenvectors of the effective model at $\lambda = 0$ [cf. figure 2.4] with their respective parity are:

$$\begin{aligned}
|\epsilon_0\rangle &= |P_-^{(1)}, 0_{phon}\rangle \quad \epsilon_0 = \epsilon = 0.95 \qquad \langle\hat{P}\rangle = \exp(i\pi \times 0) = +1 \\
|\epsilon_1\rangle &= |P_-^{(1)}, 1_{phon}\rangle \quad \epsilon_1 = \omega_v + \epsilon = 1.05 \qquad \langle\hat{P}\rangle = \exp(i\pi) = -1 \\
|\epsilon_2\rangle &= |P_+^{(1)}, 0_{phon}\rangle \quad \epsilon_2 = 2g + \epsilon = 1.05 \qquad \langle\hat{P}\rangle = \exp(i\pi) = -1 \\
|\epsilon_3\rangle &= |P_-^{(1)}, 2_{phon}\rangle \quad \epsilon_3 = 2\omega_v + \epsilon = 1.15 \qquad \langle\hat{P}\rangle = \exp(i2\pi) = +1
\end{aligned} \tag{2.22}$$

Therefore, the states $|\epsilon_2\rangle$ and $|\epsilon_3\rangle$, belong to different subspaces $\forall\lambda$ and we expect a crossing of these energy levels [cf. green and yellow curves, figure 2.4a]. We have to notice that in figure 2.3 we chose $2g = \omega_v$ ($g = 0.05$ and $\omega_v = 0.1$). In this case, the pairs of eigenstates $|\epsilon_n\rangle$ and $|\epsilon_{n+1}\rangle$ with $n = 1$, 3, 5 ... are degenerate at $\lambda = 0$, see figure 2.4a. So, in order to be able to assign a label to each eigenstate [cf. (2.22)], we can change the phonon frequency to $\omega_v = 0.075$, which removes the degeneracy at $\lambda = 0$, see figure 2.4b.

We can see in figure 2.5 that the parity (2.16) of the *effective Rabi* model (2.15) is conserved [dotted lines, figure 2.3]. Since the value of parity jumps, we have a crossing of the energy levels. However, this does not happen in the case of the full model *Holstein-Quantum-Rabi* (1.35) (or (2.2)). In general the HQR model does not conserve the parity in the representation of H_{eff}. The value of the parity does not jump because we have an anticrossing of eigenstates [continuous curves, figure 2.3]. As we have done a RWA to get the *effective Rabi* model (2.15), the counterrotaing terms of the light-matter *Rabi* are responsible for the non-conservation of the parity (2.16) [cf. figure 2.5] and the presence of anticrossings in the energy spectrum of the full model HQR [cf. figure 2.3]. Besides, we can observe another *Ultrastrong* effect in the parity when $\lambda \gtrsim 2$, see figure 2.5a. We are going to see in the next two sections two different strategies[3] to perturbatively treat these counterrotating terms present in the HQR Hamiltonian (1.35).

[2] In the *polariton subspace*.

[3] Although, both are two second order corrections of perturbation theory.

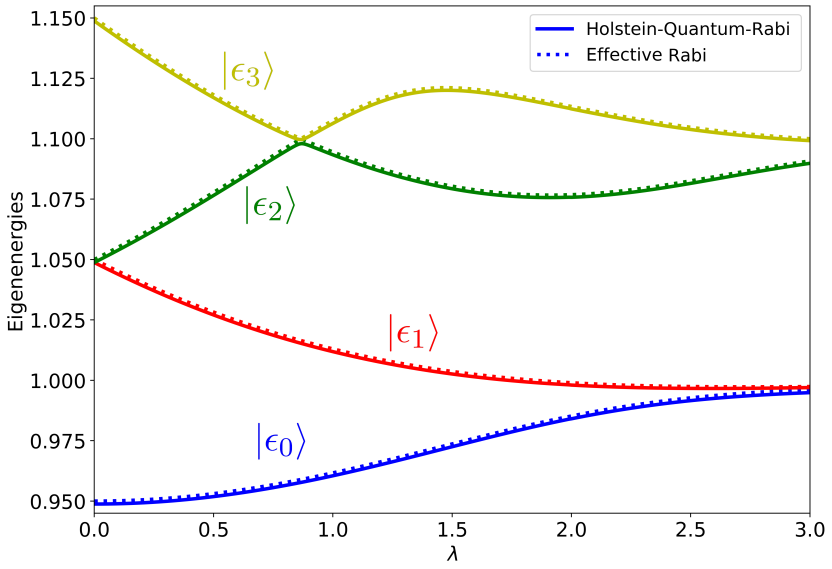

(a)

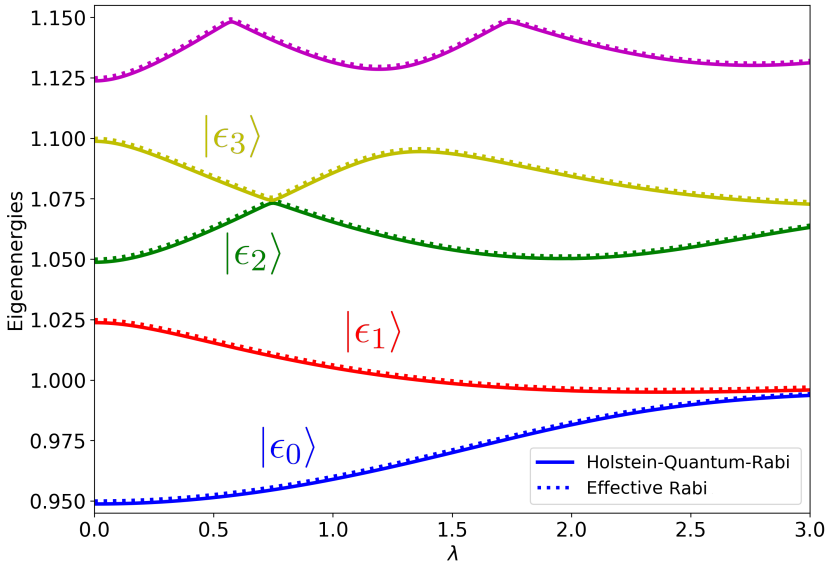

(b)

Figure 2.4: At ***bare resonance***, first energies of polariton subspace obtained using exact diagonalization, as a function of λ. The continuous lines have been obtained using the *Holstein-Quantum-Rabi* Hamiltonian (1.35) (or (2.2)) and the dotted ones using the *effective Rabi* Hamiltonian (2.15) (a) $\omega_v = 0.1$ (b) $\omega_v = 0.075$. The rest of the parameters: $g = 0.05$, $\omega_c = \Delta = 1$.

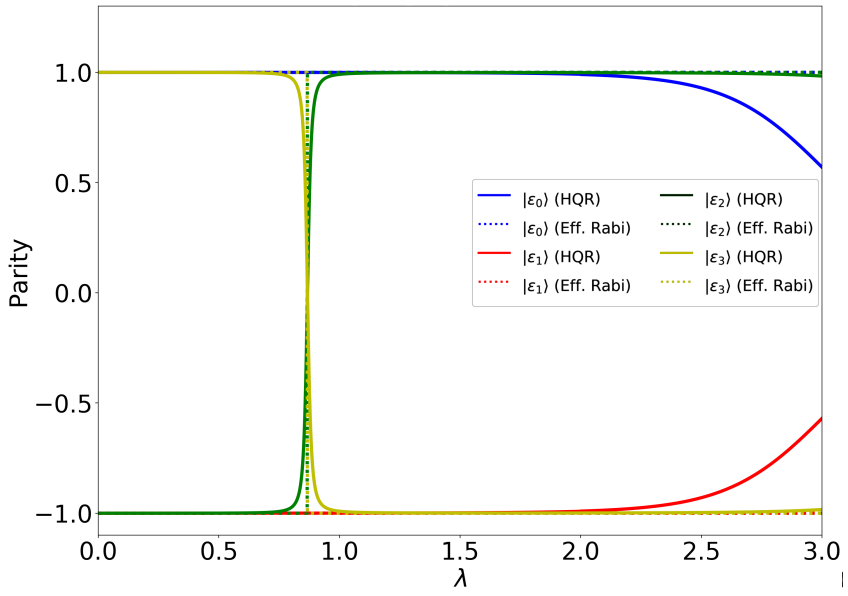

(a)

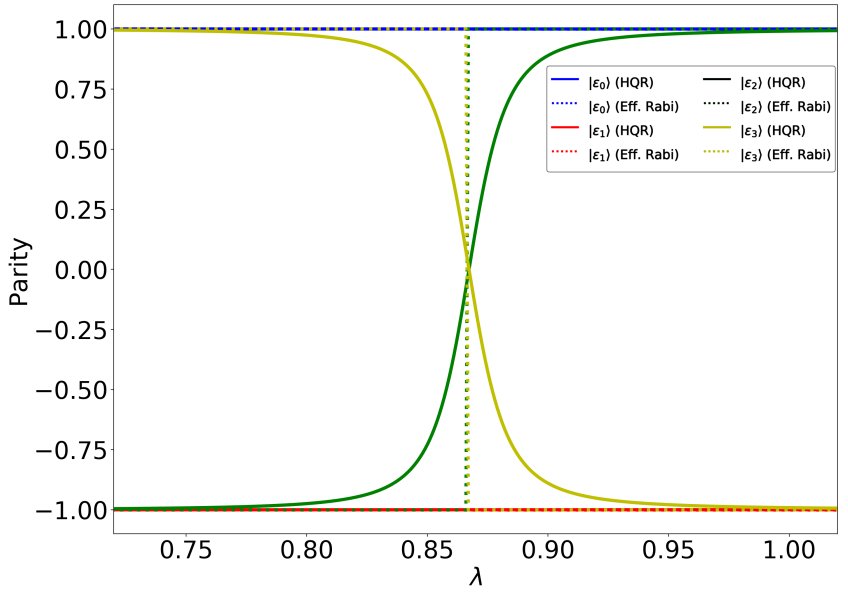

(b)

Figure 2.5: At ***bare resonance***: (a) The expected value of the parity operator $\langle \hat{P} \rangle$. The continuous lines have been obtained using the *Holstein-Quantum-Rabi* Hamiltonian (1.35) (or (2.2)) and the dotted ones using the *effective Rabi* Hamiltonian (2.15). We have used the same color for its corresponding energy levels [cf. figure 2.4]. (b) Zoom of the crossing/anticrossing region. Parameters: $\Delta = \omega_c = 1$, $g = 0.05$ and $\omega_v = 0.1$.

2.3 Bloch-Siegert correction

In this section, we are going to treat the light-matter couterrotating terms of our model (2.2)[4] using perturbation theory (see for instance, Cohen-Tannoudji's book [97]). The perturbation theory will give us a correction over the energies of the model without the counterrotating terms (RWA). This correction is known as *Bloch-Siegert correction*. Thus, we will understand better the *ultrastrong effects* produced by these terms. For convinience, we rewrite the model (2.2):

$$\begin{aligned} H = &\underbrace{\omega_c \hat{a}^\dagger \hat{a} + \Delta \hat{\sigma}^+ \hat{\sigma}^- + \omega_v \hat{b}^\dagger \hat{b}}_{H_0} + \underbrace{g(D(\lambda)\hat{a}^\dagger \hat{\sigma}^- + D^\dagger(\lambda)\hat{a}\hat{\sigma}^+)}_{H_R} \\ &+ \underbrace{g(D(\lambda)\hat{a}^\dagger \hat{\sigma}^+ + D^\dagger(\lambda)\hat{a}\hat{\sigma}^-)}_{H_{CR}} \end{aligned} \tag{2.23}$$

Now, we are going to restrict our basis size, in order to simplify our problem. The chosen basis is $\{|\uparrow\ 0_{phot}\ \tilde{n}_{phon}\rangle\,,\ |\downarrow\ 1_{phot}\ 0_{phon}\rangle\}$. These states are eigenstates of H_0. Thus, we can obtain the representation of $H_0 + H_R$ in this basis:

$$H_0 + H_R = \begin{pmatrix} \Delta + \omega_v \tilde{n} & g_{\text{eff}} \\ g_{\text{eff}} & \omega_c \end{pmatrix} \tag{2.24}$$

where the effective light-matter coupling g_{eff} depends on the Franck-Condon factors $g_{\text{eff}} = gD_{\tilde{n}0}(\lambda)$, in the case of $\tilde{n} = 0$, $D_{\tilde{0}0}(\lambda) = e^{-\lambda^2/2}$. These *Franck-Condon factors* can easily be calculated, see Brandes' notes [80]. We have included some of them; and the formula to calculate them in the appendix E [cf. equations (E.1) and (E.2)].

Using the chosen basis ($\{|\uparrow\ 0_{phot}\ \tilde{n}_{phon}\rangle\,,\ |\downarrow\ 1_{phot}\ 0_{phon}\rangle\}$), we also project the counterrotating terms H_{CR} on it. With these things in mind, we apply perturbation theory in this subspace until second order, where the counterrotating terms H_{CR} are the perturbation. Thus, we obtain that the Hamiltonian $H_0 + H_R$ after the perturbation correction is:

$$H_0 + H_R = \begin{pmatrix} \Delta + \omega_v \tilde{n} & g_{\text{eff}} \\ g_{\text{eff}} & \omega_c - \delta_{BS} \end{pmatrix} \tag{2.25}$$

where δ_{BS} is the correction, obtained from perturbation theory, known as *Bloch-Siegert correction*:

$$\delta_{BS} = g^2 \sum_{\tilde{m}=0}^{\infty} \frac{2|D_{\tilde{m}0}(\lambda)|^2}{\omega_c + \Delta + \tilde{m}\omega_v} \approx \frac{2g^2}{\omega_c + \Delta + \lambda^2 \omega_v} \tag{2.26}$$

[4] We can do the same with the model (1.35). They are equivalent models under an unitary transformation.

We have taken $\tilde{m} \approx \lambda^2$ in the denominator where the function $|D_{\tilde{m}0}(\lambda)|^2$ has approximately its maximum. We justify the approximation in the appendix E.2 [cf. also the inset of figure 2.6]. Therefore, an effect of the counterrotating terms is the reduction of the effective cavity frequency $\omega_c - \delta_{BS}$. Besides, light-matter coupling is renormalized through the *Franck-Condon* factors between the states which the light-matter coupling involves. This new light-matter coupling between the basis states is the g_{eff}.

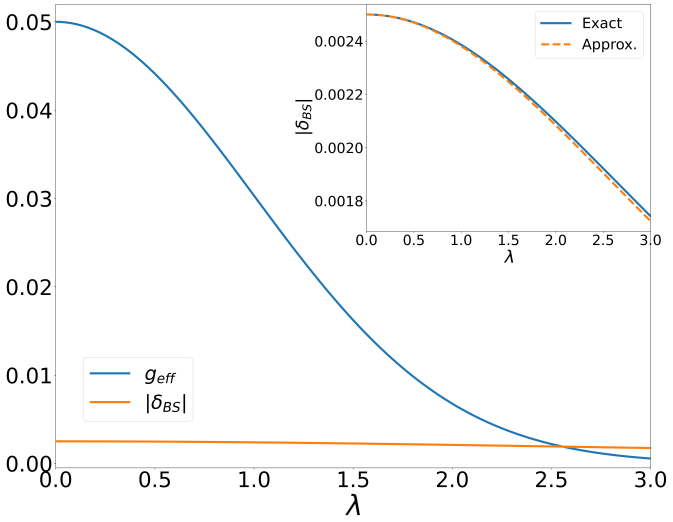

Figure 2.6: At ***bare resonance***, comparison between the effective light-matter coupling $g_{\text{eff}} = ge^{-\lambda^2/2}$ and the *Bloch-Siegert correction* δ_{BS}. Inset: Exact δ_{BS} versus its approximation, see equation (2.26). Parameters: $\Delta = \omega_c = 1$, $g = 0.05$ and $\omega_v = 0.1$.

As a consequence, even though nominally the system is at *bare resonance* $\omega_c = \Delta$, the dressing provided by H_{CR} brings the system out of resonance $\omega_c - \delta_{BS} \neq \Delta$. As we will see in the next chapter, this will have consequences on the system dynamics. The Bloch-Siegert correction (2.26) is thus a measure of the relevance of the counterrotating terms. Thus, when $\lambda \gtrsim 2$ the Bloch-Siegert correction $|\delta_{BS}|$ and the g_{eff} are comparable [cf. figure 2.6]. This will be the regime where we get *Ultrastrong effects* in the dynamics, as we will describe in the next chapter. Furthermore, these effects can also be observed in the energy spectrum [through the presence of anticrossings, see figure 2.3] and the parity as well [see change in parity for $\lambda \gtrsim 2$, cf. figure 2.5].

In order to show that these effects come from the counterrotating terms, we are going to put the HQR model at resonance, by modifying the value of the bare cavity frequency ω_c. Considering the *Bloch-Siegert* shift (in the case $\tilde{n}_{phon} = 0$), the resonant condition occurs when:

$$\Delta = \omega_c - \delta_{BS} = \omega_c - \frac{2g^2}{\omega_c + \Delta + \lambda^2 \omega_v} \tag{2.27}$$

We denote this new resonance dondition (2.27) as ***dressed resonance***.

Thus, the value of ω_c which keeps the system at resonance is approximately:

$$\omega_c = \sqrt{\Delta^2 + 2g^2 + \omega_v\lambda^2\Delta + (\omega_v\lambda^2/2)^2} - \omega_v\lambda^2/2 \tag{2.28}$$

At ***dressed resonance***, we can recalculate the energy spectrum of HQR and we recover the crossings using (2.28), see figure 2.7 (black lines). Thus, our hypothesis is that the anticrossing dissapears when the system is at *dressed resonance*. Similarly in the *dressed resonant condition*, we also see that we recover the "jumps" in the parity (when the crossings occur in the energy spectrum) and cancel the change of the parity for $\lambda \gtrsim 2$, see figure 2.8 (continuous lines). In this figure, we have recalculated the parity (2.16) of the eigenstates of the HQR model at ***dressed resonance*** [cf. equation (2.27)]. Although, in general, the HRQ does not conserve the parity in the representation of the *effective Rabi* model (2.15), we have obtained that this model conserve it at *dressed resonance*.

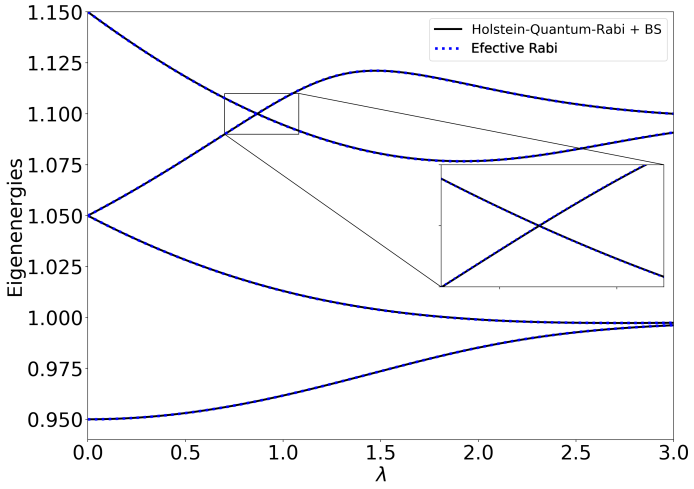

Figure 2.7: Comparison between the *Holstein-Quantum-Rabi* energy spectrum at ***dressed resonance*** [black lines, cf. Hamiltonian (1.35) (or (2.2))] and the *effective Rabi* energy spectrum at ***bare resonance*** [dotted blue lines, cf. Hamiltonian (2.15)] in the *polariton subspace*. Parameters: $\Delta = 1$, $g = 0.05$ and $\omega_v = 0.1$. Here, we have changed the cavity frequency ω_c to (2.28) in order to cancel the *Ultrastrong effects*.

On the other side, the shift $-\delta_{BS}$ produced in the photon energy ω_c is not the only effect of the counterrotating terms over the energies of the system. These terms also produce an energy shift $-\delta_{BS}/2$ in the vibrartional frequency ω_v of the *ground state subspace* $\{|\downarrow 0_{phot} m_{phon}\rangle\}$. We can find a more detailed calculation of these perturbative corrections including the *ground state subspace* in the appendix F. Here and in the next chapter, we have not included this shift over the *ground state subspace* because it is not relevant in the energy spectrum of the *polariton subspace* and in the dynamics of the system (chapter 3). However, we will take this shift into account in the chapter 4.

In summary, in this section we have seen that the couterrotaing terms produce a Bloch-Siegert correction of the cavity frecuency ω_c (using second order perturbation theory) and anticrossings in the energy spectrum when we are at *nominal* or ***bare resonance*** and we have not calculated the good resonant condition using the Bloch-Siegert correction yet. At ***dressed resonance***, the HQR reduces drastically the gaps of the anticrossings obtainig crossings (at least at first sight) and conserves the parity (2.16) in the representation of the *effective Rabi* Hamiltonian (2.15).

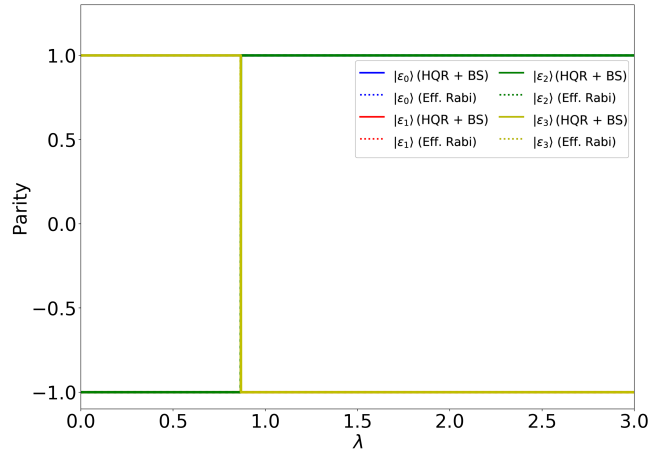

(a)

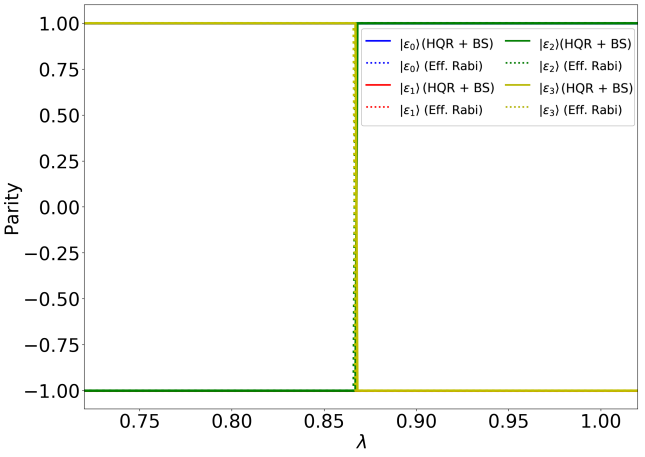

(b)

Figure 2.8: (a) The expected value of the parity operator $\langle \hat{P} \rangle$ (2.16) in the *effective Rabi* model representation. The continuous lines have been obtained using the *Holstein-Quantum-Rabi* Hamiltonian at ***dressed resonance*** (1.35) (or (2.2)) and the dotted ones using the *effective Rabi* Hamiltonian at ***bare resonance*** (2.15). We have used the same color code for its corresponding energy levels [cf. figure 2.4]. (b) Zoom of the crossing/anticrossing region. Parameters: $\Delta = 1$, $g = 0.05$ and $\omega_v = 0.1$.

2.4 Shrieffer-Wolff transformation (SW)

In this new section, we are going to improve our *effective Rabi* model (2.15) in order to get the anticrossings present at ***bare resonance*** in the HQR model. For this, we consider aditional terms in the *effective Rabi* Hamiltonian that arise from the counterrotating terms in the *Holstein-Quantum-Rabi* Hamiltonian. Again, we will use second order perturbation theory, but here we will correct the Hamiltonian instead of the energies.

In order to improve the *effective Rabi* model (2.15) we are going to start the discussion from (2.13), which we rewrite here for convenience:

$$H_{pol} = \begin{pmatrix} \epsilon_{+,1} & 0 \\ 0 & \epsilon_{-,1} \end{pmatrix} + \omega_v \left(\hat{b}^\dagger \hat{b} + \lambda \begin{pmatrix} \lambda_+ & \Lambda \\ \Lambda & \lambda_- \end{pmatrix} (\hat{b}^\dagger + \hat{b} + \lambda) \right)$$

As we saw in the section 2.1, this model was obtained projecting the *Holstein-Quantum-Rabi* model on the subspace of the two first polaritons[5] of the *Jaynes-Cummings* model (1.10) $\{|P_+^{(1)}\rangle\,,\ |P_-^{(1)}\rangle\}$ (this projection can be done over the Hamiltonians (1.35) or (2.2), both are equivalents). In other words, we neglected the light-matter counterrotating terms and obtained the *Jaynes-Cummings* model on the basis $\{|P_+^{(1)}\rangle\,,\ |P_-^{(1)}\rangle\}$ plus the Holstein model (1.26).

The effect of applying the counterrotating terms $(\hat{a}^\dagger\hat{\sigma}^+ + \hat{a}\hat{\sigma}^-)$ over the basis of the polaritons $\{|P_+^{(1)}\rangle\,,\ |P_-^{(1)}\rangle\}$ of one excitation (a photon or a matter excitation), is to create or destroy 2 excitations. Thus, the counterrotating terms enlarge the basis to the polaritons of three excitations $\{|P_+^{(3)}\rangle\,,\ |P_-^{(3)}\rangle\}$.

In this section, we will apply a perturvative technique over the *Rabi* model (1.2) to include the effect of the counterrotating terms in the basis $\{|P_+^{(1)}\rangle\,,\ |P_-^{(1)}\rangle\}$ and then add the *Holstein* Hamiltonian (1.26) in this basis. Thus, we will get an alternative version of (2.13), but taking into account the counterrotating terms. So, in the basis $\{|P_+^{(1)}\rangle\,,\ |P_-^{(1)}\rangle\,,\ |P_+^{(3)}\rangle\,,\ |P_-^{(3)}\rangle\}$, the *Rabi* Hamiltonian has the form of:

$$H = H_0 + gV = \begin{pmatrix} H_A & 0 \\ 0 & H_B \end{pmatrix} + g \begin{pmatrix} 0 & v^\dagger \\ v & 0 \end{pmatrix} \tag{2.29}$$

where H_0 is the *Jaynes-Cummings* Hamiltonian (1.10) (the unperturbed Hamiltonian), H_A and H_B the *Jaynes-Cummings* Hamiltonians in the subspaces $\{|P_+^{(1)}\rangle\,,\ |P_-^{(1)}\rangle\}$ and $\{|P_+^{(3)}\rangle\,,\ |P_-^{(3)}\rangle\}$ respectively, and the perturbation $V = \hat{a}^\dagger\hat{\sigma}^+ + \hat{a}\hat{\sigma}^-$ comprises the counterrotating terms which connect the subspaces of one and three excitations. The operators v are the projections of V on each subspace.

[5] Recall equations (2.8) and (2.9).

The perturvative technique which will apply over (2.29) is know as *Schrieffer-Wolff (SW) canonical transformation* (see the Cini's book [98]). This is a unitary transformation e^S which diagonalizes (2.29):

$$H \to \tilde{H} = e^S H e^{-S} = \begin{pmatrix} \tilde{H}_A & 0 \\ 0 & \tilde{H}_B \end{pmatrix} \tag{2.30}$$

So, the first objective is to obtain $\tilde{H}_A$, the *Jaynes-Cummings* model with the perturbative corrections in the basis $\{|P_+^{(1)}\rangle\,,\ |P_-^{(1)}\rangle\}$. Firstly, we can rewrite $\tilde{H}$ using the Baker-Campbell-Haussdorf formula:

$$\tilde{H} = e^S(H_0+gV)e^{-S} = H_0+gV+[S,H_0]+g[S,V]+\frac{1}{2!}[S,[S,H_0]]+\frac{g}{2!}[S,[S,V]]+\cdots \tag{2.31}$$

So, we need to find an operator S which diagonalizes $\tilde{H}$. For this, we suppose that $S = gS_1 + g^2S_2 + \cdots$. Replacing this into (2.31), neglecting the orders g^3 and superior, and imposing $S_2 = 0$, we obtain:

$$\tilde{H} \approx H_0 + gV + g[S_1, H_0] + \frac{g^2}{2}[S_1,[S_1,H_0]] \tag{2.32}$$

Now, imposing that $[S_1, H_0] = -V$, we get:

$$\tilde{H} \approx H_0 + H_{int} \tag{2.33}$$

where:

$$H_{int} = \frac{g^2}{2}[S_1, V] \tag{2.34}$$

Finally, using as an ansatz of S_1:

$$S_1 = \begin{pmatrix} 0 & -s^\dagger \\ s & 0 \end{pmatrix} \tag{2.35}$$

We find that (2.34) is a block diagonal matrix. There are not any mixture matrix elements between the subspaces $\{|P_+^{(1)}\rangle\,,\ |P_-^{(1)}\rangle\}$ and $\{|P_+^{(3)}\rangle\,,\ |P_-^{(3)}\rangle\}$. Thus, in the subspace $\{|P_+^{(1)}\rangle\,,\ |P_-^{(1)}\rangle\}$, the correction H_{int} reads (see [98] for more details):

$$(H_{int})_{mn} = -\frac{g^2}{2}\sum_{\nu\in B} V^\dagger_{m\nu}V_{\nu n}\left[\frac{1}{E_\nu^{(B)} - E_m^{(A)}} + \frac{1}{E_\nu^{(B)} - E_n^{(A)}}\right] \tag{2.36}$$

where n and m run over the basis $\{|P_+^{(1)}\rangle\,, |P_-^{(1)}\rangle\}$ and ν over $\{|P_+^{(3)}\rangle\,, |P_-^{(3)}\rangle\}$. Besides, $V_{\nu,n} = \langle P_\nu^{(3)}|V|P_n^{(1)}\rangle$ with $\nu = \pm$, $n = \pm$, and; $E_n^{(A)} = \{\epsilon_{+,1}, \epsilon_{-,1}\}$ and $E_\nu^{(B)} = \{\epsilon_{+,3}, \epsilon_{-,3}\}$. After some algebra, in the subspace $\{|P_+^{(1)}\rangle\,,\ |P_-^{(1)}\rangle\}$, we arrive to:

$$H_{int} = \begin{pmatrix} \alpha_+ & \tilde{\Lambda} \\ \tilde{\Lambda} & \alpha_- \end{pmatrix} \tag{2.37}$$

where:

$$\alpha_{\pm} = \langle P_{\pm}^{(1)}|H_{int}|P_{\pm}^{(1)}\rangle \qquad \tilde{\Lambda} = \langle P_{-}^{(1)}|H_{int}|P_{+}^{(1)}\rangle \tag{2.38}$$

The analytical expressions of (2.38) can be found in the appendix D. Thus, gathering the *Jaynes-Cummings*, the *Shrieffer-Wolff* correction H_{int} and the Holstein Hamiltonian (1.26) in the basis $\{|P_{+}^{(1)}\rangle, |P_{-}^{(1)}\rangle\}$, we arrive to an alternative version of the effective model (2.13), but taking into account the counterrotating terms:

$$H_{pol} = \begin{pmatrix} \epsilon_{+,1} & 0 \\ 0 & \epsilon_{-,1} \end{pmatrix} + \begin{pmatrix} \alpha_{+} & \tilde{\Lambda} \\ \tilde{\Lambda} & \alpha_{-} \end{pmatrix} + \omega_v \left(\hat{b}^{\dagger}\hat{b} + \lambda \begin{pmatrix} \lambda_{+} & \Lambda \\ \Lambda & \lambda_{-} \end{pmatrix} (\hat{b}^{\dagger} + \hat{b} + \lambda) \right) \tag{2.39}$$

that is Hamiltonian (2.13) plus the *SW* correction (2.37). Recall that the parameters $\lambda_{\pm}$ and Λ are defined in (2.9).

The next step is to get an improved version of the model (2.15) including the *SW* correction. So, as we did when deriving (2.13) we will apply the Polaron transformation $U_P^{(1)} = \exp\left(-\lambda(\hat{b}^{\dagger} - \hat{b})/2\right)$. After some algebra, we obtain:

$$H = \underbrace{\left[\frac{\epsilon_{+,1} - \epsilon_{-,1}}{2} + \frac{\alpha_{+} - \alpha_{-}}{2}\right]\hat{\sigma}_z + \left[\frac{\epsilon_{+,1} + \epsilon_{-,1}}{2} + \frac{\alpha_{+} + \alpha_{-}}{2}\right]}_{\text{If } \delta = 0 \text{ and we do not use the SW transformation: } \hat{\Delta}\hat{\sigma}_P^{+}\hat{\sigma}_P^{-}} + \frac{\omega_v \lambda^2}{4} + \tilde{\Lambda}\hat{\sigma}_x$$
$$+ \omega_v(\hat{b}^{\dagger}\hat{b} + \lambda\Lambda\hat{\sigma}_x(\hat{b}^{\dagger} + \hat{b})) + \omega_v\lambda\left(\underbrace{\left[\frac{\lambda_{+} - \lambda_{-}}{2}\right]}_{\text{If: } \delta=0\to 0}\hat{\sigma}_z + \underbrace{\left[\frac{\lambda_{+} + \lambda_{-}}{2}\right]}_{\text{If: } \delta=0\to 1/2} - \frac{1}{2}\right)(\hat{b}^{\dagger} + \hat{b}) \tag{2.40}$$

where $\hat{\sigma}_x = \hat{\sigma}_P^{+} + \hat{\sigma}_P^{-}$.

This model simplifies at *bare resonance* ($\delta = 0$), obtaining an improved version of the *effective Rabi* model (2.15), the *effective Shrieffer-Wolff* model:

$$H_{\text{SW}} = (\hat{\Delta} + (\boldsymbol{\alpha}_{+} - \boldsymbol{\alpha}_{-}))\hat{\sigma}_P^{+}\hat{\sigma}_P^{-} + \omega_v\hat{b}^{\dagger}\hat{b} + \hat{g}(\hat{\sigma}_P^{+} + \hat{\sigma}_P^{-})(\hat{b}^{\dagger} + \hat{b}) + \tilde{\Lambda}\hat{\sigma}_x + \epsilon - \boldsymbol{\alpha}_{-} \tag{2.41}$$

where, $\hat{\Delta} = 2g$, $\hat{g} = \omega_v\lambda/2$ and $\epsilon = \omega_c + \omega_v\lambda^2/4 - g$. As in *effective Rabi* model (2.15), we have projected the HQR model over the first two polaritons of the JC and applied the polaron transformation $U_P^{(1)}$. But, we have added a second order perturbation correction (2.37). Thus, the *SW* transformation gives us:

- A change in the splitting between the polaritons $|P_{\pm}^{(1)}\rangle$: $\hat{\Delta} \to \hat{\Delta} + (\alpha_{+} - \alpha_{-})$.
- A change in the energy shift of all levels: $\epsilon \to \epsilon - \alpha_{-}$.
- An additional term $\tilde{\Lambda}\hat{\sigma}_x$ that does not conserves parity (2.16).

Therefore, the new term $\propto \hat{\sigma}_x$ which emerges from the counterrotating terms is the reason because the *effective SW* model (2.41) does not preserve the parity (2.16). This term breaks the parity symmetry in a *Rabi*-like model, cf. [13]. Physically, it can be undertood as an spontaneous transition in the two-level system formed by the first two JC polaritons. A transition which is not mediated by the phonons [cf. [13] for more details]. Thus, at ***bare resonance***, we can check this by plotting the energy spectrum of the new *effective SW* model (2.41) versus the HQR model (1.35) (or (2.2)). The result shown in figure 2.9, obtaining the anticrossings in the *effective SW* model eigenenergies (blue curves) characteristic fo the HQR model at *bare resonance*.

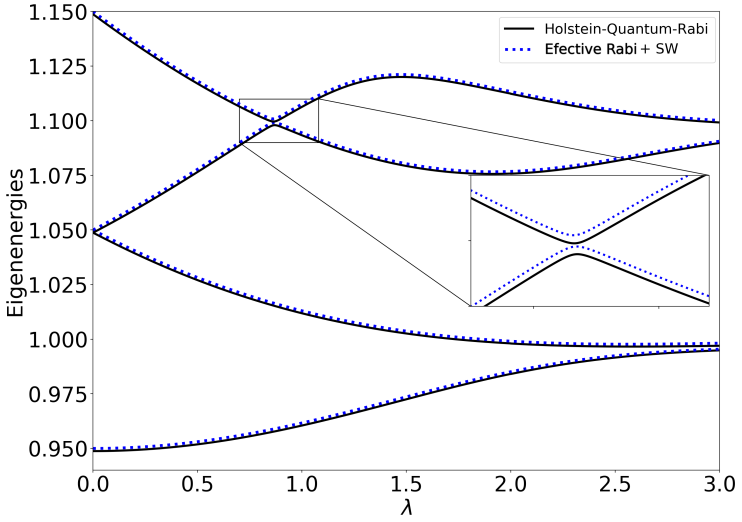

Figure 2.9: At ***bare resonance***, comparison between the *Holstein-Quantum-Rabi* energy spectrum [black lines, cf. equation (1.35) (or (2.2))] and the *effective SW* energy spectrum (dotted blue lines, see equation (2.41)). Parameters: $\omega_c = \Delta = 1$, $g = 0.05$ and $\omega_v = 0.1$.

Again, we can also compare the expected value of the parity (2.16) $\langle \hat{P} \rangle$ for each eigenvalue. Thus, at ***bare resonance***, comparing the new *effective SW* model (2.41) versus the HQR model (1.35); we do not have "jumps" [recall figure 2.5] in the parity (2.16), since we have antincrossings in the energy spectrum and the parity (2.16) is not conserved. We can see these results in the figure 2.10.

In short, projecting HQR over the JC polaritons and after a polaron transformation $U_P^{(1)}$, we have added a second order perturbation (2.37) correction. While the counterrotating terms produce a shift in the cavity frequency [Bloch-Siegert, cf. section 2.3] in the representation of the basis $\{|\uparrow\ 0_{phot}\ \tilde{n}_{phon}\rangle\,, |\downarrow\ 1_{phot}\ 0_{phon}\rangle\}$, here, we have a new term $\propto \hat{\sigma}_x$ which breaks the parity symmetry in the representation of the *effective Rabi* model (2.15) at ***bare resonance***. Again, a second order perturbative correction given by the counterrotating terms is the responsible of the anticrossings in the energy spectrum.

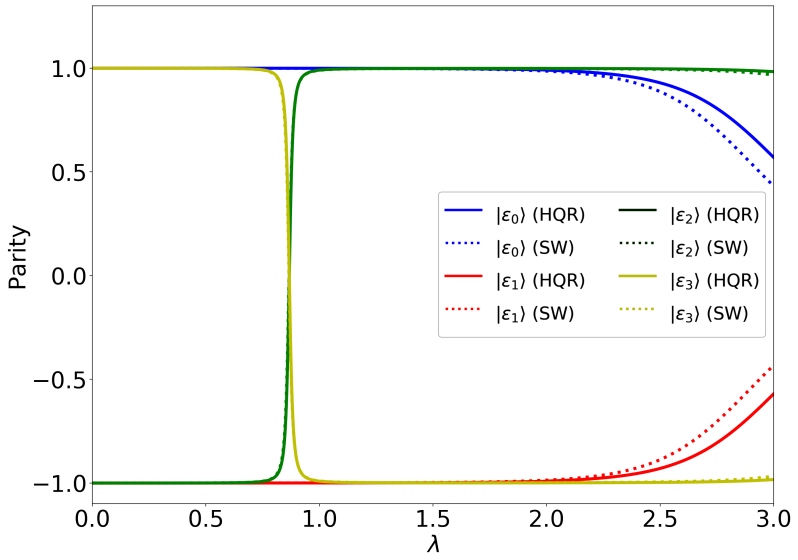

(a)

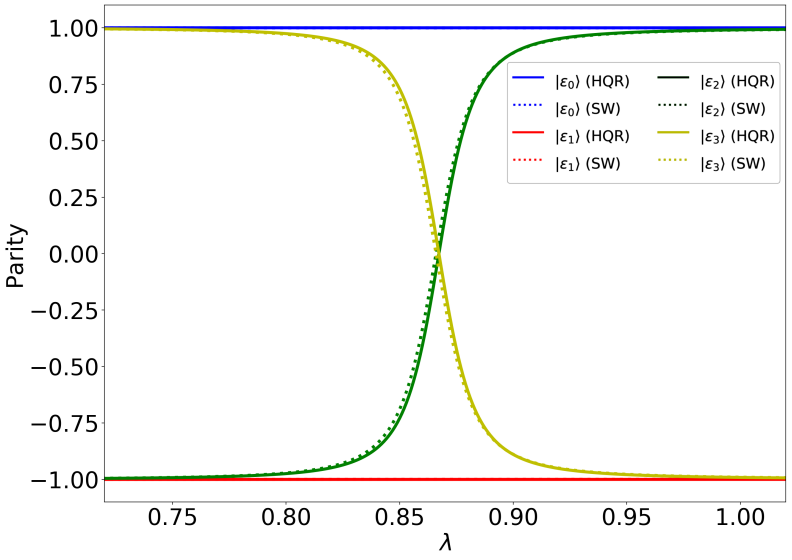

(b)

Figure 2.10: At ***bare resonance***: (a) The expected value of the parity operator $\langle \hat{P} \rangle$ (2.16). We have used the same color for its corresponding energy levels [cf. figure 2.4]. The continuous lines have been obtained using *Holstein-Quantum-Rabi* Hamiltonian (1.35) (or (2.2)) and the dotted ones using the *effective SW* Hamiltonian (2.41). (b) Zoom of the crossing/anticrossing region. Parameters: $\omega_c = \Delta = 1$, $g = 0.05$ and $\omega_v = 0.1$.

2.5 Analytical approximations of eigenvalues and eigenvectors

In this section, we use a third approach. We use a Polaron-like transformation to quasi-diagonalize the *effective Rabi* model (2.15):

$$H_{\text{eff}} = \frac{\hat{\Delta}}{2}(\hat{\sigma}_z + 1) + \omega_v \hat{b}^\dagger \hat{b} + \hat{g}\hat{\sigma}_x(\hat{b}^\dagger + \hat{b}) + \tilde{\epsilon}$$

The objective of this section is to obtain analytical expression for the eigenvectors and eigenvalues of the polariton sector. The Polaron-like transformation which we use for that task is:

$$U_P^{(2)} = \exp\left(\hat{\sigma}_x \alpha(\hat{b}^\dagger - \hat{b})\right) \tag{2.42}$$

Here, α is a variational parameter. It is convenient to make the change $\hat{\sigma}_x \to \hat{\sigma}_z$. So, under this change of basis, we propose the following ansatz for the ground state of our *effective Rabi* model (2.15):

$$|gs\rangle = e^{\hat{\sigma}_z \alpha(\hat{b}^\dagger - \hat{b})} |0_{phon}\rangle \left(\theta |-\rangle + \beta |+\rangle\right) \tag{2.43}$$

where $|\pm\rangle$ are eigenstates of $\hat{\sigma}_z$ ($\hat{\sigma}_z |\pm\rangle = \pm |\pm\rangle$). Now, we are going to calculate the energy of our proposed ansatz and minimize it with regard to α:

$$\epsilon_{gs} = \langle gs|H_{\text{eff}}|gs\rangle = \langle \psi_s| \langle 0_{phon}| {U_P^{(2)}}^\dagger H_{\text{eff}} U_P^{(2)} |0\rangle |\psi_s\rangle \tag{2.44}$$

where $|\psi_s\rangle = \theta |-\rangle + \beta |+\rangle$. In order to minimize ϵ_{gs}, $|\psi_s\rangle$ has to fulfil:

$$|\psi_s\rangle = \frac{|+\rangle - |-\rangle}{\sqrt{2}} \tag{2.45}$$

Supposing $\alpha \in \mathbb{R}$, we obtain the energy analytical expression for the ground state [cf. appendix G for more details]:

$$\boxed{\epsilon_{gs} = \frac{\hat{\Delta}}{2}\left(1 - e^{-2\alpha^2}\right) + 2\hat{g}\alpha + \omega_v \alpha^2 + \epsilon} \tag{2.46}$$

where $\hat{\Delta} = 2g$, $\hat{g} = \lambda\omega_v/2$ and $\epsilon = \omega_c + \omega_v\lambda^2/4 - g$. Minimizing ϵ_{gs}, we obtain the following value of α:

$$\boxed{\alpha = -\frac{\hat{g}}{\tilde{\Delta} + \omega_v}} \tag{2.47}$$

where $\tilde{\Delta} = \hat{\Delta} e^{-2\alpha^2}$. So, in order to get $\tilde{\Delta}$, we have to solve numerically the following transcendental equation:

$$\boxed{\tilde{\Delta} = \hat{\Delta} \exp\left[-2\frac{\hat{g}^2}{(\tilde{\Delta} + \omega_v)^2}\right]} \tag{2.48}$$

Thus, the equations (2.47-2.48) give us the value of the variational parameter α. Now, we are going to apply the Polaron transformation (2.42) after the change of basis $\hat{\sigma}_x \leftrightarrow \hat{\sigma}_z$ ($U_P^{(2)} = \exp(\hat{\sigma}_z \alpha(\hat{b}^\dagger - \hat{b}))$), over the *effective Rabi* model (2.15):

$$H_{\text{eff}} = \frac{\hat{\Delta}}{2}(\hat{\sigma}_x + 1) + \omega_v \hat{b}^\dagger \hat{b} + \hat{g}\hat{\sigma}_z(\hat{b}^\dagger + \hat{b}) + \tilde{\epsilon} \tag{2.49}$$

where we have already applied the change of basis $\hat{\sigma}_x \leftrightarrow \hat{\sigma}_z$ in the latter equation. Thus, applying the Polaron transformation $U_P^{(2)} = e^{\hat{\sigma}_z \alpha(\hat{b}^\dagger - \hat{b})}$ and approximating the displacement operators for their linear terms $D(\pm 2\alpha) = \exp[\pm 2\alpha(\hat{b}^\dagger - \hat{b})] \approx e^{-2\alpha^2}(1 \pm 2\alpha(\hat{b}^\dagger - \hat{b}))$ [cf. Appendix H for more details], we finally obtain an *effective Jaynes-Cummings* model:

$$H_{\text{JC}}^{\text{eff}} = \omega_v \hat{b}^\dagger \hat{b} + \tilde{\Delta}\hat{\sigma}_P^+ \hat{\sigma}_P^- + \tilde{g}_{eff}(\hat{b}\hat{\sigma}_P^+ + \hat{b}^\dagger \hat{\sigma}_P^-) + \tilde{\epsilon} - \frac{\tilde{\Delta}}{2} \tag{2.50}$$

where:

$$\tilde{\Delta} = 2ge^{-2\alpha^2}, \quad \tilde{\epsilon} = \omega_v \left(\alpha(\lambda + \alpha) + \frac{\lambda^2}{4}\right) + \omega_c, \quad \tilde{g}_{eff} = -2\tilde{\Delta}\alpha \tag{2.51}$$

In the new effective Hamiltonian (2.50) the traditional role in the matter is now played by the one-excitation light-matter polaritons[6] $\{|P_+^{(1)}\rangle, |P_-^{(1)}\rangle\}$; and the role of photons is played by the phonons. Thus, we can diagonalize it and analytically obtain the first energy level of our spectrum:

$$|\epsilon_0\rangle = |P_-^{(1)}\ 0_{phon}\rangle, \qquad \epsilon_0 = \tilde{\epsilon} - \frac{\tilde{\Delta}}{2} \tag{2.52}$$

$$|\epsilon_1\rangle = \tfrac{1}{\sqrt{\delta_-^2+1}}(\delta_- |P_+^{(1)}\ 0_{phon}\rangle + |P_-^{(1)}\ 1_{phon}\rangle), \qquad \epsilon_1 = \beta_- + \tilde{\epsilon} \tag{2.53}$$

$$|\epsilon_2\rangle = \tfrac{1}{\sqrt{\delta_+^2+1}}(\delta_+ |P_+^{(1)}\ 0_{phon}\rangle + |P_-^{(1)}\ 1_{phon}\rangle), \qquad \epsilon_2 = \beta_+ + \tilde{\epsilon} \tag{2.54}$$

where:

$$\beta_\pm = \frac{\omega_v \pm \sqrt{\tilde{\Delta}^2(1 + 16\alpha^2) + \omega_v(\omega_v - 2\tilde{\Delta})}}{2} \qquad \delta_\pm = \frac{2\beta_\mp - \tilde{\Delta}}{4\alpha\tilde{\Delta}} \tag{2.55}$$

[6] Recall that we have to apply the two Polaron transformations ($U_P^{(0)} = \exp(-\lambda\hat{\sigma}^+\hat{\sigma}^-(\hat{b}^\dagger - \hat{b}))$ and $U_P^{(2)} = \exp(\hat{\sigma}_x \alpha(\hat{b}^\dagger - \hat{b}))$) over the polaritons (2.8).

At *bare resonance*, if we now compare these analytical expressions (2.52-2.54) with the exact diagonalization of the *Holstein-Quantum-Rabi* model (1.35) (or (2.2)) and with the *effective Shrieffer-Wolff* model (2.41), we obtain a good agreement. A representative case is shown in figure 2.11. Although, the quantitative agreement with the exact results provided by this polaron approach is worse than the one provided by the *effective Shrieffer-Wolff* model [cf. section 2.4], the polaron approach is simpler and provide semianalytical expressions (2.52-2.54).

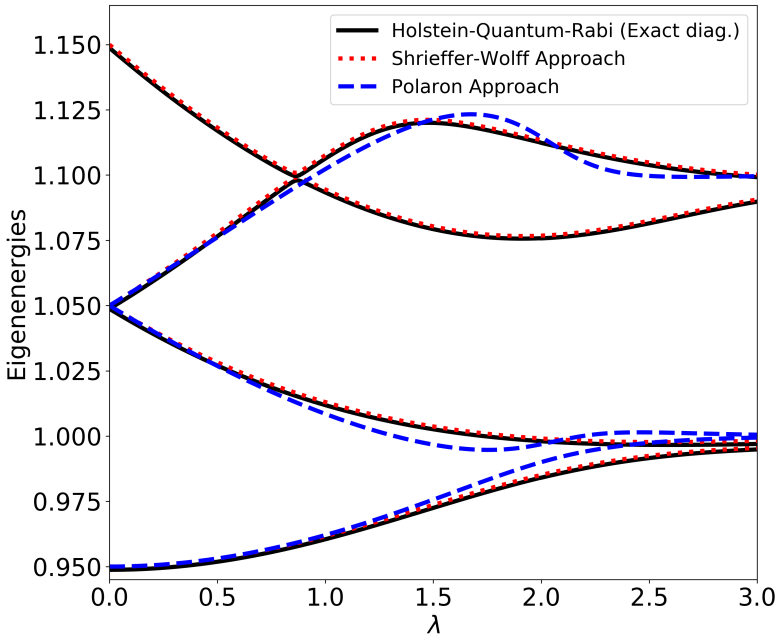

Figure 2.11: At ***bare resonance***, comparison between the analytical expressions for the energy spectrum (2.52-2.54) (blue dashed lines), the exact diagonalization of the *Holstein-Quantum-Rabi* model (1.35) (or (2.2)) (continuous black curves) and the *Shrieffer-Wolff* effective model (2.41) (dotted red curves). Parameters: $\Delta = \omega_c = 1.0$, $g = 0.05$ and ω_v.

2.6 Conclusions

Let us sum up the main results of this chapter. In section 2.1, we first started from the *Holstein-Quantum-Rabi* (HQR) model (1.35). Projecting HQR over the two first JC polaritons and applying the polaron transformation $U_P^{(0)} = \exp\left(-\lambda\hat{\sigma}^+\hat{\sigma}^-(\hat{b}^\dagger - \hat{b})\right)$, we obtained the *effective Rabi* model (2.15) for the polariton sector:

$$H_{\text{eff}} = \hat{\Delta}\hat{\sigma}_P^+\hat{\sigma}_P^- + \omega_v\hat{b}^\dagger\hat{b} + \hat{g}(\hat{\sigma}_P^+ + \hat{\sigma}_P^-)(\hat{b}^\dagger + \hat{b}) + \epsilon$$

Although, this model reproduces very well the energy spectrum of the polariton sector, this *Rabi*-like Hamiltonian commutes with the parity (2.16) operator. Thus, the *effective Rabi* model conserves the parity and has crossings in the energy spectrum at ***bare resonance*** ($\Delta = \omega_c$). However, the HQR does not commute with the parity (2.16) and has anticrossings.

In section 2.3, we included the counterrotating terms using perturbation theory, finding an energy shift: the *Bloch-Siegert* correction. The counterrotaing terms are responsible of the anticrossings in the energy spectrum at ***bare resonance***. They produce a shift in the cavity frequency ω_c leading the system out-of-resonance.

In general the HQR does not conserves the parity. However, at ***dressed resonance*** ($\Delta = \omega_c - \delta_{BS}$), we have dicovered that HQR model conserves the parity (2.16) in the representation of the *effective Rabi* model (2.15).

In section 2.4, we used the *Shrieffer-Wolff* transformation in order to improve our *effective Rabi* model (2.15). We have added a second order perturbative correction in the representation of the *effective Rabi* model (2.15). Thus, the effect of the couterrotating terms is mainly codified in a $\hat{\sigma}_x$-term:

$$H_{\text{SW}} = (\hat{\Delta} + (\boldsymbol{\alpha}_+ - \boldsymbol{\alpha}_-))\hat{\sigma}_P^+\hat{\sigma}_P^- + \omega_v\hat{b}^\dagger\hat{b} + \hat{g}(\hat{\sigma}_P^+ + \hat{\sigma}_P^-)(\hat{b}^\dagger + \hat{b}) + \tilde{\Lambda}\hat{\sigma}_x + \epsilon - \boldsymbol{\alpha}_-$$

This extra $\hat{\sigma}_x$-term added to the *effective Rabi* Hamiltonian takes into account the counterrrotating terms in this representation. Thus, at ***bare resonance***, this new Hamiltonian H_{SW} no longer commutes with the parity (2.16) and has anticrossings as HQR model in the polariton sector.

Finally, in the section 2.5, we have obtained a semianalytical expression for the energy spectrum in the polariton sector. Here, we have departed from the *effective Rabi* model (2.15) and applied a polaron transformation $U_P^{(2)} = \exp\left(\hat{\sigma}_x\alpha(\hat{b}^\dagger - \hat{b})\right)$, where α is a variational parameter which minimizes the ground state ansatz (2.43) in the polariton sector [the black curves in figure 2.2]. After this we obtain an *effective Jaynes-Cummings* model:

$$H_{\text{JC}}^{\text{eff}} = \omega_v\hat{b}^\dagger\hat{b} + \tilde{\Delta}\hat{\sigma}_P^+\hat{\sigma}_P^- + \tilde{g}_{eff}(\hat{b}\hat{\sigma}_P^+ + \hat{b}^\dagger\hat{\sigma}_P^-) + \tilde{\epsilon} - \frac{\tilde{\Delta}}{2}$$

Thus, we obtain analytical expression for eigenvalues and eigenvectors of the polariton subspace. These are polaritons composed by a mixture between the JC light-matter polaritons (2.8) and the phonon excitations.

Chapter 3

The dynamics

In the last chapter, we have already seen the main effective models and analytical expressions for the energy spectrum. We have also seen some *ultrastrong effects* such as the spectrum anticrossings (*bare resonance*) or the change of the resonance condition (*dressed resonance*). Here, we discuss the dynamics of the *Holstein-Quantum-Rabi model* (1.35). We are going to divide the chapter in two parts.

In the first part, we will analyse the *Rabi oscillations* versus the matter-phonon coupling λ and its *Ultrastrong effects* [cf. sections 3.1 and 3.2]. In the second part of the chapter [cf. section 3.3], we will analyse the influence of the energy losses in the dynamics.

3.1 Main Rabi frequency and ultrastrong effects

To study the *Rabi oscillations*, we are going to use the same parameters used in the last chapter: $g = 0.05$, $\Delta = \omega_c = 1$ (*bare resonance*), $\omega_v = 0.1$ and $\lambda \in [0,\ 3]$. Besides, we are going to start with one photon in the optical cavity: $|\psi(t=0)\rangle = |\downarrow\ 1_{phot}\ 0_{phon}\rangle$.

Using exact diagonalization[1] with the *Holstein-Quantum-Rabi* (1.35), we calculate the expected value of the number of photons $\langle \hat{a}^\dagger \hat{a} \rangle\,(t)$ and the number of excitons $\langle \hat{\sigma}^+ \hat{\sigma}^- \rangle\,(t)$ versus time for several values of λ, see figure 3.1. Since $g/\omega_c = 0.05$. In principle, we can do the *Rotating Wave Approximation* and we expect that our *effective Rabi* model (2.15) explains the *Rabi* oscillations [cf. figure 3.1]:

$$H_{\text{eff}} = \hat{\Delta}\hat{\sigma}_P^+\hat{\sigma}_P^- + \omega_v \hat{b}^\dagger \hat{b} + \hat{g}(\hat{\sigma}_P^+ + \hat{\sigma}_P^-)(\hat{b}^\dagger + \hat{b}) + \epsilon, \qquad \text{where: } \hat{g} = \lambda\omega_v/2$$

[1] All the numerical calculations will be done with *QuTip*, a tool based on *Python*, specialised on *Quantum mechanics* calculations.

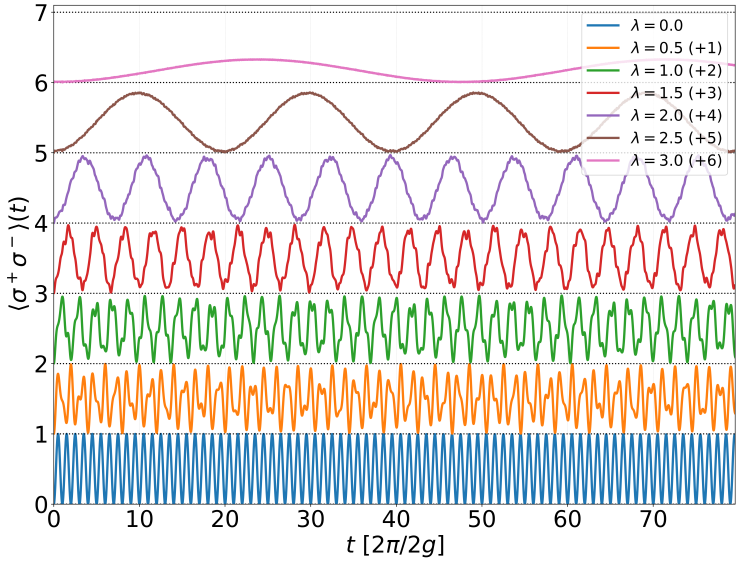

(a)

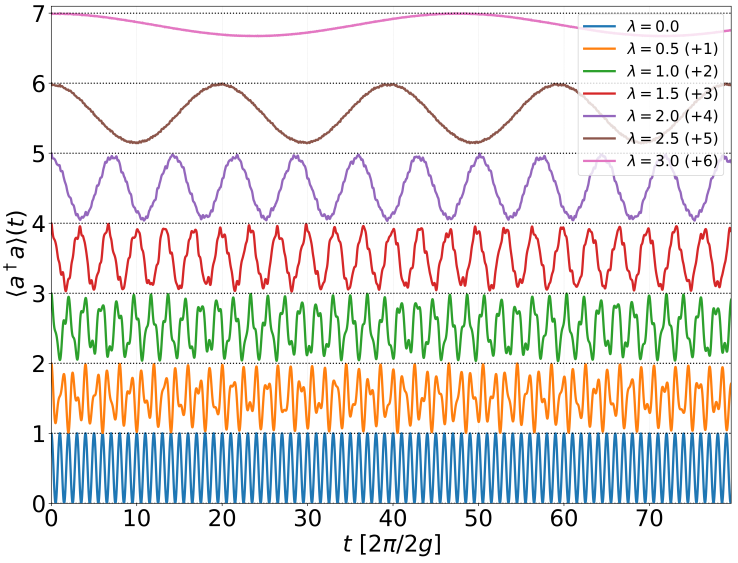

(b)

Figure 3.1: At ***bare resonance***: (a) Rabi oscillations for $\langle \hat{\sigma}^+ \hat{\sigma}^- \rangle (t)$ (b) Rabi oscillations for $\langle \hat{a}^\dagger \hat{a} \rangle (t)$. We have summed a constant [see legend] for each value of λ in order to visualize each case independently. Parameters: $g = 0.05$, $\Delta = \omega_c = 1$, $\omega_v = 0.1$, $\lambda = 0.0 - 3.0$ and $|\psi(t=0)\rangle = |\downarrow \ 1_{phot} \ 0_{phon}\rangle$; the time is in units of $2\pi/2g$.

Recall that the *effective Rabi* model (2.15) was obtained restricting to the polaritons $|P_\pm^{(1)}\rangle$ of the *Jaynes-Cummings* model (1.10), [cf. section 2.1]. Besides, our initial state is $|\psi(t=0)\rangle = |\downarrow \ 1_{phot} \ 0_{phon}\rangle$. So, we expect that the dynamics is restricted to the one excitation subspace, see 2.2 (black lines), and explained by (2.15).

Furthermore, this *effective Rabi* model (2.15) is a resonant *Rabi* model since $\hat{\Delta} = 2g = \omega_v$ for the case $g = 0.05$ and $\omega_v = 0.1$. So, we would expect complete *Rabi oscillations* i.e. an oscillation from 0 to 1. In fact, we obtain a good match between *Rabi oscilations* of the exact calculation of the HQR model and the *effective Rabi* model (2.15) for $\lambda < 2$ [cf. figure 3.2]. However, this does not occur for $\lambda \gtrsim 2$. Thus, we are going to focus on two aspects of the dynamics in this section: The dependence with λ of the main frequency of the *Rabi oscillations* and the incomplete *Rabi oscillations* for $\lambda \gtrsim 2$.

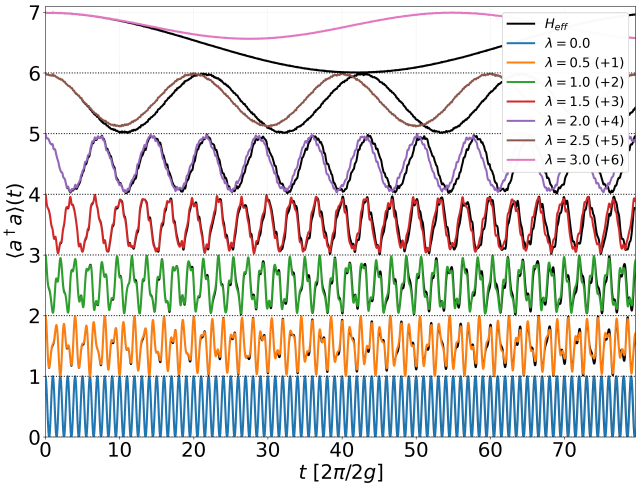

Figure 3.2: At ***bare resonance***, *Rabi* oscillations for $\langle \hat{a}^\dagger \hat{a} \rangle (t)$ versus *effective Rabi* model (2.15), black curves. Parameters: $g = 0.05$, $\Delta = \omega_c = 1$, $\omega_v = 0.1$, $\lambda = 0.0 - 3.0$ and $|\psi(t=0)\rangle = |\downarrow \ 1_{phot} \ 0_{phon}\rangle$.

An educated guess is that the dynamics is dominated by the first states of the spectrum. In section 2.5, we have obtained an analytical approximation for the first three energy levels (2.52-2.54). These energy levels are proportional to the light-matter *Jaynes-Cummings* polaritons $|P_\pm^{(1)}\rangle$ of one photon and the states of zero and one phonons $|0_{phon}\rangle$, $|1_{phon}\rangle$. Besides, our initial state is a cavity photon and zero phonons and matter excitations, $|\psi(t=0)\rangle = |\downarrow \ 1_{phot} \ 0_{phon}\rangle$. Thus, the main *Rabi frequency* Ω_R depends on λ as the energy difference of the lowest energy levels of the polariton subspace. In other words, the energy difference between the eigenstates $|\epsilon_0\rangle \propto |P_-^{(1)}, 0_{phon}\rangle$ (2.52) and $|\epsilon_1\rangle \propto |P_+^{(1)}, 0_{phon}\rangle$, $|P_-^{(1)}, 1_{phon}\rangle$ (2.53). Then, the main *Rabi frequency* is $\Omega_R = \epsilon_1 - \epsilon_0$:

$$\Omega_R = g e^{-2\alpha^2(\lambda)} + \frac{\omega_v - \sqrt{4g^2 e^{-4\alpha^2(\lambda)}(1 + 16\alpha^2(\lambda)) + \omega_v(\omega_v - 4g e^{-2\alpha^2(\lambda)})}}{2} \tag{3.1}$$

where the value of α can be computed solving the transcendental equation (2.48). The comparison between (3.1) and the main frequency in the exact calculation [cf. figure 3.1] is drawn in figure 3.3. Apparently, we obtain a good agreement between the analytical and numerical approach in figure 3.3a. How-

ever, if we focus on the small *Rabi frequencies* by plotting the same quantities in logarithm scale [cf. figure 3.3b], we clearly see that there is a disagreement when $\lambda \gtrsim 2$.

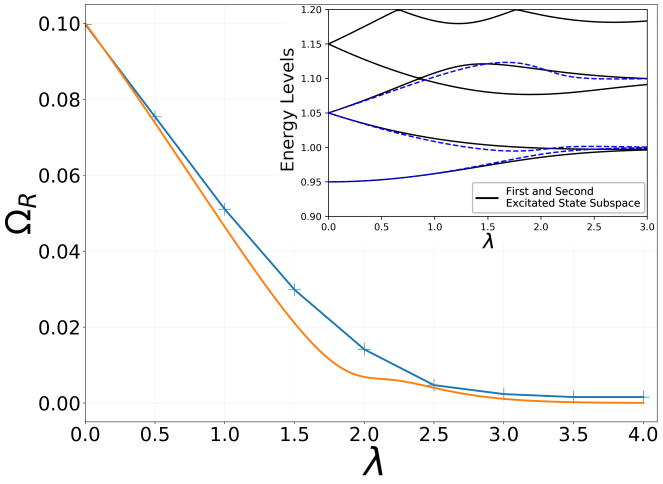

(a)

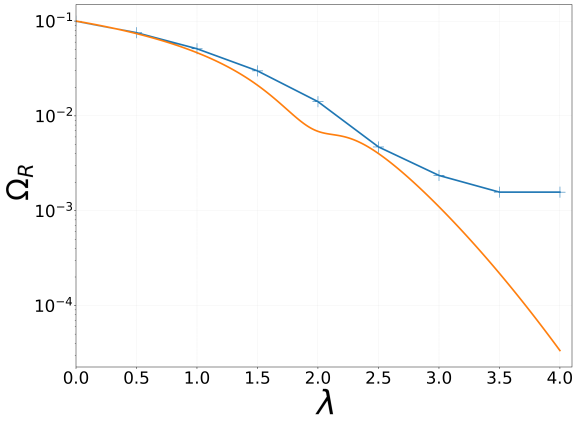

(b)

Figure 3.3: At ***bare resonance***: (a) Main *Rabi frequency* versus the coupling λ. Analytical expression (3.1) (orange line) and the main frequency obtained using the *Fast Fourier transform* (blue dots) of the *Rabi* oscillations obtained in figure 3.1. We use the same parameters. (b) The same but in logarithm scale.

How can we explain this disagreement between the analytical and numerical calculus for $\lambda \gtrsim 2$? [cf. figure 3.3b] In the last chapter, we have seen that the Bloch-Siegert correction δ_{BS} is relevant when $\lambda \gtrsim 2$ [cf. figure 2.6] at *bare resonance*. This second order correction is an effect of the couterrotating terms which changes the value of the cavity frequency [cf. section 2.3]. Thus, the system is really out-of-resonance when the bare values are $\omega_c = \Delta$.

Then, we can think that the disagreement of the figure 3.3b is an *Ultrastrong effect*. Since, we have to remember that the validity of the equations (2.52-2.54) is subjected to the *bare resonance condition* $\delta = \Delta - \omega_c = 0$; and this condition is violated when the *Bloch-Siegert correction* carries the system to out-of-resonance ($\Delta \neq \omega_c - \delta_{BS}$, recall section 2.3). Besides, this correction and the effective light-matter coupling has a comparable value $g_{\text{eff}} \sim \delta_{BS}$ for $\lambda \gtrsim 2$, see figure 3.4. Finally, the counterrotating terms are the origin of the incomplete *Rabi oscillations*. This incompleteness is the manifestation that our system is out-of-resonance. In figure 3.4, we have also plotted the difference between the maximum P_{max} and the minimum P_{min} of the oscillations (blue line). So, when $P_{max} - P_{min} = 1$, we have complete oscillations and when $P_{max} - P_{min} < 1$ we have incomplete ones. Thus, when $\lambda \gtrsim 2$ and the counterrotating terms are relevant, we find $P_{max} - P_{min} \ll 1$.

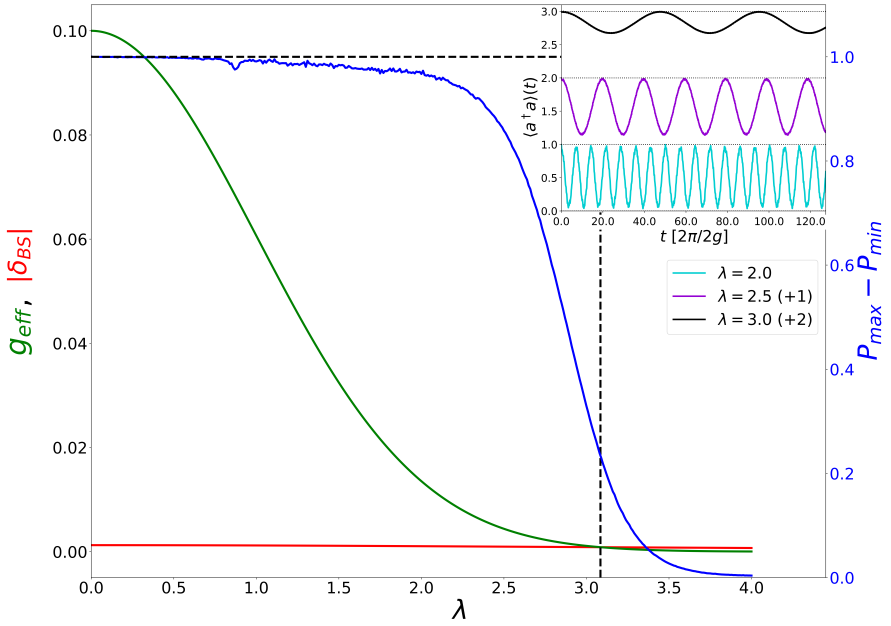

Figure 3.4: At ***bare resonance*** (using the parameter of figure 3.1): Left axis, comparison between the effective light-matter effective coupling and the *Bloch-Siegert correction* $|\delta_{BS}|$ versus λ. Right axis, difference between the minimum and maximum of the *Rabi oscillations* versus λ. The inset corresponds to the *Rabi oscillations* of the expect number of photons $\langle \hat{a}^\dagger \hat{a} \rangle (t)$ for three different values of λ. The incomplete *Rabi oscillations* are apparent.

We can check these effects changing the value of the cavity frequency ω_c imposing the ***dressed resonance condition*** ($\Delta = \omega_c - \delta_{BS}(\lambda)$) and using the equation (2.28). Thus, we have a new value of $\omega_c > 1$ for each value of λ. Recalculating the time evolution of the system and the expected values $\langle \hat{a}^\dagger \hat{a} \rangle (t)$ and $\langle \hat{\sigma}^+ \hat{\sigma}^- \rangle (t)$, we obtain complete *Rabi oscillations*, see figure 3.5.

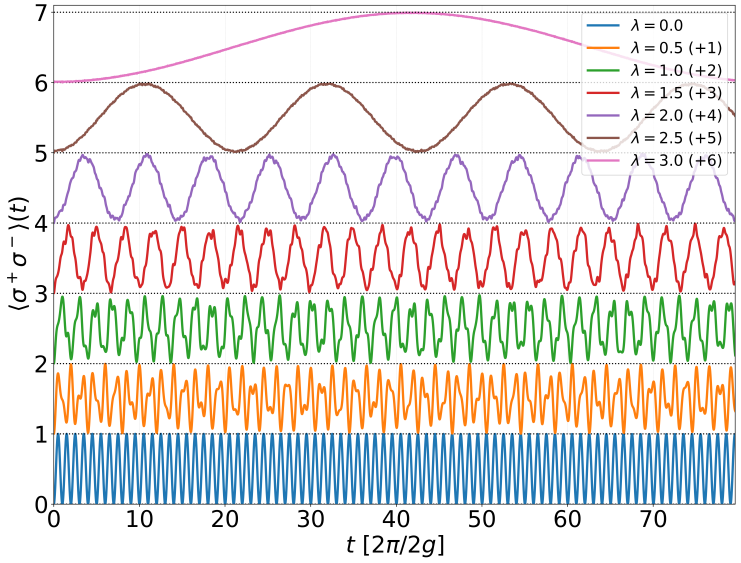

(a)

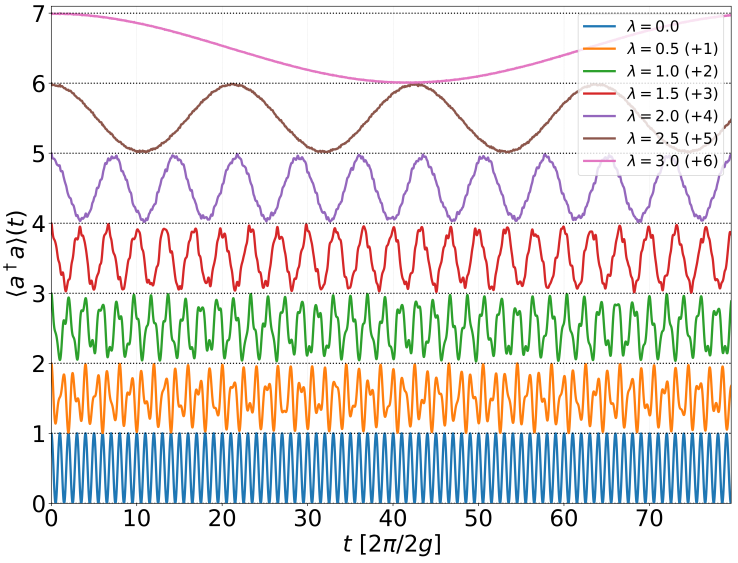

(b)

Figure 3.5: At ***dressed resonance***: (a) Rabi oscillations of $\langle \hat{\sigma}^{+}\hat{\sigma}^{-} \rangle (t)$ (b) Rabi oscillations of $\langle \hat{a}^{\dagger}\hat{a} \rangle (t)$. We have summed a constant [see legend] for each value of λ in order to visualize each case independently. Parameters: $g = 0.05$, $\Delta = 1$, $\Delta = \omega_c - \delta_{BS}(\lambda, \omega_c)$, $\omega_v = 0.1$, $\lambda = 0.0 - 3.0$ and $|\psi(t=0)\rangle = |\downarrow\ 1_{phot}\ 0_{phon}\rangle$.

At ***dressed resonance***, we can also recalculate the main *Rabi* frequency of the HQR model obtained in figure 3.5 using *Fast Fourier transform* and compare it with the analytical value obtained by the equation (3.1). We obtain a good agreement between them and correct the value of the frequency for $\lambda \gtrsim 2$, see figure 3.6. Therefore, we have checked that these effects clearly are *Ultrastrong effects*.

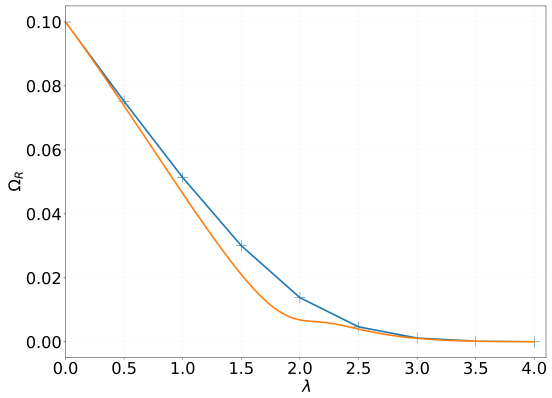

(a)

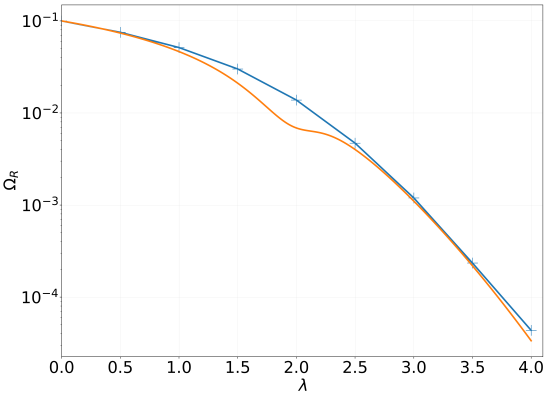

(b)

Figure 3.6: At ***dressed resonance***: (a) Main *Rabi frequency* versus λ. The analytical expression (3.1) (orange curve) and the main *Rabi* frequency of *Fast Fourier transform* (blue dots), see figure 3.1 (b) Same plot but in logarithm scale. Parameters: $g = 0.05$, $\Delta = 1$, $\Delta = \omega_c - \delta_{BS}$, $\omega_v = 0.1$, $\lambda = 0 - 3$ and $|\psi(t=0)\rangle = |\downarrow 1_{phot}0_{phon}\rangle$.

These effects do not fulfil the rule of thumb $g/\omega_c > 0.1$ where we would expect *Ultrastrong effects*. The reason is that the effective light-matter coupling[2] g_{eff} is "dressed" [cf. section 2.3]. This renormalization of the light-matter coupling depends on the overlaps between the phonon states, i.e. the *Frack-Condon factors*. As the effective light-matter coupling depends on the coupling λ: $g_{\text{eff}} = ge^{-\lambda^2/2}$. This dependence enables that $g_{\text{eff}}(\lambda) \sim \delta_{BS}$ for $\lambda \gtrsim 2$ [cf. figure 3.4]. In other words, the effective light-matter couplign g_{eff} is comparable to the pertubation theory correction (δ_{BS}).

[2]Coupling between the main states involved in the *Rabi oscillations* $|\uparrow 0_{phot}\tilde{0}_{phon}\rangle$ and $|\downarrow 1_{phot}0_{phon}\rangle$.

3.2 Rabi frequencies

In the last section, we have just seen some *Ultrastrong effects* and an analytical expression for the main *Rabi frequency*. However, the problem is more complex. In figure 3.5, it is shown that for intermediate values of $0.0 \lesssim \lambda \lesssim 1.5$, there are many frequencies involved. At *bare resonance*, we plot the normalized weight of each *Rabi frequency* Ω_R for each value of λ using the *Fast Fourier transform*, see figure 3.7.

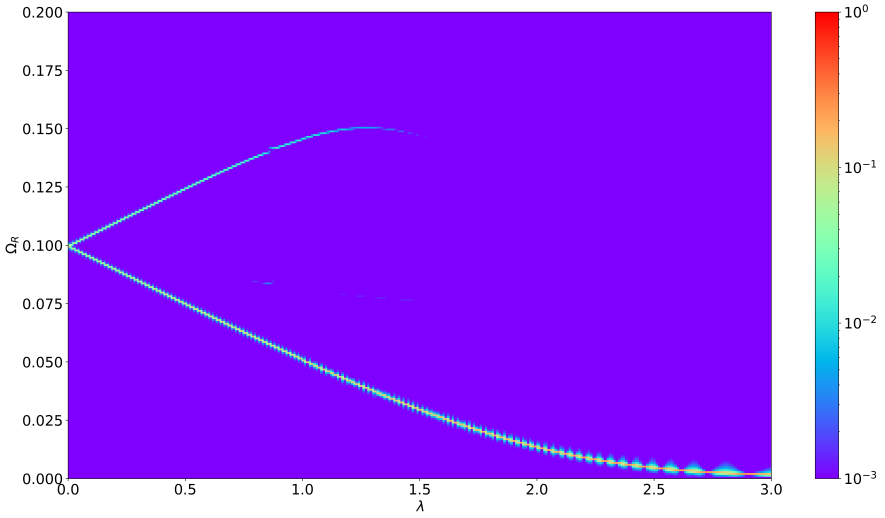

(a)

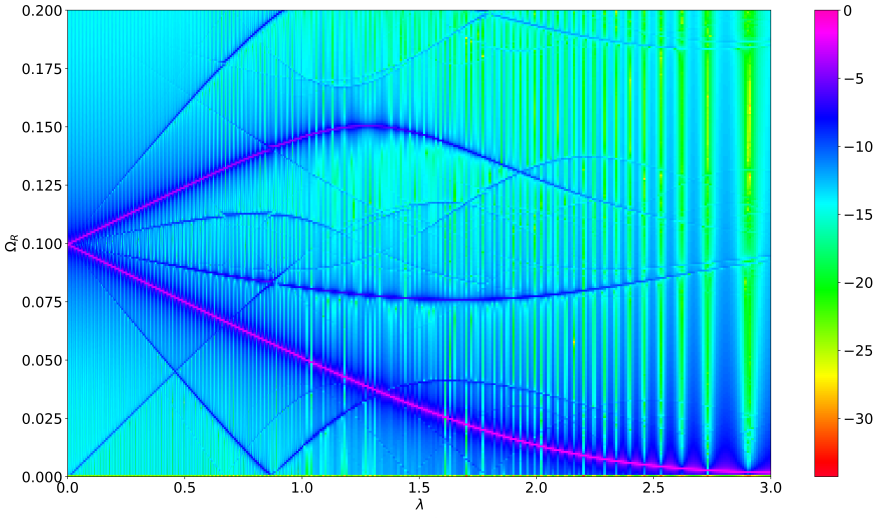

(b)

Figure 3.7: At ***bare resonance***: (a) Colour plot of the *Rabi frequencies* weights versus λ. The weights are normalized. (b) The same plot, but in logarithm scale. Parameters: $g = 0.05$, $\Delta = \omega_c = 1$, $\omega_v = 0.1$, $\lambda = 0.0 - 3.0$ and $|\psi(t=0)\rangle = |\downarrow\ 1_{phot}\ 0_{phon}\rangle$.

3.2.1 Numerical analysis

There are two or three *Rabi frequences* which take a relevant role in the dynamics, see figure 3.7a. In order to see the origin of these oscillations, we express[3] $\langle \hat{\sigma}^+ \hat{\sigma}^- \rangle (t)$ in terms of the eigenvalues and eigenvectors of our system $\{|\epsilon_0\rangle, |\epsilon_1\rangle, ...\}$:

$$|\psi(t)\rangle = \sum_j c_j \exp\left[-i\epsilon_j t\right] |\epsilon_j\rangle \qquad \text{where: } c_j = \langle \epsilon_j | \psi(0) \rangle \tag{3.2}$$

$$\langle \psi(t) | \hat{\sigma}^+ \hat{\sigma}^- | \psi(t) \rangle = \sum_{nm} p_{nm} \exp\left[-i(\epsilon_m - \epsilon_n)t\right] \tag{3.3}$$

where $p_{nm} = c_n^* c_m \langle \epsilon_n | \hat{\sigma}^+ \hat{\sigma}^- | \epsilon_m \rangle$. In particular, as a first approximation, we can limit ourselfs to the polariton subspace [cf. black energy levels of figure 2.2], if we neglect the light-matter counterrotating terms. Then, we would expect that the frequencies, given by the exponential of (3.3), correspond to the energy differences between eigenstates of the polariton subspace. Thus, we obtain that the two main frequencies are the energy differences $\epsilon_1 - \epsilon_0$ and $\epsilon_2 - \epsilon_0$ involving the first three eigenstates where ϵ_0, ϵ_1, ... are now the eigenergies of the polariton subspace, see figure 3.8a.

Two cases are studied: (i) $\omega_v = 2g$ ($\omega_v = 0.1$) and (ii) $\omega_v \neq 2g$ ($\omega_v = 0.075$). In figure 3.8 it is checked that the different *Rabi* frequencies correspond to the energy differences of the polariton eigenstates. We have to notice that in the case $\omega_v = 0.075$ (figure 3.8b) there is a gap between the two main frequencies ($\epsilon_1 - \epsilon_0$ and $\epsilon_2 - \epsilon_0$). This is due to the fact that when $\lambda = 0$, $\epsilon_1 < \epsilon_2$ [cf. the equations (2.22), $|P_\pm^{(1)}\rangle$ are approximately the *Jaynes-Cummings* polaritons of 1 photon]. Qualitatively, in the case $\omega_v \neq 2g$, we observe that the main frequency is $\epsilon_2 - \epsilon_0$ for $\lambda \lesssim 1.0$. Then, for larger values of λ, this frequency disappears and is substituted by the frequency $\epsilon_1 - \epsilon_0$. However, in the case $2g = \omega_v$, these two frequencies ($\epsilon_1 - \epsilon_0$ and $\epsilon_2 - \epsilon_0$) have similar relevance, but it is the frequency $\epsilon_2 - \epsilon_0$ which disappears for large values of the coupling λ, see figure 3.8.

[3] We can do the same for $\langle \hat{a}^\dagger \hat{a} \rangle (t)$

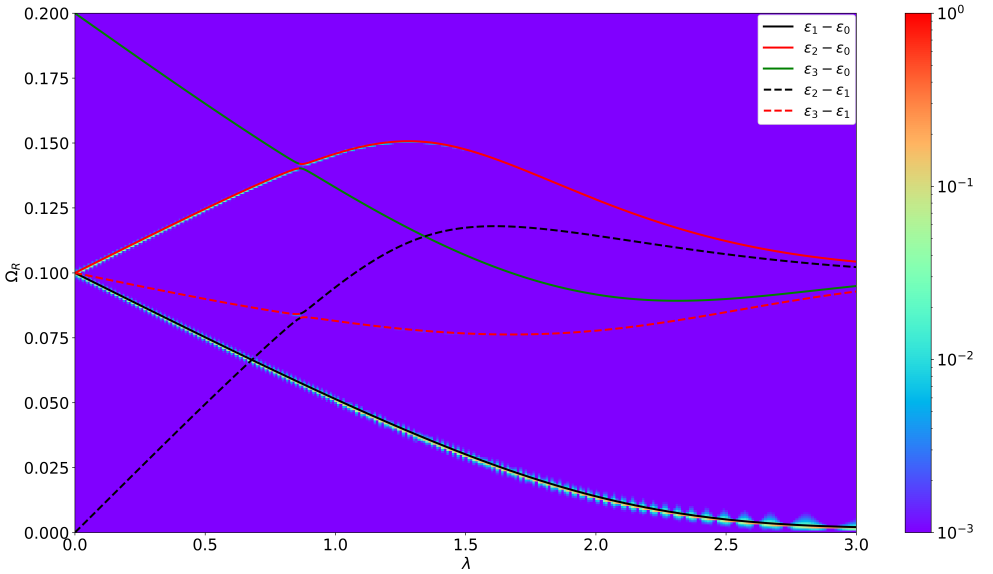

(a)

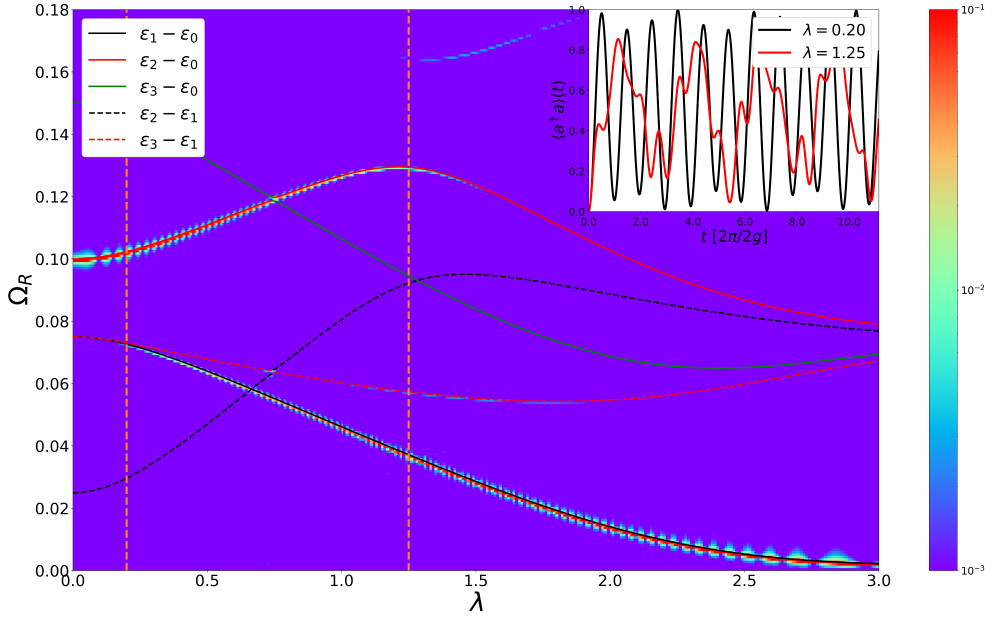

(b)

Figure 3.8: At ***bare resonance***: (a) Colour plot of the *Rabi frequencies* weights versus λ in the case of $2g = \omega_v$ ($\omega_v = 0.1$). The weights are normalized. The lines are the energy differences between the energies of the eigenstates of the polariton subspace [cf. black energy levels of figure 2.2]. (b) The same plot, but in the case of $2g \neq \omega_v$ ($\omega_v = 0.075$). Parameters: $g = 0.05$, $\Delta = \omega_c = 1$, $\lambda = 0.0 - 3.0$ and $|\psi(t=0)\rangle = |\downarrow\ 1_{phot}\ 0_{phon}\rangle$.

3.2.2 Analytical analysis

In this section, we are going to obtain analytical approximations for the weights p_{nm}, see equation (3.3). We are going to do three different approximations to the problem. The first approximation is to use the *effective Rabi model* (2.15) obtained in the last chapter and neglect[4] their counterrotaing terms:

$$H \approx \hat{\Delta}\hat{\sigma}_P^+\hat{\sigma}_P^- + \omega_v\hat{b}^\dagger\hat{b} + \hat{g}(\hat{\sigma}_P^+\hat{b} + \hat{\sigma}_P^-\hat{b}^\dagger) + \epsilon \tag{3.4}$$

where $\hat{\Delta} = 2g$, $\hat{g} = \lambda\omega_v/2$ y $\epsilon = \omega_c + \omega_v\lambda^2/4 - g$. Under the representation of the Hamiltonian (3.4), the initial state ($|\psi(0)\rangle = |\downarrow\ 1_{phot}\ 0_{phon}\rangle$) and the operator number of matter excitations ($\hat{\sigma}^+\hat{\sigma}^-$) are:

$$|\psi(0)\rangle = \frac{D(\lambda/2)}{\sqrt{2}}(|P_+^{(1)}\rangle - |P_-^{(1)}\rangle)\otimes|0_{phon}\rangle \qquad \hat{\sigma}^+\hat{\sigma}^- \longrightarrow \frac{1}{2}(1+\hat{\sigma}_x) \tag{3.5}$$

where $\hat{\sigma}_x = \hat{\sigma}_P^+ + \hat{\sigma}_P^-$, and $|P_\pm^{(n)}\rangle$ the *Jaynes-Cummings* polaritons (2.8) in the case of one photon $n = 1$ and *bare resonance* $\delta = \Delta - \omega_c = 0$. We can compare the energy spectrum of the model (2.15) with the simplified model (3.4). As we can see in figure 3.9, the energy level of each model has a very similar behaviour for $\lambda \lesssim 1$.

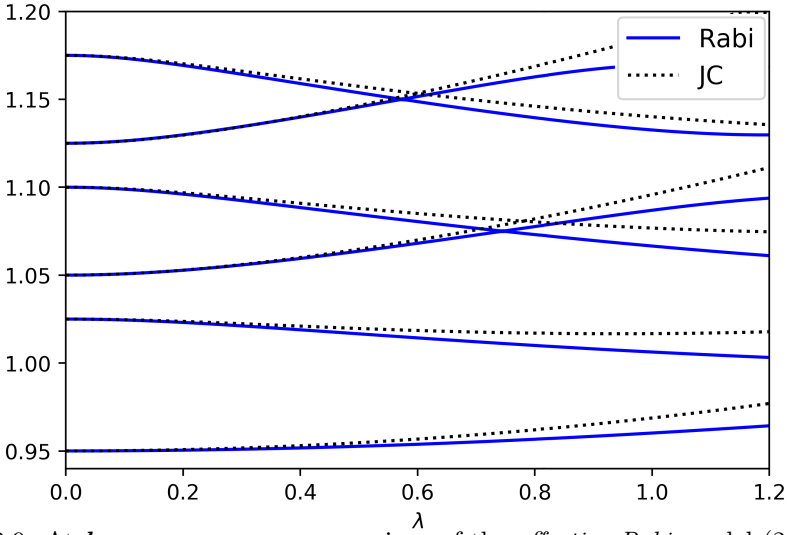

Figure 3.9: At ***bare resonance***, comparison of the *effective Rabi* model (2.15) with the counterrotating terms (blue lines) and without the counterrotating terms (black dotted lines (3.4)). Parameters: $g = 0.05$, $\Delta = \omega_c = 1$ and $\omega_v = 0.075$.

So, we can diagonalize the Hamiltonian (3.4) and obtain analytical expressions for the weights p_{10} and p_{20}. In order to do that we calculate $\langle\hat{\sigma}^+\hat{\sigma}^-\rangle(t)$ or $\langle\psi(t)|\sigma_x|\psi(t)\rangle/2$ in the representation of (3.4). Thus, we obtain:

$$\frac{1}{2}\langle\psi(t)|\hat{\sigma}_x|\psi(t)\rangle = -\frac{1}{2}[2p_{10}\cos((\epsilon_1-\epsilon_0)t) + 2p_{20}\cos((\epsilon_2-\epsilon_0)t)] \tag{3.6}$$

[4]**Do not cofuse** it with the *effective JC* model (2.50). This is a **different** model.

where the weights p_{10} and p_{20} corresponding to the frequencies $\epsilon_1 - \epsilon_0$ and $\epsilon_2 - \epsilon_0$ are:

$$p_{(1,2)0} = \frac{1}{2}\frac{(\tau_{\mp,0}|D_{0\tilde{0}}(\lambda/2)|^2 - D_{1\tilde{0}}(\lambda/2)D^{\dagger}_{0\tilde{0}}(\lambda/2))\tau_{\mp,0}}{\tau^2_{\mp,0}+1} \tag{3.7}$$

where $\tau_{\pm,n}$ are:

$$\tau_{\pm,n} = \frac{\hat{\delta} \pm \sqrt{4\hat{g}^2(n+1)+\hat{\delta}}}{2\hat{g}\sqrt{n+1}}, \qquad \hat{\delta} = \hat{\Delta} - \omega_v = 2g - \omega_v \tag{3.8}$$

The second approach consists on diagonalizing the *effective Jaynes-Cummings* model (2.50) in order to obtain the weights of p_{10} and p_{20}. We have to remember that in order to obtain (2.50), we used the Polaron transformation $U_P^{(2)} = e^{\sigma_x\alpha(b^\dagger - b)}$ and the approximation $D(-2\alpha) = e^{-2\alpha(b^\dagger - b)} = e^{-2|\alpha|^2}e^{-2\alpha b^\dagger}e^{2\alpha b} \approx e^{-2|\alpha|^2}(1 - 2\alpha(b^\dagger - b))$. Thus, we have to modify the initial condition (3.5) taking into account the Polaron transformations:

$$|\tilde{\psi}(0)\rangle = \frac{D(\lambda/2+\alpha)}{\sqrt{2}}(|P^{(1)}_+\rangle - |P^{(1)}_-\rangle) \otimes |0_{phon}\rangle \tag{3.9}$$

So, after some algebra using this modified initial condition (3.9) and the eigenvectors and eigenenergies (2.52-2.54), we can obtain the new analytical expressions for p_{10} and p_{20}. In the end, we only have to do the replacements $\lambda/2 \to \lambda/2 + \alpha$ and $\tau_{\pm,0} \to \delta_{\pm,0}$ in the expressions (3.7):

$$p_{(1,2)0} = \frac{1}{2}\frac{(\delta_{\pm,0}|D_{0\tilde{0}}(\lambda/2+\alpha)|^2 - D_{1\tilde{0}}(\lambda/2+\alpha)D^{\dagger}_{0\tilde{0}}(\lambda/2+\alpha))\delta_{\mp,0}}{\delta^2_{\mp}+1} \tag{3.10}$$

where the analytical expression of $\delta_{\pm,n}$ is much more complicated than $\tau_{\pm,0}$ and it requires to solve a transcendental equation. It can be found in the appendix I.1. In this appendix, we also discuss some other weights of other frequencies [cf. appendix I.2]. Finally, the third approach consist on obtaining the weights p_{10} and p_{20} numerically from the *effective Rabi* model (2.15).

At ***bare resonance***, we compare the three different approaches with the numerical calculus of the weights p_{10} and p_{20} using the HQR model (1.35) [cf. figure 3.10, continuous curves[5]]. Thus, we obtain that the best approach corresponds to the *effective Rabi* model (2.15) (dashed curves) while the analytical expressions (3.10) of the *effective Jaynes-Cummings* model (2.50) give us more qualitative information.

[5]The crossing between the weights of the frequencies $\epsilon_2 - \epsilon_0$ and $\epsilon_3 - \epsilon_0$ are due to the anticrossing of the energies ϵ_2 and ϵ_3 in the spectrum [cf. figure 2.2]. Recall, we are at ***bare resonance***

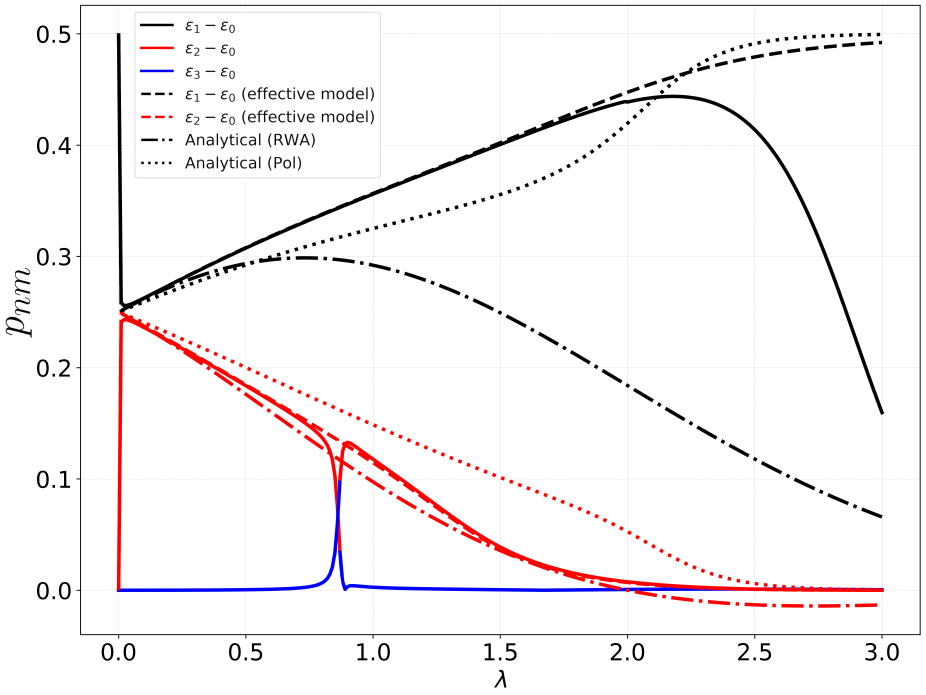

(a)

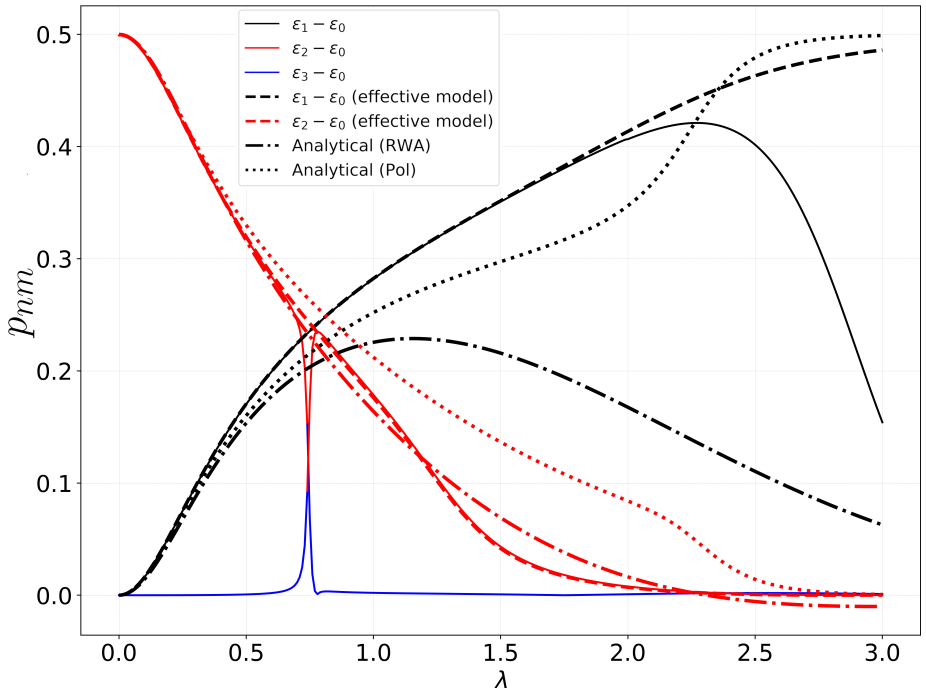

(b)

Figure 3.10: At ***bare resonance***: Analytical weights (3.7) (dashed-dotted curves); numerical weights (continuous curves) from *Holstein-Quantum-Rabi* (1.35); numerical weights (dashed curves) from *effective Rabi* (2.15) and numerical weights (dotted curves) from *effective Jaynes-Cummings* (2.50) of p_{20} (red curve) and p_{10} (black curve); (a) $2g = \omega_v$ (b) $2g \neq \omega_v$ ($\omega_v = 0.075$). Parameters: $g = 0.05$, $\Delta = 1$, $\omega_c = \Delta$ and $|\psi(0)\rangle = |\downarrow 1_{phot} 0_{phon}\rangle$.

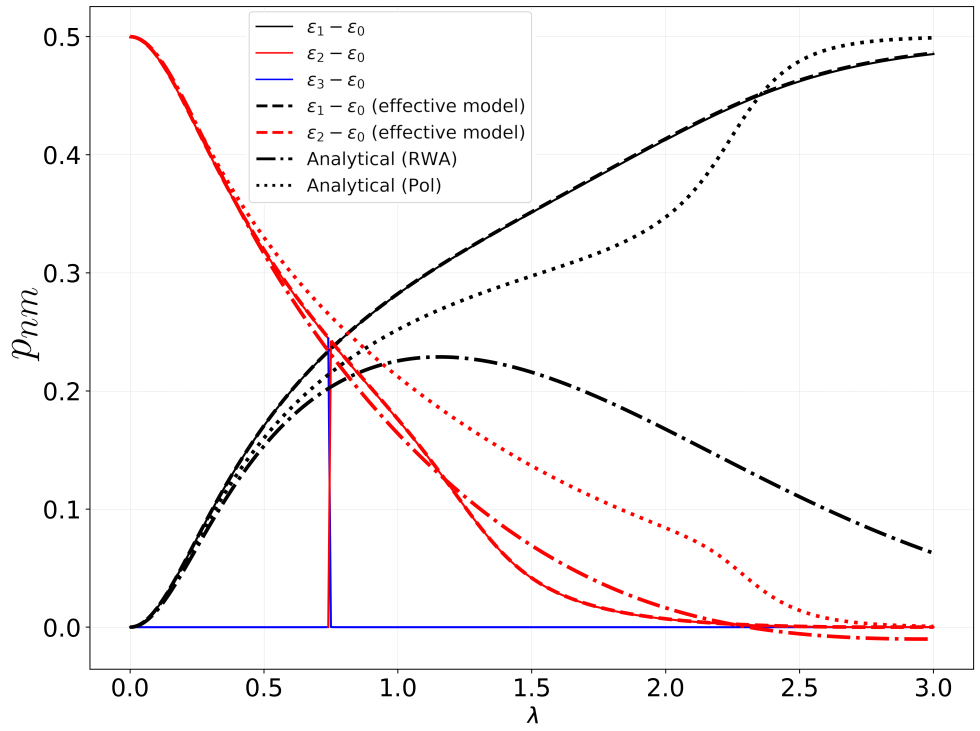

Figure 3.11: At ***dressed resonance*** (of the HQR model): Analytical weights (3.7) (dashed-dotted); numerical weights (continuous) from HQR (1.35); numerical weights (dashed) from (2.15) and analytical weights (dotted) from (2.50) of p_{20} (red curve) and p_{10} (black curve). Parameters: $g = 0.05$, $\Delta = 1$, $\Delta = \omega_c - \delta_{BS}$ and $\omega_v = 0.075$.

Finally, we have to mention that the decrease of the weight p_{10} for $\lambda \gtrsim 2$, see figure 3.10, it is due to the loss of the ***bare resonance condition*** $\delta = \Delta - \omega_c = 0$, due to the *Bloch-Siegert* correction. We can check this recalculating the weights p_{10} and p_{20} of the HQR model, but at *dressed resonance* ($\Delta = \omega_c - \delta_{BS}(\lambda)$), see figure 3.11. Thus, the *Holstein-Quantum-Rabi* (1.35) (continuous curves) and the *effective Rabi* (2.15) (dashed curves) weights, numerically obtained, are almost equal. At ***dressed resonance***, we recover the crossings instead of anticrossings and the weight p_{10} increases for $\lambda \gtrsim 2$.

3.3 Dynamics - Energy losses

To warm up let us discuss matter losses in the *Holstein* model eq. (1.26). Considering only matter losses with a initial state $\rho(t=0) = |\uparrow\ \tilde{0}_{phon}\rangle\langle\uparrow\ \tilde{0}_{phon}|$ and neglecting the transitions $|\downarrow\ n_{phon}\rangle \to |\uparrow\ \tilde{k}_{phon}\rangle$ and $|\downarrow\ k_{phon}\rangle \to |\uparrow\ \tilde{n}_{phon}\rangle$ in our master equation, see appendix J.1.1 for details. We find:

$$\langle\hat{\sigma}^+\hat{\sigma}^-\rangle(t) \approx \exp\left[-\gamma_{matter}\sum_{\omega_{\tilde{0}m}>0}\omega_{\tilde{0}m}\Gamma_{\tilde{0}\to m}t\right] \tag{3.11}$$

where $\omega_{\tilde{n}m} = (\Delta + \tilde{n}\omega_v) - m\omega_v$ and $\Gamma_{\tilde{n}\to k} = |\langle k|\tilde{n}\rangle|^2 = |D_{k\tilde{n}}(-\lambda)|^2$ are the weights of the transitions $|\uparrow \tilde{n}_{phon}\rangle \to |\downarrow k_{phon}\rangle$. The $D_{\tilde{m}n}(\alpha) = \langle\tilde{m}|n\rangle = \langle m|e^{\alpha(\hat{b}-\hat{b})}|n\rangle$ are Franck-Condon factors [cf. appendix E] which renormalize as a function of λ the transitions. Thus, the exponential decay given by the matter losses γ_{matter} is renormalized by the factor:

$$\gamma_{\tilde{n}}(\lambda,\omega_v) = \sum_{\omega_{\tilde{n}m}>0}\omega_{\tilde{n}m}\Gamma_{\tilde{n}\to m}(\lambda) \qquad \text{when: } \tilde{n}=0 \tag{3.12}$$

This factor is a sum over all the transitions, which fulfill $\omega_{\tilde{n}m} > 0$, weighted by the *Franck-Condon* factors $\Gamma_{\tilde{n}\to m}$. This equation (3.12) gives a very good match with the numerical calculus, see figure see figure J.1 of appendix J.1.1. Furthermore, it can be shown that $\lim_{\omega_v\to 0^+}\gamma_{\tilde{n}}(\lambda,\omega_v) = 1$ [cf. appendix J.1.2]. In other words, the renormalization disappears for a continuum of frequencies of vibration.

Once, we have understood the case of the *Holstein* model (1.26). We are going to study the case of small matter losses in the *Holstein-Quantum-Rabi* model (1.35). Using as parameters: $\omega_v = 0.1$, $\Delta = \omega_c = 1.0$ (***bare resonance***), $\lambda = 0.0 - 4.0$, $g = 0.05$ and an initial state of one photon in the cavity $\rho(t=0) = |\downarrow\ 1_{phot}\ 0_{phon}\rangle\langle\downarrow\ 1_{phot}\ 0_{phon}|$, we numerically compute[6] $\langle\hat{a}^\dagger\hat{a}\rangle(t)$ in the case of $\gamma_{matter} = 0.0$ (black curves) and with a few losses $\gamma_{matter} = 1.0\times10^{-4}$ ($\gamma_{phot} = \gamma_{phon} = 0$ in both cases), see figure 3.12.

[6] We can do the same with matter excitations $\langle\hat{\sigma}^+\hat{\sigma}^-\rangle(t)$

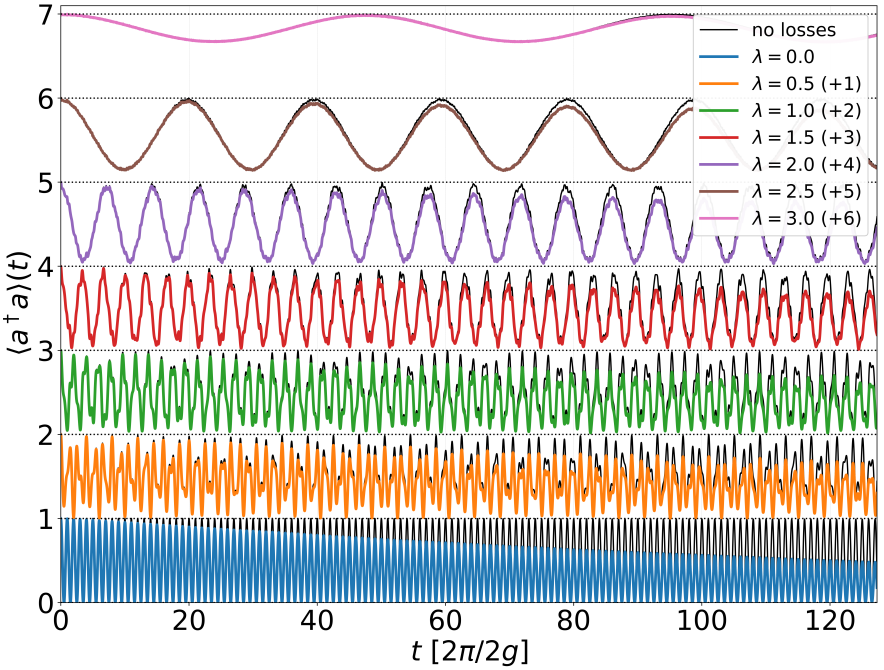

Figure 3.12: At ***bare resonance***, time evolution of the expected value of the number photons $\langle \hat{a}^\dagger \hat{a} \rangle (t)$, the black curves are without energy losses, the other colours with $\gamma_{matter} = 1.0 \times 10^{-4}$. Parameters: $\omega_v = 0.1$, $\Delta = \omega_c = 1.0$, $g = 0.05$, $\lambda = 0.0 - 3.0$ and $\rho(t=0) = |\downarrow\ 1_{phot}\ 0_{phon}\rangle \langle\downarrow\ 1_{phot}\ 0_{phon}|$.

Calculating the quotient between the *Rabi oscillations* with and without losses [cf. figure J.4 of the appendix J.2.1], we numerically obtain the decay of the *Rabi oscillations*, fitting the decay to an exponential. We notice that this decay coincides with the one obtained by a *Holstein* model (1.26) with an initial state $|\psi(t=0)\rangle = |\uparrow\ \tilde{0}_{phon}\rangle$, see figure 3.13 to compare the analytical versus numerical. The only difference is a factor $1/2$. Thus, the exponential decay γ of $\langle \hat{a}^\dagger \hat{a} \rangle (t) \propto \exp[-\gamma t]$ as a function of λ is:

$$\gamma(\lambda) = \frac{\gamma_{matter}}{2} \sum_{\omega_{\tilde{0}m} > 0} \omega_{\tilde{0}m} \Gamma_{\tilde{0} \to m}(\lambda) = \frac{\gamma_{matter} \gamma_{\tilde{0}}(\lambda)}{2} \tag{3.13}$$

Qualitatively, the system only losses energy when the molecule is in the exited electronic state. At that time, we have found that the system has the same exponential decay (3.13) as it would have within the *Holstein* model (1.26). However, we have a series of *Rabi* oscillations and in average the molecule is excited only half of the time. As the only loss channel is the matter one, this would explain the factor $1/2$ in equation (3.13).

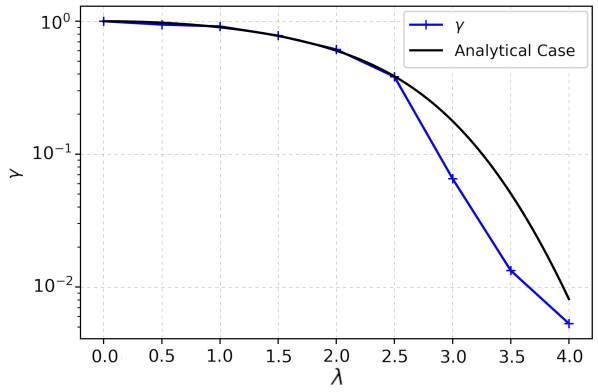

(a)

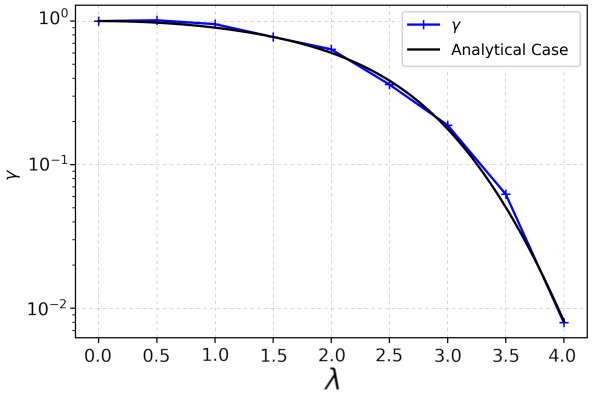

(b)

Figure 3.13: Analytical decay (3.13) versus numerical one as a function of λ in logarithmic scale. Parameters: $\omega_v = 0.1$, $g = 0.05$, $\Delta = 1.0$ and $\rho(t=0) = |\downarrow\ 1_{phot}\ 0_{phon}\rangle\langle\downarrow\ 1_{phot}\ 0_{phon}|$. (a) ***bare resonance*** ($\omega_c = \Delta$), (b) ***dressed resonance*** ($\Delta = \omega_c - \delta_{BS}$).

Using the analytical decay (3.13), we obtain a good match with the numerical decay for $\lambda < 2.5$, see figure 3.13a (*bare resonance*). Nevertheless, there is a discrepancy for $\lambda > 2.5$. We have seen that this region is where the system is out-of-resonance due to the courterrotating terms. At ***dressed resonance*** ($\Delta = \omega_c - \delta_{BS}$), [cf. section 2.3, equation (2.28)] , we recover the simple decay dependence given by (3.13), see figure 3.13b.

Let us analyze the *Lindblad* spectrum in order to see the transitions which play a role in the dynamics. Vectorizing the Lindbladian, we can get its left-eigenvectors $\rho_l^{(j)}$ and right-eigenvectors $\rho_r^{(j)}$ with an eigenvalue $\lambda^{(j)}$. Thus, the expected value of an observable $\hat{O}$ can be written as:

$$\langle \hat{O} \rangle (t) = \sum_j e^{\lambda^{(j)} t} \langle \rho_l^{(j)} | \rho(0) \rangle \operatorname{Tr}[\rho_r^{(j)} \hat{O}] = \sum_j p_j e^{\lambda^{(j)} t} \tag{3.14}$$

where: $p_j = \langle \rho_l^{(j)} | \rho(0) \rangle \operatorname{Tr}[\rho_r^{(j)} \hat{O}]$

Consider the dynamics for $\hat{O} = \langle \hat{a}^\dagger \hat{a} \rangle$, using as parameters $\omega_v = 0.1$, $g = 0.05$ ($2g = \omega_v$), $\lambda = 1.0$, $\Delta = 1$, $\Delta = \omega_c - \delta_{BS}(\lambda)$ (***dressed resonance***), $\gamma_{matter} = 1.0 \times 10^{-3}$ and $\rho(t=0) = |\downarrow\ 1_{phot}\ 0_{phon}\rangle\langle\downarrow\ 1_{phot}\ 0_{phon}|$, we obtain the most relevant eigenvectors classified by their weight p_j, see table 3.1.

j	$p_j / \sum_j \lvert p_j \rvert$	$\lambda^{(j)}$
1	2.21×10^{-1}	-4.71×10^{-4}
2	1.92×10^{-1}	-4.25×10^{-4}
3	1.65×10^{-1}	$-4.48 \times 10^{-4} + 5.14 \times 10^{-2} i$
3*	1.65×10^{-1}	$-4.48 \times 10^{-4} - 5.14 \times 10^{-2} i$

Table 3.1: The most relevant Lindblad eigenvectors in the dynamics of $\langle a^\dagger a \rangle (t)$. Parameters: $\omega_v = 0.1$, $g = 0.05$ ($2g = \omega_v$), $\lambda = 1.0$, $\Delta = 1$, $\Delta = \omega_c - \delta_{BS}(\lambda)$ (***dressed resonance***) and $|\psi(t=0)\rangle = |\downarrow\ 1_{phot}\ 0_{phon}\rangle$.

There are two eigenvectors (**1** and **2**) which are the responsible for the long term decay of the number of photons. Besides, we have a pair of complex conjugate eigenvectors (**3** and **3***) responsible of the most relevant *Rabi frequency*. These have a real part of the same order as the eigenvectors **1** and **2**. Thus, the *Rabi oscillations* disappear at the same rate. These four Lindblad eigenstates capture the dynamics of our system. In figure (3.14), we compare the dynamics of only four eigenstates (black) with the total Lindblad spectrum (red).

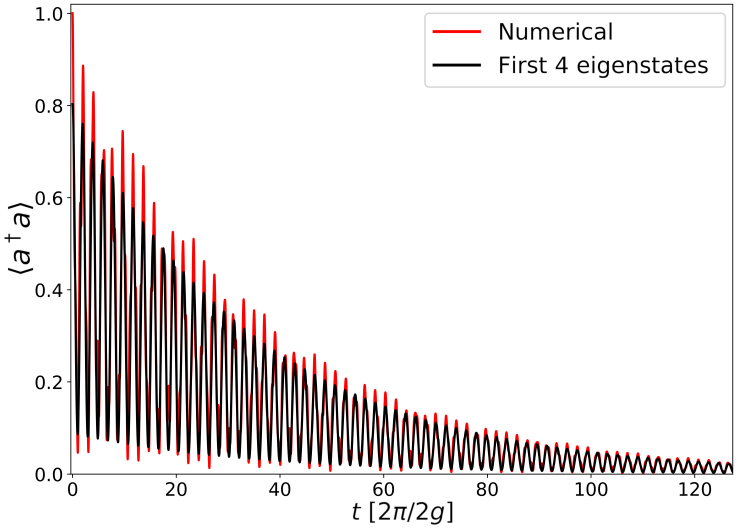

Figure 3.14: Time evolution of the expected value of the number of photons $\langle \hat{a}^\dagger \hat{a} \rangle (t)$, complete time evolution (red curve) and time evolution with the four Lindblad eigenvectors of the table 3.1 (black curve). Parameters: $\gamma_{matter} = 1.0 \times 10^{-3}$, $\omega_v = 0.1$, $g = 0.05$ ($2g = \omega_v$), $\lambda = 1.0$, $\Delta = 1$, $\Delta = \omega_c - \delta_{BS}(\lambda)$ (***dressed resonance***) and $\rho(t=0) = |\downarrow\ 1_{phot}\ 0_{phon}\rangle\langle\downarrow\ 1_{phot}\ 0_{phon}|$.

Which transitions between states are mediated by these Lindblad eigenstates? In order to do that task, we compute the weight p_j for the projectors[7] $|\epsilon_n\rangle\langle\epsilon_n|$ and $|\downarrow 0_{phot} m_{phon}\rangle\langle\downarrow 0_{phot} m_{phon}|$. Thus, one of the biggest contribution comes from the Lindblad eigenstate **1**. We obtain a weight $p_j > 0$ for the projector $|\epsilon_0\rangle\langle\epsilon_0|$ (i.e. losses population in that states), while the projectors $|\downarrow 0_{phot} m_{phon}\rangle\langle\downarrow 0_{phot} m_{phon}|$ have weights $p_j < 0$, gainning population. An equivalent reasoning can be done with the Lindblad eigenvector **2** [cf. table J.2, appendix J.2.2]. Thus, we obtain several transitions between de polariton and ground state subspaces, cf. figure 3.15.

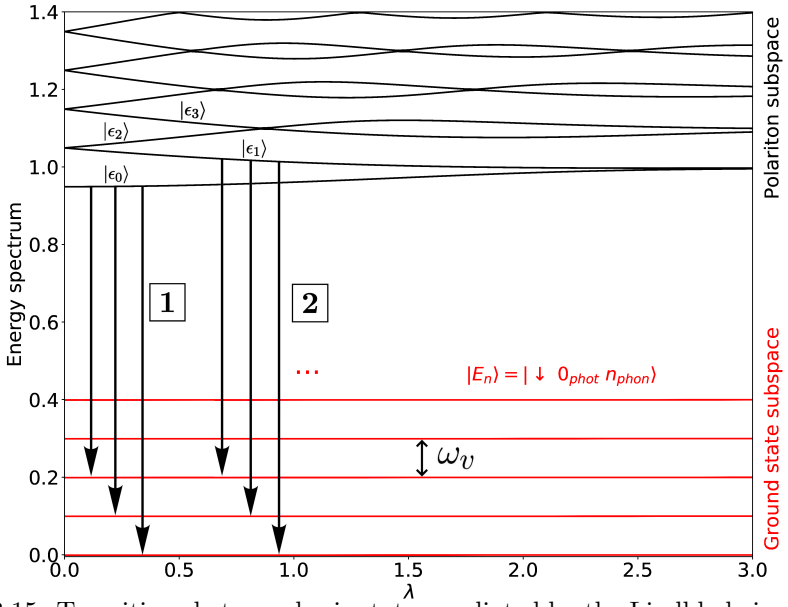

Figure 3.15: Transitions between basis states mediated by the Lindblad eigenstates **1** and **2**.

These transitions explain the increase in the number of phonons[8] $\langle\hat{b}^\dagger\hat{b}\rangle(t)$ in the dynamics, see figure J.7 and table J.3. We also compute the weights p_j of other basis states in order to obtain the transitions mediated by the Lindblad eigenstates **3** and **3*** responsible of the *Rabi oscillations*. In particular, we find that these eigenstates exchange energy between these states [red highlighted, cf. figure 3.16]:

$$\boxed{\begin{array}{l}|\uparrow\ 0_{phot}\ \tilde{0}\rangle\ \ (p_j = -2.07\times10^{-1})\\ |\uparrow\ 0_{phot}\ \tilde{1}\rangle\ \ (p_j = -6.61\times10^{-2})\\ \hline |\downarrow\ 1_{phot}\ 1\rangle\ \ (p_j = -5.38\times10^{-2})\end{array}} \longleftrightarrow \boxed{\begin{array}{l}\mathbf{3}\\ \mathbf{3}^*\end{array}} \longleftrightarrow \boxed{\begin{array}{l}|\downarrow\ 1_{phot}\ 0\rangle\\ (p_j = 1.98\times10^{-1})\end{array}}$$

[7] The states $|\epsilon_n\rangle$ are the eigenstates of the HQR in the polariton subspace

[8] Number of phonons in the representation of the Hamiltonian (2.2) after applying the Polaron transformation $U_P^{(0)}$ (2.1) which diagonalizes the Holstein Hamiltonian (1.26).

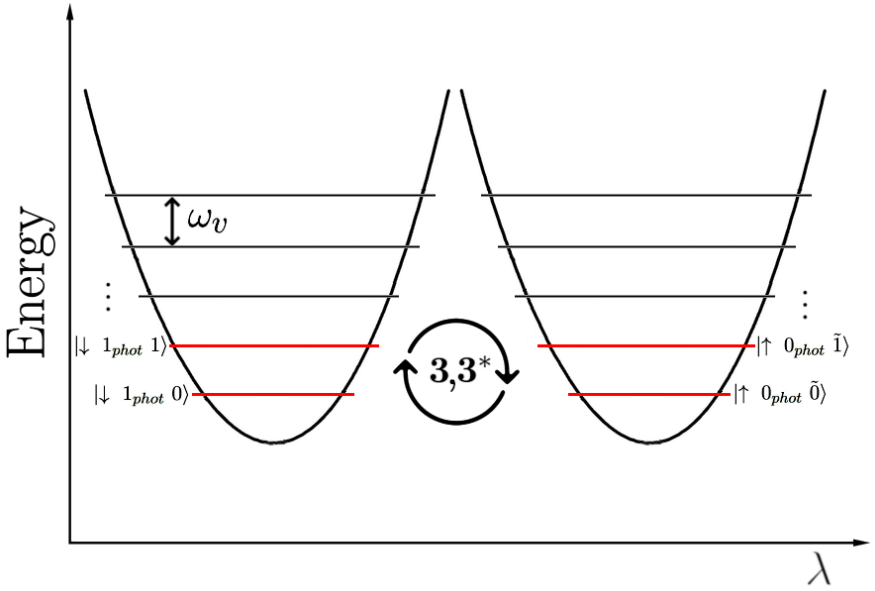

Figure 3.16: Transitions between basis states mediated by the Lindblad eigenstates **3** and **3***.

To sum up, the matter losses are responsible of the decay of the number of photons due to transitions between the polariton $\{|\epsilon_n\rangle\}$ and the ground state subspaces $\{|\downarrow\ 0_{phot}\ n_{phon}\rangle\}$ (see transitions of Lindblad eigenstates **1** and **2**). Besides, it produces the decay of the *Rabi oscillations* given by **3** and **3***.

Using the same parameters, we study the dynamics with photon losses $\gamma_{phot} = 10^{-4}$ and $\gamma_{matter} = \gamma_{phot} = 0$. We obtain the decay for different $\lambda's$ calculating the quotient between the dynamics with and without photon losses [cf. figures J.9 of appendix J.3 for details]. Then, we have plotted this quotient in logarithmic scale and we get a straight line characteristic of an exponential decay, see figure 3.17. Thus, we have obtained that the exponential decay $\gamma(\lambda)$ of $\langle\hat{a}^\dagger\hat{a}\rangle(t)$ corresponds to $\gamma \approx \gamma_{phot}/2$, as we can see in figure 3.17. So, there is no renormalization of the decay with the coupling λ. The only renormalization corresponds to the same factor $1/2$ which we obtained when we considered only matter losses. Therefore, we conclude that the exponential decay of $\langle\hat{a}^\dagger\hat{a}\rangle(t)$ and $\langle\hat{\sigma}^+\hat{\sigma}^-\rangle(t)$ including both matter and photon losses follows the next expression:

$$\boxed{\gamma(\lambda) = \frac{1}{2}(\gamma_{phot} + \gamma_{matter}\gamma_{\tilde{0}}(\lambda))} \tag{3.15}$$

where $\gamma_{\tilde{0}}(\lambda)$ is (3.12).

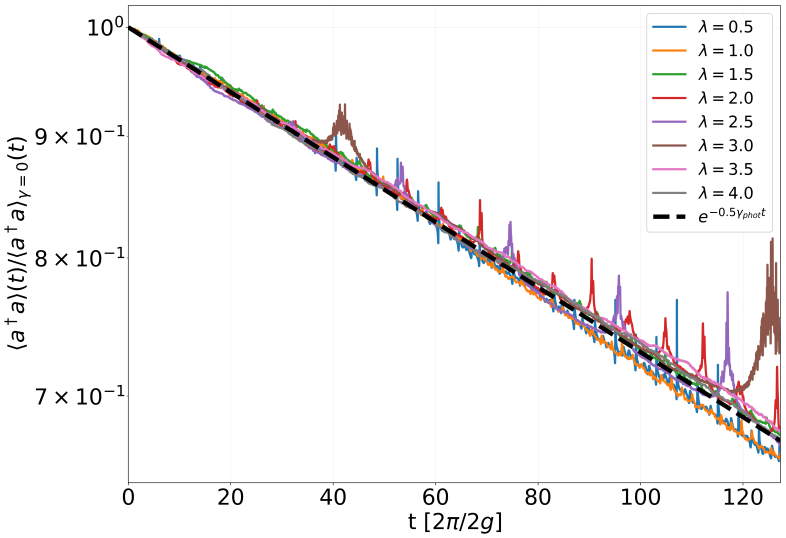

Figure 3.17: Quotient between the $\langle a^\dagger a\rangle(t)$ with and without photon losses. The black dashed is the exponential $\propto \exp[-\gamma_{matt}t/2]$. Parameters: $\gamma_{phot} = 10^{-4}$, $\omega_v = 0.1$, $g = 0.05$, $\Delta = 1$, $\Delta = \omega_c - \delta_{BS}(\lambda)$ (***dressed resonance***) and $\rho(t=0) = |\downarrow\ 1_{phot}\ 0_{phon}\rangle\langle\downarrow\ 1_{phot}\ 0_{phon}|$.

We also study the effect of the phonon losses in the system. Keeping the system at ***dressed resonance*** ($\Delta = \omega_c - \delta_{BS}(\lambda)$), we impose the energy losses $\gamma_{phot} = \gamma_{matter} = 0$ and $\gamma_{phon} = 5 \times 10^{-2}$ to study the phonon losses in the dynamics. The other parameters: $\rho(t=0) = |\downarrow\ 1_{phot}\ 0_{phon}\rangle\langle\downarrow\ 1_{phot}\ 0_{phon}|$, $\omega_v = 0.1$, $g = 0.05$ and $\lambda = 1.0$. We have chosen these losses because they present interesting features in the dynamics.

On the one hand, if we calculate the Lindblad eigenstates of the number of photons $\langle\hat{a}^\dagger\hat{a}\rangle(t)$, we find three important ones [cf. table J.4 of appendix J.4.1 for details]. The stationary eigenstate **1** with $\lambda^{(j)} \approx 0$ and two complex conjugate **2** and **2*** with $\lambda^{(j)} = -1.52 \times 10^{-3} \pm 5.14 \times 10^{-2} i$ responsible of the *Rabi oscillations*. On the other hand, if we obtain the Lindblad eigenstates for the number of phonons $\langle\hat{b}^\dagger\hat{b}\rangle(t)$ (in the representation of the Hamiltonian (2.2)), we get two eigenstates **1** and **3** with $\lambda^{(j)} < 0$ responsible of the decay of the number of phonons. Also, we obtain two complex conjugate Lindblad eigenvectors **2** and **2*** responsible of the oscillation in the number of phonons. See the figure J.12, the tables J.4-J.5 and the appedix J.4.1 for more details.

Again, we obtain the transitions mediated by the Lindblad eigenstates **1** and **3**, see figure 3.18. In other words the effect of the phonon losses over the system is to decay the system to the ground state of the polariton subspace $|\epsilon_0\rangle$. We can check this plotting the stationary number of photons, phonons and matter excitations obtained numerically versus the same excitations of the $|\epsilon_0\rangle$ for several values of λ, see figures J.12-J.13 of appendix J.4.1 for more details.

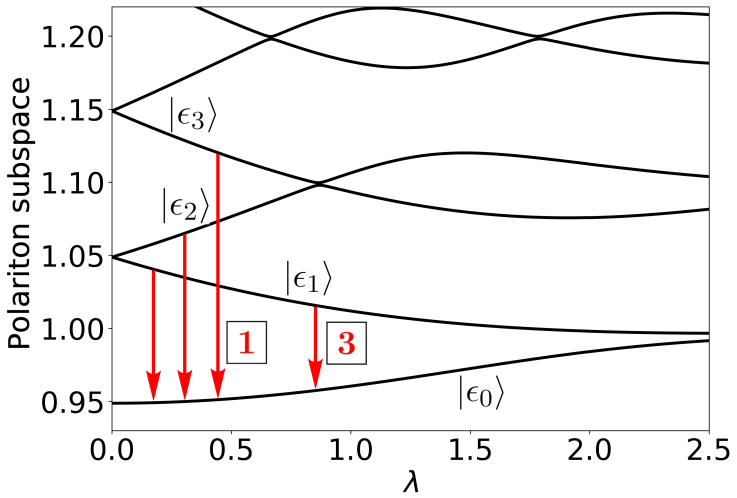

Figure 3.18: Transitions between basis states mediated by the Lindblad eigenstates **1** and **3**.

Hereafter, we study the dynamics with the combination of the matter and phonon losses $\gamma_{matter} = 10^{-3}$, $\gamma_{phon} = 5 \times 10^{-2}$ with $\gamma_{matter} \ll \gamma_{phon}$. An interesting case with two decay regimes as we can see in the expected value of the $\langle \hat{a}^\dagger \hat{a} \rangle (t)$, see figure 3.19. The other parameters used are the same as in the previous case. In other cases, such as $\gamma_{matter} \sim \gamma_{phon}$ or $\gamma_{matter} \gg \gamma_{phon}$, we do not appreciate relevant changes in the dynamics with respect to the case of the figure 3.14 (if we add photon losses, they only change the long term decay).

First, we analyze the most important Lindblad eigenstates for the time evolution of the $\langle \hat{a}^\dagger \hat{a} \rangle (t)$, see table J.7 of appendix J.4.2 for details. We find an eigenstate **1** with an eigenvalue $\lambda^{(j)} = -4.71 \times 10^{-4}$ responsible of the decay in the long term dynamics and a pair of complex conjugate **2** and **2*** with $\lambda^{(j)} = -1.97 \times 10^{-3} \pm 5.14 \times 10^{-4} i$ responsible of the *Rabi oscillations*. Besides, the decay of **2** and **2*** (real part of $\lambda^{(j)}$) is bigger and they produce the fading of the *Rabi oscillations* in the short term dynamics. We have also checked that these three Lindblad eigenstates reproduce all the dynamics, see figure 3.19, black curve.

We get the transitions mediated by the Lindblad eigenvector **1** calculating the weights p_j of the Lindblad spectrum for the expected values of some projectors. In particular, the eigenstates $|\epsilon_n\rangle \langle \epsilon_n|$ of the polariton subspace and the states $|\downarrow 0_{phot} n_{phon}\rangle \langle \downarrow 0_{phot} n_{phon}|$. Also, we have found two important Lindblad eigenstates **2** and **3** for the projectors $|\epsilon_n\rangle \langle \epsilon_n|$ and $|\downarrow 0_{phot} n_{phon}\rangle \langle \downarrow 0_{phot} n_{phon}|$, see table J.8 of appendix J.4.2 for more details. Thus, we found transtions between the polariton and ground state subpaces mediated by these Lindblad eigenstates, see figure 3.20.

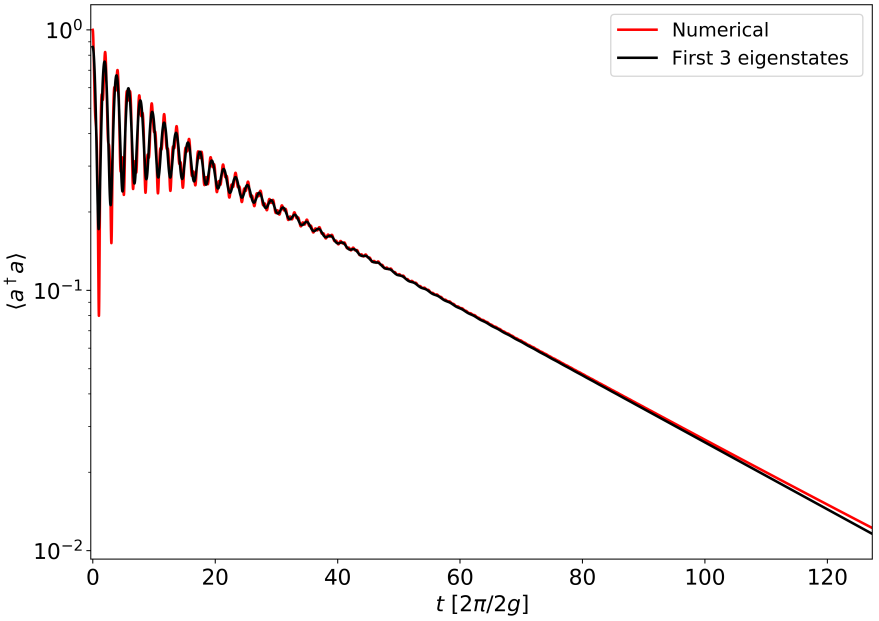

Figure 3.19: Time evolution of $\langle \hat{a}^\dagger \hat{a} \rangle (t)$, the complete time evolution (red curve) and the time evolution with the three Lindblad eigenvectors, cf. (3.14) (black curve). Parameters: $\gamma_{phon} = 5 \times 10^{-2}$, $\gamma_{phot} = 0$, $\gamma_{matter} = 10^{-3}$, $\lambda = 1$, $\omega_v = 0.1$, $g = 0.05$ $(2g = \omega_v)$, $\Delta = 1$, $\Delta = \omega_c - \delta_{BS}(\lambda)$ (***dressed resonance***) and $\rho(t = 0) = |\downarrow\ 1_{phot}\ 0_{phon}\rangle \langle\downarrow\ 1_{phot}\ 0_{phon}|$.

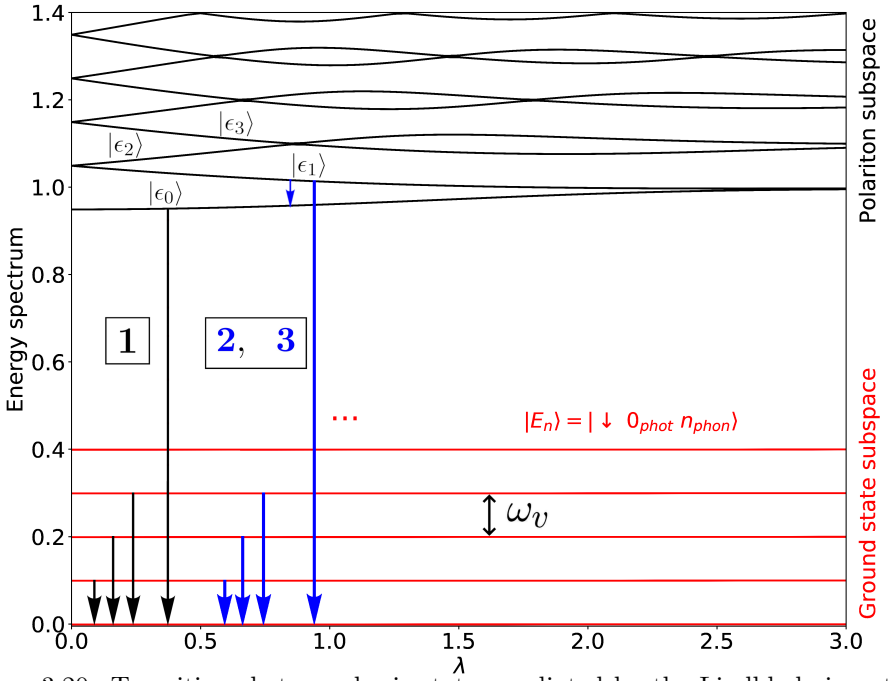

Figure 3.20: Transitions between basis states mediated by the Lindblad eigenstates **1**, **2** and **3**.

We can understand better the dynamics, if we plot the time evolution of $\langle|\epsilon_n\rangle\langle\epsilon_n|\rangle(t)$, $n = 0$, 1, 2 and 3, see figure 3.22. We have distinguished three cases: (a) only matter losses (dotted curves), in this case the all the eigenstates suffer a decay, (b) only phonon losses (dashed curves), here the eigenstates $|\epsilon_n\rangle$ with $n > 0$ suffer a decay which populates the ground state $|\epsilon_0\rangle$ and (c) the case which combines the matter and phonon losses (continuous curves). In this last case, we can see a competition between the phonon and matter losses. First, as $\gamma_{matter} \ll \gamma_{phon}$, the excited eigenstates $|\epsilon_n\rangle$ with $n > 0$ rapidly decay and populate the ground state of the polariton sector, see the peak in the curve of $|\epsilon_0\rangle$. Then, for long term dynamics, the matter losses dominate and all the eigenstates decay.

Thus, the phonon losses are responsible to decay the system from the eigenstates $|\epsilon_n\rangle$ with $n > 0$ to the ground state $|\epsilon_0\rangle$. Also, they produce an increase in the real part of the eigenvalues $\lambda^{(j)}$ of the Lindblad eigenstates **2** and **2*** producing the extinction of the *Rabi oscillations*. These Lindblad eigenstates are only responsible of the *Rabi oscillations* [cf. appendix J.4.2, figures J.16 for more details] and produce an exchange of energy between the states:

$$\boxed{\begin{array}{l}|\uparrow 0_{phot}\tilde{0}\rangle \ \ (p_j = -1.85\times10^{-1})\\ |\uparrow 0_{phot}\tilde{1}\rangle \ \ (p_j = -4.94\times10^{-2})\\ \hline |\downarrow 1_{phot}1\rangle \ \ (p_j = -3.87\times10^{-2})\end{array}} \longleftrightarrow \boxed{\begin{array}{l}\mathbf{2}\\ \mathbf{2}^*\end{array}} \longleftrightarrow \boxed{\begin{array}{l}|\downarrow 1_{phot}0\rangle\\ (p_j = 1.63\times10^{-1})\end{array}}$$

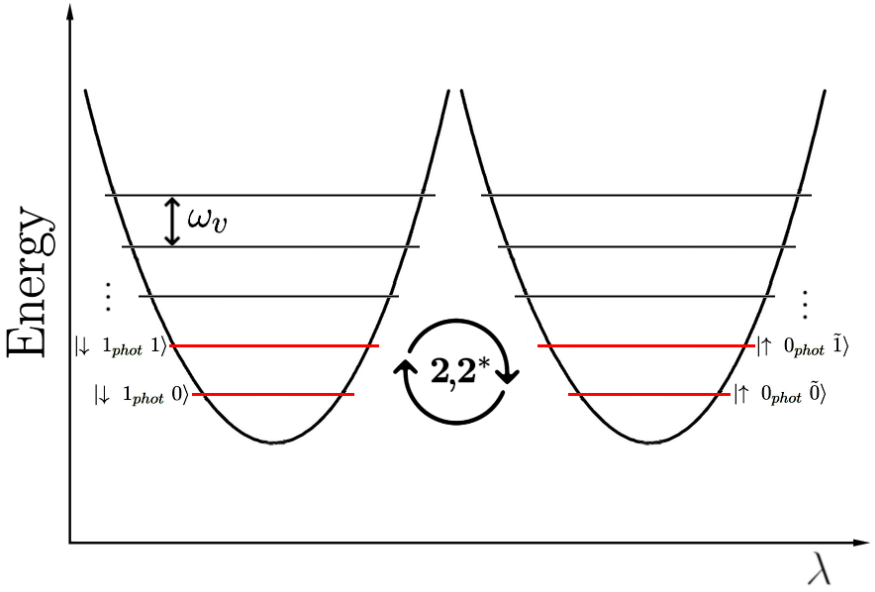

Figure 3.21: Transitions between basis states mediated by the Lindblad eigenstates **2** and **2***.

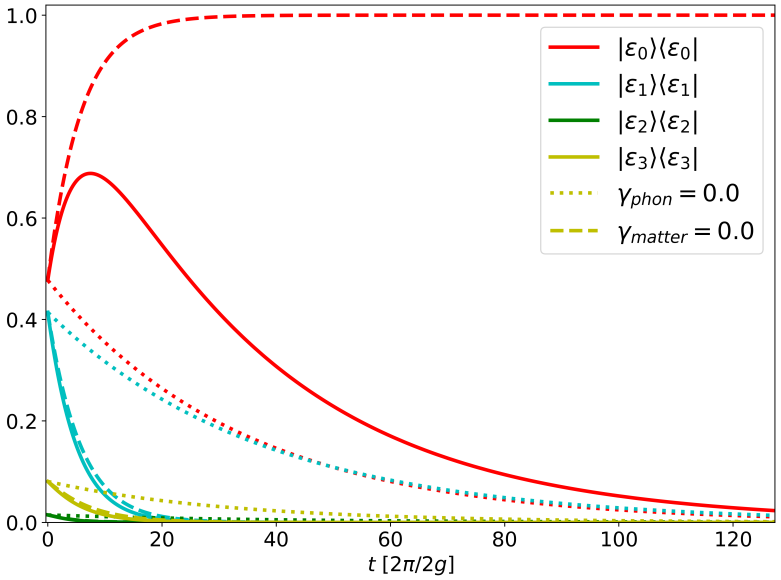

Figure 3.22: Time evolution of the projectors over the eigenstates of the polariton subspace $\langle|\epsilon_n\rangle\langle\epsilon_n|\rangle$, with $n = 0,\ 1,\ 2$ and 3. Three cases: $\gamma_{matter} = 10^{-3}$, $\gamma_{phon} = 5.0 \times 10^{-2}$ (continuous curves), $\gamma_{matter} = 10^{-3}$, $\gamma_{phon} = 0$ (dotted curves) and $\gamma_{matter} = 0$, $\gamma_{phon} = 5.0 \times 10^{-2}$ (dashed curves). Parameters: $\gamma_{phot} = 0$, $\omega_v = 0.1$, $g = 0.05$ $(2g = \omega_v)$, $\Delta = 1$, $\Delta = \omega_c - \delta_{BS}(\lambda)$ (***dressed resonance***) and $\rho(t=0) = |\downarrow\ 1_{phot}\ 0_{phon}\rangle\langle\downarrow\ 1_{phot}\ 0_{phon}|$.

In summary, we have found that the decay produced by γ_{matter} is renormalized by the Franck-Condon factors (cf. equation 3.13). Also, it produces transitions from the subspace $|\epsilon_n\rangle$ to the $|\downarrow 0_{phot} n_{phon}\rangle$. Then the photon losses produce an exponential decay $\approx \gamma_{phot}/2$. Finally, the phonon losses do not produce a change in the long term decay of $\langle\hat{a}^\dagger\hat{a}\rangle(t)$ (or $\langle\hat{\sigma}^+\hat{\sigma}^-\rangle(t)$). They extinguish *Rabi oscillations* (weak coupling) and decay the system to the ground state $|\epsilon_0\rangle$ of the polariton subspace.

So, in the case of $\gamma_{matter} \gg \gamma_{phot},\ \gamma_{phon}$, the matter-phonon coupling λ is resposible for modifying the conditions of strong coupling. Since, the decay is modified with λ [cf. equation 3.13]. Thus, we can obtain the critical matter losses γ_c for which a bigger value is *weak coupling* regime and a smaller one the *strong coupling regime*:

$$\frac{\Omega_R(\lambda)}{\gamma_{matter}\gamma_{\tilde{0}}(\lambda)/2} = 1 \ \longrightarrow\ \gamma_c \equiv \gamma_{matter} = \frac{\Omega_R(\lambda)}{\gamma_{\tilde{0}}(\lambda)/2} \tag{3.16}$$

where $\Omega_R(\lambda) = \epsilon_1 - \epsilon_0$ is the main *Rabi frequency* (3.1). In figure 3.23, we have plotted the boundary between *weak* and *strong coupling*, analytical versus numerical. Thus, as the coupling λ increase, smaller losses are required to reach the strong coupling regime.

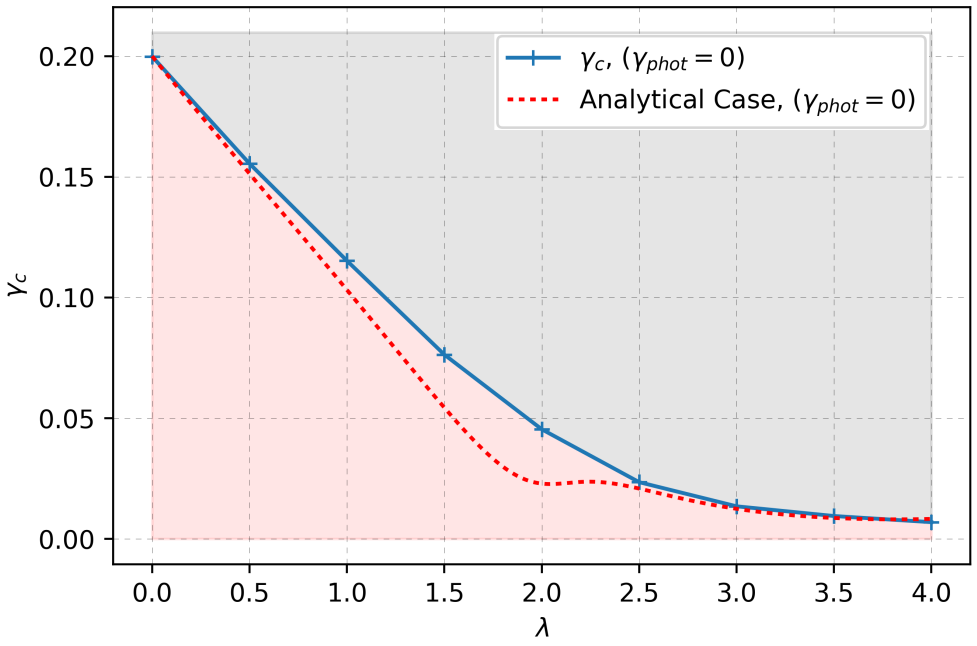

Figure 3.23: $\gamma_c(\lambda)$ the red area corresponds to *strong coupling* and the grey one to the *weak coupling* regime. The blue curve corresponds to the numerical calculus and the red dash line to the analytical expression (3.16). Parameters: $\omega_v = 0.1$, $g = 0.05$ ($2g = \omega_v$), $\lambda = 1.0$, $\Delta = 1$, $\Delta = \omega_c - \delta_{BS}(\lambda)$ (***dressed resonance***), $\gamma_{phot} = \gamma_{phon} = 0$, and $\rho(t = 0) = |\downarrow\ 1_{phot}\ 0_{phon}\rangle\langle\downarrow\ 1_{phot}\ 0_{phon}|$.

Chapter 4

Noise Spectrum

In the last chapters, we have studied the energy spectrum and the dynamics of the *Holstein-Quantum-Rabi* model. In this chapter, we will study its noise spectrum $S(\omega)$.

4.1 Linear Response theory and $S(\omega)$

Our system of interest is described by a Hamiltonian H_0. The system is proven through an external perturbation or driving, $\epsilon f(t)\hat{A}$. Thus, the total Hamiltonian is:

$$H = H_0 + \epsilon f(t)\hat{A} \tag{4.1}$$

The objective of this chapter is the study of the noise spectrum $S(\omega)$. This is the Fourier transform of the correlation function $S_{BA}(t)$ of an operator $\hat{B}$ and an external driving $\hat{A}$:

$$S_{BA}(t) = \langle \hat{B}(t)\hat{A} \rangle - \langle \hat{B} \rangle \langle \hat{A} \rangle \tag{4.2}$$

In other words, $S(\omega)$ is:

$$S(\omega) = \int_{-\infty}^{\infty} S_{BA}(t) e^{i\omega t} dt \tag{4.3}$$

Besides the two point correlation $S_{BA}(t)$ will be computed under the assumption that the perturbation is small enough ($\epsilon \ll 1$), so linear response theory can be used (see, for example, chapter 3 of [7]). The full dynamics including both dissipation and decoherence is splitted in two terms:

$$\dot{\rho}(t) = \mathcal{L}_0 \rho(t) + \epsilon f(t) \mathcal{L}_1 \rho(t) \tag{4.4}$$

where $\mathcal{L}_0$ is the Lindbladian superoperator [cf. equations 1.63 and 1.64]:

$$\mathcal{L}_0[\,\cdot\,] = -i[H_0,\ \cdot\,] + \mathcal{D}[\,\cdot\,] \tag{4.5}$$

with $\mathcal{D}[\,\cdot\,] = \sum_{\omega>0} \sum_k \omega \gamma_k (\hat{A}_k(\omega)\ \cdot\ \hat{A}_k^\dagger(\omega) - \frac{1}{2}\{\hat{A}_k^\dagger(\omega)\hat{A}_k(\omega),\ \cdot\,\})$ and the linear superoperator $\mathcal{L}_1$ is the perturbation:

$$\mathcal{L}_1[\,\cdot\,] = -i[\hat{A},\ \cdot\,] \tag{4.6}$$

We write the solution as:

$$\rho = \rho_0 + \epsilon\rho_1(t) \tag{4.7}$$

with $\dot{\rho_0} = 0$ and $\mathcal{L}_0\rho_0 = 0$ (stationary solution without driving). Discarding $o(\epsilon^2)$ terms:

$$\dot{\rho}_1(t) = \mathcal{L}_0\rho_1(t) + f(t)\mathcal{L}_1\rho_0 \tag{4.8}$$

Its solution is:

$$\rho_1(t) = \int_{-\infty}^{t} e^{(t-s)\mathcal{L}_0} f(s)\mathcal{L}_1\rho_0 ds \tag{4.9}$$

This formalism is particularly useful for calculating observable variations. Consider any observable $\hat{B}$ [cf. equation (4.7)]:

$$\Delta B(t) = \langle \hat{B} \rangle_{\rho(t)} - \langle \hat{B} \rangle_0 = \epsilon \mathrm{Tr}[B\rho_1(t)] \tag{4.10}$$

where $\langle B \rangle_0 = \mathrm{Tr}[\hat{B}\rho_0]$. Besides, using (4.9), we can write:

$$\Delta B(t) = \epsilon \mathrm{Tr}\left[\int_{-\infty}^{t} \hat{B} e^{(t-s)\mathcal{L}_0} f(s)\mathcal{L}_1\rho_0 ds \right] \tag{4.11}$$

Defining the *response function* $R_{BA}(t)$:

$$R_{BA}(t) = \theta(t)\mathrm{Tr}[\hat{B}e^{t\mathcal{L}_0}\mathcal{L}_1\rho_0] \tag{4.12}$$

where $\theta(t)$ is the Heaviside function, we finally get:

$$\Delta B(t) = \epsilon \int_{-\infty}^{\infty} R_{BA}(t-s) f(s) ds \tag{4.13}$$

Therefore, the response $\Delta B(t)$ of the system is the convolution of the response function $R_{BA}(t)$ and the perturbation $f(t)$. If the perturbation is a delta function $f(t) = \delta(t - t_0)$, we obtain:

$$\Delta B(t) = \epsilon R_{BA}(t - t_0) \tag{4.14}$$

Thus, we can interpret the response function ϵR_{BA} as the Green function of the problem. In other words, it is the value of the response at time t when the system is excited at time t_0. Using the Fourier transform of (4.13), we obtain that:

$$\Delta B(\omega) = \epsilon \chi_{BA}(\omega) f(\omega) \tag{4.15}$$

Here:

$$\Delta B(\omega) = \int_{-\infty}^{\infty} \Delta B(t) e^{i\omega t} dt \qquad \chi_{BA}(\omega) = \int_{-\infty}^{\infty} R_{BA}(t) e^{i\omega t} dt \tag{4.16}$$

$$f(\omega) = \int_{-\infty}^{\infty} f(t) e^{i\omega t} dt \tag{4.17}$$

The Fourier transform of the response function $\chi_{BA}(\omega)$ is known as the *generalized susceptibility*. However, our objective is to calculate the noise spectrum $S(\omega)$. They are related by the *Fluctuation Dissipation theorem* [cf. chapter 3 of [7]]:

$$S(\omega) = \hbar \frac{1}{1 - e^{-\beta\hbar\omega}} 2\mathrm{Im}(\chi_{BA}(\omega)) \tag{4.18}$$

where[1] $\beta = 1/k_B T$. Here, we restrict to the case of zero temperature $T = 0$:

$$S(\omega) = 2\mathrm{Im}(\chi_{BA}(\omega)) \tag{4.19}$$

In order to calculate $\chi_{BA}(\omega)$, we are going to suppose that the perturbation $\mathcal{L}_1$ has been acting since $t = -\infty$ and then it is disconnected at $t = 0$. Thus, we have that $f_r(t) \equiv f(t) = \theta(-t)$. Substituting it into the equation (4.13), we obtain the relation:

$$\frac{d(\Delta B_r(t))}{dt} = -\epsilon R_{BA}(t) \tag{4.20}$$

where $\Delta B_r(t)$ is the response when $f(t) = \theta(-t)$. Using the equations (4.20), (4.10) the $\chi_{BA}(\omega)$ is:

$$\begin{aligned} \chi_{BA}(\omega) &= -\frac{1}{\epsilon}\left(\Delta B_r(t=0) + i\omega \int_0^\infty ds \Delta B_r(s) e^{i\omega s}\right) \\ &= \mathrm{Tr}(\hat{B}\rho_1(0)) + i\omega \int_0^\infty ds\ \mathrm{Tr}(\hat{B}\rho_1(s)) e^{i\omega s} \end{aligned} \tag{4.21}$$

Using equation (4.8) and neglecting the second order terms in ϵ^2, $\rho_1(0)$ reads:

$$\mathcal{L}_0\rho_1(0) = -\mathcal{L}_1\rho_0 \quad \rightarrow \quad \rho_1(0) = -\mathcal{L}_0^{-1}\mathcal{L}_1\rho_0 \tag{4.22}$$

In the $\mathcal{L}_0$ basis, we have $\mathcal{L}_1\rho_0 = \sum_\alpha a_\alpha \rho^{(\alpha)}$ with[2] $a_\alpha = \langle \rho^{(\alpha)} | \mathcal{L}_1\rho_0 \rangle$, therefore:

$$\rho_1(0) = -\sum_\alpha \frac{a_\alpha}{-i\omega_\alpha}\rho^{(\alpha)} = -\sum_\alpha \frac{ia_\alpha}{\omega_\alpha}\rho^{(\alpha)} \tag{4.23}$$

with $-i\omega_\alpha$ and $\rho^{(\alpha)}$ respectively the $\mathcal{L}_0$-eigenvalues and $\mathcal{L}_0$-eigenvectors. As the perturbation is disconnected at $t = 0$, the evolution is governed by the Lindbladian $\mathcal{L}_0$:

$$\rho_1(t) = -\sum_\alpha \frac{ia_\alpha}{\omega_\alpha}\rho^{(\alpha)} e^{-i\omega_\alpha t} \tag{4.24}$$

Inserting the latter in (4.21), we finally get:

$$\chi_{BA}(\omega) = i\sum_\alpha \frac{a_\alpha}{\omega - \omega_\alpha}\mathrm{Tr}[\hat{B}\rho^{(\alpha)}] \tag{4.25}$$

[1] Where k_B is the Blotzman constant and T the temperature.

[2] Where $|\rho\rangle$ is the "vectorized" density matrix ρ.

4.2 Holstein-Quantum-Rabi

Let's apply this general theory to the main model discussed in this thesis, the HQR model, equation (1.35). We are going to calculate the noise spectrum $S(\omega)$. In particular, the Fourier transform of the correlation function an operator $\hat{B} = \hat{a} + \hat{a}^\dagger$ porportional to the electric field with the system submitted to a perturbation or external driving of the same type i.e. $\hat{A} = \hat{a} + \hat{a}^\dagger$. We calculate this quantity $S(\omega)$ due to its interest in the experimental research (cf. [99] for more details).

4.2.1 Ultrastrong effects in the noise spectrum

First, we are going to calculate numerically the noise spectrum $S(\omega)$ versus the matter-phonon coupling λ and both matter and light losses γ_{matter} and γ_{phot} respectively (we will assume good cavities, with $\gamma_{phon} = 0$). $S(\omega)$ will give us the transitions from the eigenstates $|\epsilon_n\rangle$ of the HQR (1.35) in the polariton subspace to the eigenstates $|E_n\rangle \approx |\downarrow 0_{phot} n_{phon}\rangle$ of the ground state subspace, see figure 4.1.

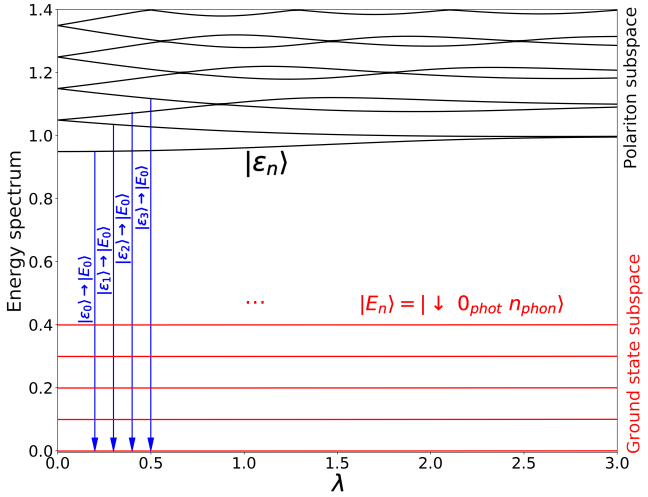

Figure 4.1: Scheme of the energy spectrum of the HQR model (1.35) versus the coupling λ. The black energy levels ($|\epsilon_n\rangle$) are the energy levels of the polariton subspace of the *Rabi* model and the red ones ($|E_n\rangle = |\downarrow 0_{phot} n_{phon}\rangle$) the subspace of the ground state of the *Rabi* model ($|gs\rangle_{Rabi} \approx |\downarrow 0_{phot}\rangle$). The vertical blue arrows indicate the transitions $|\epsilon_n\rangle \to |E_0\rangle$.

The Lindblad eigenvalues $\lambda^{(\alpha)} = -i\omega_\alpha$ have an imaginary part $\mathrm{Im}(\lambda^{(\alpha)})$ responsible of the oscillations and a real part $\mathrm{Re}(\lambda^{(\alpha)})$ responsible of the decay of the expected values of the observables, recall the equation (3.14). So, $\mathrm{Im}(\lambda^{(\alpha)})$ fixes the position of the peaks and $\mathrm{Re}(\lambda^{(\alpha)})$ the width of the peaks of $S(\omega)$, see the last equation (4.25). Using as parameters $\lambda = 0.25$, $\Delta = \omega_c = 1.0$ (***bare resonance***), $\gamma_{phon} = 0.0$, $\omega_v = 0.1$ and $\rho_0 = |\downarrow 0_{phot} 0_{phon}\rangle \langle \downarrow 0_{phot} 0_{phon}|$, we have calculated the noise spectrum $S(\omega)$ for the HQR model, see figure 4.2. We can see that the different allowed transitions cannot be resolved when the energy losses increase the width of the peaks.

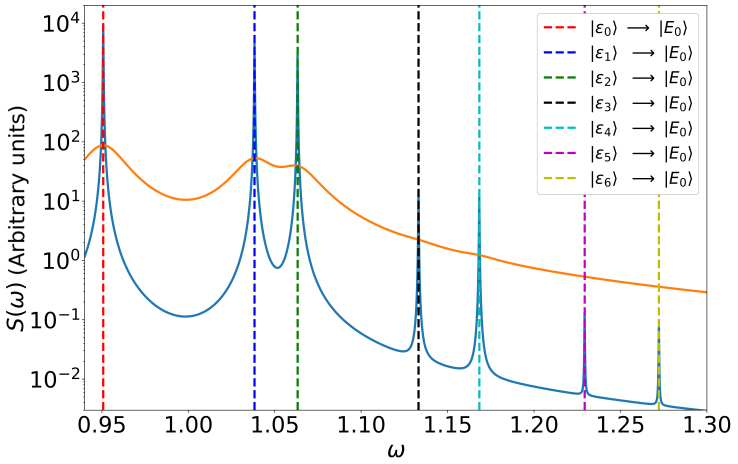

Figure 4.2: Noise spectrum for different values of energy losses: $\gamma_{matter} = \gamma_{phot} = 2.5 \times 10^{-4}$ (blue) and $\gamma_{matter} = \gamma_{phot} = 2.5 \times 10^{-2}$ (orange). The vertical lines indicate the transitions between the polariton and ground state subspaces of the energy spectrum $|\epsilon_n\rangle \rightarrow |E_0\rangle$. Parameters: $\Delta = \omega_c = 1.0$ (***bare resonance***), $\lambda = 0.25$, $\gamma_{phon} = 0.0$, $\omega_v = 0.1$ and $\rho_0 = |\downarrow 0_{phot}0_{phon}\rangle \langle\downarrow 0_{phot}0_{phon}|$.

We are going to study the effect of the counterrotating terms on the noise spectrum $S(\omega)$. Thus, we can compare the noise spectrum $S(\omega)$ of the HQR model [cf. eq. (1.35)] with the same model after the RWA the *Holstein-Quantum-Jaynes-Cummings* (HQJC), the Hamiltonian H_{HJC}, recall equation (2.6).

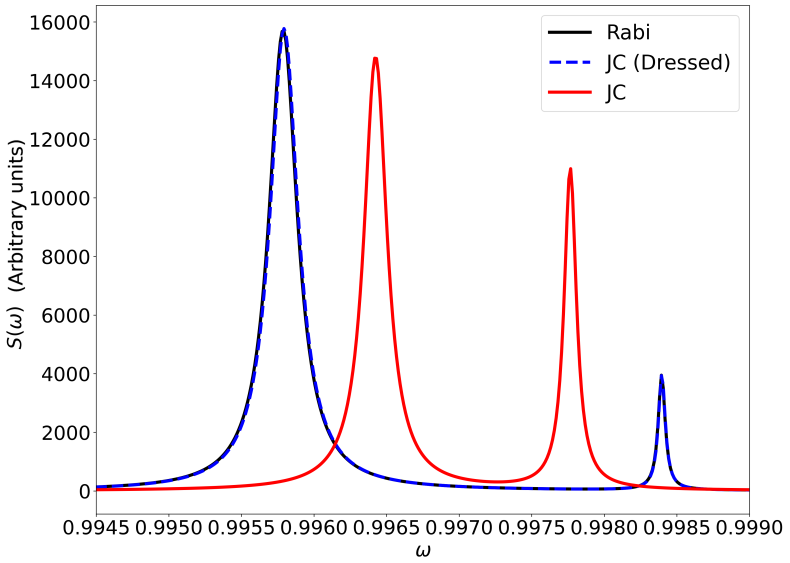

Figure 4.3: Noise spectrum $S(\omega)$ comparison between the HQR (***bare resonance***,black curve) [cf. eq. (1.35)], the HQJC (***bare resonance***, red curve) [cf. eq. (2.6)] and the Dressed HQJC (dashed blue) [cf. eq. (4.26)]. Parameters: $\Delta = 1.0$, $\lambda = 3.0$, $\gamma_{matter} = \gamma_{phot} = 2.5 \times 10^{-4}$, $\gamma_{phon} = 0.0$, $\omega_v = 0.1$ and $\rho_0 = |\downarrow 0_{phot}0_{phon}\rangle \langle\downarrow 0_{phot}0_{phon}|$.

On the one hand, we do not appreciate changes until $\lambda \gtrsim 2$ where the ***bare resonance condition*** $\omega_c = \Delta = 1$ is violated. For example, the case of $\lambda = 3.0$ and $\gamma_{matter} = \gamma_{phot} = 2.5 \times 10^{-4}$ changes the position of the peaks and their height, see black and red curves of the figure 4.3. These peaks correspond to the transitions $|\epsilon_0\rangle \to |\downarrow 0_{phot}0_{phon}\rangle$ and $|\epsilon_1\rangle \to |\downarrow 0_{phot}0_{phon}\rangle$.

On the other hand, we can study the case of higher losses, $\gamma_{matter} = \gamma_{phot} = 2.5 \times 10^{-2}$. In this case, the two peaks obtained in figure 4.3 coalesce into one peak. At ***bare resonance***, the difference between the HQR and HQJC lies in the form of the peak. The HQR model (black curve) gives an asymmetrical peak while is computed with the HQJC model (red curve) is symmetric, see figures 4.4a and 4.4b for the cases $\lambda = 3.0$ and 3.5. This change of the form is only appreciated for high values of the coupling $\lambda \gtrsim 2$.

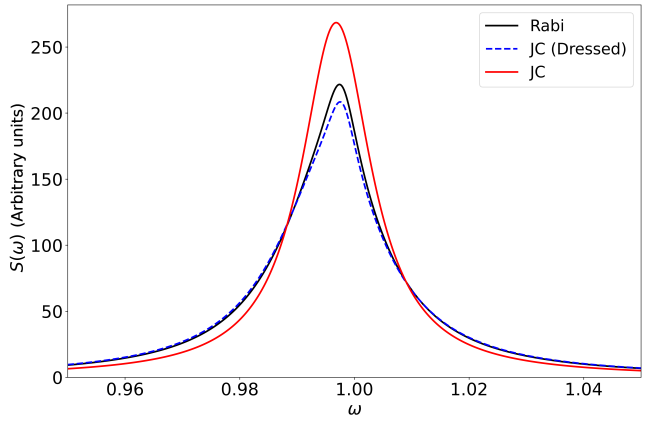

(a)

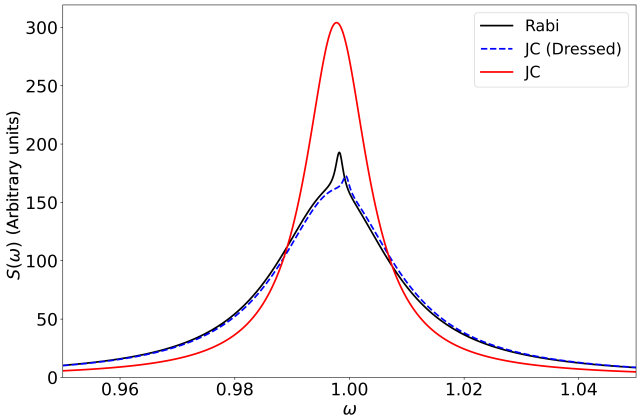

(b)

Figure 4.4: Noise spectrum $S(\omega)$ comparison between the HQR (***bare resonance***, black curve) [cf. eq. (1.35)], the HQJC (***bare resonance***, red curve) [cf. eq. (2.6)] and the Dressed HQJC (dashed blue) [cf. eq. (4.26)] (a) $\lambda = 3.0$ (b) $\lambda = 3.5$. Parameters: $\Delta = 1.0$, $\gamma_{matter} = \gamma_{phot} = 2.5 \times 10^{-2}$, $\gamma_{phon} = 0.0$, $\omega_v = 0.1$ and $\rho_0 = |\downarrow 0_{phot}0_{phon}\rangle \langle\downarrow 0_{phot}0_{phon}|$.

We know that the position of the peaks depend on the energy differences between the polariton and ground state subspaces of the HQR energyspectrum [cf. figure 4.1]. Besides, as we have already anticipated in section 2.3, the counterrotating terms also produce a *Bloch-Siegert* shift in the phonon frequency $(\omega_v - \delta_{BS}/2)$ in the gound state subspace $\{|\downarrow\ 0_{phot}\ m_{phon}\rangle\}$ [cf. appendix F for more details]. Therefore, we also have to take into account this shift.

Thus, we can dress *Holstein-Quantum-Jaynes-Cummings* in order to include these shifts in the energies produced by the counterrotating terms. In this way, we can obtain a *Jaynes-Cummings*-like model, equivalent to HQR model at *bare resonance*, which can describe the noise spectrum. In oder to do that task we have to take into account:

- First, we add a shift[3] $\delta_{BS}/2$ to Δ and ω_c. In other words:
  - $\Delta \to \Delta + \delta_{BS}(\omega_c, \lambda)/2 \equiv \tilde{\Delta}$
  - $\omega_c \to \omega_c + \delta_{BS}(\omega_c, \lambda)/2 \equiv \tilde{\omega}_c$

  This simulates the shift $-\delta_{BS}/2$ over the ground state subspace $\{|\downarrow\ 0_{phot}\ m_{phon}\rangle\}$.
- Second, in order to simulate that the system is out-of-resonance $\Delta - \omega_c = -\delta_{BS}(\omega_c, \lambda)$, we add to $\tilde{\omega}_c$ the shift $-\delta_{BS}(\tilde{\omega}_c, \tilde{\Delta}, \lambda)$: $\tilde{\omega}_c - \delta_{BS}(\tilde{\omega}_c, \tilde{\Delta}, \lambda)$. This procedure is necessary for each value of λ.

Thus, our dressed Hamiltonian is:

$$\begin{aligned} H_{HJC}^{dress} =& (\tilde{\omega}_c - \delta_{BS}(\tilde{\omega}_c, \tilde{\Delta}, \lambda))\hat{a}^\dagger\hat{a} + \tilde{\Delta}\hat{\sigma}^+\hat{\sigma}^- + g(\hat{a}^\dagger\hat{\sigma}^- + \hat{a}\hat{\sigma}^+) \\ &+ \omega_v(\hat{b}^\dagger\hat{b} + \lambda\hat{\sigma}^+\hat{\sigma}^-(\hat{b}^\dagger + \hat{b} + \lambda)) \end{aligned} \tag{4.26}$$

We call this model the **Dressed *Holstein-Quantum-Jaynes-Cummings*** model (**Dressed HQJC**). Thus, with a renormalized parameters, we have obtained a *Jaynes-Cummings*-like model which replicates not only the dynamics, but also the noise spectrum $S(\omega)$ of the HQR model, see blue dashed curves of figures 4.3 and 4.4.

In short, recall that the *effective Rabi* model (2.15) is the HQJC model in the polariton sector. Therefore, the *Dressed HQJC* is equivalent to include the *Bloch-Siegert* shift in the *effective Rabi* model in oder to simulate the effect of the counterrotating terms.

[3] We impose $m_{phon} = 0$ and study the case of *bare resonance* $\omega_c = \Delta = 1$.

Afterwards, we study the case of $\lambda = 3.0$ for different values of the energy losses γ_{matter} and γ_{phot}, see figure 4.5. The continuous curves are the HQR model and the black dashed curve the HQJC model for $\gamma_{matter} = \gamma_{phot} = 2.5 \times 10^{-2}$. Comparing this last case ($\gamma_{matter} = \gamma_{phot} = 2.5 \times 10^{-2}$), we see the form asymmetry of the curve. Moreover, we can see how the two original peaks coalesce each other when we increase the energy losses, as we expected.

Finally, in the inset of the figure 4.5, we have plotted the quotient P_M/P_m between the value of the biggest P_M and the second biggest peak P_m for the case of low energy losses ($\gamma_{matter} = \gamma_{phot} = 2.5 \times 10^{-4}$) versus the coupling λ. Thus, when $P_M/P_m = 1$ the two peaks have the same height, in other case not. At *bare resonance*, we have compared the HQR (blue curve) and the HQJC (orange curve). As we expected, the case of the HQJC is almost symmetrical ($P_M/P_m \approx 1$) and the case of the HQR not ($P_M/P_m > 1$). In particular, this is especially clear for the cases with $\lambda > 2$, as we have already seen in figure 4.2. Thus, the counterrotating terms are responsible of the change in the height and position of the peaks for small losses and the asymmetry of the peaks from for high losses.

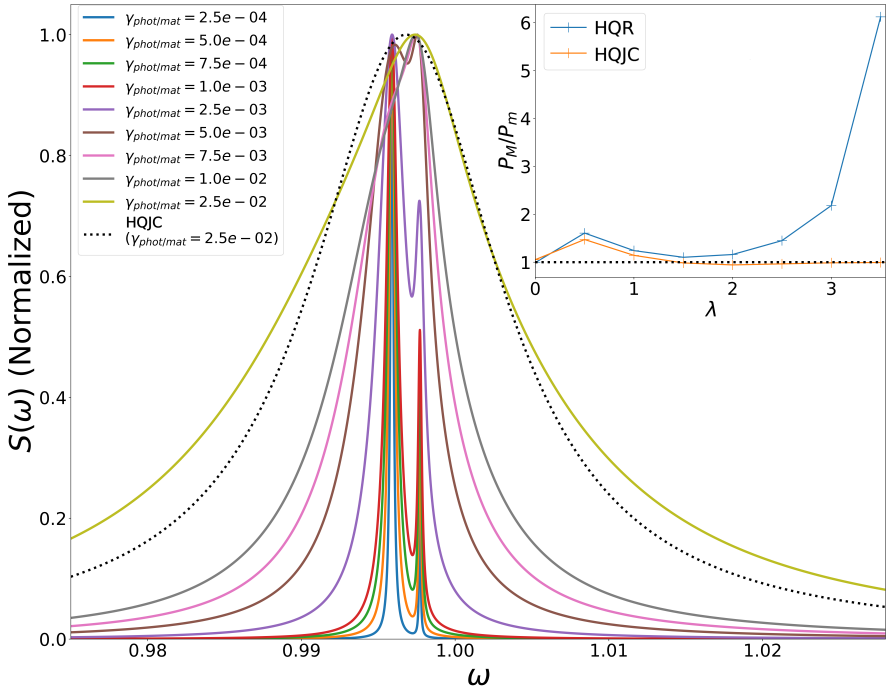

Figure 4.5: At ***bare resonance***, noise spectrum $S(\omega)$ of the HQR model [cf. eq. (1.35)] for different values of the energy losses $\gamma_{matter} = \gamma_{phot}$. The black dashed curve corresponds to $\gamma_{matter} = \gamma_{phot} = 2.5 \times 10^{-2}$ for the HQJC [cf. eq. (2.6)]. Inset: the quotient of the two biggest peaks of $S(\omega)$ versus the coupling λ for the HQR and the HQJC ($\gamma_{matter} = \gamma_{phot} = 2.5 \times 10^{-4}$). Parameters: $\omega_c = \Delta = 1$, $g = 0.05$, $\omega_v = 0.1$, $\lambda = 3.0$, $\gamma_{phon} = 0.0$ and $\rho_0 = |\downarrow 0_{phot} 0_{phon}\rangle \langle \downarrow 0_{phot} 0_{phon}|$.

4.2.2 Analytical approach

We can also obtain some extra information calculating approximatelly the noise spectrum $S(\omega)$. In order to do that task, we will follow the method of calculation exposed in the section 4.1 and use some extra approximations. Thus, we will restrict the calculus to the first three energy levels of the polarition subspace ($|\epsilon_0\rangle$, $|\epsilon_1\rangle$ and $|\epsilon_2\rangle$, see figure 4.1, black curves) and the first energy level of the ground state subspace ($|E_0\rangle$, see figure 4.1, red curves). Taking into account all these considerations, we arrive to the following expression for the noise spectrum:

$$S(\omega) = \sum_{j=0}^{2} \left(\frac{2\omega |\langle \epsilon_j | (\hat{a}^\dagger + \hat{a}) | E_0 \rangle|^2 \gamma_j}{(\omega - \omega_j)^2 + (\omega_j \gamma_j)^2} + \frac{2\omega |\langle \epsilon_j | (\hat{a}^\dagger + \hat{a}) | E_0 \rangle|^2 \gamma_j}{(\omega + \omega_j)^2 + (\omega_j \gamma_j)^2} \right) \tag{4.27}$$

where $\omega_j = \epsilon_j - E_0$ are the energy differences of the transitions (imaginary part of Lindblad eigenvalues) and γ_j are the energy losses (real part of Lindblad eigenvalues) modified by the Franck-Condon factors:

$$\gamma_j = \frac{1}{2} (\gamma_{matt} |\langle \epsilon_j | (\hat{\sigma}^+ + \hat{\sigma}^-) | E_0 \rangle|^2 + \gamma_{phot} |\langle \epsilon_j | (\hat{a}^\dagger + \hat{a}) | E_0 \rangle|^2) \tag{4.28}$$

So, as we can see in figure 4.6, the analytical expression (4.27) gives us a good approximation of the noise spectrum $S(\omega)$ at a qualitative level. Futhermore, we can define two new analytical expressions (4.29) and (4.31). First, we remove the Franck-Condon renormalization in the decay γ_j obtaining (4.29) a first approximation:

$$S^{(1)}(\omega) = \sum_{j=0}^{2} \left(\frac{2\omega |\langle \epsilon_j | (\hat{a}^\dagger + \hat{a}) | E_0 \rangle|^2 \gamma}{(\omega - \omega_j)^2 + (\omega_j \gamma)^2} + \frac{2\omega |\langle \epsilon_j | (\hat{a}^\dagger + \hat{a}) | E_0 \rangle|^2 \gamma}{(\omega + \omega_j)^2 + (\omega_j \gamma)^2} \right) \tag{4.29}$$

$$\gamma = \frac{1}{2} (\gamma_{matt} + \gamma_{phot}) \tag{4.30}$$

Furthermore, removing all the Franck-Condon renormalization a simple formula is obtained (4.31):

$$S^{(0)}(\omega) = \sum_{j=0}^{2} \left(\frac{2\omega\gamma}{(\omega - \omega_j)^2 + (\omega_j \gamma)^2} + \frac{2\omega\gamma}{(\omega + \omega_j)^2 + (\omega_j \gamma)^2} \right) \tag{4.31}$$

Comparing these expressions (4.29-4.31) with the original one (4.27), we can understand both peak width and height. On the one hand, in the case of low energy losses ($\gamma_{matter} = \gamma_{phot} = 2.5 \times 10^{-4}$, see figure 4.7), the renormalization of losses γ_j due to the *Franck-Condon* factors [cf. equation (4.28)], absent $S^{(1)}(\omega)$, give us the difference in the peak width. Then, removing all the Franck-Condon renormalization, as in $S^{(0)}(\omega)$, it leads to symmetric peaks.

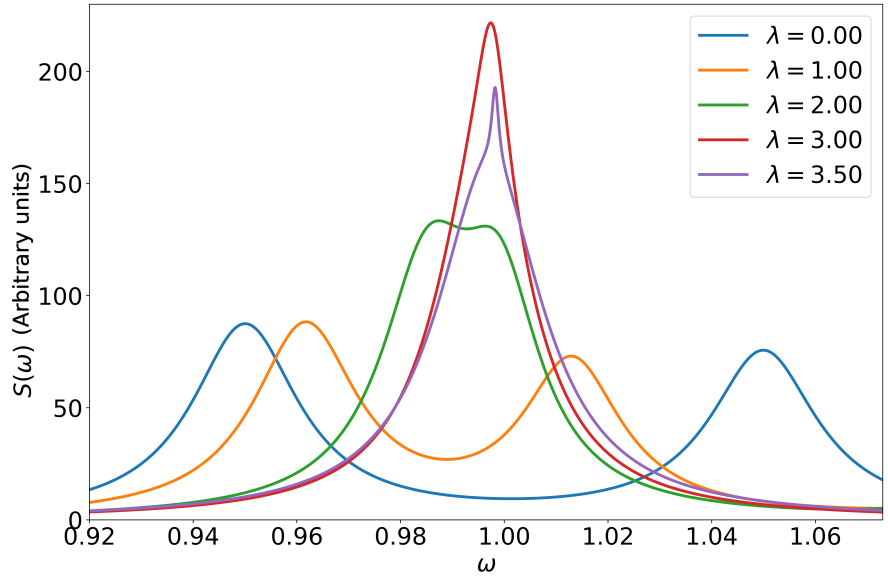

(a)

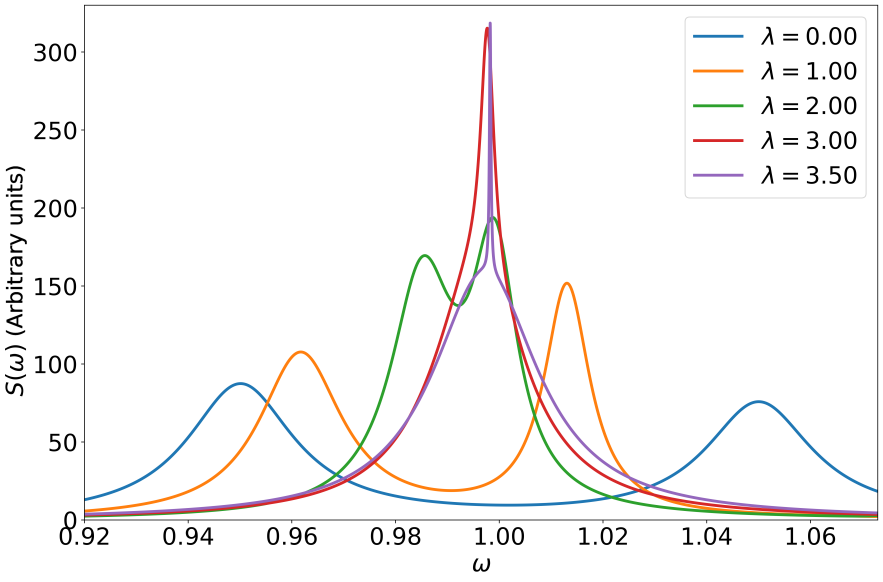

(b)

Figure 4.6: At ***bare resonance***, noise spectrum $S(\omega)$ for different values of λ (a) numerical case and (b) analytical case using the equation (4.27). Parameters: $\Delta = \omega_c = 1.0$, $\omega_v = 0.1$, $\lambda = 0.0 - 3.5$, $\gamma_{matter} = \gamma_{phot} = 2.5 \times 10^{-2}$, $\gamma_{phon} = 0.0$ and $\rho_0 = |\downarrow 0_{phot} 0_{phon}\rangle \langle \downarrow 0_{phot} 0_{phon}|$.

On the other hand, in the case of high losses ($\gamma_{matter} = \gamma_{phot} = 2.5 \times 10^{-2}$, see figure 4.8), we see that, the Franck-Condon factors are responsible for the asymmetries of both form and height of the peaks in the noise spectrum $S(\omega)$.

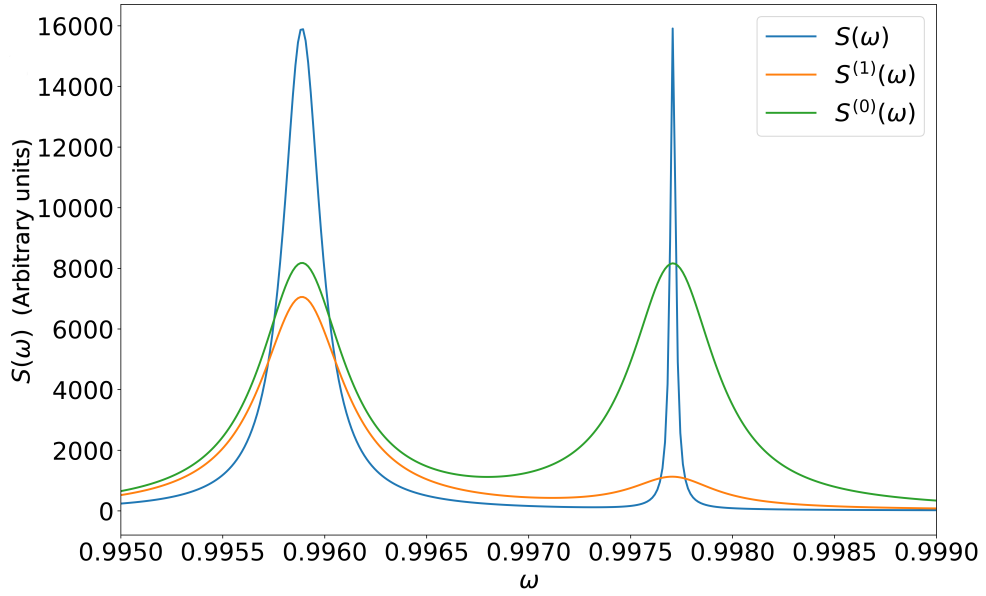

Figure 4.7: At ***bare resonance***, analytical calculus of the noise spectrum $S(\omega)$ for $\lambda = 3.0$, we distinguish 3 equations (4.27), (4.29) and (4.31). Parameters: $\Delta = \omega_c = 1.0$, $\omega_v = 0.1$, $\gamma_{matter} = \gamma_{phot} = 2.5 \times 10^{-4}$, $\gamma_{phon} = 0.0$ and $\rho_0 = |\downarrow 0_{phot} 0_{phon}\rangle \langle \downarrow 0_{phot} 0_{phon}|$.

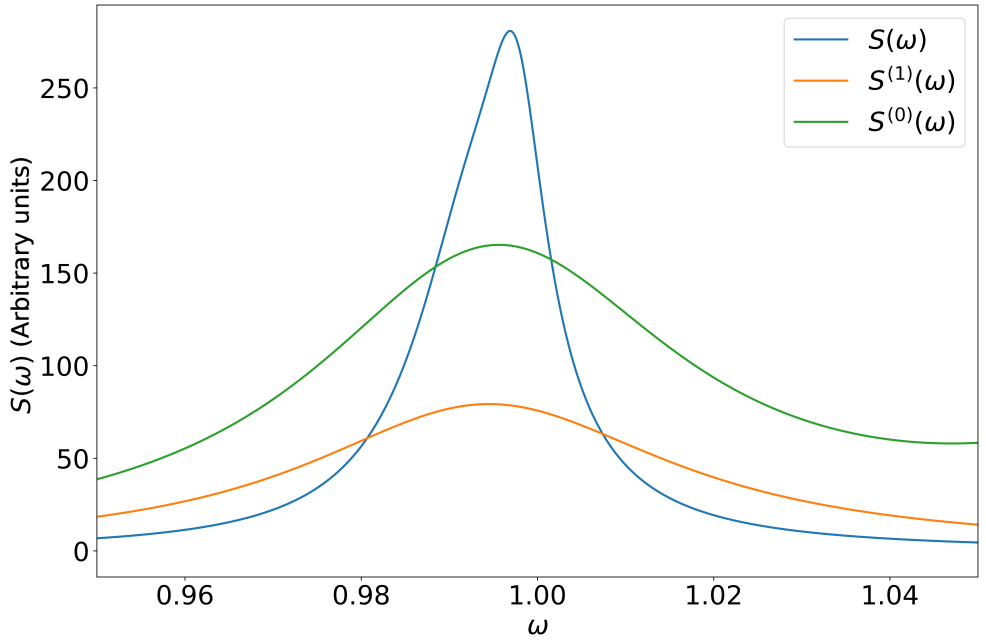

Figure 4.8: At ***bare resonance***, analytical calculus of the noise spectrum $S(\omega)$ for $\lambda = 3.0$, we distinguish 3 equations (4.27), (4.29) and (4.31). Parameters: $\Delta = \omega_c = 1.0$, $\omega_v = 0.1$, $\gamma_{matter} = \gamma_{phot} = 2.5 \times 10^{-2}$, $\gamma_{phon} = 0.0$ and $\rho_0 = |\downarrow 0_{phot} 0_{phon}\rangle \langle \downarrow 0_{phot} 0_{phon}|$.

Chapter 5

Bound States

We have already studied the energy spectrum, the dynamics of the system and the noise spectrum $S(\omega)$ of a molecule placed in a cavity. In this last chapter, we are going to study a different setup. We will couple the molecule to a waveguide. The aim will be to study the influence of the matter-vibrational coupling in the localized states formed in the waveguide setup.

5.1 Introduction

The recent advances in atom nanophotonics integration [37, 100, 101] have increased the interest in this field in the last years. The typical system consists of an emitter, for instance an atom, coupled to the modes of an electromagnetic field of a photonic media such as photonic crystals, quantum dots, nanophoptonic waveguides or other photonic nanostructures. Thus, the interaction of a quantum system with discrete energy levels with these photonic media with bounded dispersion relations $\omega(k)$ produces the appearance of localized states. These states, known as *bound states*, consist on a localized photon cloud surrounding the emitter [102].

All these developments have inspired many theoretical studies of long-range atom interaction [8, 103, 104], the scattering of photons with the emitter [105] or the study of the emitter spontaneous decay in *waveguide-QED* [106]. Here, we are going to coupled a molecule (two-level system) to the central site of a chain of bosonic sites coupled with each other to first neighbours (*tight-binding* model), see figure 5.1. This models a set of coupled cavities (either because they are the real photonic system to consider, or because we study a discretized waveguide). As we have said, we will consider that the molecule has a vibrational mode and we will study the influence of the matter-phonon coupling λ in the *bound states* of the system.

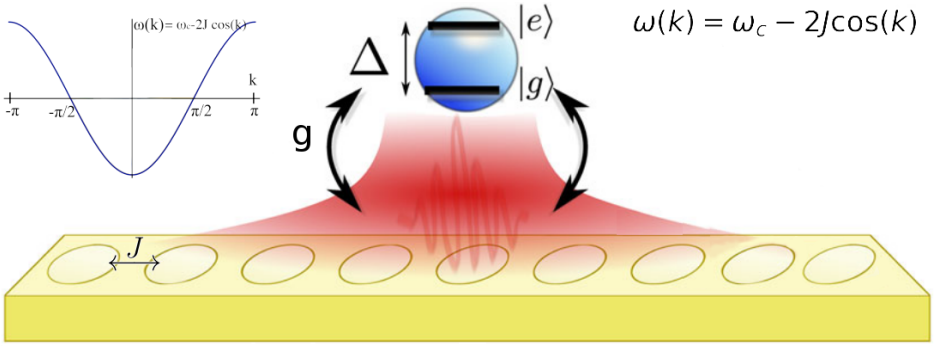

Figure 5.1: Schematic figure of a discretized waveguide where a two-level system is coupled to the central site. J is the coupling between the waveguide sites to first neighbours (*tight-binding*, cosine dispersion relation $\omega(k)$) and g the light-matter coupling.

We are going to divide this chapter in two main sections. The first one [section 5.2] will deal with the coupling a two-level system to the central site, using a *Jaynes-Cummings* coupling. In the second one [section 5.3], we will add the *Holstein* coupling to a phonon mode, as we did with the *Rabi* model (1.2) in the previous chapters. We will not take into account the influence of the counterrotating terms, as in this extended setup the molecule-photon coupling is usually small.

5.2 Jaynes-Cumming model

As we have already said, we are going to study in this section the energy spectrum of a two-level system (with excitation energy Δ) coupled to a series of $2N+1$ electromagnetic cavities (from the $n=-N$ to the $n=N$), coupled with a nearest neighbour coupling J. The coupling between the photons in the central cavity ($n=0$) and the two-level system will be as in the *Jaynes-Cummings* model (1.10). Thus, the Hamiltonian of the system is:

$$H = \sum_{n=-N}^{N} \omega_c \hat{a}_n^\dagger \hat{a}_n - J \sum_{n=-N}^{N} (\hat{a}_{n+1}^\dagger \hat{a}_n + \hat{a}_n^\dagger \hat{a}_{n+1}) + \Delta \hat{\sigma}^+ \hat{\sigma}^- + g(\hat{a}_0^\dagger \sigma^- + \hat{a}_0 \sigma^+) \tag{5.1}$$

However, before we study the coupled system, let us consider the isolated waveguide first. The photonic Hamiltonian is:

$$H_B = \sum_{n=-N}^{N} \omega_c \hat{a}_n^\dagger \hat{a}_n - J \sum_{n=-N}^{N} (\hat{a}_{n+1}^\dagger \hat{a}_n + \hat{a}_n^\dagger \hat{a}_{n+1}) \tag{5.2}$$

where we are going to assume $a_{N+1} = a_{-N}$ (periodic boudary conditions). We can easily diagonalize it by changing to momentum space, in other words:

$$\hat{a}_k = \frac{1}{\sqrt{2N+1}} \sum_{n=-N}^{N} e^{-i\frac{2\pi k}{2N+1}n} \hat{a}_n \quad \longrightarrow \quad \hat{a}_n = \frac{1}{\sqrt{2N+1}} \sum_{k=-N}^{N} e^{i\frac{2\pi k}{2N+1}n} \hat{a}_k \tag{5.3}$$

and taking into account[1]:

$$\sum_{n=-N}^{N} e^{i(k-k')\frac{2\pi}{2N+1}n} = (2N+1)\delta_{kk'} \tag{5.4}$$

Thus, we arrive to the following Hamiltonian:

$$H_B = \sum_{k=-N}^{N} \omega(k) \hat{a}_k^\dagger \hat{a}_k \tag{5.5}$$

where:

$$\omega(k) = \omega_c - 2J \cos\left(\frac{2\pi}{2N+1}k\right) \tag{5.6}$$

So, the eigenstates of this system are the photons with momentum k, $|\psi_k\rangle = |0...1_k...0\rangle \equiv |1_k\rangle$. The discretization imposes momentums from $k = \frac{-2\pi N}{2N+1}$ to $k = \frac{2\pi N}{2N+1}$. Besides, their eigenenergies are circumscribed to the energy band between $\omega_c - 2J$ and $\omega_c + 2J$. These are known as propagating states.

Now, we consider the molecule-waveguide system (5.1) case. Changing again to momentum space, we obtain:

$$H = \sum_{k=-N}^{N} \omega(k) a_k^\dagger a_k + \Delta\sigma^+\sigma^- + \tilde{g} \sum_{k=-N}^{N} (a_k^\dagger \sigma^- + a_k \sigma^+) \quad \text{with:} \quad \tilde{g} = \frac{g}{\sqrt{2N+1}} \tag{5.7}$$

We can express their one-particle sector eigenstates in the basis $\{|\uparrow\ 0_k\rangle, |\downarrow\ 1_k\rangle\}$, where $|\uparrow\downarrow\rangle$ means the excited or ground state of the two-level system. In this basis, any eigenstate of energy E_n in the one-particle sector can be expressed as:

$$|\psi_n\rangle = c_e\, |\uparrow\ 0_k\rangle + \sum_{k=-N}^{N} c_k\, |\downarrow\ 1_k\rangle \tag{5.8}$$

where the occupation $\langle\psi_n|\hat{a}_m^\dagger \hat{a}_m|\psi_n\rangle$ of this state on the waveguide site m is:

$$\langle\psi_n|\hat{a}_m^\dagger \hat{a}_m|\psi_n\rangle = \frac{1}{2N+1} \sum_{k,\ k'=-N}^{N} e^{i\frac{2\pi}{2N+1}(k'-k)m} c_{k'}^* c_k \tag{5.9}$$

[1]Its can be shown using the geometric series: $\sum_{k=0}^{n-1} ar^k = a(1-r^n)/(1-r)$

We are going to calculate the eigenstates of the system in the one-particle sector [cf. equation (5.8)]. Besides, applying the definition of eigenstate, $H\,|\psi_n\rangle = E_n\,|\psi_n\rangle$, we get:

$$(\Delta c_e \tilde{g} \sum_k c_k)\,|\uparrow\ 0_k\rangle + \sum_k (c_k\omega(k) + c_e\tilde{g})\,|\downarrow\ 1_k\rangle = E_n(c_e\,|\uparrow\ 0_k\rangle + \sum_k c_k\,|\downarrow\ 1_k\rangle) \tag{5.10}$$

Identifying the terms, we find:

$$\tilde{g}c_e + (\omega_c - 2J\cos(k))c_k = E_n c_k \tag{5.11}$$

$$\Delta c_e + \tilde{g}\sum_k c_k = E_n c_e \tag{5.12}$$

So, using the equation (5.11) and neglecting the term $\propto \tilde{g} \ll 1$, we can obtain an expression for $\cos(k)$:

$$\cos(k) \approx \frac{1}{2J}[\omega_c - E_n] \tag{5.13}$$

Thus using the last equation, we find two types of solutions:

- **Propagating states:** Eigenstates with a real momentum asociated or in other words $|\cos(k)| \leqslant 1$. Then, we obtain eigenstates with an oscillatory occupation [cf. equation (5.9)] and with energies within the energy band between $\omega_c - 2J$ and $\omega_c + 2J$.

- **Evanescence states:** Eigenstates whose associated momentum is complex or $|\cos(k)| > 1$, with energies outside the energy band. Thus, they are characterized by an exponential decay in the waveguide occupation [cf. equation (5.9)]. These states are also known as *bound states*. States which are localized in a specific region (in our case around the the central site ($n = 0$) in the chain of electromagnetic cavities [cf. figure 5.3]).

Using this criteria, we can give a momentum k to each propagating state, see figure 5.2 (where exact diagonalization has been done for a representative system with $J = 1$, $\omega_c = 3.05$, $\Delta = 0.7$ and $2N + 1 = 241$ sites). Besides, we have obtained a *bound state* with energy $E \approx 0.6980$ [cf. figure 5.2, red line]. Figure 5.3 compares occupation $\langle\psi_n|\hat{a}_m^\dagger\hat{a}_m|\psi_n\rangle$ in the cavity m for a eigenstate $|\psi_n\rangle$ for the *bound state* $E_n \approx 0.6980$ with a propagating state $E_n \approx 1.0670$.

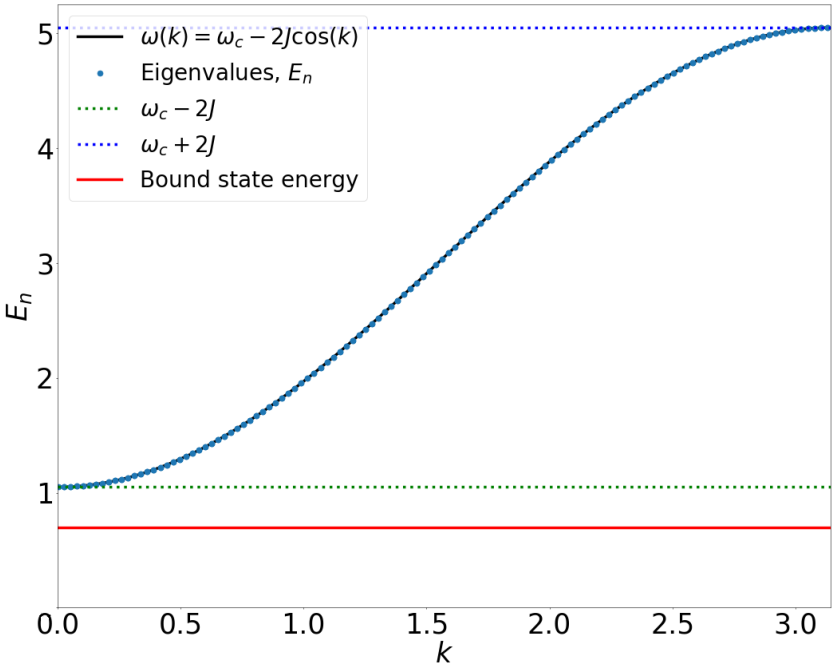

Figure 5.2: Propagating eigenstates (blue dots) of the Hamiltonian (5.1), classified by their momentum k. The red line indicate the energy of the *Bound state* of the system. Parameters: $J = 1$, $g = 0.05$, $\omega_c = 3.05$ and $\Delta = 0.7$.

Now, we are going to obtain an analytical expression for the *bound state* energy. In order to do that, we obtain an expression for c_k from equation (5.11):

$$c_k = \frac{\tilde{g} c_e}{E_n - \omega(k)} \tag{5.14}$$

and substituting it into equation (5.12), we obtain:

$$c_e \left(\Delta - E_n + \sum_{k=-N}^{N} \frac{\tilde{g}^2}{E - \omega(k)} \right) = 0 \tag{5.15}$$

So, we need to compute the discrete sum (known as *self-energy*). For this, we change the discrete sum to an integral and perform the change of variable $y = e^{ik}$:

$$\sum_{k=-N}^{N} \frac{\tilde{g}^2}{E_n - \omega(k)} \longrightarrow \frac{g^2}{2\pi} \int_{-\pi}^{\pi} \frac{1}{E_n - \omega_c + 2J\cos(k)} dk = -\frac{ig^2}{2J\pi} \oint \frac{dy}{(y - y_+)(y - y_-)} \tag{5.16}$$

where:

$$y_\pm = \gamma \pm \sqrt{\gamma^2 - 1} \qquad \text{with:} \quad \gamma = \frac{\omega_c - E_n}{2J} \tag{5.17}$$

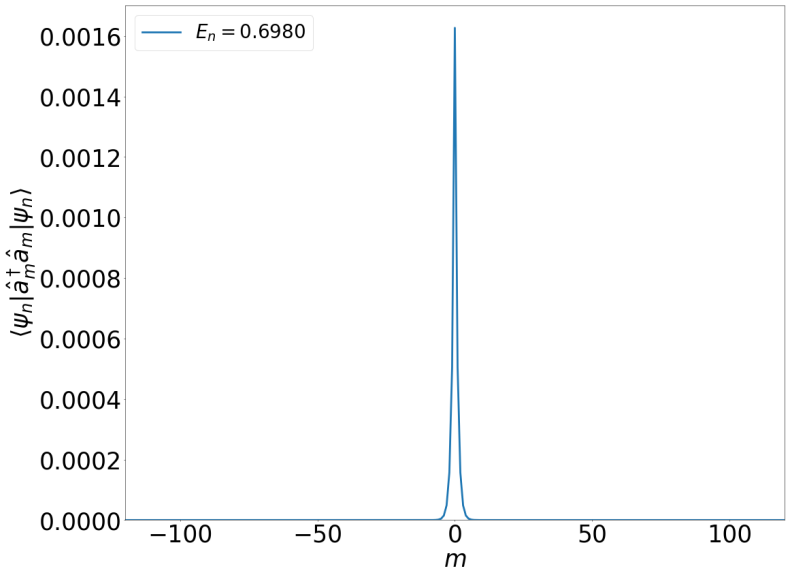

(a)

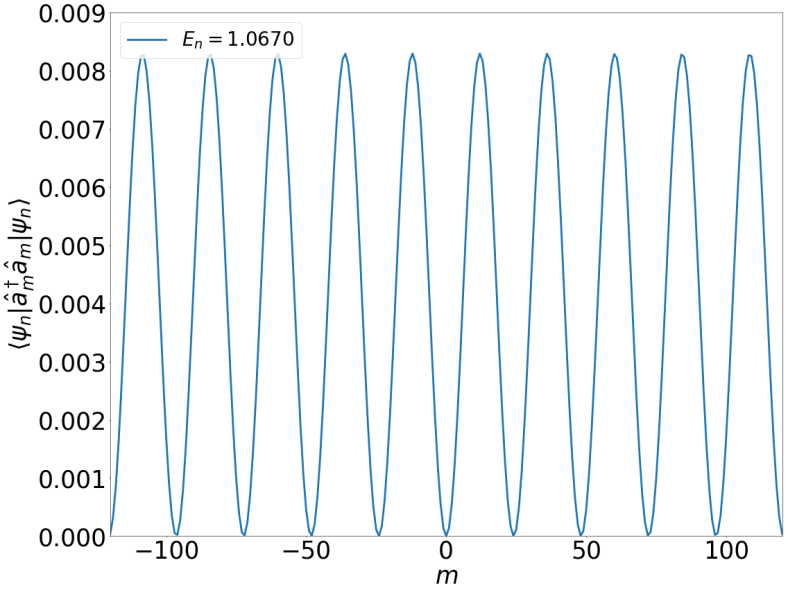

(b)

Figure 5.3: Occupation $\langle\psi_n|\hat{a}_m^\dagger\hat{a}_m|\psi_n\rangle$ of the m cavity for (a) the *Bound state* of energy $E_n \approx 0.6980$ and (b) a propagating eigenstate of energy $E_n \approx 1.0670$. Parameters: $J = 1$, $g = 0.05$, $\omega_c = 3.05$ and $\Delta = 0.7$.

After change of variables, the integral becomes to an integral in the complex plane of the unit circle centered in the origin. Imposing E_n to be below the energy band ($E_n < \omega_c - 2J$) implies $\gamma > 1$. Thus, the $y_\pm$ roots are real numbers. Clearly $y_+ > 1$, so in this case the pole outside the unit circle. But, is y_- inside or outside the unit circle?

The answer is that y_- is inside the unit circle, since defining the function $f(\gamma) = \gamma - \sqrt{\gamma^2 - 1}$, we have:

$$f'(\gamma) = 1 - \frac{\gamma}{\sqrt{\gamma^2 - 1}} < 0 \qquad \forall \gamma > 1 \tag{5.18}$$

In other words, $f(\gamma)$ is a decreasing function and its maximum is when $\gamma = 1$. In this case $f(1) = 1$ and we conclude that $y_- < 1, \forall \gamma > 1$. If we had found an *bound state* above the energy band ($E_n > \omega_c + 2J$), using the same reasoning, we would have found that y_+ would have been inside and y_- outside. We can solve the integral using the *residues theorem* (if we have $E_n < \omega_c - 2J$ we have a "$-$" and if $E_n > \omega_c + 2J$ we have a "$+$" in the integral (5.19)):

$$\oint \frac{dy}{(y - y_+)(y - y_-)} = 2\pi i \text{Res}(y_\mp) = \mp \frac{\pi i}{\sqrt{\left(\frac{\omega_c - E_n}{2J}\right)^2 - 1}} \tag{5.19}$$

Therefore:

$$\sum_{k=-N}^{N} \frac{\tilde{g}^2}{E_n - \omega(k)} \approx \mp \frac{g^2}{2\sqrt{\left(\frac{\omega_c - E_n}{2J}\right)^2 - 1}} \tag{5.20}$$

Substituting the last expression into (5.15):

$$\Delta - E_n \mp \frac{g^2}{2J\sqrt{\left(\frac{\omega_c - E_n}{2J}\right)^2 - 1}} = 0 \tag{5.21}$$

We can solve (5.21) numerically and obtain the energy of the *bound state*. For the parameters used in figure 5.2, we obtain $E_n \approx 0.6980$ which is virtually the same as the value obatined with exact diagonalization. Now, we are going to obtain an approximate analytical expression for the energy of the *bound state* below the energy band ($E_n < \omega_c - 2J$). We are very close to the inferior limit of the energy band ($\omega_c - 2J$). Thus, using a Taylor expansion:

$$\omega(k) = \omega_c - 2J\cos(k) \approx \omega_c - 2J + Jk^2 \tag{5.22}$$

Going back to the equation (5.16) and making the change of variables $z = k/\alpha$, where α is:

$$\alpha = \sqrt{\frac{(\omega_c - 2J) - E_n}{J}} \tag{5.23}$$

We get:

$$\sum_{k=-N}^{N} \frac{\tilde{g}^2}{E_n - \omega(k)} \longrightarrow \frac{g^2}{2\pi} \int_{-\pi}^{\pi} \frac{1}{E_n - \omega_c + 2J\cos(k)} dk$$
$$\approx \frac{g^2}{2\pi} \int_{-\pi}^{\pi} \frac{1}{E_n - \omega_c + 2J - Jk^2} dk = -\frac{g^2}{2\pi J\alpha^2} \int_{-\pi}^{\pi} \frac{dk}{1 + (k/\alpha)^2}$$
$$= -\frac{g^2}{\pi J\alpha} \arctan(\pi/\alpha) \approx -\frac{g^2}{\pi J\alpha} \frac{\pi}{2} = -\frac{g^2}{2J^{1/2}} \frac{1}{\sqrt{(\omega_c - 2J) - E_n}}$$

where we have taken into account $\alpha \approx 0$ because we are close to the energy band limit. Substituting this result into the equation (5.15), we obtain:

$$E_n = \Delta - \frac{g^2}{2J^{1/2}} \frac{1}{\sqrt{\omega_c - 2J - E_n}} \tag{5.24}$$

In this approximation, we have considered that the term $\propto g^2$ is much smaller than Δ and have treated it as a perturbation. Equation (5.24) can be solved self-consistently. However, as $E_n \approx \Delta$, we can obtain a good approximation (in the first order in g^2) by replacing $E_n \approx \Delta$ in the right-hand side of equation (5.24). Then:

$$E_n \approx \Delta - \frac{g^2}{2J^{1/2}} \frac{1}{\sqrt{\omega_c - 2J - \Delta}} \tag{5.25}$$

With this last equation (5.25) we obtain $E_n \approx 0.6979$ for the parameters used in the figure 5.2 which is very similar to the value obtained using exact diagonalization $E_n \approx 0.6980$.

5.3 Holstein-Quantum-Jaynes-Cummings model

The objective of this last section will be the study of the *bound states* which appear when the discrete quantum system is a vibrating molecule. We treat this system with the *Holstein-Quantum-Jaynes-Cummings* Hamiltonian in the coupling to the central site of our waveguide. Thus, the Hamiltonian of our system will be:

$$H = \sum_{n=-N}^{N} \omega_c \hat{a}_n^\dagger \hat{a}_n - J \sum_{n=-N}^{N} (\hat{a}_{n+1}^\dagger \hat{a}_n + \hat{a}_n^\dagger \hat{a}_{n+1}) + \Delta \hat{\sigma}^+ \hat{\sigma}^- + g(\hat{a}_0^\dagger \sigma^- + \hat{a}_0 \sigma^+) +$$
$$+ \omega_v (\hat{b}^\dagger \hat{b} + \lambda \hat{\sigma}^+ \hat{\sigma}^- (\hat{b}^\dagger + \hat{b} + \lambda)) \tag{5.26}$$

or, changing to momentum space:

$$H = \sum_{k=-N}^{N} \omega(k) a_k^\dagger a_k + \Delta\sigma^+\sigma^- + \tilde{g} \sum_{k=-N}^{N} (a_k^\dagger \sigma^- + a_k \sigma^+) + \omega_v(\hat{b}^\dagger \hat{b} + \lambda\hat{\sigma}^+\hat{\sigma}^-(\hat{b}^\dagger + \hat{b} + \lambda)) \tag{5.27}$$

However, before we study the full Hamiltonian, we focus on the simplified case of $\lambda = 0$:

$$H = \sum_{k=-N}^{N} \omega(k) a_k^\dagger a_k + \Delta\sigma^+\sigma^- + \tilde{g} \sum_{k=-N}^{N} (a_k^\dagger \sigma^- + a_k \sigma^+) + \omega_v \hat{b}^\dagger \hat{b} \tag{5.28}$$

In this section as representative parameters, we will take: $J = 1$ as energy unit, $\omega_c = 3.05$ (this ensure that the energy band has positive values of the energy) and $2N + 1 = 81$ sites in the chain. The other parameters are the typical used in the last chapters: $\Delta = 1.0$, $\omega_v = 0.1$ and $g = 0.05$. The dimension of the phonon subspace will be $N_{phon} = 20$.

Thus, when we calculate (exact diagonalization) the *bound states* of the model (5.28), we get 20 *bound states* which come from each subspace with 0, 1, 2, ..., 19 phonons. This is reasonable because for $\lambda = 0$ the phonon Hilbert subspace is uncoupled from the matter and light subspaces. In other words, we obtain a *bound state* of energy E_0 and then a series of phonon replicas with energies:

$$E_n = E_0 + n\omega_v \tag{5.29}$$

Besides, we obtain a corresponding phonon replicas of the energy bands of propagating photons.

Therefore, in the case of $\lambda \neq 0$, the question that we should answer is: Are still these *bound states* localized states for $\lambda \neq 0$? In order to answer this question it is convenient to apply a Polaron transformation as we did in the case of a single cavity. Applying the transformation $U_P^{(0)} = e^{-\lambda\hat{\sigma}^+\hat{\sigma}^-(\hat{b}^\dagger - \hat{b})}$ to our model (5.27):

$$U_P^{(0)\dagger} H U_P^{(0)} = \sum_k \omega(k)\hat{a}_k^\dagger \hat{a}_k + \Delta\hat{\sigma}^+\hat{\sigma}^- + \tilde{g}\sum_k (\hat{a}_k^\dagger \sigma^- D^\dagger(\lambda) + \hat{a}_k \sigma^+ D(\lambda)) + \omega_v \hat{b}^\dagger \hat{b} \tag{5.30}$$

where $D(\lambda) = e^{\lambda(\hat{b}^\dagger - \hat{b})}$. Thus, using the basis $\{|\uparrow\ 0_k\ \tilde{0}\rangle, |\uparrow\ 0_k\ \tilde{1}\rangle, ..., |\downarrow\ 1_k\ 0\rangle, |\downarrow\ 1_k\ 1\rangle, ...\}$, in the one light-matter excitation subspace, a state can be written as:

$$|\psi\rangle = \sum_n c_e^n |\uparrow\ 0_k\ \tilde{n}\rangle + \sum_n \sum_k c_k^n |\downarrow\ 1_k\ n\rangle \tag{5.31}$$

Thus, we are going to consider the three lowest *bound states* at $\lambda = 0$: $|\psi_0\rangle$, $E_0 = 0.995$; $|\psi_1\rangle$, $E_1 = 1.095$ and $|\psi_2\rangle$, $E_2 = 1.195$. We will study the depedence with λ of their weights in the basis states of the one-particle sector ($|\langle\psi_m|\uparrow\ 0_k\ \tilde{n}\rangle|^2$ and $|\langle\psi_m|\downarrow\ 1_k\ n\rangle|^2$) [cf. equation (5.31)].

First, the eigenstate $|\psi_0\rangle$ has weight in the state $|\downarrow 1_k 0_{phon}\rangle$ for $\lambda \ll 1$. Then, for $\lambda \geq 1$, we obtain a mixture of the states $\{|\downarrow 1_k 0_{phon}\rangle\,,\ |\downarrow 1_k 1_{phon}\rangle\,,\ ...\}$, see figure 5.4b. But the main characteristic is that the eigenstate $|\psi_0\rangle$ has most of the weight in the state $|\uparrow 0_k \tilde{0}_{phon}\rangle$ and zero in the states $|\uparrow 0_k \tilde{n}_{phon}\rangle$ for $\tilde{n}_{phon} > 0$, see figure 5.4a.

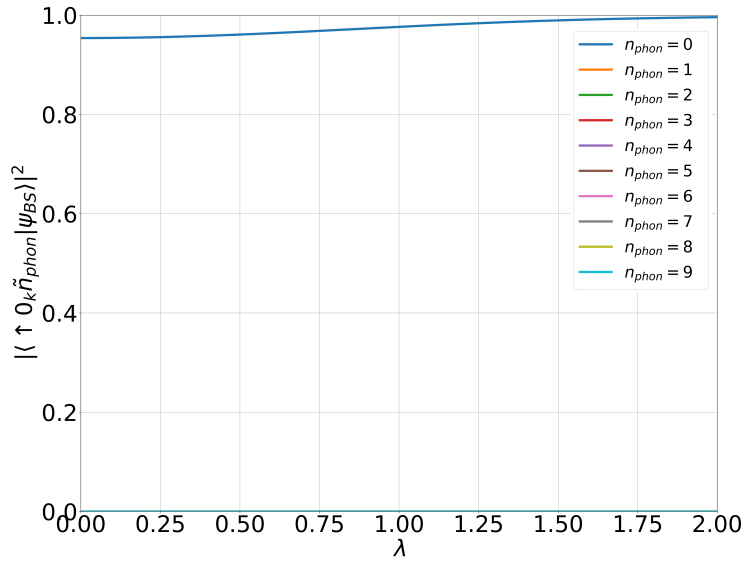

(a)

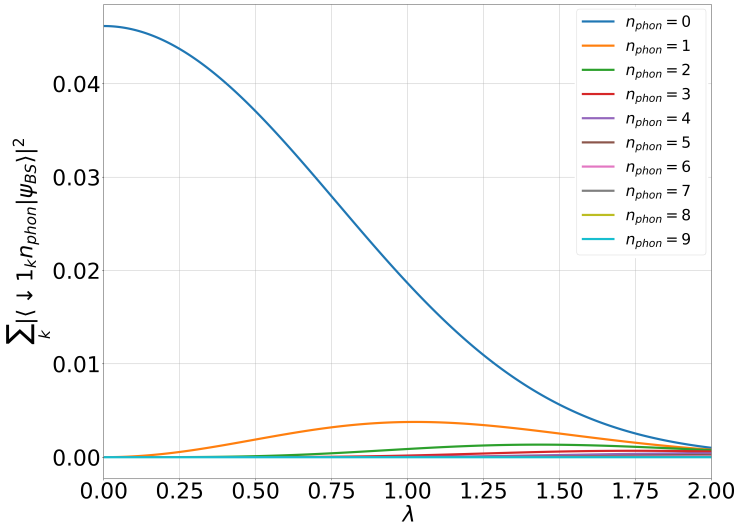

(b)

Figure 5.4: Weights of the eigenstate $|\psi_0\rangle$ of energy $E_0 = 0.995$ (at $\lambda = 0$) (a) $|\,\langle\psi_0|\uparrow\ 0_k\ \tilde{n}\rangle\,|^2$ and (b) $\sum_k |\,\langle\psi_0|\downarrow\ 1_k\ n\rangle\,|^2$ as a function of λ. Parameters: $\omega_v = 0.1$, $J = 1$, $\omega_c = 3.05$, $\Delta = 1$, $g = 0.05$, $N_{phon} = 20$ and $2N + 1 = 81$.

Second, the eigenstate $|\psi_1\rangle$ has weight in the state $|\downarrow 1_k 1_{phon}\rangle$ for $\lambda \ll 1$. Then, for $\lambda \geq 1$, we obtain a mixture of the states $\{|\downarrow 1_k 0_{phon}\rangle\,,\ |\downarrow 1_k 1_{phon}\rangle\,,\ ...\}$, cf. figure 5.5b. As well, the main characteristic is that the eigenstate $|\psi_1\rangle$ has most of the weight in the state $|\uparrow 0_k \tilde{1}_{phon}\rangle$ and zero in the states $|\uparrow 0_k \tilde{n}_{phon}\rangle$ for $\tilde{n}_{phon} > 0$, cf. figure 5.5a.

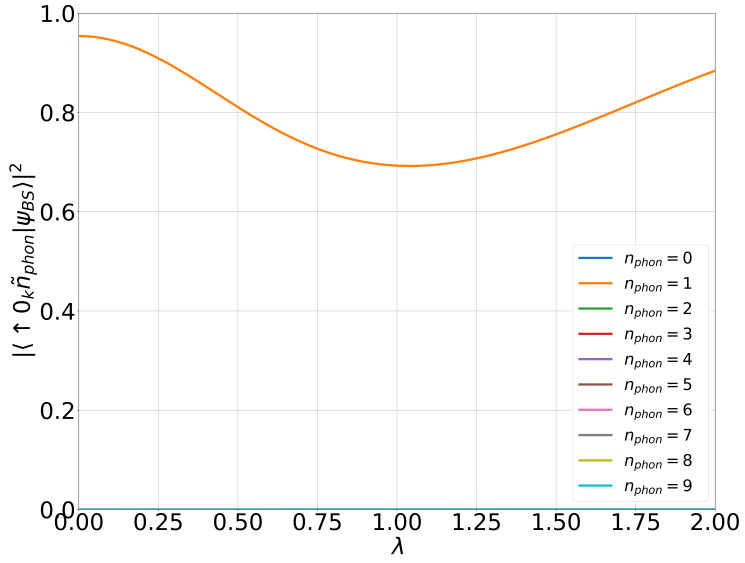

(a)

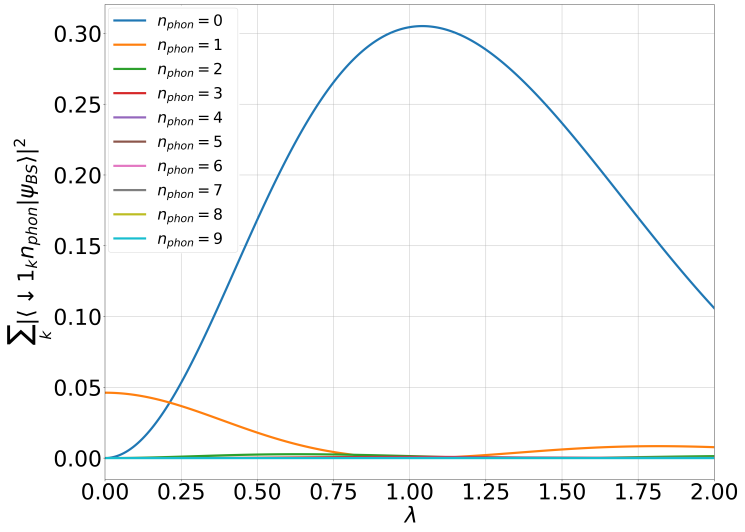

(b)

Figure 5.5: Weights of the eigenstate $|\psi_1\rangle$ of energy $E_1 = 1.095$ (at $\lambda = 0$) (a) $|\langle\psi_1|\uparrow\ 0_k\ \tilde{n}\rangle|^2$ and (b) $\sum_k |\langle\psi_1|\downarrow\ 1_k\ n\rangle|^2$ as a function of λ. Parameters: $\omega_v = 0.1$, $J = 1$, $\omega_c = 3.05$, $\Delta = 1$, $g = 0.05$, $N_{phon} = 20$ and $2N + 1 = 81$.

Third, the eigenstate $|\psi_2\rangle$ has weight in the state $|\downarrow 1_k 2_{phon}\rangle$ for $\lambda \ll 1$. Then, for $\lambda \geq 1$, we obtain a mixture of the states $\{|\downarrow 1_k 0_{phon}\rangle\,,\ |\downarrow 1_k 1_{phon}\rangle\,,\ ...\}$, see figure 5.6b. And again its main characteristic is that the eigenstate $|\psi_2\rangle$ has almost all the weight in the state $|\uparrow 0_k \tilde{2}_{phon}\rangle$ and zero in the states $|\uparrow 0_k \tilde{n}_{phon}\rangle$ for $\tilde{n}_{phon} > 0$, see figure 5.6a.

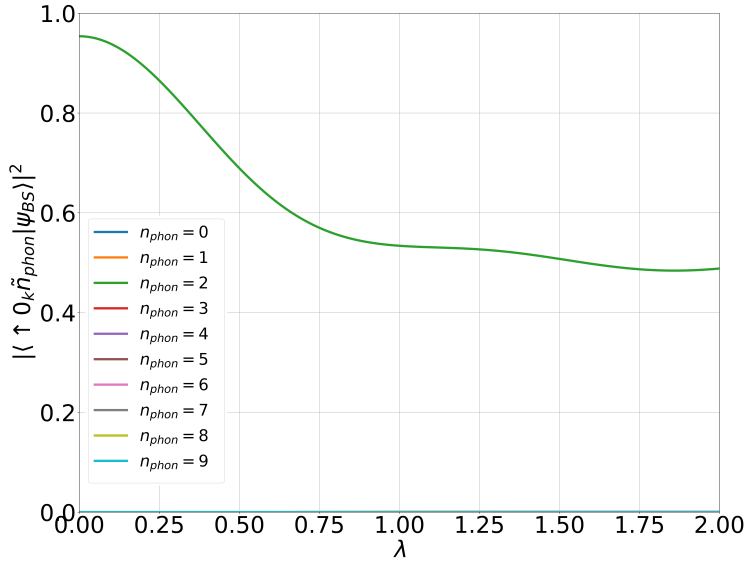

(a)

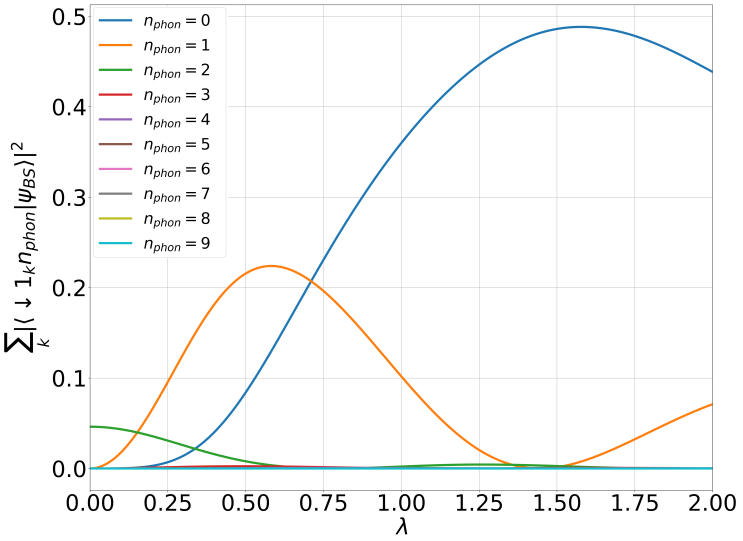

(b)

Figure 5.6: Weights of the eigenstate $|\psi_2\rangle$ of energy $E_0 = 1.195$ (at $\lambda = 0$) (a) $|\langle\psi_2|\uparrow\ 0_k\ \tilde{n}\rangle|^2$ and (b) $\sum_k |\langle\psi_2|\downarrow\ 1_k\ n\rangle|^2$ as a function of λ. Parameters: $\omega_v = 0.1$, $J = 1$, $\omega_c = 3.05$, $\Delta = 1$, $g = 0.05$, $N_{phon} = 20$ and $2N + 1 = 81$.

Thus, the eigenstates $|\psi_0\rangle$, $|\psi_1\rangle$ and $|\psi_2\rangle$ have a weight in the basis states $|\uparrow 0_k\tilde{0}_{phon}\rangle$,$|\uparrow 0_k\tilde{1}_{phon}\rangle$ and $|\uparrow 0_k\tilde{2}_{phon}\rangle$ respectively and a mixture of $\{|\downarrow 0_k 0_{phon}\rangle, |\downarrow 0_k 1_{phon}\rangle, ...\}$. So, we can use the following hypothesis for the m-*bound state* of m phonons (at least with m phonons at $\lambda = 0$):

$$|\psi_m\rangle = c_e\,|\uparrow\ 0_k\ \tilde{m}\rangle + \sum_n \sum_k c_k^n\,|\downarrow\ 1_k\ n\rangle \tag{5.32}$$

We will use this state (5.32) to get the criterion for distinguishing a *bound state* from a propagating one. First of all, we apply the definition of eigenstate $H\,|\psi_m\rangle = E_m\,|\psi_m\rangle$:

$$\begin{aligned} H\,|\psi_m\rangle &= (\Delta + m\omega_v)c_e\,|\uparrow\ 0_k\ \tilde{m}\rangle + \sum_{n,k}\omega(k)c_k^n\,|\downarrow\ 1_k\ n\rangle) \\ &+ \tilde{g}c_e D^\dagger(\lambda)\sum_k |\downarrow\ 1_k\ \tilde{m}\rangle + \tilde{g}D(\lambda)\sum_{n,k} c_k^n\,|\uparrow\ 0_k\ n\rangle + \omega_v\sum_{n,k} c_k^n n\,|\downarrow\ 1_k\ n\rangle \end{aligned}$$

Using the closure relation $\mathbb{1} = |\uparrow \tilde{m}_{phon}\rangle\langle\uparrow \tilde{m}_{phon}| + \sum_n |\downarrow\ n_{phon}\rangle\langle\downarrow\ n_{phon}|$:

$$D(\lambda)\,|n\rangle = D_{\tilde{m}n}(\lambda)\,|\tilde{m}\rangle \qquad D^\dagger(\lambda)\,|\tilde{m}\rangle = \sum_n D^\dagger_{n\tilde{m}}\,|n\rangle$$

and substituting the last expressions we have:

$$\begin{aligned} H\,|\psi_m\rangle &= \left((\Delta + \tilde{m}\omega_v)c_e + \tilde{g}\sum_{n,k} c_k^n D_{\tilde{m}n}\right)|\uparrow\ 0_k\ \tilde{m}\rangle \\ &+ \sum_{n,k}\left((\omega(k) + n\omega_v)c_k^n + \tilde{g}D^\dagger_{n\tilde{m}}c_e\right)|\downarrow\ 1_k\ n\rangle \\ &= E_m\left(c_e\,|\uparrow\ 0_k\ \tilde{m}\rangle + \sum_n\sum_k c_k^n\,|\downarrow\ 1_k\ n\rangle\right) \end{aligned} \tag{5.33}$$

Indentifing the terms we have:

$$E_m c_e = (\Delta + m\omega_v)c_e + \tilde{g}\sum_{n,k} c_k^n D_{\tilde{m}n} \tag{5.34}$$

$$E_m c_k^n = (\omega(k) + n\omega_v)c_k^n + \tilde{g}D^\dagger_{n\tilde{m}}c_e \tag{5.35}$$

As we did in the last section 5.2, we obtain the following equation of $\cos(k)$ from (5.35) considering that $\tilde{g} \ll 1$:

$$\cos(k) = \frac{1}{2J}[\omega_c + n\omega_v - E_m + \tilde{g}\frac{c_e}{c_k^n}D^\dagger_{n\tilde{m}}] \approx \frac{1}{2J}[\omega_c + n\omega_v - E_m] \tag{5.36}$$

Thus using (5.36), we calculate the value of $\cos(k)$ for each value of the number of phonons n with an associated weight $|c_k^n|^2$, for a particular eigenstate $|\psi_m\rangle$, E_m. We distinguish:

- **Localized weights:** $|c_k^n|^2$ for $|\cos(k)| > 1$. In other words, a complex momentum.
- **Propagating weights:** $|c_k^n|^2$ with a real momentum k, ($|\cos(k)| \leqslant 1$).

So, we have: (1) Localized weight: $P_{loc}^m = \sum_n |c_k^n|^2$ for complex k's and (2) a propagating weight: $P_{prop}^m = \sum_n |c_k^n|^2$ for real k's. Thus, we can define the fraction of localization P_m of a given eigenstate $|\psi_m\rangle$ as:

$$P_m = \frac{P_{loc}^m}{P_{loc}^m + P_{prop}^m} \tag{5.37}$$

Once we have a criteria to distinguish between a localized and a propagating state, we can plot the localized weights P_m for different values of λ. In figure 5.7, we have plotted the twenty *bound states* replicas found in the case of $\lambda = 0$. We have labeled[2] them by their number of phonons at $\lambda = 0$. Thus, with the exception of the *bound state* of the smallest energy, the other *bound states* loose their localize character for large values of λ. The phonon replicas of the *bound state* with energy E_0 have energies $\omega_c + \Delta - 2J < E_n < \omega_c + \Delta - 2J + m\,\omega_v = \infty$. They hybridize with the popagating modes lossing their localized character at $\lambda = 0$.

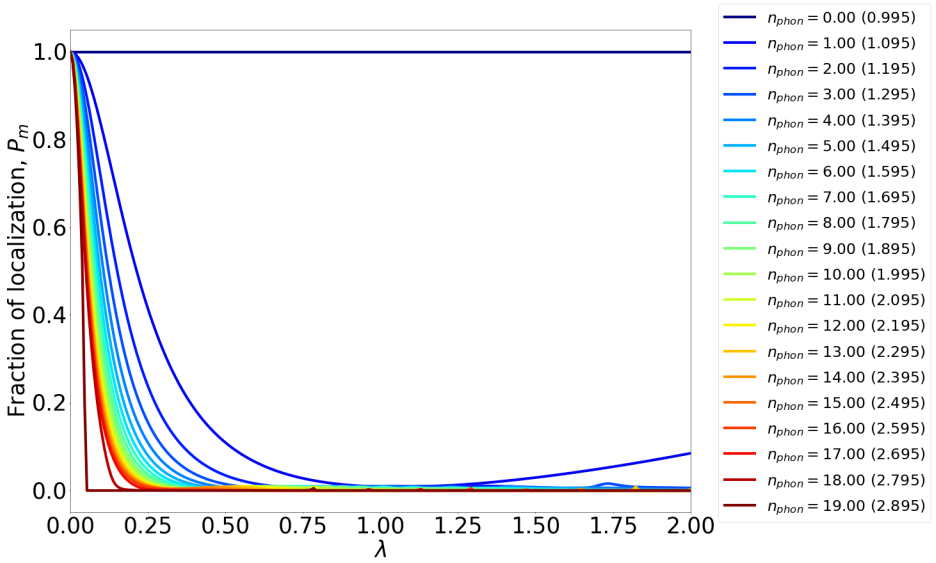

Figure 5.7: Localization weights fractions P_m of the twenty phonon *bound states* replicas found at $\lambda = 0$. The brakets of the legend indicate the energy of the *bound state* at $\lambda = 0$. Parameters: $\omega_v = 0.1$, $J = 1$, $\omega_c = 3.05$, $\Delta = 1$, $g = 0.05$, $N_{phon} = 20$ and $2N + 1 = 81$.

[2]The bracket of the legend of figure 5.7 indicate the energy of the *bound state* at $\lambda = 0$

Thus, we can plot the photon occupation in the chain of the *bound state* of energy $E_1 \approx 1.095$ (the *bound state* of one phonon at $\lambda = 0$) for different values of λ, see figure 5.8. For $\lambda = 0$ is clearly a localized state around the central site $n = 0$, but it becomes a propagating state for $\lambda > 0$.

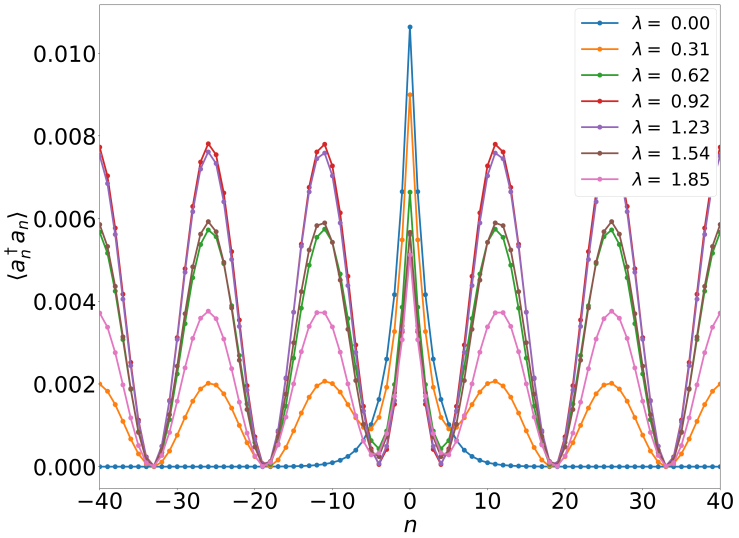

Figure 5.8: Photon occupation of the chain of the state with the second smallest energy (at $\lambda = 0$, $E_1 \approx 1.095$) for several values of λ. We can see its delocalization for $\lambda > 0$. Parameters: $\omega_v = 0.1$, $J = 1$, $\omega_c = 3.05$, $\Delta = 1$, $g = 0.05$, $N_{phon} = 20$ and $2N + 1 = 81$.

Now, we are going to obtain analytically the energies for the eigenstates which are *bound states* at $\lambda = 0$. In order to do that, first, we obtain an expression of c_k^n from the equation (5.35) and substitute it in the equation (5.34) obtaining:

$$\left[\Delta + m\omega_v - E_m + \sum_n \left(\sum_k \frac{\tilde{g}^2 |D_{\tilde{m}n}|^2}{E_m - (\omega_v n + \omega(k))} \right) \right] c_e = 0 \tag{5.38}$$

So, solving numerically the following expression 5.39, we can obtain the different *bound states*:

$$\Delta + m\omega_v - E_m + \sum_n \left(\sum_k \frac{\tilde{g}^2 |D_{\tilde{m}n}|^2}{E_m - (\omega_v n + \omega(k))} \right) = 0 \tag{5.39}$$

Besides, we can simplify the last expression and calculate the sum over k of the self-energy term, changing the discrete sum to an integral and doing a change of variables $z = e^{ik}$:

$$\begin{aligned} S_n = \frac{g^2}{2N+1} \sum_{k=-N}^{N} \frac{1}{E_m - (\omega(k) + n\omega_v)} \rightarrow \\ \frac{g^2}{2\pi} \int_{-\pi}^{\pi} \frac{1}{E_m - \omega_c - n\omega_v + 2J\cos(k)} dk = -\frac{ig^2}{2\pi J} \oint \frac{dz}{(z - z_+)(z - z_-)} \end{aligned} \tag{5.40}$$

where:

$$z_{\pm} = -\gamma_n(E_m) \pm \sqrt{\gamma_n^2(E_m) - 1} \qquad \gamma_n(E_m) = \frac{E_m - (\omega_c + n\omega_v)}{2J} \tag{5.41}$$

As we did in section 5.2, we have done a change of variables $z = e^{ik}$. We will consider two cases: First, if our energy E_m fulfils $|\gamma_n| > 1$ and using the same reasonings of the last section. It can be easily shown that $z_+ > 1$ (outside the unit circle) and $0 < z_- < 1$ (inside the unit circle). Thus, the integral is equal to the residue $2\pi i Res(z_-)$:

$$2\pi i Res(z_-) = 2\pi i \lim_{z \to z_-} (z - z_-) f(z) \quad \text{where: } f(z) = \frac{1}{(z - z_+)(z - z_-)} \tag{5.42}$$

Thus, we obtain:

$$S_n = -\frac{ig^2}{2\pi J} \oint \frac{dz}{(z - z_+)(z - z_-)} = \frac{g^2}{J} Res(z_-) = -\frac{g^2}{2J} \frac{1}{\sqrt{\gamma_n^2(E_m) - 1}} \tag{5.43}$$

Second , if $|\gamma_n| < 1$, we have:

$$z_{\pm} = -\gamma_n(E_m) \pm i\sqrt{1 - \gamma_n^2(E_m)} \equiv re^{i\alpha} \tag{5.44}$$

So, the poles $z_{\pm}$ are no longer real numbers. If we calculate their modulus r and their argument α, we obtain:

$$r = \gamma_n^2 + 1 - \gamma_n^2 = 1 \qquad \alpha = \arctan\left(\frac{\sqrt{1 - \gamma_n^2}}{\gamma_n}\right) \tag{5.45}$$

Therefore, our poles are two complex numbers, complex conjugate over the unit circle centered at the origin of coordinates. However, this is a delicate case. For example, if we study the case of $E_1 \approx 1.09$ [cf. figure 5.10a], we have two cases: $|\gamma_n| > 1$ for $n \leq 1$ and $|\gamma_n| < 1$ for $n = 0$. In the first case, the discrete sum S_n converges for $n \leq 1$ and matches with the integral (5.43), see figure 5.9a for the case $n = 1$. But, in the second case, the sum S_n does not converge for $n = 0$, see figure 5.9b. So, we use the integral (5.43) for $|\gamma_n| > 1$ and the discrete sum S_n for $|\gamma_n| < 1$, since it cannot be calculated using the integral method. Thus, we have to solve numerically the next equation in order to obtain the energies of the states E_m which are *bound* at $\lambda = 0$:

$$\Delta + m\omega_v - E_m + \frac{g^2}{2J}\left[\frac{1}{2N+1} \sum_{|\gamma_n|<1} \sum_{k=-N}^{N} \frac{1}{\gamma_n(E_m) + \cos\left(2\pi k/(2N+1)\right)} - \sum_{|\gamma_n|>1} \frac{|D_{n\tilde{m}}|^2}{\sqrt{\gamma_n^2(E) - 1}}\right] = 0 \tag{5.46}$$

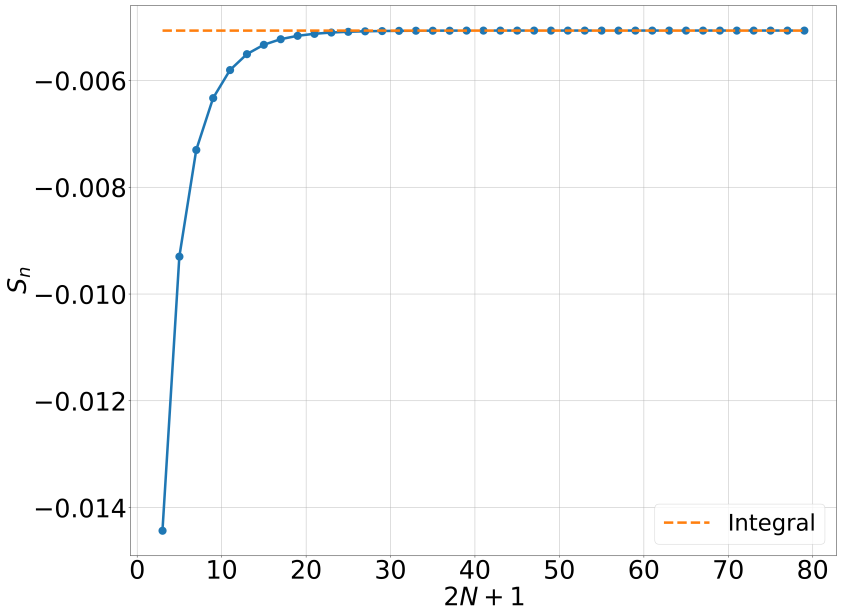

(a)

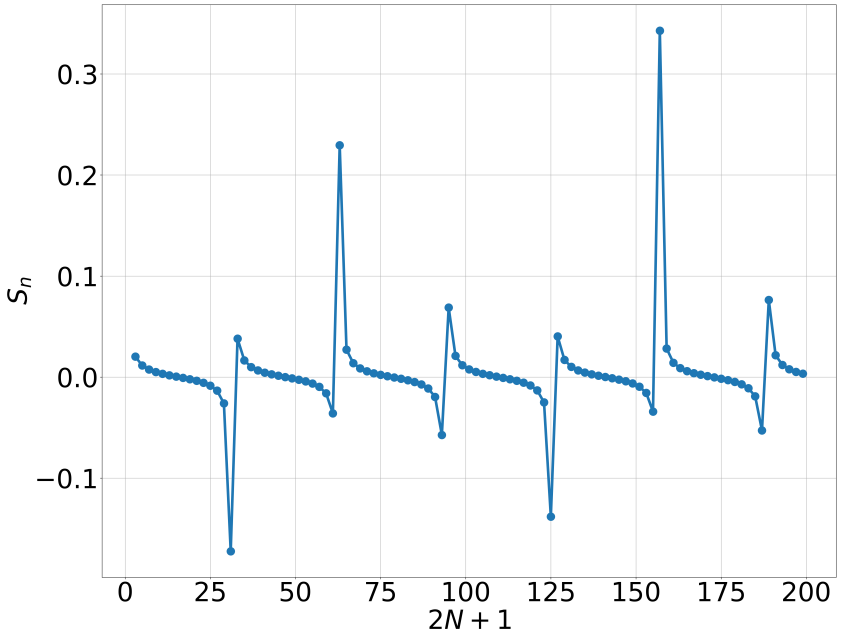

(b)

Figure 5.9: (a) Sum S_n versus the number of sites $2N+1$ for $n=1$ and $m=1$. (b) The same case with $n=0$. Parameters: $\omega_v = 0.1$, $J=1$, $\omega_v = 0.1$, $\omega_c = 3.05$, $\Delta = 1$, $g = 0.05$, $N_{phon} = 20$ and $2N+1 = 81$.

We can see the comparison between the numerical result using equation (5.46) and the exact diagonalization method for the first three *bound states* E_n (*bound* at $\lambda = 0$) in the figure 5.10b:

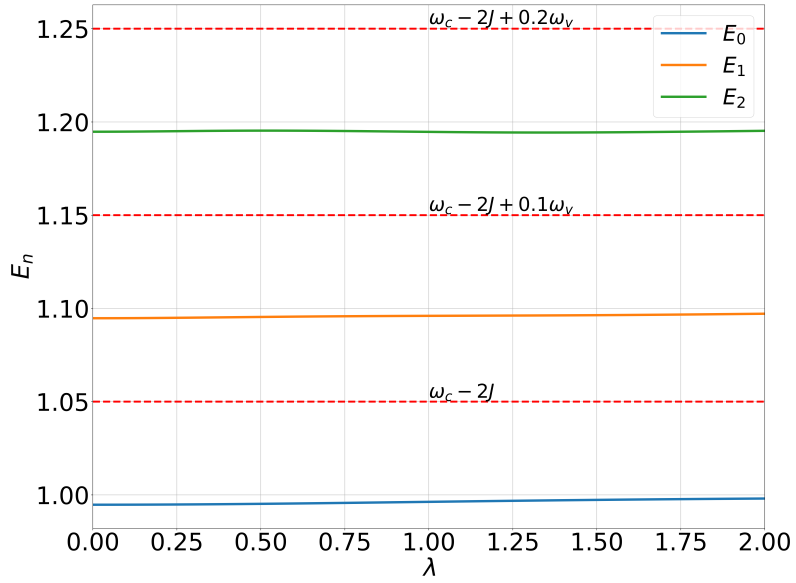

(a)

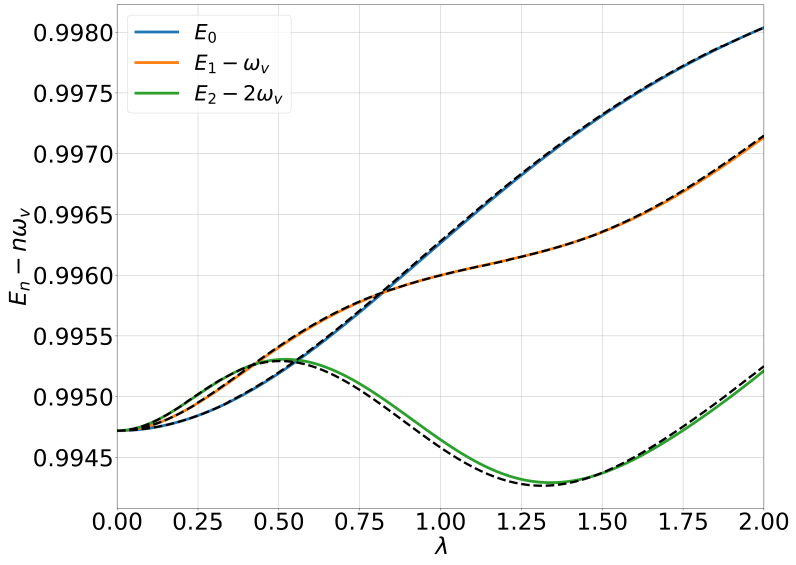

(b)

Figure 5.10: (a) *Bound state* energies E_0, E_1 and E_2 with 0, 1 and 2 phonons as a function of λ. (b) *Bound state* energies E_0, $E_1 - \omega_v$ and $E_2 - 2\omega_v$ with 0, 1 and 2 phonons as a function of λ. The coloured lines correspond to the exact diagonalization calculus and the black dashed lines the numerical result obtain from equation (5.46). Parameters: $\omega_v = 0.1$, $J = 1$, $\omega_v = 0.1$, $\omega_c = 3.05$, $\Delta = 1$, $g = 0.05$, $N_{phon} = 20$ and $2N + 1 = 81$.

The physical reason because we need to use the discrete sum instead the integral result is the longitude of the chain of cavities. We could use the integral result in the case of the poles over the integration path. However, it gives us the result of the self-energy for an infinitely long chain. As, we are using moderate long chains and we want to compare the exact diagonalization result with the "analytical" one, we have to use the discrete sum. The way to simulate an infinitely long chain would be to put some absorption at the limits of the chains. Thus, we would avoid the reflexion of the propagating photons and the formation of stationary waves.

In a nutshell, we have obtained the behaviour of the *bound states* of the system as a function of the matter-phonon coupling λ. Only the *bound state* of minimum energy keeps its localized behaviour. The rest of the *bound states* that would appear at $\lambda = 0$ become propagating states for $\lambda > 0$, see figure 5.8. Furthermore, we have obtained an approximate expression for these eigenstates [cf. equation (5.32)] and an equation (5.46) to get their energy numerically.

Chapter 6

Conclusions

Throughout this thesis, we have studied some aspects of the field of the *molecular cavity QED*. In particular, the influence of the matter-phonon coupling λ and the *ultrastrong* effects of a system formed by a molecule embedded in a electromagnetic cavity. Thus, we have covered the state of the art in the field of *cavity QED* and the main techniques in the chapter 1. Then, we have studied the energy spectrum of the *Holstein-Quantum-Rabi* (HQR) model (1.35) in the chapter 2. Continuing with the study of the dynamics of the system: the *Rabi oscillations*, considering different channels for energy loss, in the chapter 3. Afterwards, in chapter 4, we have calculated the noise spectrum and study what effect the counterrotating terms have on it. Finally, we have studied the *bound states* that appear when we embed a molecule in a waveguide [cf. chapter 5]. In the following sections, we sum up the main results and conclusions obtained throughout these chapters.

6.1 Energy spectrum

In the chapter 2, we studied the energy spectrum of the HQR model (1.35). Thus, we distinguished two subspaces for low energies. One formed by the phonon replicas of the ground state of the light-matter *Rabi* model (1.2) (red curves, the ground state subspace) and the other the phonon replicas of the eigenstates that come from the light-matter polaritons of the *Rabi* model (black curves, the polariton subspace), recall figure 2.2.

At ***bare resonance*** ($\omega_c = \Delta = 1$), we also obtained an *effective Rabi* model (2.15) which reproduces very well the energy spectrum of the HQR model [cf. figure 2.3] in the polariton sector. In this effective model, the light-

matter *Jaynes-Cummings* polaritons[1] and the phonons take the role as matter excitations and photons respectively. But, we obtained some differences with respect to the HQR model (1.35). The full HQR model does not conserve the parity (2.16) while the *effective Rabi* model does (2.15). Thus, the *effective Rabi* model (2.15) presents crossings instead of the proper HQR (1.35) anticrossigns in the energy spectrum at ***bare resonance***.

These spectrum anticrossings are due to the counterrotating terms. Although, we are at ***bare resonance*** ($\Delta = \omega_c$) the counterrotating terms produce a shift $-\delta_{BS}$ [cf. (2.26)] in the photon energy ω_c at second order of perturbation theory in the HQR model. This takes the system out-of-resonance when the effective[2] light-matter coupling is of the same order as the correction δ_{BS} (when $\lambda \gtrsim 2$). Knowing the value of this shift allow us to calculate the corrected resonance condition, the ***dressed resonance*** ($\Delta = \omega_c - \delta_{BS}$). In general, the HQR model has anticrossings in the energy spectrum and does not conserve the parity in the representation of the *effective Rabi* model. However, we have found that the parity is conserved and we have crossings[3] when the HQR model is at ***dressed resonance*** [cf. figures 2.7 and 2.8b]. In order to do that we change the value of ω_c to fulfill the new resonance condition: $\Delta = \omega_c - \delta_{BS}(\omega_c, \Delta, \omega_v, \lambda)$.

On the other hand, at ***bare resonance***, we improved our *effective Rabi* model (2.15) in order to include the anticrossings and the non-conservation of parity (2.16) observed in the HQR model at *bare resonance* ($\Delta = \omega_c$). In order to do that task, we used again perturbation theory to second order. Using the *Shrieffer-Wolff* transformation [cf. equation (2.41)], we added an extra term $\propto \sigma_x$ to our *effective Rabi* Hamiltonian (2.15). Thus, this new effective model (2.41) includes the anticrossings in the spectrum and does not conserves the parity as the HQR does at *bare resonance*, see figures 2.9 and 2.10.

Finally, we obtained approximate analytical expressions (2.52-2.54) for the energy levels of the polariton sector of the HQR model (1.35). In order to do that we obtained a third model that could be diagonalized. This is the *effective Jaynes-Cummings* Hamiltonian (2.50), obtained after a Polaron transformation a other approximations.

[1] Mixed states of light and matter excitations

[2] The light matter coupling $g_{\text{eff}} = g\,\langle\tilde{n}|D(\lambda)|0\rangle$ weighted by the Franck-Condon factors.

[3] at least at first sight

6.2 Dynamics

In the next chapter 3, we focused on the dynamics of the system when we have one photon in the cavity at $t = 0$ and the system is at ***bare resonance*** $\Delta = \omega_c$. First, we studied the *Rabi oscillations* of the number of photons[4] $\langle \hat{a}^\dagger \hat{a} \rangle$ as a function of the coupling λ without considering energy losses. We obtained that the main *Rabi* frequency Ω_R comes from the exchange of energy between the two lowest energy levels in the polariton subspace $|\epsilon_0\rangle$ and $|\epsilon_1\rangle$.

In other words, it is in this polariton subspace where the dynamics take place where no energy losses are present. Thus, we have an approximate analytical function of the *Rabi* frequency $\Omega_R = \epsilon_1 - \epsilon_0$ as a function of λ [cf. equation (3.1)]. However, the system is out-of-resonance[5] for $\lambda \gtrsim 2$ and the analytical expression does not work, recall figure 3.3. As well, the *Rabi oscillations* are no longer complete, see figure 3.4. These are *ultrastrong effects* which disappear when the HQR is at ***dressed resonance*** using the *Bloch-Siegert* correction (2.26) obtained in chapter 2. Thus, we have obtained *ulstrastrong effects* in spite of the fact that $g \ll 0.1\Delta$. The reason is that the effective couplings $g_{eff}(\lambda)$ between states are of the same order of magnitude of the *Bloch-Siegert* correction δ_{BS} for $\lambda > 2$ due to the *Franck-Condon* factors, see figure 2.6.

Besides, there is more than one *Rabi* frequency for intermediate couplings $\lambda = 0.0 - 1.5$, see figure 3.7. These frequencies come from the energy exchanges between the energy levels of the polariton subspace. We also obtain some approximate expressions for the weights of the different frequencies as a function of λ. These analytical expressions only give us the qualitative behaviour of the *Rabi* frequencies as we saw in figure 3.10. Thus, we found that two frequencies, $\epsilon_1 - \epsilon_0$ and $\epsilon_2 - \epsilon_0$, take an important role in the dynamics, see figure 3.8.

The second part of the chapter 3 is devoted to energy losses in the dynamics using the *master equation* formalism. We have considered all three channels of losses: the photon leakage γ_{phot}, the exciton decay γ_{matt} and the phonon decay γ_{phon}. The conclusions of this section have been done with the HQR model at ***dressed resonace*** because the dynamics is simplified in that condition.

Thus, we find the photon losses produce an exponential decay $\propto \exp(-t\gamma_{phot}/2)$ in the excitations $\langle \hat{a}^\dagger \hat{a} \rangle (t)$ and $\langle \hat{\sigma}^+ \hat{\sigma}^- \rangle (t)$ with an additional factor $1/2$ in the exponent, see figure 3.17. This factor $1/2$ comes from the fact that we have *Rabi oscillations* and, in average, we have a photon in the cavity the half of

[4] The same for matter excitations, $\langle \hat{\sigma}^+ \hat{\sigma}^- \rangle$.

[5] Recall the *Bloch-Siegert* shift δ_{BS} produced by the counterrotaitng terms when the HQR model is at ***bare resonance*** ($\omega_c = \Delta$).

the time and the molecule exited the other half of the time. However, the exciton decay depends on λ and is renormalized by the *Franck-Condon* factors $|\langle m|\tilde{n}\rangle|^2$ between the phonon states of the ground and excited states of matter [cf. figure 3.13]. Thus, due to the exciton decay γ_{matt}, the number of photon $\langle\hat{a}^\dagger\hat{a}\rangle(t)$ and matter excitations $\langle\hat{\sigma}^+\hat{\sigma}^-\rangle(t)$ decay as in the case of the *Holstein* model with an initial state $|\psi(t=0)\rangle = |\uparrow \tilde{0}_{phon}\rangle$ but with an additional factor 1/2, see equation (3.13).

Then, in oder to get the transitions in the dynamics, we studied the *Lindblad* eigenspectrum. We found that the exciton decay γ_{matt} is responsible of the transitions $|\epsilon_0\rangle, |\epsilon_1\rangle \to |\downarrow 0_{phot} n_{phon}\rangle$ between the polariton and the ground state subspace.

Afterwards, we focus on the role of the phonon energy losses γ_{phon} in the dynamics. We also study the *Lindblad* eigenspectrum. These losses are responsible for the decay the system to the ground state of the polariton subspace: $|\epsilon_0\rangle$ [cf. figure 3.22]. Thus, when $\gamma_{phon} > \gamma_{matt},\ \gamma_{phot}$, we obtain another effect of the phonon losses. They extinguish the *Rabi oscillations* in the long term dynamics, see figure 3.19. In this case, we found that the system first decays to the eigenstate $|\epsilon_0\rangle$, from where, it decays to the ground state subspace $|\downarrow 0_{phot} n_{phon}\rangle$ in the long term dynamics.

Finally, we have to notice that the effective decay produced by the matter losses γ_{matt} depends on λ. Thus, the condition, to reach *strong coupling* regime, changes with λ when the matter losses dominate ($\gamma_{matt} \gg \gamma_{phot}\ \gamma_{phon}$). We have found that reaching the strong coupling regime requires a less lossy system when vibrations are considered, and that this condition becomes more stringent with increasing λ [cf. figure 3.23].

6.3 Noise spectrum and bound states

In chapter 4, we study the *ultrastrong effects* of the *noise spectrum* $S(\omega)$ of the HQR model for the case of $\gamma_{matt},\ \gamma_{phot} \gg \gamma_{phon}$. The peaks of the noise spectrum give us the transitions between the polariton and the ground state subspace, see figure 4.1. At ***bare resonance***, we obtained some *ultrastrong* effects: In the case of small energy losses, the position of the peaks is shifted since the counterrotating terms produce a shift in the energy spectrum [cf. figure 4.3], recall the *Bloch-Siegert* correction (2.26). Besides, the counterrotating terms produce an asymmetry in the *noise spectrum* of the two most important peaks, (see the inset of figure 4.5, where we compare the peak heights with and without the counterrotating terms). In the case of large energy losses, the counterrotating terms produce a change in the peak form, see figure 4.4.

However, we can only appreciate these effects for values of $\lambda > 2$, and when the system is out-of-resonance due to *ultrastrong* effects.

Furthermore, we obtained an approximate analytical expression for the *noise spectrum* $S(\omega)$, see equation (4.27), showing that at a qualitative level that the *Franck-Condon* factors are responsible for these *ultrastrong* effects. We have not studied in detail the energy losses in the *noise spectrum* or the role of the phonon channel of losses (aspects which can be explored in future work).

Finally, we embedded our system to the central site of a waveguide, see equation (5.26). In chapter 5, we studied the *bound states* which appear and their dependence with the matter-phonon coupling λ. We obtained an approximate expression for the *bound states* of the system, see equation (5.32). These states are *bound* at $\lambda = 0$. In other words, they are localized surrounding the emisor (two-level system) forming a "photon cloud". However, these states (with the exception of the lowest energy state) lose their localized character for $\lambda > 0$, see figure 5.7. These "*bound states*" hybridize with the propagating states of other energy bands losing their localized character. Also, we obtained the equation (5.46) which its numerical solutions give us the dependence with λ of the energies of these "*bound states*".

Chapter 7

Conclusiones

A lo largo de esta tesis hemos estudiado varios aspectos del campo conocido como *Electrodinámica Cuántica de cavidades con moléculas* o en inglés *molecular cavity QED*. En particular, la influencia del acoplo materia-vibración λ y de los efectos *ultrastorng* de una molécula dentro de una cavidad electromagnética. Así, cubrimos el estado del arte del campo de la *Electrodinámica Cuántica de cavidades* en el capítulo 1. Después, estudiamos el espectro de energías del modelo *Holstein-Quantum-Rabi* (HQR) (1.35) en el capítulo 2. Continuamos con el estudio de la dinámica del sistema: las *oscilaciones Rabi* y las pérdidas de energía en el capítulo 3. Tras ello, en el capítulo 4, calculamos el *espectro de ruido* (*noise spectrum*) y estudiamos algunos efectos *ultrastrong* presentes en él. Finalmente, estudiamos los *estados ligados* o *bound states* que aparecen cuando insertamos una molécula en una guía de ondas [cf. capítulo 5]. En las siguientes secciones vamos a resumir los principales resultados y conclusiones obtenidos a lo largo de todos estos capítulos.

7.1 Espectro de energías

En el capítulo 2, estudiamos el espectro de energías del modelo HQR (1.35). Así, distinguimos dos subespacios en el rango de bajas energías. El primero está formado por las réplicas de fonones del estado fundamental del modelo de *Rabi* luz-materia (1.2) (curvas rojas, el subespacio del estado fundamental). El segundo son los autoestados formados por las réplicas de fonones de los polaritones luz-materia del modelo de *Rabi* (curvas negras, el subespacio de los polaritones), véase figura 2.2.

Además de esto, en el caso de ***resonancia desnuda*** (*bare resonance*), obtuvimos un modelo de *Rabi efectivo* (2.15) el cuál reproduce muy bien el espectro de energías del modelo HQR en el subespacio de los polaritones [véase

figura 2.3]. En este modelo efectivo los polaritones[1] luz-materia del *Jaynes-Cummings* y los fonones toman respectivamente el papel que las excitaciones de materia y los fotones tienen en el modelo de *Rabi* (1.2). Sin embargo, obtenemos algunas diferencias con respecto al modelo HQR (1.35). El modelo HQR no conserva la paridad (2.16) mientras que el modelo *Rabi efectivo* (2.15) si que lo hace. Así, el modelo *Rabi efectivo* (2.15) tiene cruces en el espectro en vez de los anticruces propios del espectro de energías del modelo HQR en ***resonancia desnuda***.

Estos anticruces del espectro son debidos a los términos contrarrotantes. Aunque estemos en ***resonancia desnuda*** ($\Delta = \omega_c$), los términos contrarrotantes producen un "shift" $-\delta_{BS}$ [cf. (2.26)] en la energía del fotón ω_c a segundo orden de teoría de perturbaciones del model HQR. Esto lleva al sistema a estar fuera de resonancia cuando el acoplamiento efectivo[2] luz-materia es del mismo orden que la corrección δ_{BS} (cuando $\lambda \gtrsim 2$). Conociendo el valor de este "shift" nos permite calcular correctamente la condición de resonancia, la ***resonancia vestida*** (*dressed resonance*) $\Delta = \omega_c - \delta_{BS}$. En general, el modelo HQR tiene anticruces en el espectro de energías y no conserva la paridad en la representación del modelo *Rabi efectivo*. Sin embargo, hemos encontrado que la paridad se conserva y tenemos cruces de niveles de energía cuando el modelo HQR está en ***resonancia vestida*** [cf. figuras 2.7 y 2.8b]. Para ello cambiamos el valor de la frecuencia de los fotones ω_c para que satisfaciese la nueva condición de resonancia: $\Delta = \omega_c - \delta_{BS}(\omega_c, \Delta, \omega_v, \lambda)$.

Por otro lado, en ***resonancia desnuda***, mejoramos nuestro modelo *efectivo Rabi* (2.15) para que incluyese tanto los anticruces como la no conservación de la paridad (2.16) observada en el modelo HQR en ***resonancia desnuda*** ($\Delta = \omega_c$). Para ello volvimos a usar teoría de perturbaciones a segundo orden. Usando la transformación de *Shrieffer-Wolff* [cf. ecuación (2.41)], añadimos un término extra $\propto \sigma_x$ a nuestor modelo *efectivo Rabi* (2.15). Así, este nuevo modelo efectivo (2.41) incluye los anticruces del espectro de energías y no conserva la paridad. Tal y como ocurría con el modelo HQR en ***resonancia desnuda***, véanse figuras 2.9 y 2.10.

Finalmente, obtuvimos expresiones analíticas aproximadas (2.52-2.54) para los niveles de energía del subespacio de los polaritonesdel modelo HQR model (1.35). Para ello obtuvimos un tercer modelo que podía ser diagonalizado. Este es el Hamiltoniando del modelo *efectivo Jaynes-Cummings* (2.50), obtenido tras una transfomación de Polarón y varias aproximaciones.

[1] Estados formados por la mezcla de excitaciones de luz y de materia.

[2] Acoplamiento luz-materia $g_{\text{eff}} = g \langle \tilde{n}|D(\lambda)|0\rangle$ pesado por los factores Franck-Condon.

7.2 La dinámica

En el capítulo 3, nos centramos en la dinámica del sistema con un estado inicial con un fotón en la cavidad y el sistema en ***resonancia desnuda***, $\Delta = \omega_c$. En primer lugar, estudiamos las *oscilaciones Rabi* en el número de fotones[3] $\langle \hat{a}^\dagger \hat{a} \rangle$ en función del acoplo λ y sin considerar pérdidas de energía por el momento. Así, obtuvimos que la frecuencia *Rabi* más importante Ω_R proviene del intercambio de energía entre los dos autoestados de menor energía del subespacio de los polaritones, es decir $|\epsilon_0\rangle$ y $|\epsilon_1\rangle$.

En otras palabras, es en este subespacio donde la dinámica tiene lugar, cuando las pérdidas energéticas con el ambiente no están presentes. Así, tenemos una función analítica aproximada para la frecuencia *Rabi* $\Omega_R = \epsilon_1 - \epsilon_0$ en función del acoplo λ, [cf. ecuación (3.1)]. Sin embargo, recordemos que el sistema no está en resonancia[4] cuando $\lambda \gtrsim 2$. Obteniendo que esta expresión analítica ya no funciona, [véase la figura 3.3]. Así mismo, las *oscilaciones Rabi* no son completas, figura 3.4. Todos estos son efectos *ultrastrong* que desaparecen cuando estamos en condiciones de ***resonancia vestida***, usando la corrección *Bloch-Siegert* obtenida en el capítulo 2. Así, estamos obteniendo efectos *ulstrastrong* a pesar de que $g \ll 0.1\Delta$. La razón es que los acoplos efectivos $g_{eff}(\lambda)$ se hacen del orden de la corrección *Bloch-Siegert* δ_{BS} cuando $\lambda > 2$; debido a los factores *Franck-Condon*, véase la figura 2.6.

Además, observamos que aparecen más de una frecuencia *Rabi* en el caso de acoplos materia-vibraciones de valores intermedios $\lambda = 0.0 - 1.5$, véase la figura 3.7. Estas frecuencias provienen de los intercambios de energía entre los autoestados del subespacio de los polaritones. También obtuvimos algunas expresiones analíticas aproximadas de cómo cambia el peso de las diferentes frecuencias *Rabi* con el acoplo λ. Estas expresiones analíticas sólo nos dan la dependencia de estos pesos a un nivel cualitativo. Como vimos en la figura 3.10 [cf. figura 3.10]. Así, encontramos dos frecuencias, $\epsilon_1 - \epsilon_0$ y $\epsilon_2 - \epsilon_0$, toman un papel relevante en la dinámica, véase la figura 3.8.

La segunda parte del capítulo 3 está dedicada a las pérdidas energéticas en la dinámica, usando el formalismo de la *ecuación maestra*. Hemos considerado tres canales de pérdidas: las pérdidas de fotones γ_{phot}, las pérdidas de excitaciones de materia (exciton decay) γ_{matt} y el decaimiento en los fonones γ_{phon}. Las conclusiones de esta sección se han hecho con el modelo HQR en ***resonancia vestida*** debido a que presenta una dinámica más sencilla.

[3] Obtuvimos idénticos resultados en el caso de las excitaciones de materia $\langle \hat{\sigma}^+ \hat{\sigma}^- \rangle$.

[4] Recuérdese que el shift *Bloch-Siegert* δ_{BS} producido por los términos contrarrotantes cuando el modelo HQR está en ***resonancia desnuda*** ($\omega_c = \Delta$).

Primeramente, encontramos que las pérdidas de fotones producen un decaimiento exponencial proporcional a $\propto \exp(-t\gamma_{phot}/2)$ en los valores esperados del número de fotones $\langle \hat{a}^\dagger \hat{a} \rangle (t)$ y de excitaciones de materia $\langle \hat{\sigma}^+ \hat{\sigma}^- \rangle (t)$ con un factor adicional $1/2$ en el exponente, véase la figura 3.17. Este factor $1/2$ proviene del hecho de que tenemos *oscilaciones Rabi* y, en promedio, tenemos un fotón en la cavidad la mitad del tiempo y la molécula excitada la otra mitad del tiempo. Por otro lado, el decaimiento producido por las pérdidas de materia (exciton decay) depende del acoplo λ y está renormalizado por los factores de *Franck-Condon* $|\langle m|\tilde{n}\rangle|^2$ entre estados de fonones con la materia excitada y en el estado fundamental [véase la figura 3.13]. Así el número de fotones $\langle \hat{a}^\dagger \hat{a} \rangle (t)$ y de excitaciones de materia $\langle \hat{\sigma}^+ \hat{\sigma}^- \rangle (t)$ decaen de manera equivalente a como lo harían en el modelo de *Holstein* con un estado inicial $|\psi(t=0)\rangle = |\uparrow \tilde{0}_{phon}\rangle$ pero con un factor adicional $1/2$, véase ecuación (3.13).

Luego, para analizar las transiciones entre estados que se producen en la dinámica, analizamos el espectro del *Lindbladiano*. Encontramos que las pérdidas en la materia γ_{matt} son responsables de las transiciones $|\epsilon_0\rangle$, $|\epsilon_1\rangle \rightarrow |\downarrow 0_{phot} n_{phon}\rangle$ entre los subespacios del estado fundamental y los polaritones.

Tras ello, nos centramos en el papel que tienen las pérdidas en el canal de fonones γ_{phon} en la dinámica. Estudiando también el espectro del *Lindbladiano*. Estas pérdidas son las responsables del decaimiento al estado fundamental del subespacio de los polaritones: $|\epsilon_0\rangle$ [véase figura 3.22]. Cuando $\gamma_{phon} > \gamma_{matt},\ \gamma_{phot}$, obtenemos otro efecto de las pérdidas de fonones: extinguen las *oscilaciones Rabi* en la dinámica a largo plazo, véase la figura 3.19. Así, encontramos que si $\gamma_{phon} > \gamma_{matt},\ \gamma_{phot}$ primero las perdidas γ_{phon} decaen el sistema al autoestado $|\epsilon_0\rangle$ y luego el resto de pérdidas lo hacen decaer al subespacio del fundamental $|\downarrow 0_{phot} n_{phon}\rangle$.

Finalmente, debido a que el decaimiento producido por las pérdidas de materia γ_{matt} depende de λ. También depende la condición para alcanzar el régimen de *strong coupling* cuando las pérdidas de materia son las dominantes ($\gamma_{matt} \gg \gamma_{phot}\ \gamma_{phon}$). Obteniendo que para alcanzar el régimen de *strong coupling* se requiere un sistema con menores pérdidas cuando las vibraciones son consideradas y, así, la condición de *strong coupling* se vuelve más exigente [cf. figura 3.23].

7.3 Espectro de ruido y estados ligados

En el capítulo 4, estudiamos los efectos *ultrastrong* en el espectro de ruido del sistema en el caso de $\gamma_{matt},\ \gamma_{phot} \gg \gamma_{phon}$. Así, los picos del espectro de ruido nos dan las transiciones entre estados del subespacio de los polaritones y del fundamental, véase la figura 4.1. En condiciones de ***resonancia desnuda***, obtuvimos algunos efectos *ultrastrong*: En el caso de pérdidas de energía pequeñas, la posición de los picos es desplazada debido a que los términos contrarrotantes producen un "shift" en el espectro de energías [véase la figura 4.3], recuérdese la corrección *Bloch-Siegert* (2.26). Además, los términos contrarrotantes producen una asimetría en la altura de los dos picos más importantes (véase el inset de la figura 4.5 donde comparamos la altura de los picos teniendo en cuenta o no los términos contrarrotantes). Por otro lado, en el caso de pérdidas de energía grandes, los términos contrarrotantes producen un cambio en la forma del pico, véase la figura 4.4. Sin embargo, sólo podemos apreciar estos efectos a valores de $\lambda > 2$, y cuando el sistema no está en resonancia debido a efectos *ultrastrong*.

Además, conseguimos una expresión analítica aproximada para el espectro de ruido $S(\omega)$, véase la ecuación (4.27), mostrando a nivel cualitativo que los factores *Franck-Condon* son responsables de estos efectos *ultrastrong*. No hemos podido estudiar la dependencia en detalle del espectro de ruido con las pérdidas del sistema ni el papel que juegan las pérdidas de fonones γ_{phon} en ella. Estos aspectos pueden ser explorados en trabajos futuros.

Finalmente, embebimos nuestro sistema en el sitio centran de una guía de ondas, véase el Hamiltoniano (5.26). En el capítulo 5, estudiamos los estados ligados o *bound states* que aparecen en torno al emisor y su dependencia con el acoplo materia-vibraciones λ. Obteniendo una expresión aproximada para los estados ligados del sistema, véase la ecuación (5.32). Estos son estados ligados a $\lambda = 0$. En otras apalabras, están localizados en torno al emisor (sistema de dos niveles) formando una "nube de fotones". Sin embargo, estos estados (con la excepción del estado de menor energía) pierden este carácter localizado cuando $\lambda > 0$, véase la figura 5.7. Estos "*bound states*" se hibridizan con los estados propagantes de otras bandas de energía perdiendo así su carácter localizado. También, obtuvimos la ecuación (5.46) cuya resolución numérica nos da la dependencia con λ de las energías de estos "*bound states*".

Appendices

Appendix A

Quantization of Electromagnetic field

A.1 Electromagnetic Field Quantization

In this section, we are going to quantize the electromagnetic classical theory, following the book of Schleich [25].

Let us write down Maxwell's equations:

$$\vec{\nabla} \cdot \vec{B} = 0 \tag{A.1}$$

$$\vec{\nabla} \times \vec{E} = -\frac{\partial \vec{B}}{\partial t} \tag{A.2}$$

$$\vec{\nabla} \cdot \vec{E} = \frac{\rho}{\epsilon_o} \tag{A.3}$$

$$\vec{\nabla} \times \vec{B} = \frac{1}{c^2} \frac{\partial \vec{E}}{\partial t} + \mu_0 \vec{j} \tag{A.4}$$

with $c = 1/\sqrt{\epsilon_o \mu_o}$ is the light velocity, ϵ_o the electric permitivity, μ_o the magnetic magnetic permeability in the vacuum; and the magnetic flux density $\vec{B}$, electric field $\vec{E}$, the charge density ρ and the current $\vec{j}$ are functions of position $\vec{r}$ and time t.

The electromagnetic field can be described using a scalar potential Φ and a magnetic vector potential $\vec{A}$:

$$\vec{E} = -\vec{\nabla}\Phi - \frac{\partial \vec{A}}{\partial t} \tag{A.5}$$

$$\vec{B} = \vec{\nabla} \times \vec{A} \tag{A.6}$$

where the scalar potential Φ and the magnetic vector potential $\vec{A}$ are functions of $\vec{r}$ and t. Thus, expressing the Maxwell's equations in terms of the potentials leave us only two equations (A.3) and (A.4).

Besides, the equations of $\vec{E}$ and $\vec{B}$ (equations (A.5) and (A.6)) are invariant under a *gauge transformation*:

$$\vec{A}' \equiv \vec{A} + \vec{\nabla}\Lambda \tag{A.7}$$

$$\Phi' \equiv \Phi - \frac{\partial \Lambda}{\partial t} \tag{A.8}$$

where $\Lambda(\vec{r}, t)$ is an arbitrary function of $\vec{r}$ and t. Thus, we obtain the same magnetic and electric fields with different scalar and vector potentials. So, we have an additional degree of freedom when we work with the potentials $\Phi(\vec{r}, t)$ and $\vec{A}(\vec{r}, t)$. Therefore, we can select the potentials in order to simplify the Maxwell's equations(A.3) and (A.4). For convenience, we are going to choose the *Coulomb Gauge* which imposes that:

$$\vec{\nabla} \cdot \vec{A} = 0 \tag{A.9}$$

Thus, invoking the Coulomb Gauge and the potentials (equations (A.5) and (A.6)) in the third and fourth equations ((A.3) and (A.4)), we obtain:

$$\vec{\nabla}^2 \vec{A} - \tfrac{1}{c^2} \tfrac{\partial^2 \vec{A}}{\partial t^2} = \vec{\nabla}\left(\tfrac{1}{c^2} \tfrac{\partial \Phi}{\partial t} \right) - \mu_o \vec{j} \tag{A.10}$$

$$-\vec{\nabla}(\vec{\nabla}\Phi) = \tfrac{\rho}{\epsilon_o} \tag{A.11}$$

In our case, we are going to quantize the electromagnetic field without charges and currents ($\rho = 0$, $\vec{j} = 0$). Thus, in this case $\Phi = 0$ and (A.10) reads:

$$\vec{\nabla}^2 \vec{A} - \frac{1}{c^2} \frac{\partial^2 \vec{A}}{\partial t^2} = 0 \tag{A.12}$$

In order to solve the wave equation (A.12), we are going to use separation of variables. Thus, the vector potential $\vec{A}$ can be written as the product of an arbitrary function of time $q(t)$, an arbitrary vector function $\vec{v}(\vec{r})$ of position $\vec{r}$ and a constant Υ which we will select latter:

$$\vec{A} = \Upsilon q(t) \vec{v}(\vec{r}) \tag{A.13}$$

Using separation of variables, we arrive to the Helmholtz equation for $\vec{v}(\vec{r})$ and the equation of an harmonic oscillator for $q(t)$:

$$\vec{\nabla}^2 \vec{v}(\vec{r}) + \vec{k}^2 \vec{v}(\vec{r}) = 0 \tag{A.14}$$

$$\ddot{q}(t) + \Omega^2 q(t) = 0 \tag{A.15}$$

where the frequency $\Omega = c|\vec{k}|$ and $\vec{k}$ is the wave vector determined by the boundary conditions, which has units of $(\text{length})^{-2}$. Besides, the Coulomb Gauge has to be fulfilled in every point of space. Thus, the Coulomb gauge implies that $\vec{\nabla} \cdot \vec{v}(\vec{r}) = 0$, or in other words, the field only has transversal components.

The specific boundary conditions of our problem also imply a discretization in the wave vector $\vec{k}$. For example in a box with conducting walls, this discretization comes from the specific geometry of our resonator or cavity. Therefore, there is a discrete set of mode functions $\vec{v}_l(\vec{r})$ where l is an integer (c.f. [25] for more details). We also impose an orthonormality condition over this mode functions $\vec{v}_l(\vec{r})$:

$$\int d^3\vec{r} \;\; \vec{v}_l(\vec{r})\vec{v}_{l'}(\vec{r}) = \delta_{ll'} \tag{A.16}$$

where $\delta_{ll'}$ is the Kronecker delta. This relation connects the normalization constant $\mathcal{N}$ of $\vec{v}(\vec{r})$ with the cavity volume V and brings an additional numerical factor. This factor can be "absorved" with the volume V in a new variable called the effective mode volume V_l. So, we can define a dimensionless $\vec{v}_l(\vec{r})$ function called $\vec{u}_l(\vec{r})$:

$$\vec{v}_l(\vec{r}) = \frac{1}{\sqrt{V_l}}\vec{u}_l(\vec{r}) \tag{A.17}$$

Thus, if the resonator geometry allows to get the modes $\vec{v}_l(\vec{r})$, the magnetic vector potential $\vec{A}$ can be expanded in many discrete modes:

$$\vec{A}(\vec{r},t) = \sum_l \frac{1}{\sqrt{\epsilon_o V_l}} q_l(t)\vec{u}_l(\vec{r}) \tag{A.18}$$

where the constant Υ takes the form of $1/\sqrt{\epsilon_o V_l}$ for convenience and $q_l(t)$ are the equivalent mode functions for the time dependent function $q(t)$.

In order to quantize the electromagnetic field, we need its Hamiltonian. This is obtained from classical energy of the electromagnetic field in the resonator:

$$\mathcal{H} = \int d^3\vec{r} \;\; \left(\frac{1}{2}\epsilon_o \vec{E}^2(\vec{r},t) + \frac{1}{2}\mu_o \vec{H}^2(\vec{r},t)\right) \tag{A.19}$$

where the relation between the magnetic flux density $\vec{B}$ and the magnetic field is $\vec{H} = \frac{1}{\mu_0}\vec{B}$. Recalling the relations[1]:

$$\vec{E}(\vec{r},t) = -\frac{\partial \vec{A}}{\partial t} \qquad \vec{H}(\vec{r},t) = \frac{1}{\mu_o}\vec{\nabla} \times \vec{A} \tag{A.20}$$

and the equation (A.18). After some algebra one obtains (c.f. [25]):

$$\mathcal{H} = \sum_l \left(\frac{1}{2}\dot{q}_l^2(t) + \frac{1}{2}\Omega_l^2 q_l^2\right) \tag{A.21}$$

[1]Inside the resonator there is no charge ($\rho = 0$) or current ($\vec{j} = 0$), so, Poisson equation implies: $\Phi = 0$.

where the energy of the system is the sum of the energies of each mode which are harmonic oscillators. Defining the following variables:

$$q_l = \sqrt{\frac{\hbar}{2\Omega_l}}(a_l + a_l^*) \qquad p_l = \frac{1}{i}\sqrt{\frac{\hbar\Omega_l}{2}}(a_l - a_l^*) \tag{A.22}$$

where q_l and p_l are the generalized position and momentum ($p_l = \dot{q}_l$), we obtain:

$$\mathcal{H} = \sum_l \frac{1}{2}\hbar\Omega_l(a_l^* a_l + a_l a_l^*) \tag{A.23}$$

Up to here, we have used a classical approach. Quantization is performed by (i) changing the classical variables into quantum operators:

$$a_l \longrightarrow \hat{a}_l \qquad a_l^* \longrightarrow \hat{a}_l^\dagger$$

such thus the quantum position and momentum operator for each mode are:

$$\hat{q}_l = \sqrt{\frac{\hbar}{2\Omega_l}}(\hat{a}_l + \hat{a}_l^\dagger) \qquad \hat{p}_l = \frac{1}{i}\sqrt{\frac{\hbar\Omega_l}{2}}(\hat{a}_l - \hat{a}_l^\dagger) \tag{A.24}$$

and (ii) imposing the commutation relations:

$$[\hat{q}_l, \hat{p}_l] = i\hbar\delta_{ll'} \qquad [\hat{a}_l, \hat{a}_{l'}^\dagger] = \delta_{ll'} \qquad [\hat{a}_l, \hat{a}_{l'}] = [\hat{a}_l^\dagger, \hat{a}_{l'}^\dagger] = 0 \tag{A.25}$$

We finally obtain:

$$\boxed{\hat{\mathcal{H}} = \sum_l \hbar\Omega_l\left(\hat{a}_l^\dagger\hat{a}_l + \frac{1}{2}\right)} \tag{A.26}$$

Also, we can substitute the relations (A.24) into (A.18) and we obtain (in the Heisenberg's picture):

$$\dot{\hat{a}}_l = \frac{i}{\hbar}[\hat{\mathcal{H}}, \hat{a}_l] \quad \longrightarrow \quad \hat{a}_l(t) = \hat{a}_l(0)e^{-i\Omega_l t} \tag{A.27}$$

$$\hat{A}(\vec{r}, t) = \sum_l \sqrt{\frac{\hbar}{2\epsilon_o V_l \Omega_l}}\vec{u}_l(\vec{r})(\hat{a}_l(t) + \hat{a}_l^\dagger(t)) \tag{A.28}$$

Using the relations (A.20), the expressions for the quantized electric and magnetic fields are:

$$\hat{\vec{E}}(\vec{r}, t) = \sum_l \sqrt{\frac{\hbar\Omega_l}{\epsilon_o V_l}}\vec{u}_l(\vec{r})\frac{i}{\sqrt{2}}(\hat{a}_l(t) - \hat{a}_l^\dagger(t)) \tag{A.29}$$

$$\hat{\vec{H}}(\vec{r}, t) = \frac{1}{\mu_o}\sum_l \sqrt{\frac{\hbar}{2\epsilon_o V_l \Omega_l}}(\vec{\nabla} \times \vec{u}_l(\vec{r}))(\hat{a}_l(t) + \hat{a}_l^\dagger(t)) \tag{A.30}$$

In conclusion, starting from the Mawell's equations, we have obtained the quantum Hamiltonian of the electromagnetic field in vacuum ($\rho = 0$ and $\vec{j} = 0$). In the appendix B, we can see how to get the matter-light coupling in a quantum framework and the *Rabi* Hamiltonian (1.2).

Appendix B

Light-Matter coupling and Rabi model

In this appendix we couple matter to light and present the derivation of the *Rabi* Hamiltonian form first principles.

First, we are going to see how to express the coupling between an atom (a proton and an electron) and the electromagnetic field. In other words, a Hamiltonian which gives us the interaction between light and matter (In this appendix we will follow the book of Nolting [34], Schleigh [25] and Zueco's [24] as main references). As a first step, it is well known that the dynamics of a free particle of mass m is given by the *Dirac equation*, a relativistic version of the *Schrödinger equation*, and the corresponding *Dirac's Hamiltonian* H_D:

$$i\hbar\frac{\partial}{\partial t}\psi = H_D\psi \tag{B.1}$$

where the Hamiltonian H_D is:

$$H_D = c\ \hat{\alpha}\cdot\vec{p} + \hat{\beta}\ mc^2 \tag{B.2}$$

where the wave function $\psi = (\psi_1, \psi_2, \psi_3, \psi_4)^T$ is a four-component spinor and the operators $\hat{\alpha}$ and $\hat{\beta}$ are:

$$\hat{\alpha} = \begin{pmatrix} 0 & \vec{\sigma} \\ \vec{\sigma} & 0 \end{pmatrix} \qquad \hat{\beta} = \begin{pmatrix} \mathbb{1}_2 & 0 \\ 0 & \mathbb{1}_2 \end{pmatrix} \tag{B.3}$$

where $\vec{\sigma} = (\sigma_x,\ \sigma_y,\ \sigma_z)$ are the Pauli matrices. Now, we can add the coupling with the electromagnetic field using the "minimal coupling" method. This is the standard method in which a particle of mass m and charge e is coupled to a field described by a vector magnetic field $\vec{A}(\vec{r},t)$ and a scalar potential $\Phi(\vec{r},t)$. This procedure consists of changing the canonical momentum $\vec{p}$ for the momentum $\vec{p} - e\vec{A}$ and adding the potential $V(\vec{r}) = e\Phi(\vec{r},t)$ to the Hamiltonian:

$$H_D = c\ \hat{\alpha}\cdot(\vec{p} - e\vec{A}) + \hat{\beta}\ mc^2 + e\Phi \tag{B.4}$$

This last Hamiltonian gives us the dynamics of a relativistic particle of mass m coupled to the electromagnetic field. However, we are interested in the non-relativistic limit $v \ll c$. In this limit, it can be shown (c.f. Nolting [34]) that the *Dirac's Hamiltonian* has the following form:

$$H_P = \frac{1}{2m}(\vec{p} - e\vec{A})^2 + e\Phi - \frac{e}{2m}\vec{\sigma}\cdot\vec{\nabla}\times\vec{A} \tag{B.5}$$

We will consider a spinless neutral atom. So, the term proportional to $\propto \vec{\nabla}\times\vec{A} \propto \vec{B}$ can be neglected. The atom will consist simply of a proton of mass m_p and an electron of mass m_e coupled to the electromagnetic field using (B.5). Thus (c.f. [25]), we can change to the coordinate system of the center of mass obtaining that the Hamiltonian of the atom coupled to a electromagnetic field is:

$$\hat{H} = \frac{\vec{P}^2}{2M} + \frac{1}{2\mu}[\vec{p} - e\vec{A}(\vec{R},t)]^2 - \frac{1}{4\pi\epsilon_0}\frac{e^2}{|\vec{r}|} \tag{B.6}$$

where $M = m_p + m_e$ is the total mass, $\vec{P}$ and $\vec{R}$ the momentum and position of the center of mass, $\mu = m_e m_p/(m_p + m_e)$ the reduced mass, $\vec{p} = \mu\dot{\vec{r}}$ is the relative momentum and $\vec{r} = \vec{r}_p - \vec{r}_e$ relative position between the electron and the proton. We have also added the Coulomb potential $V(\vec{r})$ which depends on the relative distance $|\vec{r}|$. Besides, we have used the *dipole approximation* which ensures that the vector potential $\vec{A}$ only depends on the center-of-mass coordinate, see [25].

It is convenient to work in the *Coulomb gauge* ($\vec{\nabla}\cdot\vec{A} = 0$). Then, the momentum and magnetic vector operators commute $[\hat{\vec{p}}, \vec{A}(\hat{\vec{r}},t)] = 0$. Thus, we can rewrite the last Hamiltonian as:

$$\hat{H} = \frac{\hat{\vec{P}}^2}{2M} + \hat{H}_{atom} - \frac{e}{\mu}\vec{A}(\hat{\vec{R}},t)\hat{\vec{p}} + \frac{e^2}{2\mu}\vec{A}^2(\hat{\vec{R}},t) + \hat{\mathcal{H}} \tag{B.7}$$

where we have added the quantized Hamiltonian of the free electromagnetic field $\hat{\mathcal{H}}$:

$$\hat{\mathcal{H}} = \sum_l \hbar\Omega_l\left(\hat{a}_l^\dagger\hat{a}_l + \frac{1}{2}\right) \tag{B.8}$$

where H_{atom} is known as the atom Hamiltonian:

$$H_{atom} = \frac{\vec{p}}{2\mu} + V(\vec{r}) \tag{B.9}$$

where $V(\vec{r})$ is the *Coulomb* potential. This Hamiltonian (B.7) contains many energy levels of the atom ($\hat{H}_{atom}$) and a quantized electromagnetic field with many modes of radiation. We are going to simplify this model to allow only two levels in our atom and a single mode of radiation. Moreover, we will

neglect the center-of-mass motion and the zero point energy in the free field Hamiltonian $\hat{\mathcal{H}}$. In this scheme, the model is:

$$\hat{H} = \hbar\omega_c \hat{a}^\dagger \hat{a} + \hat{H}_{atom} - \frac{e}{\mu}\vec{A}(\hat{\vec{R}}, t)\hat{\vec{p}} + \frac{e^2}{2\mu}\vec{A}^2(\hat{\vec{R}}, t) \tag{B.10}$$

Let us know consider the situation where only two atomic levels are at resonance with the field. These two atomic eigenstates are one particular excited state $|\uparrow\rangle$ (with energy $E_\uparrow = \hbar\omega_\uparrow$) and the ground state $|\downarrow\rangle$ (with energy $E_\downarrow = \hbar\omega_\downarrow$, where $E_\uparrow > E_\downarrow$). So, we can write $\hat{H}_{atom}$ as:

$$\hat{H}_{atom} = E_\uparrow |\uparrow\rangle \langle\uparrow| + E_\downarrow |\downarrow\rangle \langle\downarrow| = \hbar\Delta\ \hat{\sigma}^+\hat{\sigma}^- + \hbar\omega_\downarrow \tag{B.11}$$

where $\hbar\Delta = \hbar(\omega_\uparrow - \omega_\downarrow)$, it is the atomic transition energy. Neglecting the constant term, which corresponds just to a shift in the zero of energy, we finally obtain:

$$\hat{H}_{atom} = \hbar\Delta\hat{\sigma}^+\hat{\sigma}^- \tag{B.12}$$

Here, we have used the Pauli spin matrices which create or annihilate an excitation in the atom respectively:

$$\hat{\sigma}^+ = |\uparrow\rangle \langle\downarrow| = \begin{pmatrix} 0 & 1 \\ 0 & 0 \end{pmatrix} \qquad \hat{\sigma}^- = |\downarrow\rangle \langle\uparrow| = \begin{pmatrix} 0 & 0 \\ 1 & 0 \end{pmatrix} \tag{B.13}$$

where the used basis order is $\{|\uparrow\rangle\,,\ |\downarrow\rangle\}$.

Now, it is the turn of the interaction Hamiltonian $\hat{H}_{\vec{A}\cdot\vec{p}}$:

$$\hat{H}_{\vec{A}\cdot\vec{p}} = -\frac{e}{\mu}\vec{A}(\hat{\vec{R}}, t)\hat{\vec{p}} \tag{B.14}$$

First, we have to express our momentum operator $\hat{\vec{p}}$ in terms of the two-state basis $\{|\uparrow\rangle\,,\ |\downarrow\rangle\}$. Thus, we can relate the momentum operator $\hat{\vec{p}}$ with the position operator $\hat{\vec{r}}$ via [107][1]:

$$\hat{\vec{p}} = \mu\dot{\hat{\vec{r}}} = -\frac{i\hbar}{\mu}[\hat{\vec{r}}, \hat{H}_{atom}] \tag{B.15}$$

So, given two arbitrary eigenstates of $\hat{H}_{atom}$, we have the matrix element:

$$\langle n|\hat{\vec{p}}|m\rangle = -\frac{i\mu}{\hbar}(E_m - E_n)\langle n|\hat{\vec{r}}|m\rangle \tag{B.16}$$

where $n,\ m = \uparrow,\ \downarrow$. Next, we have to evaluate the matrix elements $\langle n|\hat{\vec{r}}|m\rangle$. In order to do that, we are going to use the eigenvectors of the position operator $\hat{\vec{r}}|\vec{r}\rangle = \vec{r}\,|\vec{r}\rangle$ and its closure relation:

$$\int d^3\vec{r}\,|\vec{r}\rangle \langle\vec{r}| = \mathbb{1} \tag{B.17}$$

[1] See chapter 20, section 20.5 of [107].

Thus, in terms of $\psi_n(\vec{r}) = \langle \vec{r}|n\rangle$ the diagonal terms are:

$$\langle n|\hat{\vec{r}}|n\rangle = \int d^3\vec{r}|\psi_n(\vec{r})|^2\vec{r} = 0 \tag{B.18}$$

due to the different parity of $|\psi_n(\vec{r})|^2$ (an even function of $\vec{r}$) and $\vec{r}$. However the off-diagonal terms are finite:

$$\langle \uparrow |\hat{\vec{p}}| \downarrow\rangle = i\mu\Delta \int d^3\vec{r}\psi^*_\uparrow(\vec{r})\vec{r}\psi_\downarrow(\vec{r}) \equiv \frac{i\mu\Delta}{e}\vec{d} \tag{B.19}$$

where we have identified that the integral is proportional to the transition dipole moment $\vec{d}$. Therefore, in the two-level basis, the momentum operator $\hat{\vec{p}}$ takes the following form:

$$\hat{\vec{p}} = \frac{i\mu\Delta}{e}(\vec{d}\hat{\sigma}^+ - \vec{d}^*\hat{\sigma}^-) \tag{B.20}$$

We also have to remember the equation (A.28) of the magnetic vector potential operator with a single mode of radiation is:

$$\hat{A}(\vec{R}, t) = \sqrt{\frac{\hbar}{2\epsilon_o V_m \omega_c}}\vec{u}(\hat{\vec{R}})(\hat{a}(t) + \hat{a}^\dagger(t)) \tag{B.21}$$

where V_m is the mode volume (related to the cavity volume) and ω_c the cavity frequency. So, gathering the equations (B.20) and (B.21) in the interaction Hamiltonian $\hat{H}_{\vec{A}\cdot\vec{p}}$ (B.14):

$$\hat{H}_{\vec{A}\cdot\vec{p}} = -i\Delta\sqrt{\frac{\hbar}{2\epsilon_0 V_m \omega_c}}(\vec{u}(\hat{\vec{R}}) \cdot \vec{d}\hat{\sigma}^+ - \vec{u}(\hat{\vec{R}})\vec{d}^*\hat{\sigma}^-)(\hat{a}(t) + \hat{a}^\dagger(t)) \tag{B.22}$$

Notice that $\vec{u}(\hat{\vec{R}}) \cdot \vec{d}$ is a complex number:

$$\vec{u}(\hat{\vec{R}}) \cdot \vec{d} = |\vec{u}(\hat{\vec{R}}) \cdot \vec{d}|e^{i\phi} \tag{B.23}$$

when we choose the phase value $\phi = \pi/2$, we find:

$$\hat{H}_{\vec{A}\cdot\vec{p}} = \hbar g(\hat{R})(\hat{\sigma}^+ + \hat{\sigma}^-)(\hat{a}(t) + \hat{a}^\dagger(t)) \tag{B.24}$$

where we have defined the light-matter coupling as:

$$g(\hat{\vec{R}}) \equiv \frac{\Delta}{\hbar}\sqrt{\frac{\hbar}{2\epsilon_o V_m \omega_c}}|\vec{u}(\hat{\vec{R}}) \cdot \vec{d}| \tag{B.25}$$

Now, it only remains to treat the $\vec{A}^2$ term in our Hamiltonian (B.10):

$$H_{\vec{A}^2} = \frac{e^2}{2\mu}\vec{A}^2(\hat{\vec{R}}, t) \tag{B.26}$$

This term is proportional to g^2 and usually it can be neglected. If it were needed to include it in the description, we can always include its effects through a Bogoliubov transformation [10, 45] of the photon degrees of freedom (notice the $H_{\vec{A}^2}$ does not involve matter operators), plus a renormalization of the parameters in the Hamiltonian. So, here we do not explicitely treat this term, and finally obtain the ***Quantum Rabi Hamiltonian*** (1.2) [5, 12]:

$$\boxed{\hat{\mathcal{H}}_{Rabi} = \omega_c \hat{a}^\dagger \hat{a} + \Delta \hat{\sigma}^+ \hat{\sigma}^- + g(\hat{\vec{R}})(\hat{\sigma}^+ + \hat{\sigma}^-)(\hat{a}^\dagger + \hat{a})} \tag{B.27}$$

where we have taken $\hbar = 1$. The *Jaynes-Paul-Cummings* Hamiltonian [15] (1963) is obtained when the counterrotating terms $\hat{\sigma}^+\hat{a}^\dagger + \hat{\sigma}^-\hat{a}$ are neglected:

$$\boxed{\hat{\mathcal{H}}_{JC} = \omega_c \hat{a}^\dagger \hat{a} + \Delta \sigma^+ \sigma^- + g(\hat{\vec{R}})(\sigma^- \hat{a}^\dagger + \sigma^+ \hat{a})} \tag{B.28}$$

Appendix C

Master equation calculations

C.1 Secular approximation

In this section, we are going to work within *Rotating Wave Approximation*. Also called *secular approximation*. We are going to follow the arguments given by Rivas' and Huelga's notes [90].

We start with equation (1.53), which describes the time evolution of the density matrix:

$$\tilde{\rho}_S(t) = \tilde{\rho}_S(0) + \varepsilon^2 \int_0^t du \sum_{\omega,\ \omega'} \sum_{\alpha,\ \beta} e^{i(\omega'-\omega)u} \Gamma^{(u)}_{\alpha\beta}(\omega) (\hat{A}_\beta(\omega)\tilde{\rho}_S(u)\hat{A}^\dagger_\alpha(\omega') - \hat{A}^\dagger_\alpha(\omega')\hat{A}_\beta(\omega)\tilde{\rho}_S(u)) \ + \ \text{h. c.} \tag{C.1}$$

Now, we can make a change of variables $v = \varepsilon^2 u$, obtaining:

$$\tilde{\rho}_S(\tau/\varepsilon^2) = \tilde{\rho}_S(0) + \int_0^\tau dv \sum_{\omega,\ \omega'} \sum_{\alpha,\ \beta} e^{i(\omega'-\omega)u} \Gamma^{(v/\varepsilon^2)}_{\alpha\beta}(\omega) (\hat{A}_\beta(\omega)\tilde{\rho}_S(v/\varepsilon^2)\hat{A}^\dagger_\alpha(\omega') - \hat{A}^\dagger_\alpha(\omega')\hat{A}_\beta(\omega)\tilde{\rho}_S(v/\varepsilon^2)) \ + \ \text{h. c.} \tag{C.2}$$

where $\tau = \varepsilon^2 t$. In this stage, we have to take the limit of weak coupling $\varepsilon \to 0$:

$$\tilde{\rho}_S(\tau) = \tilde{\rho}_S(0) + \lim_{\varepsilon\to 0} \int_0^\tau dv \sum_{\omega,\ \omega'} \sum_{\alpha,\ \beta} e^{i(\omega'-\omega)u} \Gamma^{(\infty)}_{\alpha\beta}(\omega) (\hat{A}_\beta(\omega)\tilde{\rho}_S(v)\hat{A}^\dagger_\alpha(\omega') - \hat{A}^\dagger_\alpha(\omega')\hat{A}_\beta(\omega)\tilde{\rho}_S(v)) \ + \ \text{h. c.} \tag{C.3}$$

where:

$$\lim_{\varepsilon\to 0}\tilde{\rho}_S(\tau/\varepsilon^2) = \lim_{\varepsilon\to 0} e^{iH_S\tau/\varepsilon^2}\rho_S(\tau/\varepsilon^2)e^{-iH_S\tau/\varepsilon^2} \equiv \tilde{\rho}_S(\tau) \tag{C.4}$$

Here, we have to use a mathematical result known as *Riemann-Lebesgue lemma*:

Riemann-Lebesgue lemma: *Let $f(t)$ be integrable in $[a,b]$ then:*

$$\lim_{x\to\infty}\int_a^b e^{ixt}f(t)dt = 0 \tag{C.5}$$

If we can use the above lemma, we can neglect the terms with different frequencies $\omega \neq \omega'$ and obtain the equation (1.54) if we change to the differential form of the equation:

$$\frac{d}{dt}\tilde{\rho}_S(t) = \varepsilon^2 \sum_{\omega}\sum_{\alpha,\ \beta}\Gamma^{(\infty)}_{\alpha\beta}(\omega)(\hat{A}_\beta(\omega)\tilde{\rho}_S(t)\hat{A}^\dagger_\alpha(\omega) - \hat{A}^\dagger_\alpha(\omega)\hat{A}_\beta(\omega)\tilde{\rho}_S(t)) \ + \ \text{h. c.} \tag{C.6}$$

where the terms $\Gamma^{(\infty)}_{\alpha\beta}$ are the *Fourier transforms* of the *reservoir correlation functions*:

$$\Gamma^{(\infty)}_{\alpha\beta}(\omega) \equiv \int_0^\infty ds\ e^{i\omega s}\,\langle \hat{B}^\dagger_\alpha(s)\hat{B}_\beta(0)\rangle \tag{C.7}$$

However, this is not so simple. We still have to ensure that the last integral (C.7) is convergent. In order to guarantee this we have to consider that the environment B has a continuous energy spectrum, and again, use the *Riemann-Lebesgue lemma*.

But the matter is even subtler since the *Fourier transform* has to be well defined. In general thi is the case, and we assume that our system satisfy this condition. A detailed analysis of the conditions can be found in Rivas' and Huelga's notes [90], c.f. sections 6.2.2 and 6.2.3.

C.2 Calculation of matrix elements $\gamma_{\alpha\beta}(\omega)$

In this appendix, we are going to calculate the matrix elements $\gamma_{\alpha\beta}(\omega)$, which are proportional to the real part of the equation (1.55) for our particular case. We can also rewrite the elements $\gamma_{\alpha\beta}(\omega)$ using the decomposition of the environment operators $\hat{B}_k$ into their interaction picture eigenoperators $e^{-i\omega t}\hat{B}_k(\omega)$ (following the approach described in [90]):

$$\begin{aligned}
\varepsilon^2\gamma_{\alpha\beta}(\omega) &= \varepsilon^2 \int_{-\infty}^{+\infty} ds\ e^{i\omega s}\ \langle \hat{B}_\alpha^\dagger(s)\hat{B}_\beta(0)\rangle \\
&= \varepsilon^2 \int_{-\infty}^{+\infty} ds\ e^{i\omega s}\ \mathrm{tr}_B\{\hat{B}_\alpha^\dagger(s)\hat{B}_\beta(0)\rho_B\} \\
&= \varepsilon^2 \int_{-a}^{a} d\omega' \int_{-\infty}^{+\infty} ds\ e^{i(\omega-\omega')s}\ \mathrm{tr}_B\{\hat{B}_\alpha^\dagger(\omega')\hat{B}_\beta(0)\rho_{th}\} \\
&= 2\pi\varepsilon^2 \int_{-a}^{a} d\omega' \delta(\omega-\omega')\ \mathrm{tr}_B\{\hat{B}_\alpha^\dagger(\omega')\hat{B}_\beta(0)\rho_{th}\} \\
&= 2\pi\varepsilon^2\ \mathrm{tr}_B\{\hat{B}_\alpha^\dagger(\omega)\hat{B}_\beta(0)\rho_{th}\}
\end{aligned} \tag{C.8}$$

where $\omega \in (-a, a)$, $\delta(\omega-\omega')$is the Dirac delta function, and we have assumed (1.45) that the environment is in thermal equilibrium, $\rho_B = \rho_{th}$. In order to calculate $\gamma_{\alpha\beta}(\omega)$, we recall that the interaction Hamiltonian (1.40) is:

$$H_I = (\hat{a}^\dagger+\hat{a})\underbrace{\sum_k g_k(\hat{c}_k^\dagger+\hat{c}_k)}_{\hat{B}_1} + (\hat{\sigma}^+ + \hat{\sigma}^-)\underbrace{\sum_k h_k(\hat{d}_k^\dagger+\hat{d}_k)}_{\hat{B}_2} + (\hat{b}^\dagger+\hat{b})\underbrace{\sum_k f_k(\hat{q}_k^\dagger+\hat{q}_k)}_{\hat{B}_2} \tag{C.9}$$

from where we identify the reservoir operators $\hat{B}_k$. Next, we assume that the environment has a continuous spectrum. So, first, we have to change to the continuous (C.9). Then, we can change variables from the wavevector k to the frequency $\omega(k)$ and calculate $\gamma_{\alpha\beta}(\omega)$. We are going to focus in the environment operator $\hat{B}_1$ (the calculations for others are equivalent:

$$\begin{aligned}
\hat{B}_1 &= \sum_{k=0}^{L} g_k(\hat{c}_k^\dagger+\hat{c}_k) = \underbrace{\frac{2\pi}{L}}_{\delta k}\sum_{k=0}^{L}\frac{L}{2\pi}g_k(\hat{c}_k^\dagger+\hat{c}_k) \\
&= \sum_{k=0}^{L}\delta k\frac{g_k}{\sqrt{\delta k}}\left(\frac{\hat{c}_k^\dagger}{\sqrt{\delta k}}+\frac{\hat{c}_k}{\sqrt{\delta k}}\right)\xrightarrow{\delta k\to 0}\int_0^{+\infty} g(k)((\tilde{c}_k^\dagger+\tilde{c}_k)) \\
&= \int_{\omega(0)}^{\omega(\infty)} d\omega\frac{g(k)}{\sqrt{d\omega/dk}}\left(\frac{\tilde{c}_k^\dagger}{\sqrt{d\omega/dk}}+\frac{\tilde{c}_k}{\sqrt{d\omega/dk}}\right) = \int_0^{\omega_{max}} d\omega\ g(\omega)(\hat{c}_\omega^\dagger+\hat{c}_\omega)
\end{aligned} \tag{C.10}$$

where, we have assumed that the dispersion relation $\omega = \omega(k)$ starts at $\omega = 0$ and presents a maximum frequency (ω_{max}).

As an example of the calculation the matrix element, we show the procedure for the first diagonal element:

$$\gamma_{11}(\omega) = 2\pi\varepsilon^2 \ \mathrm{tr}_B\{\hat{B}_1^\dagger(\omega')\hat{B}_1\rho_{th}\} \tag{C.11}$$

We have to distinguish two cases $\omega > 0$ and $\omega < 0$:

$$\hat{B}_1 = \int_0^{\omega_{max}} d\omega \ g(\omega)(\hat{c}_\omega^\dagger + \hat{c}_\omega) \equiv \int_{-\omega_{max}}^{\omega_{max}} d\omega \ \hat{B}_1(\omega) \tag{C.12}$$

where:

$$\begin{aligned} \hat{B}_1(\omega) &= g(\omega)\hat{c}_\omega \qquad \text{if: } \omega > 0 \\ \hat{B}_1(\omega) &= g(\omega)\hat{c}_\omega^\dagger \qquad \text{if: } \omega < 0 \end{aligned} \tag{C.13}$$

First, for the case $\omega > 0$:

$$\begin{aligned} \varepsilon^2\gamma_{11}(\omega) &= 2\pi\varepsilon^2 \ \mathrm{tr}_B\{\hat{B}_1^\dagger(\omega)\hat{B}_1\rho_{th}\} \\ &= 2\pi \ \varepsilon^2 g(\omega) \int_0^{\omega_{max}} d\omega' g(\omega') \mathrm{tr}_B\{\hat{c}_\omega(\hat{c}_{\omega'} + \hat{c}_{\omega'}^\dagger)\rho_{th}\} \\ &= 2\pi \ \varepsilon^2 g(\omega) \int_0^{\omega_{max}} d\omega' g(\omega')(\langle \hat{c}_\omega \hat{c}_{\omega'} \rangle + \langle \hat{c}_\omega \hat{c}_{\omega'}^\dagger \rangle) \end{aligned} \tag{C.14}$$

where we have to notice that:

$$\langle \hat{c}_{\omega'}^\dagger \hat{c}_\omega \rangle = \delta(\omega - \omega')\bar{n}_{\mathrm{phot}}(\omega) \tag{C.15}$$

where $\bar{n}_{\mathrm{phot}}(\omega)$ is the mean number of bosons in the thermal state ρ_{th} (see equation (1.45)) in the photon reservoir (i.e. the expected number of particles of the Bose-Einstein statistics):

$$\bar{n}_{\mathrm{phot}}(\omega) = \frac{1}{e^{\omega/k_B T_{\mathrm{phot}}} - 1} \tag{C.16}$$

Therefore, we for the case $\omega > 0$:

$$\varepsilon^2\gamma_{11}(\omega) = 2\pi \ \varepsilon^2 g^2(\omega)(1 + \bar{n}_{\mathrm{phot}}(\omega)) = 2\pi \ \varepsilon^2 J_{\mathrm{phot}}(\omega)(1 + \bar{n}_{\mathrm{phot}}(\omega)) \tag{C.17}$$

where $J_{\mathrm{phot}}(\omega) = g^2(\omega)$ is the spectral density of the "light environment", which takes into account the spectral strength of the coupling.

Equivalently, for $\omega < 0$:

$$\varepsilon^2\gamma_{11}(\omega) = 2\pi\ \varepsilon^2 J_{\text{phot}}(\omega)\bar{n}_{\text{phot}}(\omega) \tag{C.18}$$

With respect to the non-diagonal elements, the commutator relations:

$$\begin{aligned}[\hat{c}_\omega, \hat{d}_{\omega'}] = [\hat{c}_\omega, \hat{q}_{\omega'}] = [\hat{q}_\omega, \hat{d}_{\omega'}] = 0 \\ [\hat{c}_\omega, \hat{d}^\dagger_{\omega'}] = [\hat{c}_\omega, \hat{q}^\dagger_{\omega'}] = [\hat{q}_\omega, \hat{d}^\dagger_{\omega'}] = 0\end{aligned} \tag{C.19}$$

imply that all off-diagonal elements are zero. So, in our case, the *dissipator equation* (1.64) simplies to:

$$\mathcal{D}(\rho_S(t)) = \sum_\omega \sum_k 2\pi\ \varepsilon^2 J_k(\omega)\xi_k(\omega)\left(\hat{A}_k(\omega)\rho_S(t)\hat{A}^\dagger_k(\omega) - \frac{1}{2}\{\hat{A}^\dagger_k(\omega)\hat{A}_k(\omega), \rho_S(t)\}\right) \tag{C.20}$$

where $k = matt,\ phot,\ phon$, according to whether we refer to the the matter, light or phonon bath. Also, we have defined:

$$\xi_k(\omega) = \begin{cases} 1 + \bar{n}_k(\omega), & \text{for} \quad \omega > 0 \\ \bar{n}_k(\omega), & \text{for} \quad \omega < 0 \end{cases} \tag{C.21}$$

This is ageneral expression. In what follows we assume that the bath is characterized by an *Ohmnic spectral density function*, in other words $J_k(\omega) \propto \omega$. Thus, we define $2\pi\ \varepsilon^2 J_k(\omega) = \gamma_k\omega$ and finally obtain:

$$\mathcal{D}(\rho_S(t)) = \sum_\omega \sum_k \gamma_k\omega\ \xi_k(\omega)\left(\hat{A}_k(\omega)\rho_S(t)\hat{A}^\dagger_k(\omega) - \frac{1}{2}\{\hat{A}^\dagger_k(\omega)\hat{A}_k(\omega), \rho_S(t)\}\right) \tag{C.22}$$

where γ_k accounts the intensity of the dissipation into the matter, light or phonon reservoirs (γ_{matt}, γ_{phot} and γ_{phon}). This completes the derivation of equation (1.60).

Appendix D

Shrieffer-Wolff Method for computing the effective Hamiltonian in the Polariton sector

In this appendix, we give the analytical expressions of the correction H_{int} (2.37) in the basis $\{|P_+^{(1)}\rangle\,,\ |P_-^{(1)}\rangle\}$:

$$H_{int} = \begin{pmatrix} \alpha_+ & \tilde{\Lambda} \\ \tilde{\Lambda} & \alpha_- \end{pmatrix} \tag{D.1}$$

After performing a Shrieffer-Wolff transformation, we obtain:

$$\begin{aligned} \alpha_\pm = \langle P_\pm^{(1)}|H_{int}|P_\pm^{(1)}\rangle = -\frac{2g^2}{\tau_{\pm1}^2+1}\Bigg[&\frac{\tau_{+3}^2}{2\omega_c + g(\sqrt{3}\tau_{+3}-\tau_{\pm1})}\frac{1}{\tau_{+3}^2+1} \\ &+ \frac{\tau_{-3}^2}{2\omega_c + g(\sqrt{3}\tau_{-3}-\tau_{\pm1})}\frac{1}{\tau_{-3}^2+1}\Bigg] \end{aligned} \tag{D.2}$$

$$\begin{aligned} \tilde{\Lambda} = \langle P_-^{(1)}|H_{int}|P_+^{(1)}\rangle = -\frac{g^2}{\sqrt{(\tau_{-1}^2+1)(\tau_{+1}^2+1)}}\Bigg[&\Bigg(\frac{1}{2\omega_c + g(\sqrt{3}\tau_{+3}-\tau_{-1})} \\ &+ \frac{1}{2\omega_c + g(\sqrt{3}\tau_{+3}-\tau_{+1})}\Bigg)\frac{\tau_{+3}^2}{\tau_{+3}^2+1} + \Bigg(\frac{1}{2\omega_c + g(\sqrt{3}\tau_{-3}-\tau_{-1})} \\ &+ \frac{1}{2\omega_c + g(\sqrt{3}\tau_{-3}-\tau_{+1})}\Bigg)\frac{\tau_{-3}^2}{\tau_{-3}^2+1}\Bigg] \end{aligned} \tag{D.3}$$

where the values of $\tau_{\pm n}$ are given in (2.9).

Appendix E

Franck-Condon factors

We can easily obtain these Franck-Condon factors using the notes of Brandes [80]. The $D(\lambda) = e^{\lambda(b^\dagger - b)}$ is the displacement operator and the formulas which generates these factors are:

$$D_{mn}(\alpha) = \langle m|e^{\alpha(b^\dagger - b)}|n\rangle = \sqrt{\frac{n!}{m!}}\alpha^{m-n}e^{-|\alpha|^2/2}L_n^{m-n}(|\alpha|^2) \quad m \geqslant n \tag{E.1}$$

$$D_{mn}(\alpha) = \langle m|e^{\alpha(b^\dagger - b)}|n\rangle = \sqrt{\frac{m!}{n!}}(-1)^{n-m}(\alpha^*)^{n-m}e^{-|\alpha|^2/2}L_m^{n-m}(|\alpha|^2) \quad n \geqslant m \tag{E.2}$$

where L_n^m are the associated Laguerre polynomials. Here, we have included the explicit expressions for the ones related to transitions between the 4 lowest vibrational levels:

Franck-Condon factors	λ
$\langle 0\|D(\lambda)\|0\rangle$	$e^{-\lambda^2/2}$
$\langle 1\|D(\lambda)\|0\rangle$	$e^{-\lambda^2/2}\lambda$
$\langle 1\|D(\lambda)\|1\rangle$	$e^{-\lambda^2/2}(1-\lambda^2)$
$\langle 2\|D(\lambda)\|0\rangle$	$e^{-\lambda^2/2}\frac{\lambda^2}{\sqrt{2}}$
$\langle 2\|D(\lambda)\|1\rangle$	$e^{-\lambda^2/2}\frac{\lambda}{\sqrt{2}}(2-\lambda^2)$
$\langle 2\|D(\lambda)\|2\rangle$	$e^{-\lambda^2/2}\frac{1}{2}(2-4\lambda^2+\lambda^4)$
$\langle 3\|D(\lambda)\|0\rangle$	$e^{-\lambda^2/2}\frac{\lambda^3}{\sqrt{6}}$
$\langle 3\|D(\lambda)\|1\rangle$	$e^{-\lambda^2/2}\frac{\lambda^2}{\sqrt{6}}(3-\lambda^2)$
$\langle 3\|D(\lambda)\|2\rangle$	$e^{-\lambda^2/2}\frac{\lambda}{2\sqrt{3}}(6-6\lambda^2+\lambda^4)$
$\langle 3\|D(\lambda)\|3\rangle$	$e^{-\lambda^2/2}\frac{1}{6}(6-18\lambda^2+9\lambda^4-\lambda^6)$

E.1 Properties Transition rates $\Gamma_{\tilde{n}m}$

In this section, we are going to demostrate the properties (J.11) and (J.12).

First, we can start with (J.11):

$$\begin{aligned}\sum_{m=0}^{\infty}\Gamma_{\tilde{n}m} &= \sum_{m=0}^{\infty} D_{\tilde{n}m}(\lambda)D_{m\tilde{n}}(-\lambda) = \sum_{m=0}^{\infty}\langle\tilde{n}|e^{\lambda(\hat{b}^\dagger-\hat{b})}|m\rangle\langle m|e^{-\lambda(\hat{b}^\dagger-\hat{b})}|\tilde{n}\rangle \\ &= \langle\tilde{n}|\, e^{\lambda(\hat{b}^\dagger-\hat{b})}\underbrace{\left(\sum_{m=0}^{\infty}|m\rangle\langle m|\right)}_{\mathbf{I}} e^{-\lambda(\hat{b}^\dagger-\hat{b})}\,|\tilde{n}\rangle \\ &= 1\end{aligned} \tag{E.3}$$

Notice also that, as $\langle\tilde{n}|m\rangle\langle m|\tilde{n}\rangle = |\langle\tilde{n}|m\rangle|^2 \geqslant 0$

$$0 < \sum_{m\omega_v<\omega_v\tilde{n}+\Delta}\Gamma_{\tilde{n}m}(\lambda) < 1 \tag{E.4}$$

In figure E.2, we have plotted the values of the rates $\Gamma_{\tilde{n}m}$ for several values of λ. We can see that $\Gamma_{\tilde{n}m} < 1$ (except in the case of $\lambda = 0$) and the condition $m\omega_v < \omega_v\tilde{n} + \Delta$ is a straight line above which the sum (E.4) does not include any term $\Gamma_{\tilde{n}m}$. In figure E.2, we have included two conditions ($\omega_v = 0.02$ (green line) and $\omega_v = 0.1$ (red line)) in order to see that this sum is smaller than one. We have also plotted the sum $\sum_{m<\tilde{n}+\Delta/\omega_v}\Gamma_{\tilde{n}m}(\lambda)$ as a function of $\tilde{n}$ for several values of λ and $\omega_v = 0.1$, see figure E.1.

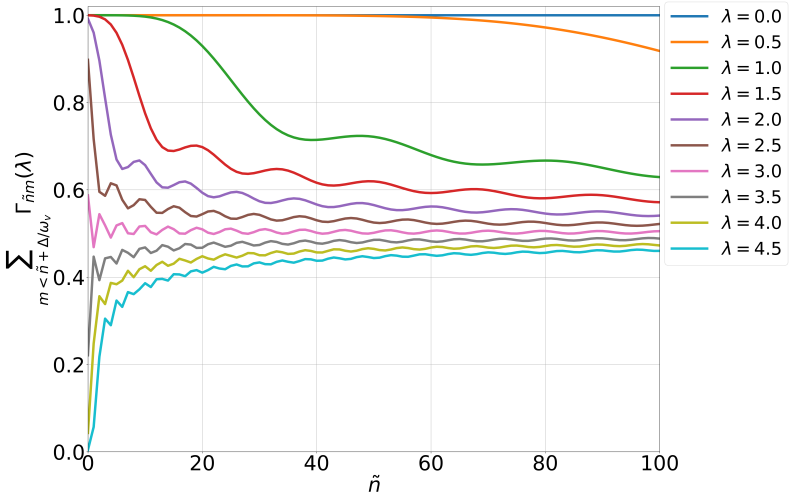

Figure E.1: Plot of the sum $\sum_{m<\tilde{n}+\Delta/\omega_v}\Gamma_{\tilde{n}m}(\lambda)$ as a function of $\tilde{n}$ for several values of λ, for the case $\omega_v = 0.1$.

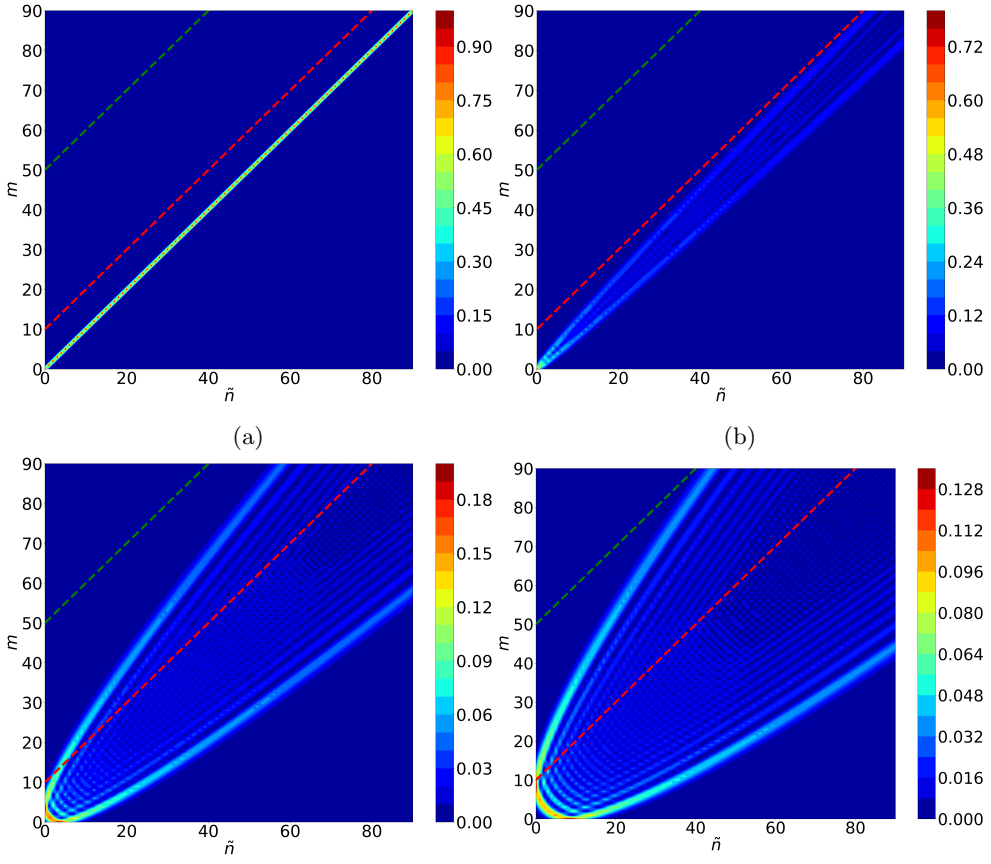

Figure E.2: $\Gamma_{\tilde{n}m}(\lambda)$ for several values of λ; (a) $\lambda = 0.0$, (b) $\lambda = 0.5$, (c) $\lambda = 2.0$ and (d) $\lambda = 3.0$. The dashed lines represent the condition $m = \tilde{n} + \Delta/\omega_v$ (the green line is for $\omega_v = 0.02$ while the red one is for $\omega_v = 0.1$).

E.2 Appoximation in the Bloch-Siegert correction

In this section, we are going to justify the approximation made in the equation (2.26):

$$\delta_{BS} = g^2 \sum_{\tilde{m}=0}^{\infty} \frac{2|D_{\tilde{m}0}(\lambda)|^2}{\omega_c + \Delta + \tilde{m}\omega_v} \approx \frac{2g^2}{\omega_c + \Delta + \lambda^2\omega_v} \tag{E.5}$$

where we replaced $\tilde{m} \to \lambda^2$ in the fraction denominator and we have taken into account that:

$$\sum_{\tilde{m}=0}^{\infty} |D_{\tilde{m}0}(\lambda)|^2 = 1 \tag{E.6}$$

We can rewrite the equation (E.5) as:

$$\delta_{BS} = g^2 \sum_{\tilde{m}=0}^{\infty} \frac{2|D_{\tilde{m}0}(\lambda)|^2}{\omega_c + \Delta + \tilde{m}\omega_v} = 2g^2 \sum_{\tilde{m}=0}^{\infty} f(\tilde{m})g(\tilde{m}, \lambda) \tag{E.7}$$

where, using the equation (E.1):

$$f(\tilde{m}) = \frac{1}{\omega_c + \Delta + \tilde{m}\omega_v} \qquad g(\tilde{m}, \lambda) = |D_{\tilde{m}0}(\lambda)|^2 = e^{-\lambda^2} \frac{(\lambda^2)^m}{m!} \tag{E.8}$$

If we plot the function $g(\tilde{m}, \lambda)$ in a colour map, see figure E.3, we obtain that the maximum of the colour map (black dashed line) is around $\tilde{m} \sim \lambda^2$ (magenta curve). For $\tilde{m} \neq \lambda^2$ the function $g(\tilde{m} \neq \lambda^2, \lambda) \sim 0$. So, we can replace the "function" $f(\tilde{m})$ for the value at $f(\tilde{m} = \lambda^2)$. Then, we can use the property (E.6) and obtain finally (E.5). Figure E.4 represents the exact value versus the approximation showing that (E.5) is a very good approximation.

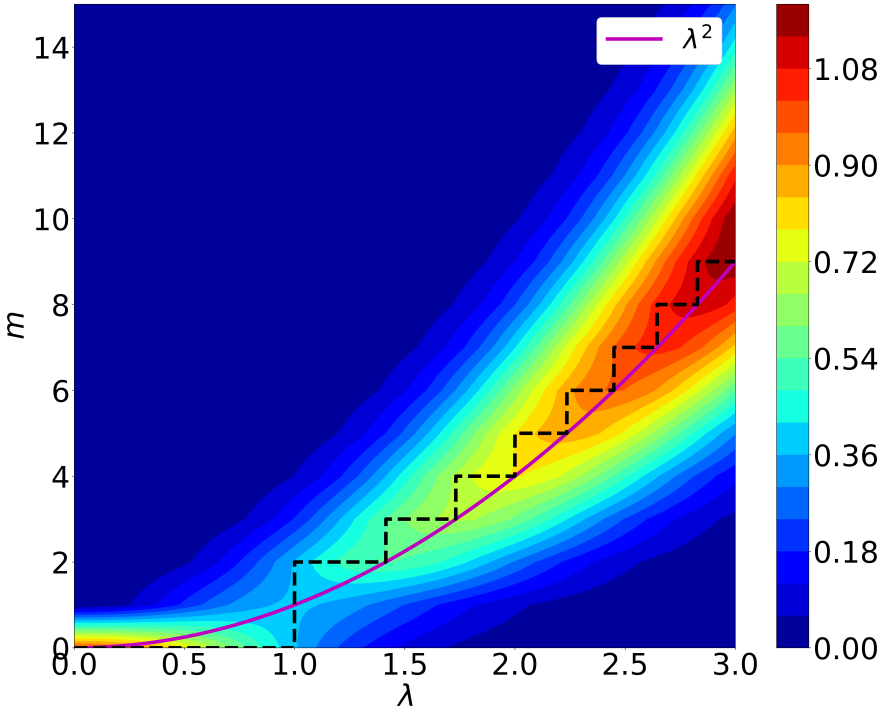

Figure E.3: Colour map of the function $g(\tilde{m}, \lambda)$, the black dashed curve is the maximum of the colour map and the magenta curve is λ^2. Parameters: $\omega_v = 0.1$, $\omega_c = 1.0$ and $\Delta = 1.0$.

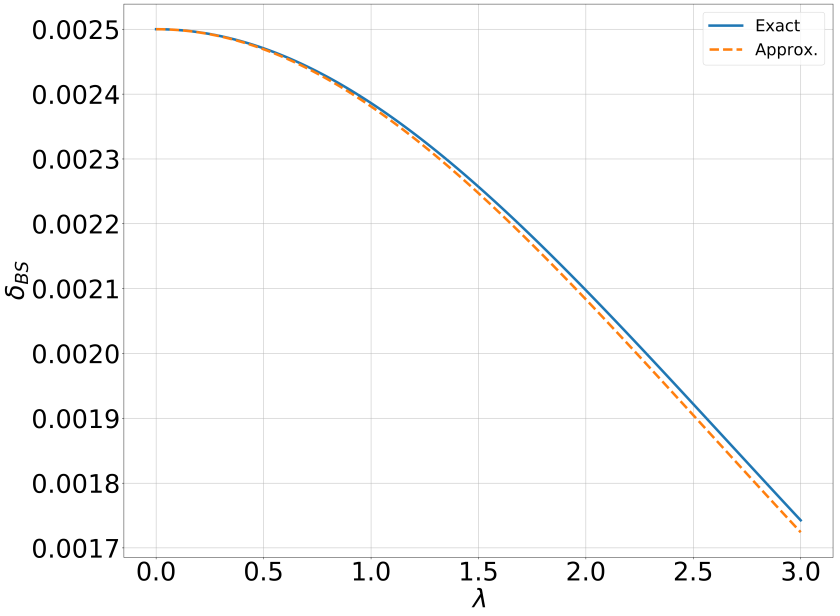

Figure E.4: Continuous line exact equation (E.5), dashed line approximate equation (E.5). Parameters: $\omega_v = 0.1$, $\omega_c = 1.0$, $\Delta = 1.0$ and $g = 0.05$.

Appendix F

Perturbation theory

In this appendix, we are going to apply perturbation theory over the Hamiltonian of the *Holstein-Quantum-Rabi* model (2.2)[1]:

$$\begin{aligned}\tilde{\mathcal{H}} = \underbrace{\omega_c \hat{a}^\dagger \hat{a} + \Delta \hat{\sigma}^+ \hat{\sigma}^- + \omega_v \hat{b}^\dagger \hat{b}}_{H_0} + \underbrace{g(D(\lambda)\hat{a}^\dagger \hat{\sigma}^- + D^\dagger(\lambda)\hat{a}\hat{\sigma}^+)}_{H_R} \\ + \underbrace{g(D(\lambda)\hat{a}^\dagger \hat{\sigma}^+ + D^\dagger(\lambda)\hat{a}\hat{\sigma}^-)}_{H_{CR}}\end{aligned} \tag{F.1}$$

with $D(\lambda) = e^{\lambda(\hat{b}^\dagger - \hat{b})}$, in other words, we have:

$$\mathcal{H} = H_0 + H_R + H_{CR} = H_0 + H_R + gV \tag{F.2}$$

where the counterrotating terms V are the perturbation with $g \ll 1$. We are going to correct the energies of H_0, as we did in section 2.3, and we will treat the non-counterrotating terms H_R exactly. However, we will expand our basis to $\{|\downarrow\ 0_{phot}\ m_{phon}\rangle\,,\ |\uparrow\ 0_{phot}\ \tilde{n}_{phon}\rangle\,,\ |\downarrow\ 1_{phot}\ m_{phon}\rangle\}$. Again, the perturbation is defined as:

$$V = D(\lambda)\hat{a}^\dagger \hat{\sigma}^+ + D^\dagger(\lambda)\hat{a}\hat{\sigma}^- \tag{F.3}$$

Thus, we define the eigenstates and eigenenergies of $H_0 + gV$ as:

$$(H_0 + gV)\,|n\rangle = E_n\,|n\rangle \tag{F.4}$$

and the eigenstates and eigenvalues of H_0

$$H_0\,|n^{(0)}\rangle = E_n^{(0)}\,|n^{(0)}\rangle \tag{F.5}$$

[1] We can do the same with the model (1.35). They are equivalent models under a unitary transformation.

where:

$$\{|1^{(0)}\rangle\,,\ |2^{(0)}\rangle\,,\ |3^{(0)}\rangle\,,\ ...\} = \{...,\ |\downarrow\ m_{phot}\ n_{phon}\rangle\,,\ ...,\ |\uparrow\ m_{phot}\ \tilde{n}_{phon}\rangle\,...\} \tag{F.6}$$

Thus, using perturbation theory, we obtain that the eigenenergies of $H_0 + gV$ are:

$$E_n = E_n^{(0)} + gE_n^{(1)} + g^2E_n^{(2)} + \dots \tag{F.7}$$

and the eigenstates are:

$$|n\rangle = |n^{(0)}\rangle + g\,|n^{(1)}\rangle + g^2\,|n^{(2)}\rangle + \dots \tag{F.8}$$

Using as basis $\{|\downarrow\ 0_{phot}\ m_{phon}\rangle\,,\ |\uparrow\ 0_{phot}\ \tilde{n}_{phon}\rangle\,,\ |\downarrow\ 1_{phot}\ m_{phon}\rangle\}$ we have:

$$\begin{aligned}
(H_0 + H_R)\,|\downarrow\ 0_{phot}\ m_{phon}\rangle &= \omega_v m_{phon}\,|\downarrow\ 0_{phot}\ m_{phon}\rangle \\
(H_0 + H_R)\,|\uparrow\ 0_{phot}\ \tilde{n}_{phon}\rangle &= (\Delta + \tilde{n}_{phon}\omega_v)\,|\uparrow\ 0_{phot}\ \tilde{n}_{phon}\rangle \\
&\quad + gD(\lambda)\,|\downarrow\ 1_{phot}\ \tilde{n}_{phon}\rangle \\
(H_0 + H_R)\,|\downarrow\ 1_{phot}\ m_{phon}\rangle &= (\omega_c + m_{phon}\omega_v)\,|\downarrow\ 1_{phot}\ m_{phon}\rangle \\
&\quad + gD^\dagger(\lambda)\,|\uparrow\ 0_{phot}\ m_{phon}\rangle
\end{aligned} \tag{F.9}$$

Therefore, in this basis (the eigenstates of H_0) $H_0 + H_R$ is:

$$H_0 + H_R = \begin{pmatrix} m_{phon}\omega_v & 0 & 0 \\ 0 & \Delta + \tilde{n}\omega_v & gD^\dagger_{\tilde{n}m}(\lambda) \\ 0 & gD_{m\tilde{n}}(\lambda) & \omega_c + m_{phon}\omega_v \end{pmatrix} \tag{F.10}$$

where $D_{\tilde{n}m}(\lambda)$ is the Franck-Condon factor. We are going to use perturbation theory in order to give a correction in the energies $\omega_v m_{phon}$, $\Delta + \omega_v\tilde{n}$ and $\omega_c + \omega_v m_{phon}$. Thus, we can include the effect of the counterrotating terms for $g \ll 1$. First, we notice that the first order correction is zero:

$$E_n^{(1)} = \langle n^{(0)}|V|n^{(0)}\rangle = 0 \tag{F.11}$$

since:

$$V\,|\uparrow\ 0_{phot}\ \tilde{n}_{phon}\rangle = 0 \tag{F.12}$$

$$V\,|\downarrow\ 1_{phot}\ m_{phon}\rangle = \sqrt{2}D(\lambda)\,|\uparrow\ 2_{phot}\ m_{phon}\rangle \tag{F.13}$$

$$V\,|\downarrow\ 0_{phot}\ m_{phon}\rangle = D(\lambda)\,|\uparrow\ 1_{phot}\ m_{phon}\rangle \tag{F.14}$$

So, we have to pass to the second order, we begin with the sate $|\uparrow\ 0_{phot}\ \tilde{n}\rangle$:

$$\sum_k \frac{|\,\langle k^{(0)}|V|\uparrow\ 0_{phot}\ \tilde{n}\rangle\,|^2}{(\Delta + \tilde{n}\omega_v) - E_k} = 0 \tag{F.15}$$

For the third basis state $|\downarrow\ 1_{phot}\ m_{phon}\rangle$, we obtain:

$$\sum_k \frac{|\langle k^{(0)}|V|\downarrow\ 1_{phot}\ m_{phon}\rangle|^2}{\omega_c + m_{phon}\omega_v - E_k} = \sum_{\tilde{n}=0}^{\infty} \frac{|\langle\uparrow\ 2_{phot}\ \tilde{n}|\sqrt{2}D(\lambda)|\uparrow\ 2_{phot}\ m_{phon}\rangle|^2}{\omega_c + m_{phon}\omega_v - (\Delta + 2\omega_c + \tilde{n}\omega_v)}$$
$$= -2\sum_{\tilde{n}=0}^{\infty} \frac{|D_{\tilde{n}m}(\lambda)|^2}{\omega_c + \Delta + (\tilde{n} - m_{phon})\omega_v}$$

and, finally, for the first basis state $|\downarrow\ 0_{phot}\ m_{phon}\rangle$, we have:

$$\sum_k \frac{|\langle k^{(0)}|V|\downarrow\ 0_{phot}\ m_{phon}\rangle|^2}{m_{phon}\omega_v - E_k} = \sum_{\tilde{n}=0}^{\infty} \frac{|\langle\uparrow\ 1_{phot}\ \tilde{n}|D(\lambda)|\uparrow\ 1_{phot}\ m_{phon}\rangle|^2}{m_{phon}\omega_v - (\Delta + \omega_c + \tilde{n}\omega_v)}$$
$$= -\sum_{\tilde{n}=0}^{\infty} \frac{|D_{\tilde{n}m}(\lambda)|^2}{\omega_c + \Delta + (\tilde{n} - m_{phon})\omega_v}$$

where, the Bloch-Siegert correction is:

$$\delta_{BS}(\omega_c, \lambda) := 2g^2 \sum_{\tilde{n}=0}^{\infty} \frac{|D_{\tilde{n}m}(\lambda)|^2}{\omega_c + \Delta + (\tilde{n} - m_{phon})\omega_v} \tag{F.16}$$

Therefore, the Hamiltonian $H_0 + H_R$ with the second order counterrotating terms correction is:

$$H_0 + H_R = \begin{pmatrix} m_{phon}\omega_v - \delta_{BS}/2 & 0 & 0 \\ 0 & \Delta + \tilde{n}\omega_v & gD^{\dagger}_{\tilde{n}m}(\lambda) \\ 0 & gD_{m\tilde{n}}(\lambda) & \omega_c + m_{phon}\omega_v - \delta_{BS} \end{pmatrix} \tag{F.17}$$

In order to correct the energies of the counterrotating terms, we will focus correction of the state with zero phonons. Thus, we will impose $m_{phon} = 0$:

$$\delta_{BS}(\omega_c, \lambda) = 2g^2 \sum_{\tilde{n}=0}^{\infty} \frac{\lambda^{2\tilde{n}} e^{-\lambda^2}}{\tilde{n}!(\omega_c + \Delta + \tilde{n}\omega_v)} = 2g^2 \sum_{\tilde{n}=0}^{\infty} \frac{|D_{\tilde{n}0}(\lambda)|^2}{\omega_c + \Delta + \tilde{n}\omega_v} \tag{F.18}$$

Thus, we arrive to the expression (2.26) obtained in the section 2.3.

Appendix G

Ground state calculation

In this appendix, we are going to obtain the ground state energy (2.46) and justify the condition (2.45).

We start from the effective Hamiltonian (2.15):

$$H_{\text{eff}} = \frac{\hat{\Delta}}{2}(\hat{\sigma}_z + 1) + \omega_v \hat{b}^\dagger \hat{b} + \hat{g}\hat{\sigma}_x(\hat{b}^\dagger + \hat{b}) + \epsilon \tag{G.1}$$

where $\hat{\sigma}_x = \hat{\sigma}_P^+ + \hat{\sigma}_P^-$. Now, we are going to change the basis $\hat{\sigma}_z \to \hat{\sigma}_x$:

$$H_{\text{eff}} = \frac{\hat{\Delta}}{2}(\hat{\sigma}_x + 1) + \omega_v \hat{b}^\dagger \hat{b} + \hat{g}\hat{\sigma}_z(\hat{b}^\dagger + \hat{b}) + \epsilon \tag{G.2}$$

We propose as ground state:

$$|gs\rangle = U_P^{(2)} |0_{phon}\rangle |\psi_S\rangle = U_P^{(2)} |0_{phon}\rangle (\theta |-\rangle + \beta |+\rangle) \qquad |\theta|^2 + |\beta|^2 = 1 \tag{G.3}$$

where $|\pm\rangle$ are eigenstates of $\hat{\sigma}_z$ ($\hat{\sigma}_z |\pm\rangle = \pm |\pm\rangle$) y $U_P^{(2)} = e^{\hat{\sigma}_z \alpha (\hat{b}^\dagger - \hat{b})}$, where $\alpha,\ \beta,\ \theta \in \mathbb{C}$. We are going to calculate the energy of $|gs\rangle$ and minimize with regard to α supposing that $\alpha \in \mathbb{R}$:

$$\epsilon_{gs}(\alpha) = \langle gs|H|gs\rangle = \langle \psi_S| \langle 0_{phon}| {U_P^{(2)}}^\dagger H_{\text{eff}} U_P^{(2)} |0_{phon}\rangle |\psi_S\rangle \tag{G.4}$$

G.1 Term containing $\hat{\sigma}_x$:

The contribution to (G.4) of the term in H_{eff} containing $\hat{\sigma}_x = |+\rangle\langle -| + |-\rangle\langle +|$:

$$\begin{aligned} &\tfrac{\hat{\Delta}}{2} \langle \psi_S| \langle 0_{phon}| {U_P^{(2)}}^\dagger \hat{\sigma}_x U_P^{(2)} |0_{phon}\rangle |\psi_S\rangle \\ &= \tfrac{\hat{\Delta}}{2} (\theta^* \langle -| + \beta^* \langle +|) \langle 0_{phon}| {U_P^{(2)}}^\dagger \hat{\sigma}_x U_P^{(2)} |0_{phon}\rangle (\theta |-\rangle + \beta |+\rangle) \\ &= \langle 0_{phon}| (\beta^* \theta e^{-(\alpha^* + \alpha)(\hat{b}^\dagger - \hat{b})} + \theta^* \beta e^{(\alpha^* + \alpha)(\hat{b}^\dagger - \hat{b})}) |0_{phon}\rangle \end{aligned}$$

Using the Baker-Campbell-Hausdorff formula:

$$\langle 0_{phon}|e^{-(\alpha^*+\alpha)(\hat{b}^\dagger-\hat{b})}|0_{phon}\rangle = \langle 0_{phon}|e^{(\alpha^*+\alpha)\hat{b}^\dagger}e^{-(\alpha^*+\alpha)\hat{b}}e^{-(\alpha^*+\alpha)^2/2}|0_{phon}\rangle$$
$$= e^{-(\alpha^*+\alpha)^2/2}\,\langle 0_{phon}|\sum_{n=0}^{\infty}\frac{(\alpha^*+\alpha)^n}{n!}(\hat{b}^\dagger)^n\sum_{m=0}^{\infty}\frac{(\alpha^*+\alpha)^m}{m!}\hat{b}^m|0_{phon}\rangle = e^{-(\alpha^*+\alpha)^2/2}$$

where only the terms $m = 0$ and $n = 0$ are different of zero. Thus, the contribution to the energy from $\hat{\sigma}_x$ is:

$$\boxed{\frac{\hat{\Delta}}{2}\,\langle\psi_S|\,\langle 0_{phon}|U_P^{(2)^\dagger}\hat{\sigma}_x U_P^{(2)}|0_{phon}\rangle\,|\psi_S\rangle = \frac{\hat{\Delta}}{2}e^{-(\alpha^*+\alpha)^2/2}(\beta^*\theta+\theta^*\beta)} \quad \text{(G.5)}$$

G.2 Term containing $\hat{b}^\dagger\hat{b}$:

Now, we are going to calculate the contribution to the energy of the term $\hat{b}^\dagger\hat{b}$ in (G.2):

$$\omega_v(\theta^*\,\langle -| + \beta^*\,\langle +|)\,\langle 0_{phon}|U_P^{(2)^\dagger}\;\hat{b}^\dagger\hat{b}\;U_P^{(2)}|0_{phon}\rangle\,(\theta\,|-\rangle + \beta\,|+\rangle)$$
$$= \omega_v\,\langle 0_{phon}|(|\theta|^2 e^{\alpha^*(\hat{b}^\dagger-\hat{b})}\hat{b}^\dagger\hat{b}\;e^{-\alpha(\hat{b}^\dagger-\hat{b})} + |\beta|^2 e^{-\alpha^*(\hat{b}^\dagger-\hat{b})}\hat{b}^\dagger\hat{b}\;e^{\alpha(\hat{b}^\dagger-\hat{b})})|0_{phon}\rangle$$

Using again the Baker-Campbell-Hausdorff formula:

$$\langle 0_{phon}|e^{-\alpha^*(\hat{b}^\dagger-\hat{b})}\hat{b}^\dagger\hat{b}\;e^{\alpha(\hat{b}^\dagger-\hat{b})}|0_{phon}\rangle = \langle 0_{phon}|e^{-\alpha^*\hat{b}^\dagger}e^{\alpha^*\hat{b}}e^{-\alpha^{*2}/2}\hat{b}^\dagger\hat{b}\;e^{\alpha\hat{b}^\dagger}e^{-\alpha\hat{b}}e^{-\alpha^2/2}|0_{phon}\rangle$$
$$= e^{-\frac{\alpha^{*2}+\alpha^2}{2}}\,\langle 0_{phon}|\sum_{z,\,l,\,m,\,n=0}^{\infty}\frac{(-\alpha^*)^z}{z!}\frac{(\alpha^*)^l}{l!}\frac{\alpha^m}{m!}\frac{(-\alpha)^n}{n!}\;(\hat{b}^\dagger)^z\hat{b}^l\;\;\hat{b}^\dagger\hat{b}\;\;(\hat{b}^\dagger)^m\hat{b}^n\;|0_{phon}\rangle$$
$$= e^{-\frac{\alpha^{*2}+\alpha^2}{2}}\sum_{l,\,m=1}^{\infty}\frac{(\alpha^*)^l}{l!}\frac{\alpha^m}{m!}\,\langle 0_{phon}|\;\hat{b}^l\;\;\hat{b}^\dagger\hat{b}\;\;(\hat{b}^\dagger)^m\;|0_{phon}\rangle = \cdots$$

Using the commutation relation $[\hat{b},\ \hat{b}^\dagger] = 1$, we obtain:

$$\hat{b}(\hat{b}^\dagger)^m = m(\hat{b}^\dagger)^{m-1} + (\hat{b}^\dagger)^m\hat{b} \quad \text{(G.6)}$$
$$\hat{b}^l\hat{b}^\dagger = l\hat{b}^{l-1} + \hat{b}^\dagger\hat{b}^l \quad \text{(G.7)}$$

So, using these last relations, we arrive to:

$$\langle 0_{phon}|e^{-\alpha^*(\hat{b}^\dagger-\hat{b})}\hat{b}^\dagger\hat{b}\;e^{\alpha(\hat{b}^\dagger-\hat{b})}|0_{phon}\rangle = \cdots = |\alpha|^2 e^{-\frac{\alpha^{*2}+\alpha^2}{2}}e^{|\alpha|^2} \quad \text{(G.8)}$$

Finally, the contribution to the energy from the term $\hat{b}^\dagger\hat{b}$ is (remember $|\theta|^2 + |\beta|^2 = 1$):

$$\boxed{\omega_v\,\langle\psi_S|\,\langle 0_{phon}|U_P^{(2)^\dagger}\;\hat{b}^\dagger\hat{b}\;U_P^{(2)}|0_{phon}\rangle\,|\psi_S\rangle = \omega_v|\alpha|^2 e^{-\frac{\alpha^{*2}+\alpha^2}{2}}e^{|\alpha|^2}} \quad \text{(G.9)}$$

G.3 Term containing $\hat{\sigma}_z(\hat{b}^\dagger + \hat{b})$:

In this subsection, we are going to calculate contribution to the energy of the term $H_B = \hat{\sigma}_z(\hat{b}^\dagger + \hat{b})$ of (G.2):

$$\langle H_B \rangle = hatg(\theta^* \langle -| + \beta^* \langle +| \rangle \langle 0_{phon}| e^{-\alpha^* \hat{\sigma}_z(\hat{b}^\dagger - \hat{b})} \underbrace{\hat{\sigma}_z(\hat{b}^\dagger + \hat{b})}_{Q} \underbrace{e^{\alpha \hat{\sigma}_z(\hat{b}^\dagger - \hat{b})}}_{U_P^{(2)}} |0_{phon}\rangle (\theta |-\rangle + \beta |+\rangle) \tag{G.10}$$

If this commutator $[Q,\ U_P^{(2)}] = 2\alpha U_P^{(2)}$ fulfills [cf. subsection G.5], we know that :

$$QU_P^{(2)} = 2\alpha U_P^{(2)} + U_P^{(2)} Q \tag{G.11}$$

Using the latter relation, we arrive to:

$$\langle H_B \rangle = \langle 0_{phon}| \Big[|\theta|^2 e^{-(\alpha - \alpha^*)(\hat{b}^\dagger + \hat{b})}(2\alpha - (\hat{b}^\dagger + \hat{b})) + |\beta|^2 e^{(\alpha - \alpha^*)(\hat{b}^\dagger + \hat{b})}(2\alpha + (\hat{b}^\dagger + \hat{b})) \Big] |0_{phon}\rangle$$

We notice that (and using again the Baker-Campbell-Hausdorff formula):

(a) $\langle 0_{phon}| e^{-(\alpha - \alpha^*)(\hat{b}^\dagger - \hat{b})} \hat{b} |0_{phon}\rangle = \langle 0_{phon}| e^{(\alpha - \alpha^*)(\hat{b}^\dagger - \hat{b})} \hat{b} |0_{phon}\rangle = 0$

(b) $\langle 0_{phon}| e^{-(\alpha - \alpha^*)(\hat{b}^\dagger - \hat{b})} \hat{b}^\dagger |0_{phon}\rangle =$

$$= \langle 0_{phon}| \sum_{n,\ m=0}^{\infty} \frac{(\alpha^* - \alpha)^n}{n!} (\hat{b}^\dagger)^n \frac{(\alpha - \alpha^*)^m}{m!} \hat{b}^m |1_{phon}\rangle = (\alpha - \alpha^*) e^{-(\alpha^* - \alpha)^2/2}$$

(c) $\langle 0_{phon}| e^{(\alpha - \alpha^*)(\hat{b}^\dagger - \hat{b})} \hat{b}^\dagger |0_{phon}\rangle = (\alpha^* - \alpha) e^{-(\alpha - \alpha^*)^2/2}$

(d) $2\alpha \langle 0_{phon}| e^{\pm(\alpha - \alpha^*)(\hat{b}^\dagger - \hat{b})} |0_{phon}\rangle = 2\alpha e^{-(\alpha^* - \alpha)^2/2}$

Finally, using the latter equation, we obtain:

$$\boxed{\langle H_B \rangle = \hat{g} \langle \psi_S| \langle 0_{phon}| U_P^\dagger\ g\hat{\sigma}_z(\hat{b}^\dagger + \hat{b})\ U_P^{(2)} |0_{phon}\rangle |\psi_S\rangle = \hat{g} e^{-(\alpha - \alpha^*)^2/2}(\alpha + \alpha^*)} \tag{G.12}$$

G.4 Ground state energy calculation:

Thus, gathering equations (G.5), (G.9) and (G.12), we obtain:

$$\epsilon_{gs}(\alpha) = \frac{\hat{\Delta}}{2}(1 + e^{-(\alpha^* + \alpha)^2/2})(\beta^* \theta + \theta^* \beta) + \hat{g} e^{-(\alpha - \alpha^*)^2/2}(\alpha + \alpha^*) + \omega_v |\alpha|^2 e^{-\frac{\alpha^{*2} + \alpha^2}{2}} e^{|\alpha|^2} + \epsilon \tag{G.13}$$

The minimization with respect to β and θ is easy as ϵ_{gs} is minimized when $\beta^* \theta + \theta^* \beta$ is a minimum. The solution is $\beta = 1/\sqrt{2}$, $\theta = -1/\sqrt{2}$. Notice

that $\langle\psi_S|\hat{\sigma}_x|\psi_S\rangle = \beta^*\theta + \theta^*\beta$, so the minimum occurs for an eigenstate with $\langle\hat{\sigma}_x\rangle = -1$. This justifies equation (2.45):

$$|\psi_s\rangle = \frac{|+\rangle - |-\rangle}{\sqrt{2}}$$

Furthermore, assumming that $\alpha \in \mathbb{R}$, we obtain:

$$\boxed{\epsilon_{gs}(\alpha) = \frac{\hat{\Delta}}{2}(1 - e^{-\alpha^2/2}) + 2\alpha\hat{g} + \omega_v\ \alpha^2 + \tilde{\epsilon}} \tag{G.14}$$

The firsrt derivative of $\epsilon_{gs}(\alpha)$ vanishes for:

$$\alpha = -\frac{\hat{g}}{\hat{\Delta}e^{-2\alpha^2} + \omega_v} \tag{G.15}$$

and, as the second derivative is bigger than zero $\forall\alpha$, α will be the value which minimize (G.14). Thus, we have justified the equation (2.46)

G.5 Demonstration of the relation (G.11)

In this section, we are going to show the relation (G.11). In general, this relation is valid for three arbitrary operators P, Q y A:

$$\text{If: } [P, A] = 0 \text{ and } [Q, A] = P \longrightarrow [Q, e^A] = Pe^A \tag{G.16}$$

We are going to show the latter theorem:

$$[Q, e^A] = [Q, \sum_{k=0}^{\infty} \frac{1}{k!}A^k] = \sum_{k=0}^{\infty}[Q, \frac{1}{k!}A^k] = \cdots$$

Now, using $[P, A] = 0$ and $[Q, A] = P$, we have to notice that:

$$\begin{aligned}
&A^kQ = A^{k-1}(QA - P) = A^{k-1}QA - A^{k-1}P = \\
&= A^{k-2}(QA - P)A - A^{k-1}P = \\
&= A^{k-2}QA^2 - 2A^{k-1P} = \overbrace{\cdots}^{k \text{ times}} \\
&\cdots = QA^k - kA^{k-1}P
\end{aligned}$$

continuing with $[Q, e^A]$:

$$\cdots = \sum_{k=0}^{\infty} \frac{1}{k!}(QA^k - A^kQ) = \sum_{k=0}^{\infty} \frac{k}{k!}A^{k-1}P = P\sum_{k=0}^{\infty} \frac{1}{k!}A^k = e^AP$$

In our case, Q, P and A are:

$$Q = \hat{\sigma}_z(\hat{b}^\dagger + \hat{b}) \tag{G.17}$$

$$P = 2\alpha \tag{G.18}$$

$$A = \alpha\hat{\sigma}_z(\hat{b}^\dagger - \hat{b}) \tag{G.19}$$

Since, they fulfil $[P, A] = 0$ and $[Q, A] = P$; we have shown that the theorem (G.11) is true in our case.

Appendix H

Janyes-Cummings effective model derivation

In order to obtain the effective Jaynes-Cummings model (2.50), we are going to start from the *effective Rabi* model (2.15):

$$H_{\text{eff}} = \frac{\hat{\Delta}}{2}(\hat{\sigma}_z + 1) + \omega_v \hat{b}^\dagger \hat{b} + \hat{g}\hat{\sigma}_x(\hat{b}^\dagger + \hat{b}) + \epsilon$$

where:

$$\hat{\Delta} = 2g \qquad \hat{g} = \frac{\omega_v \lambda}{2} \qquad \epsilon = \omega_c + \frac{\omega_v \lambda^2}{4} - g \tag{H.1}$$

Now, we are going to change the basis ($\hat{\sigma}_x \leftrightarrow \hat{\sigma}_z$) and we apply a second polaron transformation $U_P^{(2)} = e^{\alpha\hat{\sigma}_z(\hat{b}^\dagger - \hat{b})}$, where:

$$\alpha = -\frac{\hat{g}}{\tilde{\Delta} + \omega_v} \qquad \tilde{\Delta} = \hat{\Delta}e^{-2\alpha^2} \tag{H.2}$$

After the change of basis, we get:

$$H_{\text{eff}} = \frac{\hat{\Delta}}{2}(\hat{\sigma}_x + 1) + \omega_v \hat{b}^\dagger \hat{b} + \hat{g}\hat{\sigma}_z(\hat{b}^\dagger + \hat{b}) + \tilde{\epsilon}$$

We now apply the polaron transformation $U_P^{(2)} = e^{\alpha\hat{\sigma}_z(\hat{b}^\dagger - \hat{b})}$ and defining that $\hat{\sigma}_z |\uparrow\rangle = |\uparrow\rangle$ and $\hat{\sigma}_z |\downarrow\rangle = -|\downarrow\rangle$, we notice that:

$$U_P^{\dagger\,(2)}\hat{\sigma}_x U_P^{(2)} = e^{-\alpha\hat{\sigma}_z(\hat{b}^\dagger - \hat{b})}\hat{\sigma}_x e^{\alpha\hat{\sigma}_z(\hat{b}^\dagger - \hat{b})} = e^{-\alpha\hat{\sigma}_z(\hat{b}^\dagger - \hat{b})}(|\uparrow\rangle\langle\downarrow| + |\downarrow\rangle\langle\uparrow|)e^{\alpha\hat{\sigma}_z(\hat{b}^\dagger - \hat{b})} =$$
$$= e^{-2\alpha(\hat{b}^\dagger - \hat{b})}\hat{\sigma}^+ + e^{2\alpha(\hat{b}^\dagger - \hat{b})}\hat{\sigma}^- \approx e^{-2\alpha^2}((1 - 2\alpha(\hat{b}^\dagger - \hat{b}))\hat{\sigma}^+ + (1 + 2\alpha(\hat{b}^\dagger - \hat{b}))\hat{\sigma}^-)$$

where we have approximated the displacement operators to their linear terms. Taking the last relation into account, we are going to apply the polaron trans-

formation to H_{eff}:

$$H_{\text{JC}}^{\text{eff}} = {U_P^{(2)}}^{\dagger} H_{\text{eff}} U_P^{(2)} = \cdots$$

$$= \frac{\hat{\Delta}}{2} e^{-2\alpha^2}((1-2\alpha(\hat{b}^\dagger - \hat{b}))\hat{\sigma}^+ + (1+2\alpha(\hat{b}^\dagger - \hat{b}))\hat{\sigma}^-)$$

$$+\omega_v(\hat{b}^\dagger + \alpha\hat{\sigma}_z)(\hat{b} + \alpha\hat{\sigma}_z) + \hat{g}\hat{\sigma}_z(\hat{b}^\dagger + \hat{b} + 2\alpha\hat{\sigma}_z) + \tilde{\epsilon} = \frac{\tilde{\Delta}}{2}\hat{\sigma}_x + \omega_v\hat{b}^\dagger\hat{b}$$

$$-\tilde{\Delta}\alpha(\hat{\sigma}^+ - \hat{\sigma}^-)(\hat{b}^\dagger - \hat{b}) + (\omega_v\alpha + \hat{g})\hat{\sigma}_z(\hat{b}^\dagger + \hat{b}) + \omega_v\alpha^2 + 2\alpha\hat{g} + \frac{\hat{\Delta}}{2} + \tilde{\epsilon} = \cdots$$

taking into account that $\omega_v\alpha + \hat{g} = -\tilde{\Delta}\alpha$ (see (H.2)), we obtain[1]:

$$H_{\text{JC}}^{\text{eff}} = \frac{\tilde{\Delta}}{2}(\hat{\sigma}_x+1)+\omega_v\hat{b}^\dagger\hat{b}-\tilde{\Delta}\alpha(\hat{\sigma}^+-\hat{\sigma}^-)(\hat{b}^\dagger-\hat{b})-\tilde{\Delta}\alpha\hat{\sigma}_z(\hat{b}^\dagger+\hat{b})+\underbrace{\omega_v\alpha^2 + 2\alpha\hat{g} + \frac{\hat{\Delta}}{2} + \epsilon}_{\tilde{\epsilon}} - \frac{\tilde{\Delta}}{2}$$

where we have defined a new constant $\tilde{\epsilon}$:

$$\tilde{\epsilon} = \omega_v\alpha^2 + 2\alpha\hat{g} + \frac{\hat{\Delta}}{2} + \epsilon = \omega_v\alpha^2 + 2\alpha\hat{g} + \cancel{\frac{\hat{\Delta}}{2}} + \omega_c + \frac{\omega_v\lambda^2}{4} - \cancel{g}$$

where $\hat{\Delta} = 2g$:

$$\boxed{\tilde{\epsilon} = \omega_v\alpha^2 + 2\alpha\hat{g} + \omega_c + \frac{\omega_v\lambda^2}{4}} \tag{H.3}$$

Thus, the Hamiltonian is:

$$H_{\text{JC}}^{\text{eff}} = \frac{\tilde{\Delta}}{2}(\hat{\sigma}_x + 1) + \omega_v\hat{b}^\dagger\hat{b} - \tilde{\Delta}\alpha(\hat{\sigma}^+ - \hat{\sigma}^-)(\hat{b}^\dagger - \hat{b}) - \tilde{\Delta}\alpha\hat{\sigma}_z(\hat{b}^\dagger + \hat{b}) + \tilde{\epsilon} - \frac{\tilde{\Delta}}{2}$$

Now, we go back to the original basis ($\hat{\sigma}_x \leftrightarrow \hat{\sigma}_z$), and rearrange the terms of the latter equations. But, before, we have to notice that $\hat{\sigma}^+$ and $\hat{\sigma}^-$ after the change of basis are:

$$\hat{\sigma}^+ \longrightarrow \frac{1}{2}(\hat{\sigma}_z - i\hat{\sigma}_y) \tag{H.4}$$

$$\hat{\sigma}^- \longrightarrow \frac{1}{2}(\hat{\sigma}_z + i\hat{\sigma}_y) \tag{H.5}$$

Therefore the term $\hat{\sigma}^+ - \hat{\sigma}^-$ after the change of basis is:

$$\hat{\sigma}^+ - \hat{\sigma}^- \longrightarrow -i\hat{\sigma}_y = -(\hat{\sigma}_P^+ - \hat{\sigma}_P^-) \tag{H.6}$$

Thus, $H_{\text{JC}}^{\text{eff}}$ in the original basis is (with $\hat{\sigma}_x = \hat{\sigma}_P^+ + \hat{\sigma}_P^-$):

$$H_{\text{JC}}^{\text{eff}} = \frac{\tilde{\Delta}}{2}(\hat{\sigma}_z + 1) + \omega_v\hat{b}^\dagger\hat{b} + \tilde{\Delta}\alpha(\hat{\sigma}_P^+ - \hat{\sigma}_P^-)(\hat{b}^\dagger - \hat{b}) - \tilde{\Delta}\alpha(\hat{\sigma}_P^+ + \hat{\sigma}_P^-)(\hat{b}^\dagger + \hat{b})$$

$$+\tilde{\epsilon} - \frac{\tilde{\Delta}}{2} = \tilde{\Delta}\hat{\sigma}_P^+\hat{\sigma}_P^- + \omega_v\hat{b}^\dagger\hat{b} + \cancel{\tilde{\Delta}\alpha(\hat{\sigma}_P^+\hat{b}^\dagger + \hat{\sigma}_P^-\hat{b})} - \tilde{\Delta}\alpha(\hat{\sigma}_P^-\hat{b}^\dagger + \hat{\sigma}_P^+\hat{b}) -$$

$$-\cancel{\tilde{\Delta}\alpha(\hat{\sigma}_P^+\hat{b}^\dagger + \hat{\sigma}_P^-\hat{b})} - \tilde{\Delta}\alpha(\hat{\sigma}_P^-\hat{b}^\dagger + \hat{\sigma}_P^+\hat{b}) + \tilde{\epsilon} - \frac{\tilde{\Delta}}{2}$$

[1] Notice that we are sum and substrate the constant $\tilde{\Delta}/2$.

Finally, we arrive to the *effective Jaynes-Cummings* model (2.50):

$$\boxed{H_{\mathrm{JC}}^{\mathrm{eff}} = \tilde{\Delta}\hat{\sigma}_P^+\hat{\sigma}_P^- + \omega_v\hat{b}^\dagger\hat{b} - 2\tilde{\Delta}\alpha(\hat{\sigma}_P^-\hat{b}^\dagger + \hat{\sigma}_P^+\hat{b}) + \tilde{\epsilon} - \frac{\tilde{\Delta}}{2}} \tag{H.7}$$

We have to do the approximations presented in this appendix in order to obtain a good *effective Jaynes-Cummings* model. Because, if we directly neglect the counterrotaing terms of the *effective Rabi model* (2.15), we obtain a very bad approximation [cf. red dotted curves, figure H.1].

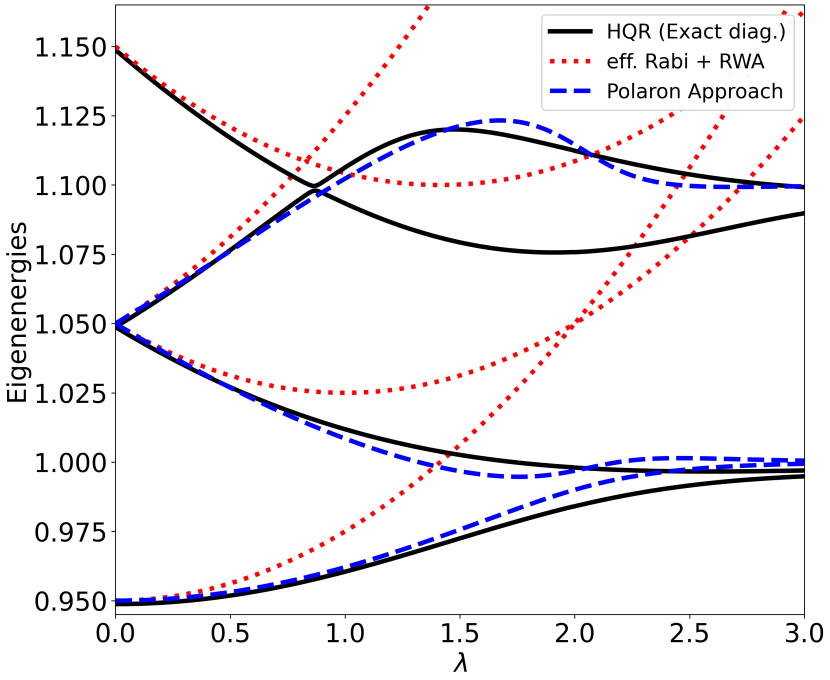

Figure H.1: At ***bare resonance***, comparison of the energy spectrum of the polariton sector between the HQR model (black curves), the *effective Jaynes-Cummings model* (2.50) (blue dahed curves) and the direct RWA over the *effective Rabi model* (2.15) (red dotted curves). Parameters: $\omega_c = \Delta = 1$, $\omega_v = 0.1$ and $g = 0.05$.

Appendix I

Analytical frequency weights

I.1 Main weights p_{10} and p_{20}

In this section we give the analytical expressions of $\delta_{\pm,n}$ which appear in the weights (3.10):

$$p_{(1,2)0} = \frac{1}{2}\frac{(\delta_{\pm,0}|D_{0\tilde{0}}(\lambda/2+\alpha)|^2 - D_{1\tilde{0}}(\lambda/2+\alpha)D^{\dagger}_{0\tilde{0}}(\lambda/2+\alpha))\delta_{\mp,0}}{\delta^2_{\mp}+1} \tag{I.1}$$

where $\delta_{\pm,n}$ and $\beta_{\pm,n}$ are:

$$\delta_{\pm,n} = \frac{2\beta_{\mp,n} - \tilde{\Delta}}{4\alpha\tilde{\Delta}\sqrt{1+n}} \tag{I.2}$$

$$\beta_{\pm,n} = \frac{\omega_v \pm \sqrt{\tilde{\Delta}^2(1+16(1+n)\alpha^2) + \omega_v(\omega_v - 2\tilde{\Delta})}}{2} \tag{I.3}$$

and

$$\tilde{\Delta} = \hat{\Delta}e^{-2|\alpha|^2} = 2ge^{-2|\alpha|^2} \tag{I.4}$$

$$\alpha = -\frac{\hat{g}}{2ge^{-2|\alpha|^2} + \omega_v} \tag{I.5}$$

I.2 Other frequencies

As we have said in section 3.2.2, we can diagonalize the *effective Jaynes-Cummings* model (2.50) and obtain more than the first three energies, cf. table I.1.

Energies	**Eigenstates** ($n = 1, 2, ...$)
ϵ_0	$\|P_0\rangle = \|0\ 0_{phon}\rangle$
ϵ_{2n-1}	$\|P_{2n-1}\rangle = \frac{1}{\sqrt{\delta_{-,n}^2+1}}\left(\|P_-^{(1)}\ n_{phon}\rangle + \delta_{-,n}\,\|P_+^{(1)}\ (n-1)_{phon}\rangle \right)$
ϵ_{2n}	$\|P_{2n}\rangle = \frac{1}{\sqrt{\delta_{+,n}^2+1}}\left(\|P_-^{(1)}\ n_{phon}\rangle + \delta_{+,n}\,\|P_+^{(1)}\ (n-1)_{phon}\rangle \right)$

Table I.1: Eigenenergies and eigenstates of the model (2.50).

With this we can compute the Fourier spectrum of the time evolution of our system. First, we calculate the weight of our initial state (3.9) in each eigenstate:

$$p_0 \equiv \langle P_0|\tilde{\psi}(0)\rangle = -\frac{1}{\sqrt{2}} D_{0\tilde{0}}(\lambda/2+\alpha) \tag{I.6}$$

$$\begin{aligned} p_{2n-1} \equiv \langle P_{2n-1}|\tilde{\psi}(0)\rangle = \frac{1}{\sqrt{2(\delta_{-,n-1}^2+1)}} (&\delta_{-,n-1} D_{n-1\ \tilde{0}}(\lambda/2+\alpha) \\ &- D_{n\tilde{0}}(\lambda/2+\alpha)) \end{aligned} \tag{I.7}$$

$$p_{2n} \equiv \langle P_{2n}|\tilde{\psi}(0)\rangle = \frac{1}{\sqrt{2(\delta_{+,n-1}^2+1)}} (\delta_{+,n-1} D_{n-1\ \tilde{0}}(\lambda/2+\alpha) - D_{n\tilde{0}}(\lambda/2+\alpha)) \tag{I.8}$$

where $n = 1,\ 2,\ ...$ and $D_{\tilde{m}n}(\alpha)$ are Franck-Condon factors [cf. appendix E]. Thus, the time evolution of the wave function is:

$$\begin{aligned} |\psi(t)\rangle = {} & p_0 e^{-i\epsilon_0 t}\,|P_-^{(1)}\ 0_{phon}\rangle \\ & + \sum_{n=0}^{\infty} \left[\frac{p_{2n+1} e^{-i\epsilon_{2n+1}t}}{\sqrt{\delta_{-,n}^2+1}} \left(|P_-^{(1)}\ (n+1)_{phon}\rangle + \delta_{-,n}\,|P_+^{(1)}\ n_{phon}\rangle \right) + \right. \\ & \left. + \frac{p_{2n+2} e^{-i\epsilon_{2n+2}t}}{\sqrt{\delta_{+,n}^2+1}} \left(|P_-^{(1)}\ (n+1)_{phon}\rangle + \delta_{+,n}\,|P_+^{(1)}\ n_{phon}\rangle \right) \right] \end{aligned}$$

With these ingredients, we can calculate the expected value of $\langle \sigma_x/2 \rangle (t)$ in order to obtain the weights of the different frequencies:

$$\langle \sigma_x/2 \rangle (t) = -\sum_{n=1}^{2} p_{n,0} \cos(\Delta\epsilon_{n,0} t) - \sum_{n=0}^{\infty} \sum_{m=3}^{4} \sum_{l=1}^{2} p_{2n+m,2n+l} \cos(\Delta\epsilon_{2n+m,2n+l} t) \tag{I.9}$$

where $\Delta\epsilon_{n,m} = \epsilon_n - \epsilon_m$. The analytical weights p_{nm} of (I.9) only give us a qualitative behaviour. Thus, the explicit version of equation (I.9) is:

$$\begin{aligned}
\frac{1}{2} \langle \psi(t) | \sigma_x | \psi(t) \rangle = & \sum_{n=1}^{2} \frac{\delta_{-,0}}{\sqrt{\delta_{-,0}^2 + 1}} p_0 p_n \cos((\epsilon_n - \epsilon_0) t) \\
& + \sum_{n=0}^{\infty} \left[\frac{\delta_{-,n+1}}{\sqrt{(\delta_{-,n+1}^2 + 1)(\delta_{-,n}^2 + 1)}} p_{2n+3} p_{2n+1} \cos((\epsilon_{2n+3} - \epsilon_{2n+1}) t) + \right. \\
& + \frac{\delta_{-,n+1}}{\sqrt{(\delta_{-,n+1}^2 + 1)(\delta_{+,n}^2 + 1)}} p_{2n+3} p_{2n+2} \cos((\epsilon_{2n+3} - \epsilon_{2n+2}) t) + \\
& + \frac{\delta_{+,n+1}}{\sqrt{(\delta_{+,n+1}^2 + 1)(\delta_{-,n}^2 + 1)}} p_{2n+4} p_{2n+1} \cos((\epsilon_{2n+4} - \epsilon_{2n+1}) t) + \\
& \left. + \frac{\delta_{+,n+1}}{\sqrt{(\delta_{+,n+1}^2 + 1)(\delta_{+,n}^2 + 1)}} p_{2n+4} p_{2n+2} \cos((\epsilon_{2n+4} - \epsilon_{2n+2}) t) \right]
\end{aligned} \tag{I.10}$$

We could do the same calculation but with the approximate model (3.4). In that case, we only have to substitute $\lambda/2 + \alpha \to \lambda/2$ and $\delta_{\pm,n} \to \tau_{\pm,n}$. So, we have obtained many spectral weights p_{nm} of the different frequencies $\epsilon_n - \epsilon_m$, as we can see in the equation (I.10). Thus, for instance, our weight p_{10} corresponds to:

$$p_{10} = -\frac{\delta_{-,0}}{\sqrt{\delta_{-,0}^2 + 1}} p_0 p_1 \tag{I.11}$$

In figure I.1, we plot the weight p_{31} for three cases: (1) The black line corresponds to the analytical expression obtained from[1] (I.10), (2) the red and blue lines are the weight obtained numerically with the *effective Rabi* model (2.15); and (3) the green and yellow lines are the weight obtained numerically with the HQR model (1.35).

[1] Expression obtained from the *effective Jaynes-Cummings* model (2.50).

In the second and third case, we have also plotted the weight p_{21} due to the crossing and anticrossing of the eigenstates of the polariton subspace $|\epsilon_3\rangle$ and $|\epsilon_2\rangle$. As we can see in the figure I.1, the analytical expression (black curve) only gives us a qualitative behaviour. Finally, we have also repeated the calculus at ***dressed resonance***, $\Delta = \omega_c - \delta_{BS}$ (by considering the "dressing" of the cavity energy due to the Bloch-Siegert term, see section 2.3). In that case, the peaks of the green and yellow curves disappear because we now have a crossing instead of an anticrossing in the HQR model, see figure I.2.

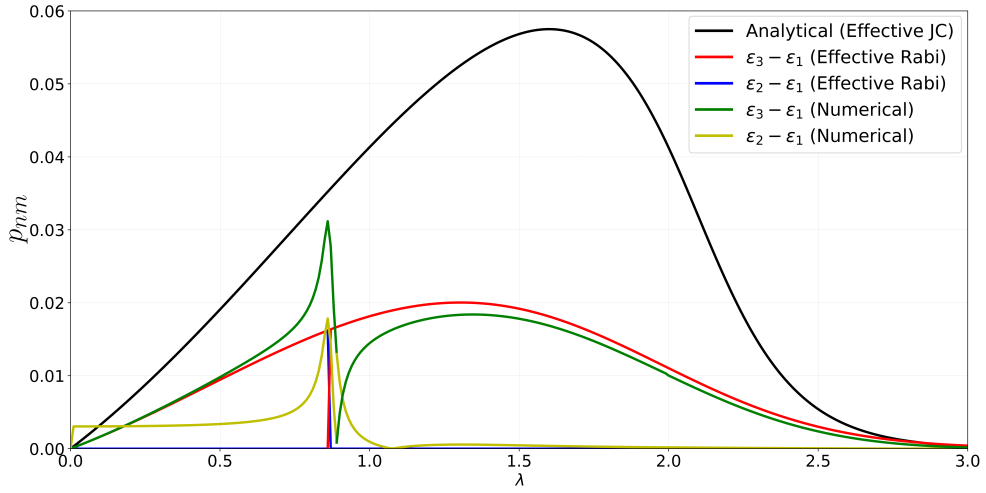

(a)

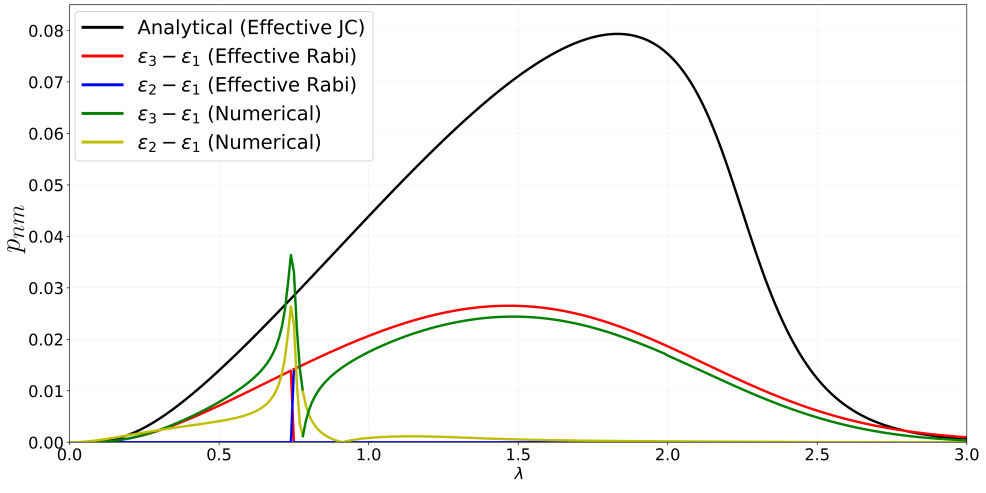

(b)

Figure I.1: At ***bare resonance***, analytical weights (black curves) from *effective Jaynes-Cummings* (2.50); numerical weights (red and blue curves) from *effective Rabi* (2.15)) and numerical weights (yellow and green curves) from *Holstein-Quantum-Rabi* (1.35) (a) case $2g = \omega_v$ (b) case $2g \neq \omega_v$ ($\omega_v = 0.075$). The other parameters are $g = 0.05$, $\Delta = 1$, $\omega_c = \Delta$ and $|\psi(0)\rangle = |\downarrow\ 1_{phot}\ 0_{phon}\rangle$.

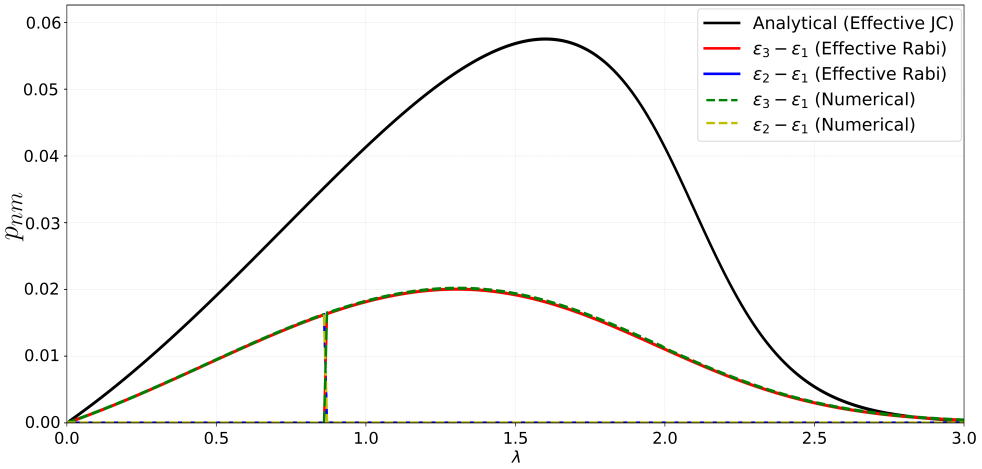

(a)

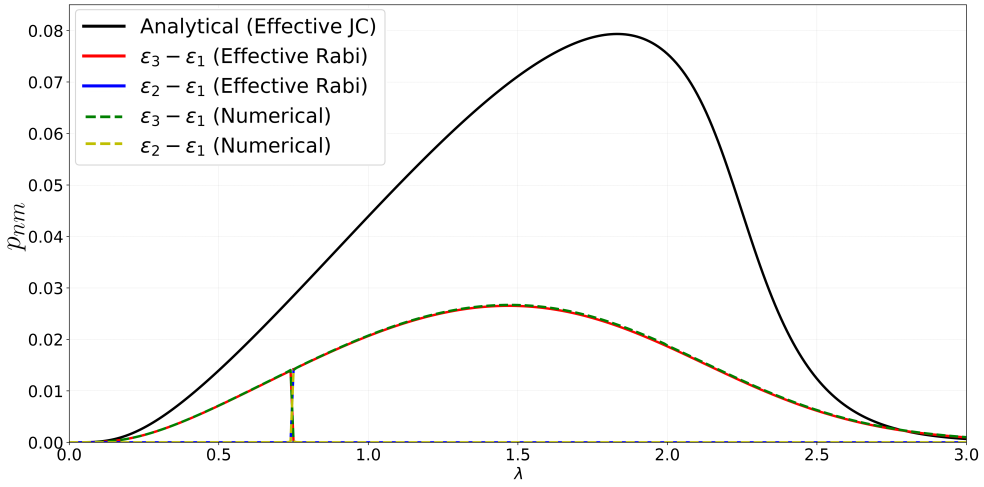

(b)

Figure I.2: At ***dressed resonance***, analytical weights (black curves) from *effective Jaynes-Cummings* (2.50); numerical weights (red and blue curves) from *effective Rabi* (2.15)) and numerical weights (yellow and green curves) from *Holstein-Quantum-Rabi* (1.35)(a) case $2g = \omega_v$ (b) case $2g \neq \omega_v$ ($\omega_v = 0.075$). The other parameters are $g = 0.05$, $\Delta = 1$, $\omega_c = \Delta + \delta_{BS}$ and $|\psi(0)\rangle = |\downarrow\ 1_{phot}\ 0_{phon}\rangle$.

However, there are some frequency combinations that they do not appear in the equation (I.9), such as the frequencies $\epsilon_n - \epsilon_0$ with $n > 2$. The reason for that it is that in order to obtain the *effective Jaynes-Cummings model* (3.4), we have approximate $D(-2\alpha) = e^{-2\alpha(b^\dagger - b)} = e^{-2|\alpha|^2} e^{-2\alpha b^\dagger} e^{2\alpha b} \approx e^{-2|\alpha|^2}(1 - 2\alpha(b^\dagger - b))$ to order α. If had approximated to α^2 order, we would have obtained:

$$H = \underbrace{\tilde{\Delta}\sigma_p^+\sigma_p^- + \Omega b^\dagger b - 2\tilde{\Delta}\alpha(b^\dagger\sigma_p^- + b\sigma_p^-) + \epsilon}_{H_0} + \alpha^2\tilde{\Delta}\underbrace{\sigma_p^z\Big((b^{\dagger 2} + b^2) - 2b^\dagger b\Big)}_{V} \tag{I.12}$$

If we treat the term V of the new Hamiltonian (I.12) as a perturbation, we can notice that the $\hat{b}$'s quadratic terms would generate frequencies such as $\epsilon_5 - \epsilon_0$. In order to obtain other terms, we should add to the Hamiltonian (I.12) terms of superior order in α.

Appendix J

Energy losses

J.1 Holstein model

J.1.1 Decay due to losses in the electronic sector

In this appendix, we are going to obtain an approximate analytical expression for the decay of the electronic (matter) excitations in the *Holstein* model (1.26):

$$H = \Delta\hat{\sigma}^{+}\hat{\sigma}^{-} + \omega_v(\hat{b}^{\dagger}\hat{b} + \lambda\hat{\sigma}^{+}\hat{\sigma}^{-}(\hat{b}^{\dagger} + \hat{b} + \lambda))$$

As we saw in section 1.5, we can easily diagonalize it using a Polaron transformation $U = \exp(-\lambda\hat{\sigma}^{+}\hat{\sigma}^{-}(\hat{b}^{\dagger} - \hat{b}))$:

$$U^{\dagger}HU = \Delta\hat{\sigma}^{+}\hat{\sigma}^{-} + \omega_v\hat{b}^{\dagger}\hat{b}$$

So, the basis, where the *Holstein* model (1.26) is diagonal, is $\{|\downarrow\ n_{phon}\rangle\,,\ |\uparrow\ \tilde{n}_{phon}\rangle\}$. We are going to calculate the expected value of matter excitations $\langle\hat{\sigma}^{+}\hat{\sigma}^{-}\rangle(t)$ when we have energy losses in the matter sector.

We consider an initial state $\rho(t=0) = |\uparrow\ \tilde{0}_{phon}\rangle\langle\uparrow\ \tilde{0}_{phon}|$, and use the master equation formalism [cf. section 1.6]:

$$\frac{d\rho(t)}{dt} = -i[H,\rho(t)] + \gamma_{matter}\sum_{\omega>0}\omega\left(A(\omega)\rho(t)A^{\dagger}(\omega) - \frac{1}{2}\{A^{\dagger}(\omega)A(\omega),\ \rho(t)\}\right) \tag{J.1}$$

where γ_{matter} is a parameter that quantifies the decay of electronic excitations and $\hat{A}(\omega) = \sum_{\epsilon'-\epsilon=\omega}|\epsilon\rangle\langle\epsilon|\,\hat{A}\,|\epsilon'\rangle\langle\epsilon'|$ is the spectral decomposition of the coupling operator $\hat{A} = \hat{\sigma}^{+} + \hat{\sigma}^{-}$ between the system and the bath [cf. section 1.6].

In the diagonal basis $\{|\downarrow\ n_{phon}\rangle\,,\ |\uparrow\ \tilde{n}_{phon}\rangle\}$, we obtain:

$$\hat{A}(\omega) = \sum_{-\Delta+(m-\tilde{k})\omega_v=\omega} D_{\tilde{k}m}(\lambda)\hat{\sigma}^+ \left|\tilde{k}\right\rangle \langle m| \ + \sum_{\Delta+(\tilde{m}-k)\omega_v=\omega} D_{k\tilde{m}}(-\lambda)\hat{\sigma}^- \left|k\right\rangle \langle \tilde{m}| \quad \text{(J.2)}$$

where $D_{\tilde{m}n}(\alpha)$ are the Franck-Condon factors [cf. appendix E]. The calculation of $\langle\hat{\sigma}^+\hat{\sigma}^-\rangle\,(t)$ is done via:

$$\langle\hat{\sigma}^+\hat{\sigma}^-\rangle\,(t) = \mathrm{Tr}[\hat{\sigma}^+\hat{\sigma}^-\rho(t)] = \sum_{\tilde{n}} \rho_{\uparrow\tilde{n}\uparrow\tilde{n}} \quad \text{(J.3)}$$

where $\rho_{\uparrow\tilde{n}\uparrow\tilde{n}} = \langle\uparrow \tilde{n}_{phon}|\rho(t)|\uparrow \tilde{n}_{phon}\rangle$ are the diagonal elements of the density matrix ρ in the basis $\{|\downarrow\ n_{phon}\rangle\,,\ |\uparrow\ \tilde{n}_{phon}\rangle\}$. So we need to obtain the diagonal elements of the master equation of the *Holstein* model (J.1).

$$\dot{\rho}_{\uparrow\tilde{n}\uparrow\tilde{n}} = \gamma_{matter}\left[\sum_{k\omega_v-(\Delta+\tilde{n}\omega_v)>\omega} \omega\ \Gamma_{k\tilde{n}}\ \rho_{\downarrow k\downarrow k} - \sum_{(\Delta+\tilde{n}\omega_v)-k\omega_v>\omega} \omega\ \Gamma_{\tilde{n}k}\ \rho_{\uparrow\tilde{n}\uparrow\tilde{n}}\right] \quad \text{(J.4)}$$

$$\dot{\rho}_{\downarrow n\downarrow n} = \gamma_{matter}\left[\sum_{(\Delta+\tilde{k}\omega_v)-n\omega_v>\omega} \omega\ \Gamma_{\tilde{k}n}\ \rho_{\uparrow\tilde{k}\uparrow\tilde{k}} - \sum_{n\omega_v-(\Delta+\tilde{k}\omega_v)>\omega} \omega\ \Gamma_{n\tilde{k}}\ \rho_{\downarrow n\downarrow n}\right] \quad \text{(J.5)}$$

where $\Gamma_{\tilde{n}k} = |\,\langle k|\tilde{n}\rangle\,|^2 = |D_{k\tilde{n}}(-\lambda)|^2$. The first equation (J.4) describes the change in $\rho_{\uparrow\tilde{n}\uparrow\tilde{n}}$ as a function of time. The first term expresses the increase of $\rho_{\uparrow\tilde{n}\uparrow\tilde{n}}$ due to a transition from a state $|\downarrow\ k_{phon}\rangle$ to the excited state $|\uparrow\ \tilde{n}_{phon}\rangle$. This transition takes place if the energy of the first state $E = k\omega_v$ is bigger than the second one $E = \Delta + \tilde{n}\omega_v$. This transition is weighted by the overlap between the vibrational states which take part in the transition i.e. the *Franck-Condon factors* $\Gamma_{\tilde{n}k}$. Thus, we can adopt the notation: $\Gamma_{k\tilde{n}} \equiv \Gamma_{k\to\tilde{n}}$.

On the other hand, the second term expresses the decrease of $\rho_{\uparrow\tilde{n}\uparrow\tilde{n}}$ due to each transition from the state $|\uparrow\ \tilde{n}_{phon}\rangle$ to states of the electronic ground state manifold $|\downarrow\ k_{phon}\rangle$ of smaller energy than $E = \Delta + \tilde{n}\omega_v$. Thus, we can adopt the notation: $\Gamma_{\tilde{n}k} \equiv \Gamma_{\tilde{n}\to k}$.

We can interpret the equation (J.5) in the same manner. The first term describes the increase in $\rho_{\downarrow n\downarrow n}$ due to transitions : $|\uparrow\ \tilde{k}_{phon}\rangle \to |\downarrow\ n_{phon}\rangle$ and the second term describes the decrease due to the transitions $|\downarrow\ n_{phon}\rangle \to |\uparrow\ \tilde{k}_{phon}\rangle$. As, our initial state is $|\psi(t=0)\rangle = |\uparrow\ \tilde{0}_{phon}\rangle$, we are going to neglect the transitions $|\downarrow\ n_{phon}\rangle \to |\uparrow\ \tilde{k}_{phon}\rangle$ and $|\downarrow\ k_{phon}\rangle \to |\uparrow\ \tilde{n}_{phon}\rangle$ the equations (J.4) and (J.5), respectively, as these transitions would require a supply of additional energy.

Thus, we arrive to the following system of equations:

$$\dot{\rho}_{\uparrow\tilde{n}\uparrow\tilde{n}} \approx -\gamma_{matter} \sum_{(\Delta+\tilde{n}\omega_v)-k\omega_v>\omega} \omega\ \Gamma_{\tilde{n}\to k}\ \rho_{\uparrow\tilde{n}\uparrow\tilde{n}} \tag{J.6}$$

$$\dot{\rho}_{\downarrow n\downarrow n} \approx \gamma_{matter} \sum_{(\Delta+\tilde{k}\omega_v)-n\omega_v>\omega} \omega\ \Gamma_{\tilde{k}\to n}\ \rho_{\uparrow\tilde{k}\uparrow\tilde{k}} \tag{J.7}$$

After some algebra, we arrive to an analytical expression for the number of matter excitations the equation (3.11), shown in section 3.3:

$$\langle \hat{\sigma}^+\hat{\sigma}^- \rangle (t) = \exp\left[-\gamma_{matter} \sum_{\omega_{\tilde{0}m}>0} \omega_{\tilde{0}m}\Gamma_{\tilde{0}\to m} t \right] \tag{J.8}$$

where $\omega_{\tilde{n}m} = (\Delta + \tilde{n}\omega_v) - m\omega_v$. Using the values $\Delta = 1$, $\omega_v = 0.1$ and $|\psi(t=0)\rangle = |\uparrow\ \tilde{0}_{phon}\rangle$, we can compare the numerical calculation with the analytical expression (J.8), see figure J.1. Thus we obtain a very good result which captures the most important exponential involved in the decay.

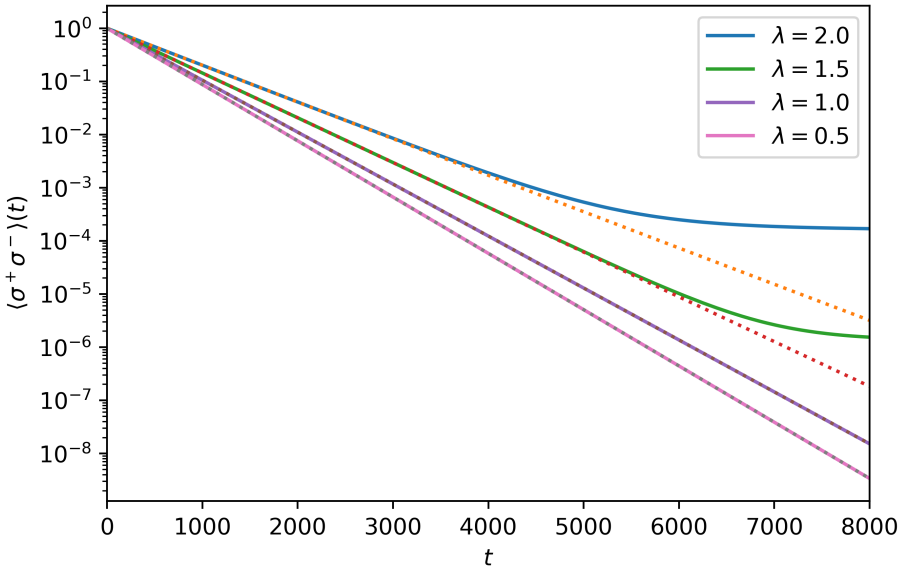

Figure J.1: Time evolution of the matter excitations $\langle \hat{\sigma}^+\hat{\sigma}^- \rangle (t)$ in the Holstein model (1.26) for several values of matter-phonon coupling λ. Parameters: $\gamma_{matter} = 2.5 \times 10^{-3}$, $\omega_v = 0.1$, $\Delta = 1$ and $\rho(t=0) = |\uparrow\ \tilde{0}_{phon}\rangle\langle\uparrow\ \tilde{0}_{phon}|$.

J.1.2 Dependence of the decay with ω_v

As we have shown in the previous section, the matter losses γ_{matter} are renormalized by the factor:

$$\gamma_{\tilde{n}}(\lambda, \omega_v) = \sum_{\omega_{\tilde{n}m}>0} \omega_{\tilde{n}m}\Gamma_{\tilde{n}\to m} \qquad \text{when: } \tilde{n}=0 \tag{J.9}$$

This factor is a sum over all the transitions, which fulfill $\omega_{\tilde{n}m} > 0$, weighted by the *Franck-Condon* factors $\Gamma_{\tilde{n}\to m}$. It can also be shown easily that the renormalization (J.9) disappears when we have a continuum of phonons i.e. when $\omega_v \to 0^+$ then $\gamma_{\tilde{n}}(\lambda) \to 1$. Thus, we have:

$$\gamma_{\tilde{n}}(\lambda) = \sum_{m<\tilde{n}+\Delta/\omega_v} \Big(\Delta + \omega_v(\tilde{n}-m)\Big)\Gamma_{\tilde{n}m} \xrightarrow{\omega_v\to 0^+}$$

$$\xrightarrow{\omega_v\to 0^+} \Delta \sum_{m<\infty} \Gamma_{\tilde{n}m} + \tilde{n}\omega_v \sum_{m<\infty} \Gamma_{\tilde{n}m} - \omega_v \sum_{m<\infty} m\Gamma_{\tilde{n}m} \xrightarrow{\omega_v\to 0^+} \sum_{m=0}^{\infty} \Gamma_{\tilde{n}m} = 1 \tag{J.10}$$

where we have used the following properties (derived in appendix E.1):

$$\sum_{m=0}^{\infty} \Gamma_{\tilde{n}m} = \sum_{m=0}^{\infty} |\langle m|\tilde{n}\rangle|^2 = 1 \tag{J.11}$$

$$\sum_{m=0}^{\infty} m\Gamma_{\tilde{n}m} < \infty \tag{J.12}$$

We can also plot $\gamma_{\tilde{0}}(\lambda)$ for several values of ω_v and numerically check that $\gamma_{\tilde{n}}(\lambda) \to 1$, see figure J.2.

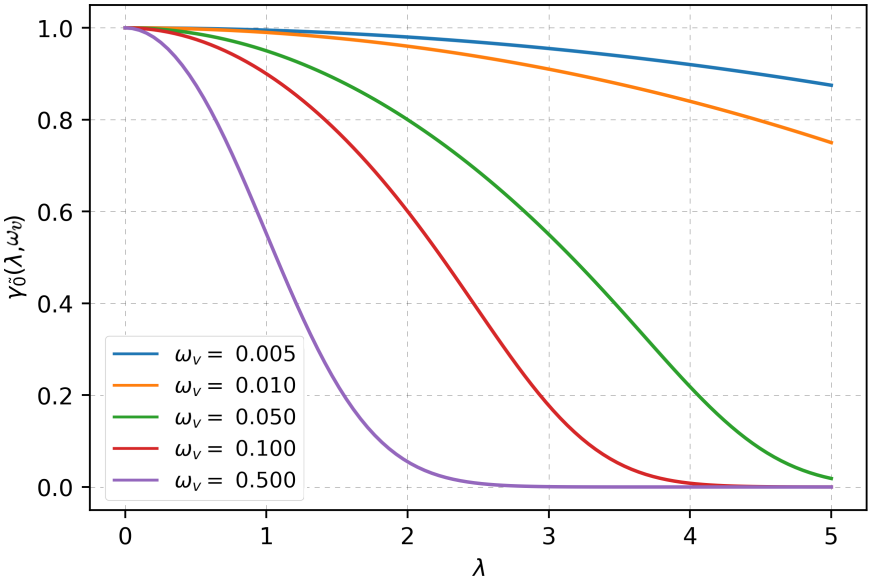

Figure J.2: $\gamma_{\tilde{0}}(\lambda)$ versus λ for several values of ω_v.

Demostration of (J.12)

Next, it is the turn to show the property (J.12):

$$\sum_{m=0}^{\infty} \underbrace{m\Gamma_{\tilde{n}m}}_{a_m} < \infty \tag{J.13}$$

In order to do that we will use D'Alambert criteria:

$$\lim_{m\to\infty} \frac{a_{m+1}}{a_m} = L \qquad \begin{cases} L < 1 & \text{convergent series} \\ L > 1 & \text{divergent series} \\ L = 1 & \text{inconclusive criterion} \end{cases} \tag{J.14}$$

So, we have:

$$\lim_{m\to\infty} \frac{a_{m+1}}{a_m} = \lim_{m\to\infty} \frac{(m+1)\Gamma_{\tilde{n}m+1}}{m\Gamma_{\tilde{n}m}} = \dots$$

For $m \geqslant \tilde{n}$, and using the definition of $\Gamma_{\tilde{n}m}$:

$$\Gamma_{\tilde{n}m}(\lambda) = |D_{\tilde{n}m}(\lambda)|^2 = \left| \sqrt{\frac{\tilde{n}!}{m!}} \lambda^{m-\tilde{n}} e^{-\lambda^2/2} L_{\tilde{n}}^{m-\tilde{n}}(\lambda^2) \right|^2 \tag{J.15}$$

We obtain:

$$\dots = \lim_{m\to\infty} \frac{(m+1)\left| \sqrt{\frac{\tilde{n}!}{(m+1)!}} \lambda^{m+1-\tilde{n}} e^{-\lambda^2/2} L_{\tilde{n}}^{m+1-\tilde{n}}(\lambda^2) \right|^2}{m\left| \sqrt{\frac{\tilde{n}!}{m!}} \lambda^{m-\tilde{n}} e^{-\lambda^2/2} L_{\tilde{n}}^{m-\tilde{n}}(\lambda^2) \right|^2} = \lim_{m\to\infty} \frac{\lambda^2}{m} \left| \frac{L_{\tilde{n}}^{m+1-\tilde{n}}(\lambda^2)}{L_{\tilde{n}}^{m-\tilde{n}}(\lambda^2)} \right|^2$$

Using the expression for the Laguerre Polinomial:

$$L_n^k(x) = \sum_{m=0}^{n} (-1)^m \frac{(n+k)!}{(n-m)!(k+m)!m!} x^m \tag{J.16}$$

We arrive to:

$$\dots = \lim_{m\to\infty} \frac{\lambda^2}{m} \left| \frac{\sum_{k=0}^{\tilde{n}} (-1)^k \frac{(m+1)!}{(\tilde{n}-k)!(m+1-\tilde{n}+k)!k!} \lambda^k}{\sum_{k=0}^{\tilde{n}} (-1)^k \frac{m!}{(\tilde{n}-k)!(m-\tilde{n}+k)!k!} \lambda^k} \right|^2 \sim \lim_{m\to\infty} \frac{\lambda^2}{m} = 0 < 1$$

So, using the D'Alambert criteria, the series converges to a finit value if $\lambda \neq 0$. In the case of $\lambda = 0$ it can easily checked that the sum gives 0, therefore, it converges. In conclusion, we have justified the result (J.12) when $\omega_v \to 0^+$.

J.2 Holstein-Quantum-Rabi model

In this section, we are going to study how the energy losses in the electronic channel chages the dynamics of the system. We will study how we obtain numerically the decay in subsection J.2.1 and the Lindblad eigenspectrum and the transitions in the subsection J.2.2.

J.2.1 Decay of excitations with losses in the electronic sector

In this section, at *bare resonance*, we are going to see the simulations to obtain the dependence of the decay with λ in the case of $\gamma_{matter} = 1.0 \times 10^{-4}$ and $\gamma_{phot} = \gamma_{phon} = 0$. The other parameters are: $\omega_v = 0.1$, $\Delta = \omega_c = 1.0$, $g = 0.05$, $\lambda = 0.0 - 3.0$ and $\rho(t=0) = |\downarrow 1_{phot}0_{phon}\rangle \langle \downarrow 1_{phot}0_{phon}|$. Thus, we calculate $\langle \hat{a}^\dagger \hat{a} \rangle (t)$ and $\langle \hat{\sigma}^+ \hat{\sigma}^- \rangle (t)$ for different values of λ, see figure J.3

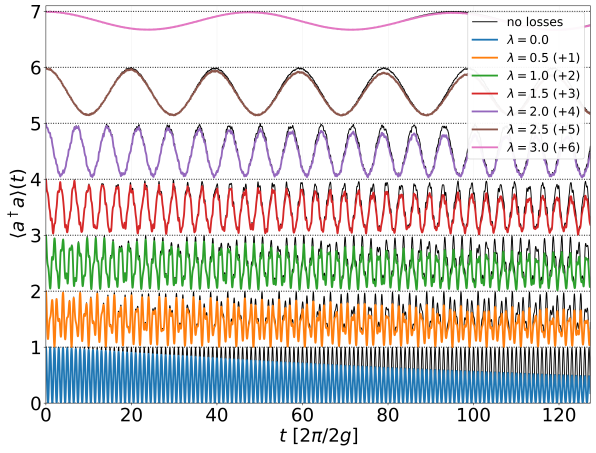

(a)

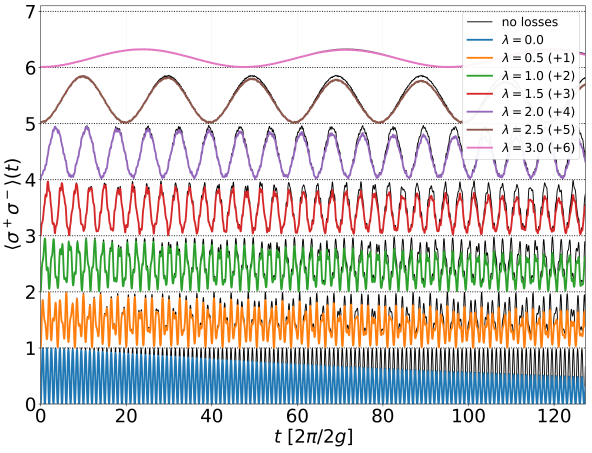

(b)

Figure J.3: At ***bare resonance***, (a) $\langle \hat{a}^\dagger \hat{a} \rangle (t)$ and (b) $\langle \hat{\sigma}^+ \hat{\sigma}^- \rangle (t)$, the black curves are without energy losses, the other colours with $\gamma_{matter} = 1.0 \times 10^{-4}$. Parameters: $\omega_v = 0.1$, $\Delta = \omega_c = 1.0$, $g = 0.05$, $\lambda = 0 - 3$ and $\rho(t=0) = |\downarrow 1_{phot}0_{phon}\rangle \langle \downarrow 1_{phot}0_{phon}|$.

In order to analyze these results, we have calculated the quotient between the time evolution of $\langle \hat{a}^\dagger \hat{a} \rangle (t)$ with and without matter losses. This quantity is represented in figure J.4, where the black dashed curves correspond to the analytical decay (3.13).

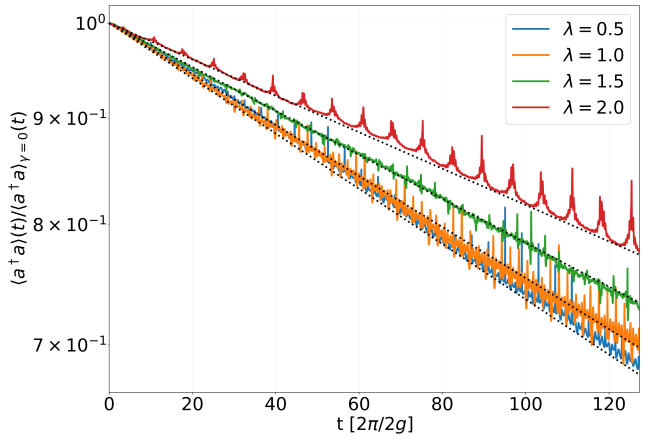

(a)

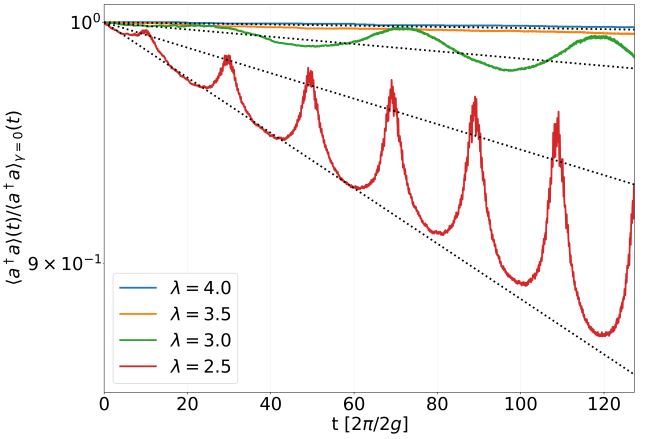

(b)

Figure J.4: At ***bare resonance***, quotient between the expected value of photons with and without energy losses $\langle \hat{a}^\dagger \hat{a} \rangle (t)$. The dashed lines are analytical exponentials $\propto \exp[-\gamma t]$ with a decay γ (3.13) (a) $\lambda = 0.0 - 2.0$ (b) $\lambda = 2.5 - 4.0$. Parameters: $\omega_v = 0.1$, $\Delta = \omega_c = 1.0$, $g = 0.05$ and $\rho(t=0) = |\downarrow\ 1_{phot}\ 0_{phon}\rangle \langle\downarrow\ 1_{phot}\ 0_{phon}|$.

Thus, we find a discrepancy between numerical and analytical decay for $\lambda > 2$, see figure J.4b. But, this discrepancy is due to the renormalization of the cavity photon energy ω_c due to the *Bloch-Siegert* effect. At ***dressed resonance***, when this renormalization is taken into account by correcting the resonance condition $\Delta = \omega_c - \delta_{BS}$, we obtain a good agreement between the simulations and the analytical solution, see figure J.5. Thus, using these simulations, we obtain the figures of the dependence 3.13 of the decay versus λ.

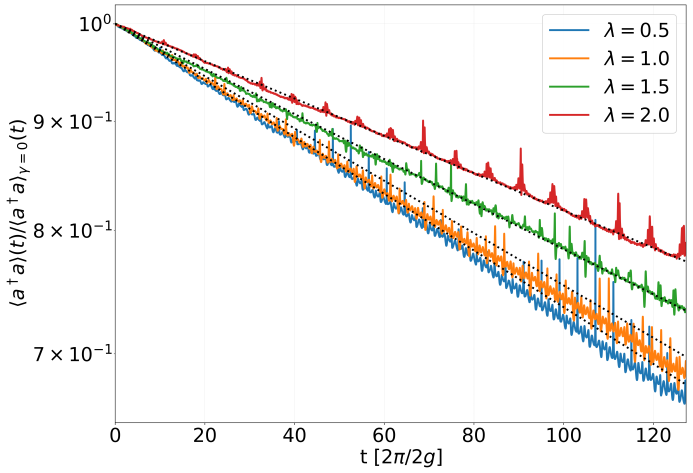

(a)

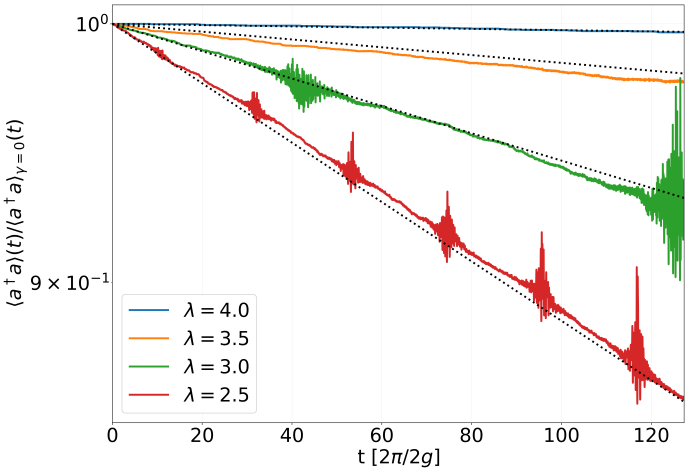

(b)

Figure J.5: At ***dressed resonance***, quotient between the expected value of photons with and without energy losses $\langle \hat{a}^\dagger \hat{a} \rangle (t)$. The dashed lines are analytical exponentials $\propto \exp[-\gamma t]$ with a decay γ (3.13) (a) $\lambda = 0.0 - 2.0$ (b) $\lambda = 2.5 - 4.0$. Parameters: $\omega_v = 0.1$, $\Delta = 1.0$ $\omega_c = \Delta + \delta_{BS}$ (*Bloch-Siegert* correction, cf. section 2.3), $g = 0.05$ and $\rho(t=0) = |\downarrow\ 1_{phot}\ 0_{phon}\rangle \langle\downarrow\ 1_{phot}\ 0_{phon}|$.

J.2.2 Lindblad Spectrum

In this section, we show the most important Lindblad eigenvector of several expected observables $\langle \hat{O} \rangle (t)$ classified by their weight p_j, see equation (3.14):

$$\langle \hat{O} \rangle (t) = \sum_j e^{\lambda^{(j)} t} \langle \rho_l^{(j)} | \rho(0) \rangle \operatorname{Tr}[\rho_r^{(j)} \hat{O}] = \sum_j p_j e^{\lambda^{(j)} t}$$

At ***dressed resonance***, using as parameters $\omega_v = 0.1$, $g = 0.05$ ($2g = \omega_v$), $\lambda = 1.0$, $\Delta = 1$, $\Delta = \omega_v - \delta_{BS}(\lambda)$, $\gamma_{matter} = 1.0 \times 10^{-3}$ and $\rho(t=0) = |\downarrow\ 1_{phot}\ 0_{phon}\rangle \langle\downarrow\ 1_{phot}\ 0_{phon}|$, we can obtain the most relevant eigenvectors

of the $\langle a^\dagger a\rangle(t)$, see table J.1. In these tables we will use a short label to name these eigenvectors. For example, the eigenvectors **3** and **3*** are complex conjugate eigenvectors.

j	$p_j/\sum_j \lvert p_j\rvert$	$\lambda^{(j)}$
1	2.21×10^{-1}	-4.71×10^{-4}
2	1.92×10^{-1}	-4.25×10^{-4}
3	1.65×10^{-1}	$-4.48\times10^{-4}+5.14\times10^{-2}i$
3*	1.65×10^{-1}	$-4.48\times10^{-4}-5.14\times10^{-2}i$

Table J.1: At ***dressed resonance***, the most relevant Lindblad eigenvectors in the dynamics of $\langle a^\dagger a\rangle(t)$. Parameters: $\omega_v=0.1$, $g=0.05$, $\lambda=1.0$, $\Delta=1$, $\Delta=\omega_c-\delta_{BS}$ and $\rho(t=0)=\lvert\downarrow 1_{phot}0_{phon}\rangle\langle\downarrow 1_{phot}0_{phon}\rvert$. The weights p_j are normalized.

We can also obtain the Lindblad eigenspectrum for the projectors $\lvert\epsilon_0\rangle\langle\epsilon_0\rvert$ and $\lvert\epsilon_1\rangle\langle\epsilon_1\rvert$:

$\langle\lvert\epsilon_0\rangle\langle\epsilon_0\rvert\rangle(t)$			$\langle\lvert\epsilon_1\rangle\langle\epsilon_1\rvert\rangle(t)$		
j	$p_j/\sum_j \lvert p_j\rvert$	$\lambda^{(j)}$	j	$p_j/\sum_j \lvert p_j\rvert$	$\lambda^{(j)}$
1	~ 1.00	-4.71×10^{-4}	**2**	~ 1.00	-4.25×10^{-4}
2	1.15×10^{-7}	-4.25×10^{-4}		4.03×10^{-8}	-4.11×10^{-4}
	-2.10×10^{-8}	-5.02×10^{-4}		-6.20×10^{-11}	-4.81×10^{-4}

Table J.2: At ***dressed resonance***, $\lambda=1$, $\gamma_{matter}=10^{-3}$, $\gamma_{phon}=0.0$ y $N_{phon}=10$

We also obtain the Lindblad spectrum of the projectors $\lvert\downarrow\ 0_{phot}n_{phon}\rangle$ of the ground state subspace obtaining weights $p_j<0$ for the eigenstates **1** and **2**. Thus, comparing with the table J.2, the Lindblad eigenvectors **1** and **2** are responsible of the transitions [cf. figure J.6]:

$$\boxed{\lvert\epsilon_0\rangle} \longrightarrow \boxed{\mathbf{1}} \longrightarrow \boxed{\lvert\downarrow\ 0_{phot}\ n\rangle\,,\quad \forall n\geqslant 0}$$

$$\boxed{\lvert\epsilon_1\rangle} \longrightarrow \boxed{\mathbf{2}} \longrightarrow \boxed{\lvert\downarrow\ 0_{phot}\ n\rangle\,,\quad \forall n\geqslant 0}$$

We can also obtain the most relevant Lindblad eigenstates of the the number of the phonons $\langle\hat{b}^\dagger\hat{b}\rangle$ in the representation of the Hamiltonian (2.2) (which diagonalizes the Holstein Hamiltonian (1.26)), see table J.3.

j	$p_j/\sum_j \lvert p_j\rvert$	$\lambda^{(j)}$
	4.86×10^{-1}	~ 0
2	-2.71×10^{-1}	-4.25×10^{-4}
1	-1.07×10^{-1}	-4.71×10^{-4}

Table J.3: At ***dressed resonance***, Lindblad spectrum of $\langle\tilde{b}^\dagger\tilde{b}\rangle(t)$ in the representation of the Hamiltonian. Parameters: $\gamma_{matter}=10^{-3}$, $\gamma_{phon}=\gamma_{phot}=0.0$, $\lambda=1$, $\omega_v=0.1$, $g=0.05$, $\Delta=1$, $\Delta=\omega_c-\delta_{BS}$ and $\rho(t=0)=\lvert\downarrow 1_{phot}0_{phon}\rangle\langle\downarrow 1_{phot}0_{phon}\rvert$.

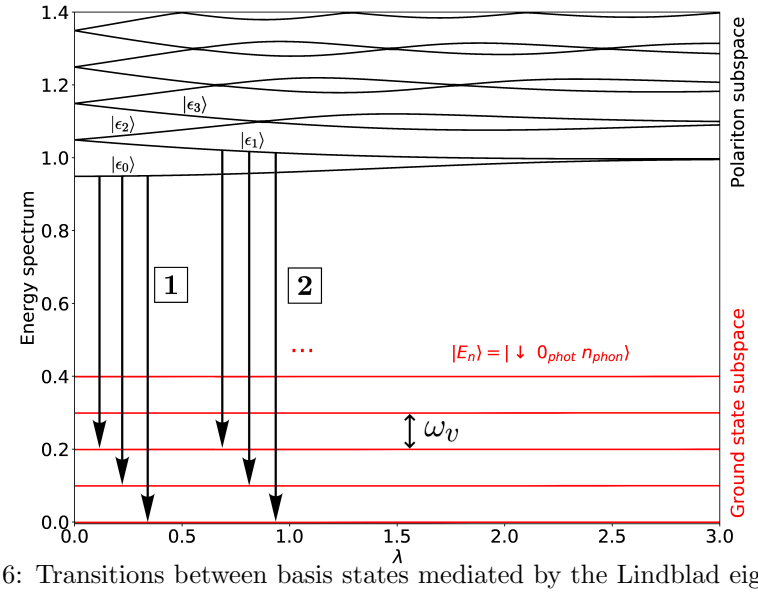

Figure J.6: Transitions between basis states mediated by the Lindblad eigenstates **3** and **3***.

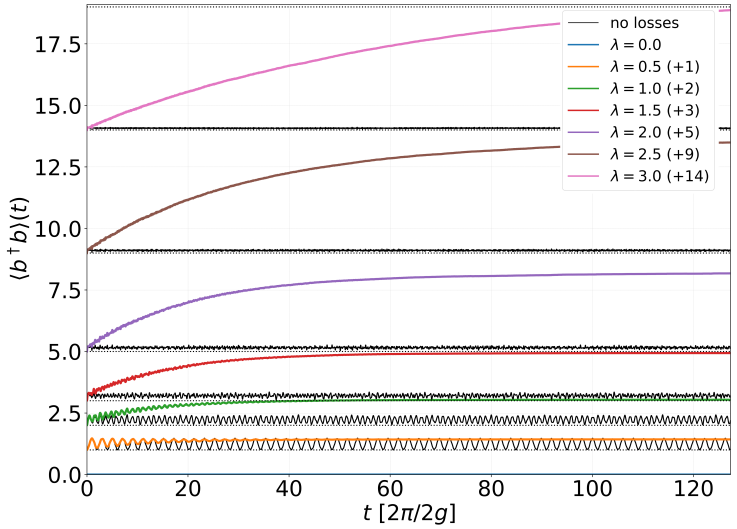

Figure J.7: At ***dressed resonance***, $\langle b^\dagger b \rangle (t)$ in the representation of the Hamiltonian (2.2) for several values of λ, we have used here a higher value of phonon losses ($\gamma_{matter} = 2.5 \times 10^{-3}$) to see the increasing of phonons easily. Parameters: $\omega_v = 0.1$, $g = 0.05$ ($2g = \omega_v$), $\Delta = 1$, $\Delta = \omega_c - \delta_{BS}$ and $\rho(t=0) = |\downarrow 1_{phot} 0_{phon}\rangle \langle \downarrow 1_{phot} 0_{phon}|$.

The transitions $|\epsilon_0\rangle\,,\ |\epsilon_1\rangle \rightarrow |\downarrow\ 0_{phot}\ n_{phon}\rangle$ [cf. figure J.6] given by **1** and **2** and the table J.3 explain the increase in the number of phonons $\langle b^\dagger b \rangle (t)$, see figure J.7. Therefore, the Lindblad eigenvectors **1** and **2** are responsible of the decay in the number of photons $\langle a^\dagger a \rangle (t)$, the transitions $|\epsilon_0\rangle\,,\ |\epsilon_1\rangle \rightarrow |\downarrow\ 0_{phot}\ n_{phon}\rangle$ and the increase of the number of phonons.

Calculating the Lindblad spectrum of several states of the basis we find that de Lindblad eigenstates **3** and **3***, responsible of the Rabi oscillations of $\langle \hat{a}^\dagger \hat{a} \rangle (t)$, cause the following transitions:

$$\boxed{\begin{array}{ll} |\uparrow\ 0_{phot}\ \tilde{0}\rangle & (p_j = -2.07 \times 10^{-1}) \\ |\uparrow\ 0_{phot}\ \tilde{1}\rangle & (p_j = -6.61 \times 10^{-2}) \\ \hline |\downarrow\ 1_{phot}\ 1\rangle & (p_j = -5.38 \times 10^{-2}) \end{array}} \longleftrightarrow \boxed{\begin{array}{l} \mathbf{3} \\ \mathbf{3}^* \end{array}} \longleftrightarrow \boxed{\begin{array}{l} |\downarrow\ 1_{phot}\ 0\rangle \\ (p_j = 1.98 \times 10^{-1}) \end{array}}$$

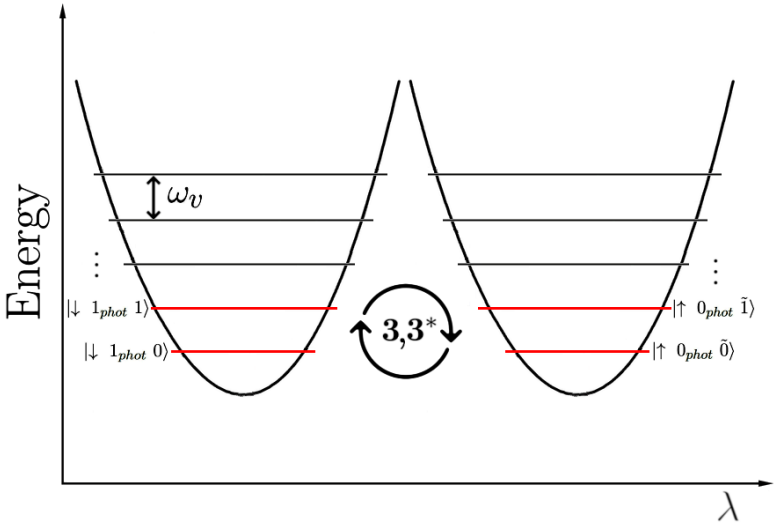

Figure J.8: Transitions between basis states mediated by the Lindblad eigenstates **3** and **3***.

J.3 Photon Losses

In this section, we are going to study the photon losses in the system at ***dressed resonance***. Since, it does not exist a perfect cavity. Some photons can scape and the mirrors are not perfectly reflecting and some can be absorved. Here, we do the same simulations plotted in figure J.3, but with photon energy losses $\gamma_{phot} = 10^{-4}$ and $\gamma_{matter} = \gamma_{phon} = 0$, see figure J.9. The other parameters: $\omega_v = 0.1$, $g = 0.05$, $\lambda = 0.0 - 3.0$, $\Delta = 1$, $\Delta = \omega_c - \delta_{BS}$ and $\rho(t=0) = |\downarrow 1_{phot}0_{phon}\rangle \langle\downarrow 1_{phot}0_{phon}|$.

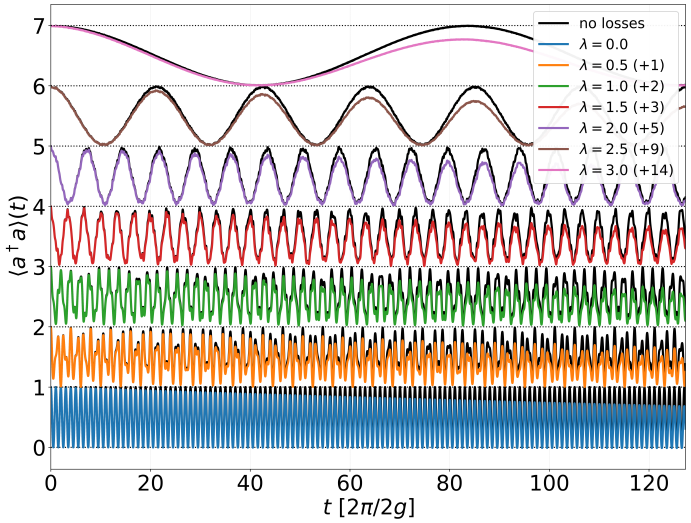

(a)

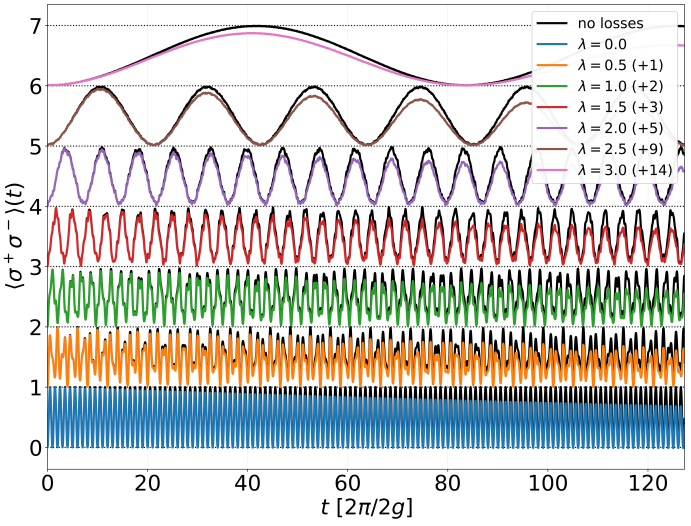

(b)

Figure J.9: At ***dressed resonance***: (a) $\langle a^\dagger a\rangle(t)$ and (b) $\langle \hat{\sigma}^+\hat{\sigma}^-\rangle(t)$ with photon losses ($\gamma_{phot} = 10^{-4}$) and without losses (black curves). Parameters: $\omega_v = 0.1$, $g = 0.05$, $\lambda = 0.0 - 3.0$, $\Delta = 1$, $\Delta = \omega_c - \delta_{BS}$ and $\rho(t=0) = |\downarrow 1_{phot}0_{phon}\rangle \langle\downarrow 1_{phot}0_{phon}|$.

J.4 Phonon Losses

Now, it is the turn of the phonon energy losses. Again, the system is not perfect and it is posible that some phonons decay maybe to a solid matrix. We are going to consider two scenarios: (i) only the phonon losses (section J.4.1) and (ii) a combitaion of the electronic (matter) decay and phonon losses (section J.4.2).

J.4.1 Only Phonon Losses

In this section, we are going to study the Lindblad spectrum in the case $\gamma_{phon} = 5 \times 10^{-2}$, $\gamma_{phot} = \gamma_{matter} = 0$ for several expected values $\langle \hat{O} \rangle (t)$ at ***dressed resonance***. The other parameters used are: $\lambda = 1$, $\omega_v = 0.1$, $g = 0.05$ $(2g = \omega_v)$, $\Delta = 1$, $\Delta = \omega_c - \delta_{BS}$ and $\rho(t=0) = |\downarrow\ 1_{phot}\ 0_{phon}\rangle \langle\downarrow\ 1_{phot}\ 0_{phon}|$. First, we can obtain the most important Lindblad eigenvectors of the $\langle a^\dagger a \rangle (t)$, $\lambda^{(j)}$ classified by their weight p_j, see table J.4.

j	$p_j / \sum_j \lvert p_j \rvert$	$\lambda^{(j)}$
1	4.63×10^{-1}	~ 0
2	1.65×10^{-1}	$-1.52 \times 10^{-3} - 5.14 \times 10^{-2} i$
2*	1.65×10^{-1}	$-1.52 \times 10^{-3} + 5.14 \times 10^{-2} i$

Table J.4: At ***dressed resonance***, Lindblad eigenvectors classified by their normalized weight $p_j / \sum_j |p_j|$ of the number of photons $\langle a^\dagger a \rangle (t)$, $\lambda^{(j)}$ are the Lindblad eigenvalues. Parameters: $\gamma_{phon} = 5 \times 10^{-2}$, $\gamma_{phot} = \gamma_{matter} = 0$, $\lambda = 1$, $\omega_v = 0.1$, $g = 0.05$ $(2g = \omega_v)$, $\Delta = 1$, $\Delta = \omega_c - \delta_{BS}$ and $\rho(t=0) = |\downarrow\ 1_{phot}\ 0_{phon}\rangle \langle\downarrow\ 1_{phot}\ 0_{phon}|$.

Thus, we find a stationary eigenstate **1** for the number of photons and a pair of complex conjugate eigenstates **2** and **2*** responsible of the *Rabi oscillations* in the number of photons. If we calculate the Lindblad spectrum for several states of the basis, we find that these pairs of Lindblad eigenstates are responsible of the transitions:

$$\boxed{\begin{array}{ll} |\uparrow\ 0_{phot}\ \tilde{0}\rangle & (p_j = -1.84 \times 10^{-1}) \\ |\uparrow\ 0_{phot}\ \tilde{1}\rangle & (p_j = -4.89 \times 10^{-2}) \\ \hline |\downarrow\ 1_{phot}\ 1\rangle & (p_j = -3.74 \times 10^{-2}) \end{array}} \longleftrightarrow \boxed{\begin{array}{l} \mathbf{2} \\ \mathbf{2}^* \end{array}} \longleftrightarrow \boxed{\begin{array}{l} |\downarrow\ 1_{phot}\ 0\rangle \\ (p_j = 1.62 \times 10^{-1}) \end{array}}$$

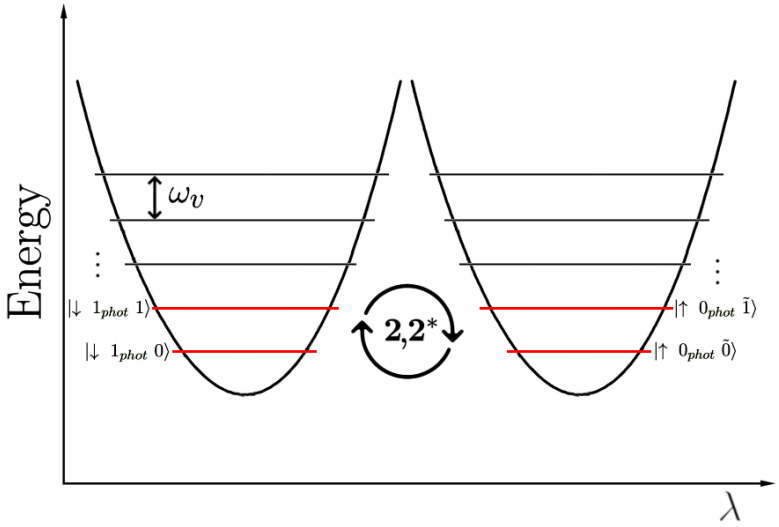

Figure J.10: Transitions between basis states mediated by the Lindblad eigenstates **2** and **2***.

We can also obtain the Lindblad eigenstates of the number of phonons $\langle \hat{b}^\dagger \hat{b} \rangle (t)$ in the representation of the Hamiltonian (2.2) after applying the Polaron transformation $U_P^{(0)}$ (2.1) which diagonalizes the Holstein Hamiltonian (1.26). See the table J.5.

j	$p_j / \sum_j \lvert p_j \rvert$	$\lambda^{(j)}$
1	1.70×10^{-1}	-2.31×10^{-3}
2	-1.40×10^{-1}	$-2.68 \times 10^{-3} - 9.44 \times 10^{-2} i$
2*	-1.40×10^{-1}	$-2.68 \times 10^{-3} + 9.44 \times 10^{-2} i$
3	1.14×10^{-1}	-3.04×10^{-3}

Table J.5: At ***dressed resonance***, Lindblad eigenvectors classified by their normalized weight $p_j / \sum_j \lvert p_j \rvert$ of the number of phonons $\langle \hat{b}^\dagger \hat{b} \rangle (t)$ (in the representation of the Hamiltonian (2.2)), $\lambda^{(j)}$ are the Lindblad eigenvalues. Parameters: $\gamma_{phon} = 5 \times 10^{-2}$, $\gamma_{phot} = \gamma_{matter} = 0$, $\lambda = 1$, $\omega_v = 0.1$, $g = 0.05$ $(2g = \omega_v)$, $\Delta = 1$, $\Delta = \omega_c - \delta_{BS}$ and $\rho(t=0) = |\downarrow\ 1_{phot}\ 0_{phon}\rangle \langle\downarrow\ 1_{phot}\ 0_{phon}|$.

We find a pair of eigenstates **1** and **3** responsible of the decay in the number of phonons. Also, a pair of complex conjugate eigenstates **2** and **2*** responsible of the *Rabi oscillations*.

$\langle\lvert\epsilon_0\rangle\langle\epsilon_0\rvert\rangle(t)$			$\langle\lvert\epsilon_1\rangle\langle\epsilon_1\rvert\rangle(t)$		
j	$p_j/\sum_j \lvert p_j\rvert$	$\lambda^{(j)}$	j	$p_j/\sum_j \lvert p_j\rvert$	$\lambda^{(j)}$
1	6.16×10^{-1}	~ 0.00	**3**	5.08×10^{-1}	-3.04×10^{-3}
3	-2.36×10^{-1}	-3.04×10^{-3}		-1.28×10^{-1}	-7.92×10^{-3}
1	-9.68×10^{-2}	-2.31×10^{-3}		-9.60×10^{-2}	-1.58×10^{-2}
	2.27×10^{-2}	-7.92×10^{-3}	**1**	8.35×10^{-2}	-2.31×10^{-3}

Table J.6: At ***dressed resonance***, Lindblad eigenvectors classified by their normalized weight $p_j/\sum_j |p_j|$ of the ground $\langle|\epsilon_0\rangle\langle\epsilon_0|\rangle(t)$ and first excited state $\langle|\epsilon_1\rangle\langle\epsilon_1|\rangle(t)$ of the polariton subspace, where $\lambda^{(j)}$ are the Lindblad eigenvalues. Parameters: $\gamma_{phon} = 5\times10^{-2}$, $\gamma_{phot} = \gamma_{matter} = 0$, $\lambda = 1$, $\omega_v = 0.1$, $g = 0.05$ $(2g = \omega_v)$, $\Delta = 1$, $\Delta = \omega_c - \delta_{BS}$ and $\rho(t=0) = |\downarrow\ 1_{phot}\ 0_{phon}\rangle\langle\downarrow\ 1_{phot}\ 0_{phon}|$.

Besides, we calculate the Lindblad spectrum for the projectors of the eigenstates $|\epsilon_n\rangle$ of the polariton subspace. In table J.6, we show the most important Lindblad eigenstates for the cases $n = 0,\ 1$. Thus, we find that the Lindblad eigenstates **1** and **3** are responsible for the decay to the eigenstate $|\epsilon_0\rangle$:

$$\boxed{|\epsilon_1\rangle} \longrightarrow \boxed{\mathbf{3}} \longrightarrow \boxed{|\epsilon_0\rangle}$$

$$\boxed{|\epsilon_3\rangle, |\epsilon_2\rangle, |\epsilon_1\rangle} \longrightarrow \boxed{\mathbf{1}} \longrightarrow \boxed{|\epsilon_0\rangle}$$

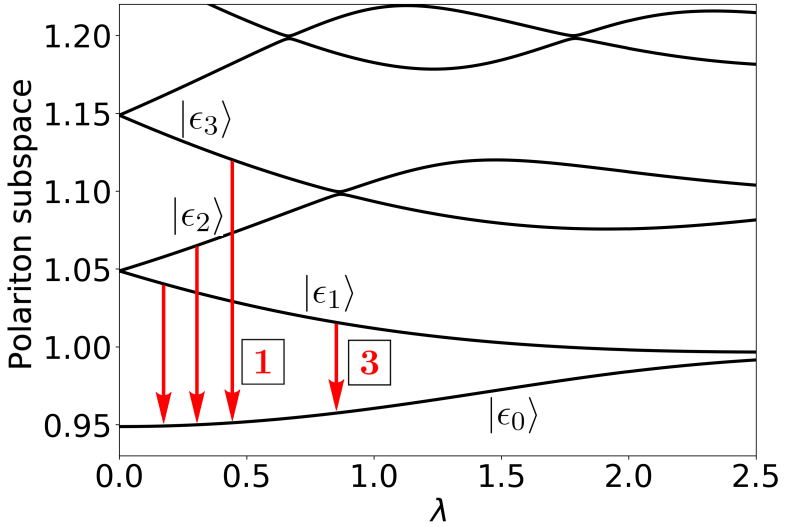

Figure J.11: Transitions between basis states mediated by the Lindblad eigenstates **1** and **3**.

We can check that the system decays to the ground state of the polariton subspace $|\epsilon_0\rangle$ plotting the number of phonons in the long term dynamics and compare it with the number of phonons of the eigenstate $|\epsilon_0\rangle$, see figure J.12b.

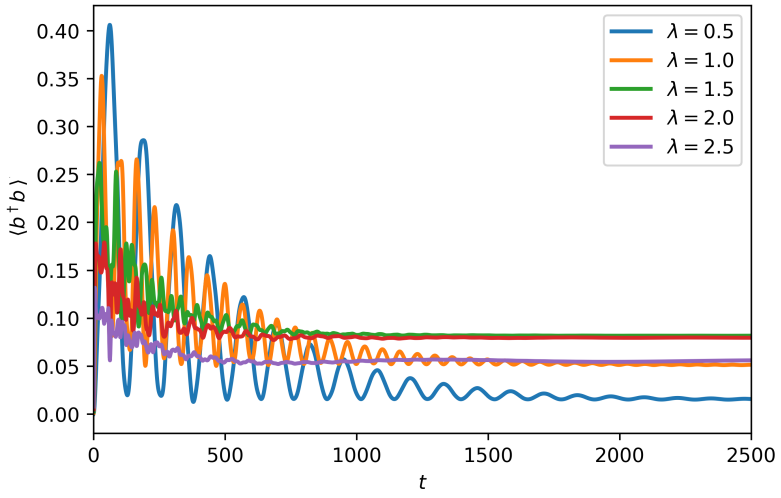

(a)

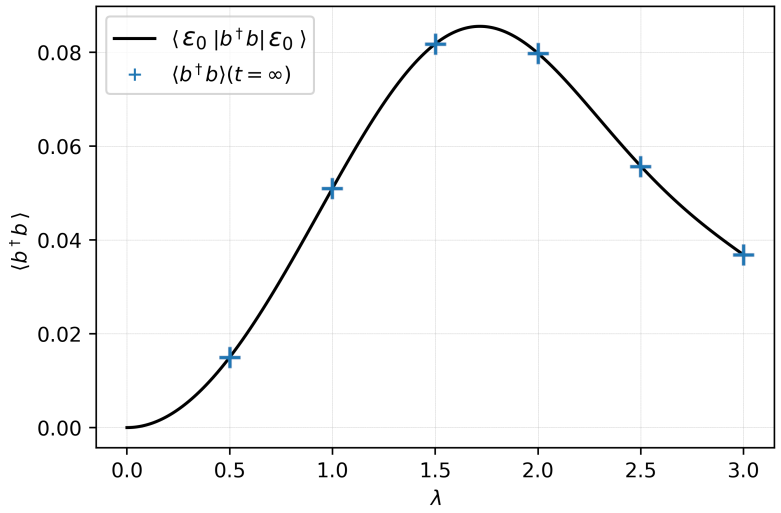

(b)

Figure J.12: At ***dressed resonance***: (a) $\langle \hat{b}^\dagger \hat{b} \rangle (t)$ (in the representation of displaced phonons used in the Hamiltonian (2.2) for $\rho(t=0) = |\downarrow 1_{phot} 0_{phon}\rangle \langle \downarrow 1_{phot} 0_{phon}|$) versus time; (b) Blue points represent the number of phonons when $t \to \infty$, the black curve the number of phonons $\langle \epsilon_0 | \hat{b}^\dagger \hat{b} | \epsilon_0 \rangle$ of the ground state $|\epsilon_0\rangle$ of the polariton subspace versus λ. Parameters: $\gamma_{phon} = 5 \times 10^{-2}$, $\gamma_{phot} = \gamma_{matter} = 0$, $\lambda = 1$, $\omega_v = 0.1$, $g = 0.05$ $(2g = \omega_v)$, $\Delta = 1$, $\Delta = \omega_c - \delta_{BS}$.

Furthermore, we can check that in the long term the system relaxes to the number of photons and matter excitations associated to having the ground state of the polariton subspace $|\epsilon_0\rangle$, see figures J.13c and J.13d.

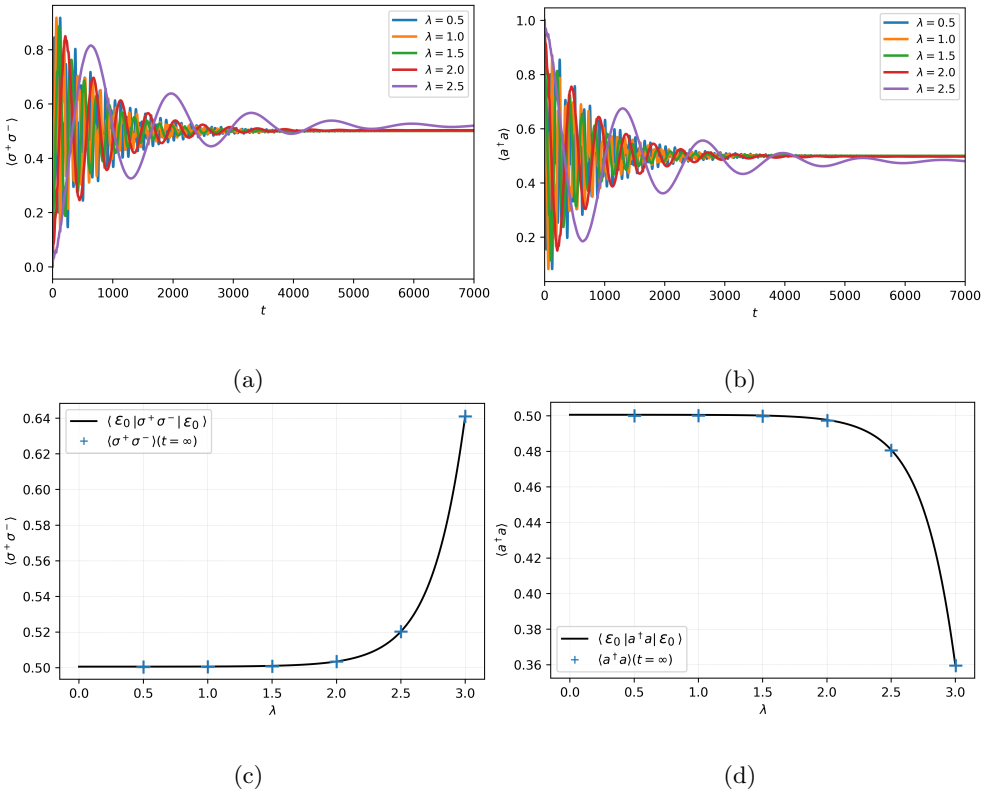

Figure J.13: At ***dressed resonance***: (a) and (b) number of matter excitations $\langle\hat{\sigma}^+\hat{\sigma}^-\rangle(t)$ and number of photons $\langle\hat{a}^\dagger\hat{a}\rangle$ versus time; (b) and (c) Blue points represent the number of photons/matter excitations when $t \to \infty$, the black curve the photons/matter excitations $\langle\epsilon_0|\hat{a}^\dagger\hat{a}|\epsilon_0\rangle$ / $\langle\epsilon_0|\hat{\sigma}^+\hat{\sigma}^-|\epsilon_0\rangle$ of the ground state $|\epsilon_0\rangle$ of the polariton subspace. Parameters: $\gamma_{phon} = 5\times10^{-2}$, $\gamma_{phot} = \gamma_{matter} = 0$, $\lambda = 1$, $\omega_v = 0.1$, $g = 0.05$ $(2g = \omega_v)$, $\Delta = 1$, $\Delta = \omega_c - \delta_{BS}$ and $\rho(t=0) = |\downarrow 1_{phot}0_{phon}\rangle\langle\downarrow 1_{phot}0_{phon}|$.

J.4.2 Calculation when losses occur both in the phonon and electronic sectors

In this section, we are going to study the Lindblad spectrum in the case $\gamma_{phon} = 5\times10^{-2}$, $\gamma_{matter} = 10^{-3}$ and $\gamma_{phot} = 0$ for several expected values $\langle\hat{O}\rangle(t)$ again at ***dressed resonance***. The other parameters are: $\lambda = 1$, $\omega_v = 0.1$, $g = 0.05$ $(2g = \omega_v)$, $\Delta = 1$, $\Delta = \omega_c - \delta_{BS}$. The initial condition is $\rho(t = 0) = |\downarrow\ 1_{phot}\ 0_{phon}\rangle\langle\downarrow\ 1_{phot}\ 0_{phon}|$. First, we can obtain the most important Lindblad eigenvectors of $\langle a^\dagger a\rangle(t)$, $\lambda^{(j)}$ classified by their weight p_j, see table J.7.

j	$p_j/\sum_j \lvert p_j\rvert$	$\lambda^{(j)}$
1	4.63×10^{-1}	-4.71×10^{-4}
2	1.64×10^{-1}	$-1.97\times10^{-3}+5.14\times10^{-4}i$
2*	1.64×10^{-1}	$-1.97\times10^{-3}-5.14\times10^{-4}i$

Table J.7: At ***dressed resonance***, Lindblad eigenvectors classified by their normalized weight $p_j/\sum_j |p_j|$ of the number of photons $\langle a^\dagger a\rangle(t)$, where $\lambda^{(j)}$ are the Lindblad eigenvalues. Parameters: $\gamma_{phon}=5\times10^{-2}$, $\gamma_{phot}=0$, $\gamma_{matter}=10^{-3}$, $\lambda=1$, $\omega_v=0.1$, $g=0.05$, $\Delta=1$, $\Delta=\omega_c-\delta_{BS}$ and $\rho(t=0)=|\downarrow 1_{phot}0_{phon}\rangle\langle\downarrow 1_{phot}0_{phon}|$.

Then, we have obtained a Lindblad eigenvector **1** which produce the long term decay of the number of photons and a pair of complex conjugate eigenstates **2** and **2*** responsible of the *Rabi oscillations* and their decay. Also, we can obtain the Lindblad spectrum for the projectors of the eigenstates $|\epsilon_0\rangle$ and $|\epsilon_1\rangle$ of the polariton subspace, see table J.8.

$\langle\lvert\epsilon_0\rangle\langle\epsilon_0\rvert\rangle(t)$			$\langle\lvert\epsilon_1\rangle\langle\epsilon_1\rvert\rangle(t)$		
j	$p_j/\sum_j \lvert p_j\rvert$	$\lambda^{(j)}$	j	$p_j/\sum_j \lvert p_j\rvert$	$\lambda^{(j)}$
1	6.17×10^{-1}	-4.71×10^{-4}	**2**	5.15×10^{-1}	-3.47×10^{-3}
2	-2.33×10^{-1}	-3.47×10^{-3}		-1.28×10^{-1}	-8.33×10^{-3}
3	-1.02×10^{-1}	-2.82×10^{-3}	**3**	9.86×10^{-2}	-2.82×10^{-3}

Table J.8: Lindblad eigenvectors classified by their normalized weight $p_j/\sum_j |p_j|$ of the ground $\langle|\epsilon_0\rangle\langle\epsilon_0|\rangle(t)$ and first excited state $\langle|\epsilon_1\rangle\langle\epsilon_1|\rangle(t)$ of the polariton subspace, where $\lambda^{(j)}$ are the Lindblad eigenvalues. Parameters: $\gamma_{phon}=5\times10^{-2}$, $\gamma_{phot}=0$ $\gamma_{matter}=10^{-3}$, $\lambda=1$, $\omega_v=0.1$, $g=0.05$ $(2g=\omega_v)$, $\Delta=1$, $\Delta=\omega_c-\delta_{BS}$ and $\rho(t=0)=|\downarrow\ 1_{phot}\ 0_{phon}\rangle\langle\downarrow\ 1_{phot}\ 0_{phon}|$.

We can obtain similar tables, but for the projectors over the states $|\downarrow 0_{phot}n_{pon}\rangle$ of the ground state subspace. Thus, the Lindblad eigenstate **1** is responsible of the following transitions:

$$\boxed{|\epsilon_0\rangle}\ \boxed{|\downarrow\ 0_{phot}\ n_{phon}\rangle\,,\quad n_{phon}>0}\ \longrightarrow\ \boxed{\mathbf{1}}\ \longrightarrow\ \boxed{|\downarrow\ 0_{phot}\ 0_{phon}\rangle}$$

If we see the table J.8, we find two important eigenstates **2** and **3**. These are responsible of the transitions:

$$\boxed{|\epsilon_1\rangle}\ \boxed{|\downarrow\ 0_{phot}\ n\rangle\,,\ n>0}\ \longrightarrow\ \boxed{\mathbf{2},\ \mathbf{3}}\ \longrightarrow\ \boxed{|\epsilon_0\rangle}\ \boxed{|\downarrow\ 0_{phot}\ 0\rangle}$$

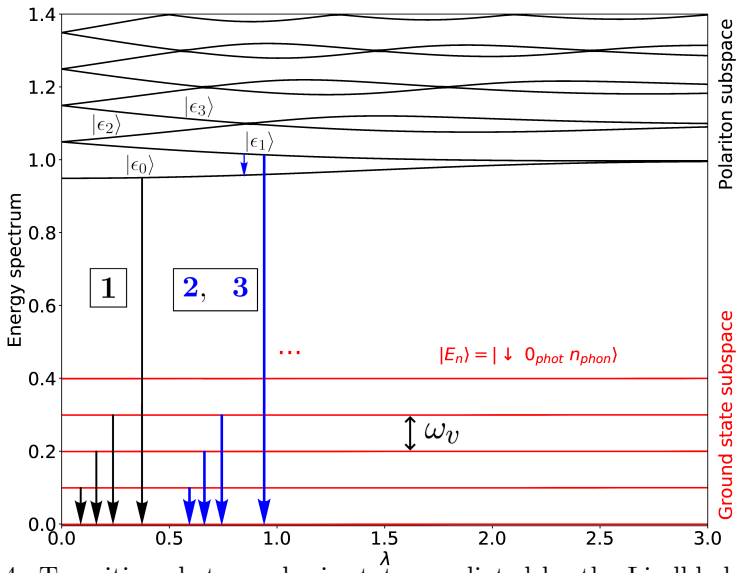

Figure J.14: Transitions between basis states mediated by the Lindblad eigenstates **1**, **2** and **3**.

If we obtain weights p_j of the Lindblad spectrum for several states of the basis, we find that the complex conjugate Lindblad eigenstates **2** and **2*** produce these transitions:

$$\begin{array}{l} |\uparrow\ 0_{phot}\ \tilde{0}\rangle\ \ (p_j = -1.85 \times 10^{-1}) \\ |\uparrow\ 0_{phot}\ \tilde{1}\rangle\ \ (p_j = -4.94 \times 10^{-2}) \\ \hline |\downarrow\ 1_{phot}\ 1\rangle\ \ (p_j = -3.87 \times 10^{-2}) \end{array} \longleftrightarrow \boxed{\begin{array}{l}\mathbf{2} \\ \mathbf{2}^*\end{array}} \longleftrightarrow \begin{array}{l} |\downarrow\ 1_{phot}\ 0\rangle \\ (p_j = 1.63 \times 10^{-1}) \end{array}$$

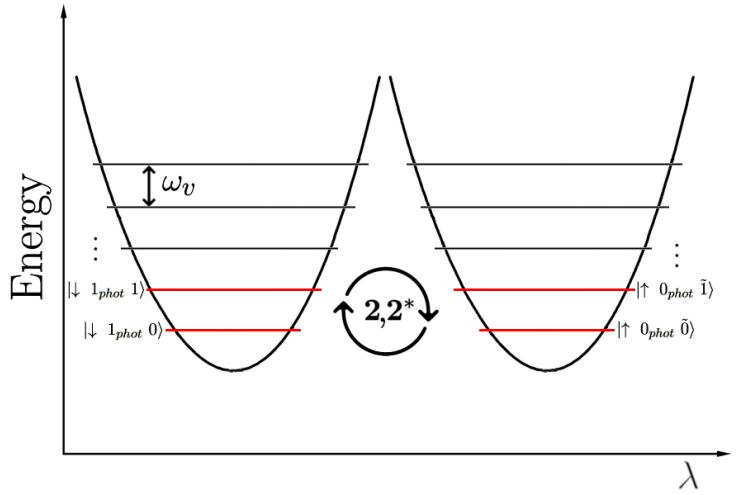

Figure J.15: Transitions between basis states mediated by the Lindblad eigenstates **2** and **2***.

The eigenstates **2** and **2*** are only responsible of the *Rabi oscillation* and their decay. In fact, we can obtain the dynamics of the number of photons $\langle \hat{a}^\dagger \hat{a} \rangle (t)$ with only these two eigenstates. Thus, we obtain *Rabi oscillations* with a zero mean value of photons, see figures J.16. The same occurs for the electronic excitations.

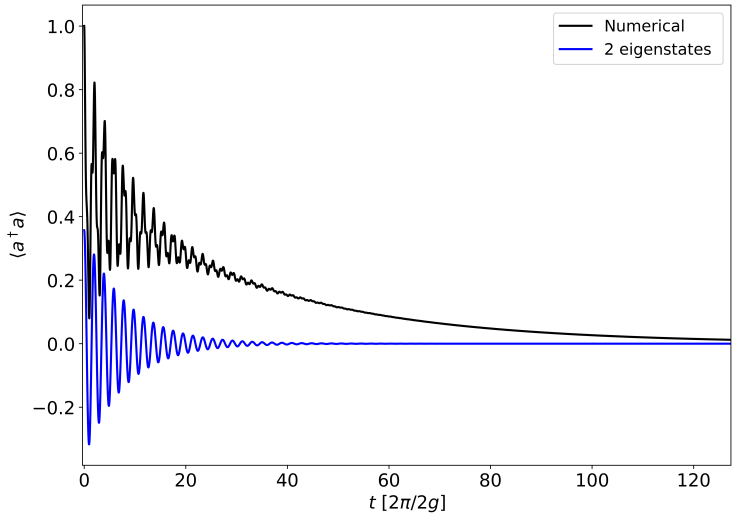

(a)

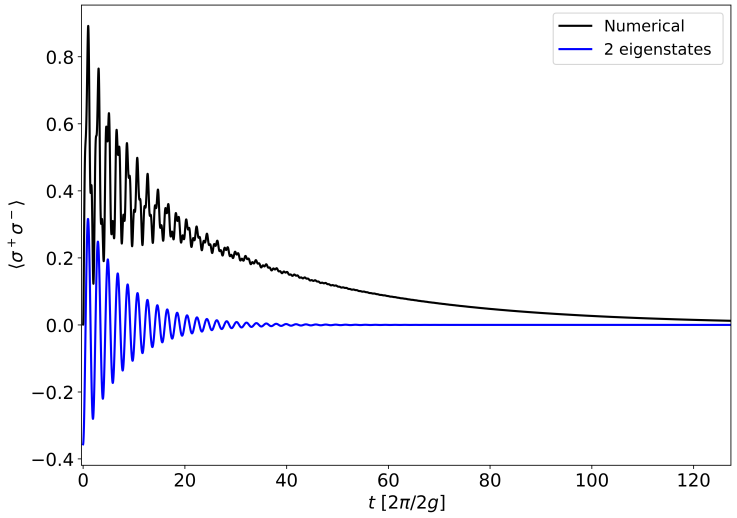

(b)

Figure J.16: At ***dressed resonance***, time evolution of the expected number of (a) photons and (b) matter excitations with the initial condition $\rho(t = 0) = |\downarrow\ 1_{phot}\ 0_{phon}\rangle \langle\downarrow\ 1_{phot}\ 0_{phon}|$. The black curve represents the time evolution with all the Lindblad eigenvectors, the blue one the time evolution limited to the Lindblad eigenvectors **2** and **2***, see table J.7. Parameters: $\gamma_{phon} = 5 \times 10^{-2}$, $\gamma_{phot} = 0$ $\gamma_{matter} = 10^{-3}$, $\lambda = 1$, $\omega_v = 0.1$, $g = 0.05$ $(2g = \omega_v)$, $\Delta = 1$, $\Delta = \omega_c - \delta_{BS}$.

In figure J.17, we have plotted the dynamics of $\langle \hat{\sigma}^{+}\hat{\sigma}^{-} \rangle (t)$ with matter losses and the comparison between the cases with (red) and without (black) phonon losses. Thus, we can see that the effect of the phonon losses in the number of matter excitations is the extintion of the *Rabi* oscillations:

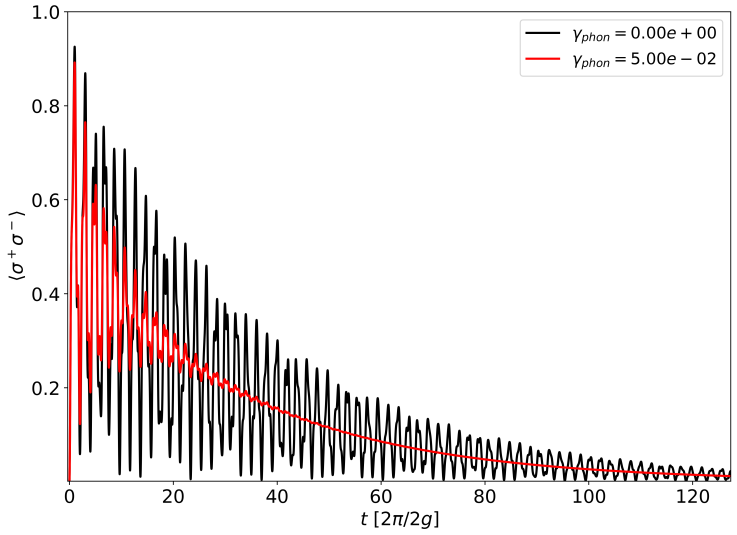

(a)

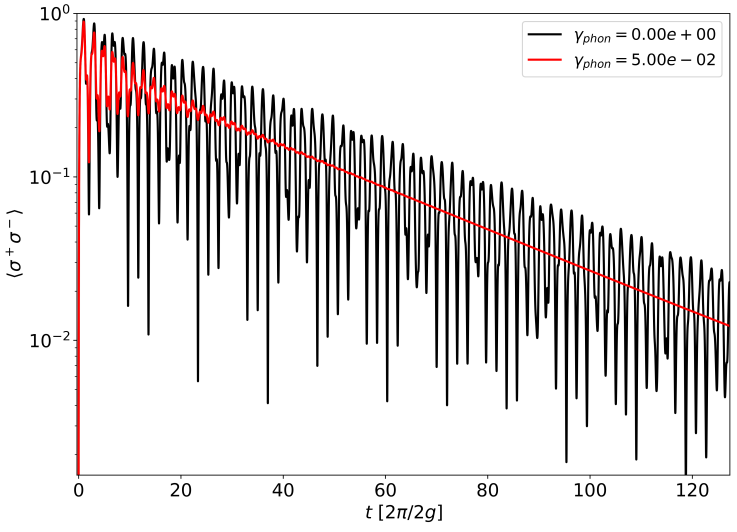

(b)

Figure J.17: At ***dressed resonance***, (a) Time evolution of the mater excitations $\langle \hat{\sigma}^{+}\hat{\sigma}^{-} \rangle (t)$, the red curve case with phonon and matter losses ($\gamma_{matter} = 10^{-3}$, $\gamma_{phon} = 5.0 \times 10^{-2}$); the black curve case with only matter losses ($\gamma_{matter} = 10^{-3}$, $\gamma_{phon} = 0$) (b) The same case but in logarithmic scale. Parameters: $\lambda = 1$, $\gamma_{phot} = 0$, $\omega_v = 0.1$, $g = 0.05$ $(2g = \omega_v)$, $\Delta = 1$, $\Delta = \omega_c - \delta_{BS}$ and $\rho(t=0) = |\downarrow\ 1_{phot}\ 0_{phon}\rangle \langle\downarrow\ 1_{phot}\ 0_{phon}|$.

We have seen the effect of the matter and phonon losses for the case $\omega_v = 2g = 0.1$. In figure J.18, we can qualitatively see that they have the same effects for the cases $\omega_v < 2g$ and $\omega_v > 2g$.

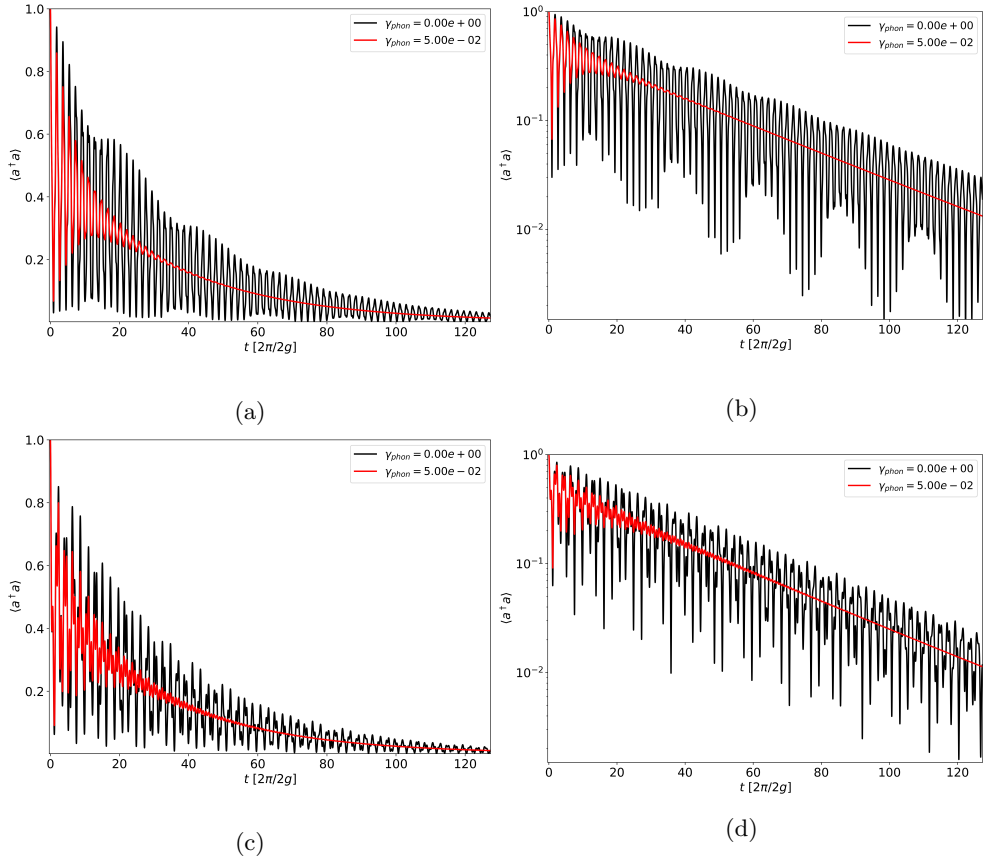

Figure J.18: At ***dressed resonance***, time evolution of the number of photons $\langle \hat{a}^\dagger \hat{a} \rangle (t)$, the red curve case with phonon and matter losses ($\gamma_{matter} = 10^{-3}$, $\gamma_{phon} = 5.0 \times 10^{-2}$); the black curve case with only matter losses ($\gamma_{matter} = 10^{-3}$, $\gamma_{phon} = 0$, (a) and (b) are the cases with $2g < \omega_v$, $\omega_v = 0.125$; (c) and (d) the cases with $2g > \omega_v$, $\omega_v = 0.075$. Parameters: $\lambda = 1$, $\gamma_{phot} = 0$, $g = 0.05$, $\Delta = 1$, $\Delta = \omega_c - \delta_{BS}$ and $\rho(t=0) = |\downarrow\ 1_{phot}\ 0_{phon}\rangle \langle\downarrow\ 1_{phot}\ 0_{phon}|$.)

Agradecimientos
Acknowledgments

No quiero terminar sin agradecer el apoyo que he recibido estos 5 años, que ha sido más que necesario. Sin este no podría haber llegado a donde estoy ahora.

Quiero empezar a agradecer en primer lugar a mi familia. A mis padres y mi hermano Carlos por haber estado ahí conmigo apoyándome y soportándome. Sin vosotros no me habría sentido capaz de llegar a terminar esta tesis. No puedo tampoco olvidarme de mi tía Ana y Fran, así como mis primos Alicia y Eduardo. Si bien estas navidades no nos hemos podido ver vuestro cariño y apoyo siempre se echa de menos. Muchas gracias a mis abuelos Leonor, Miguel, Julia y Cristóbal por haber estado conmigo desde siempre. También quiero acordarme de mis tías abuelas Leonor y Felisa así como de mi tío Pablo y mi tía Ascensión. Gracias a todos sois la pieza fundamental que me ha permitido llegar hasta aquí.

Tampoco me puedo olvidar de mis directores de tesis Luis y David. Gracias por haberme guiado y enseñado estos años. Sin vuestra ayuda, paciencia y apoyo estoy convencido que nunca habría llegado a donde estoy ahora. No me olvido tampoco de mi tutor Alejandro en la estancia de investigación en Madrid y la muy buena acogida que me brindó.

Es el turno de acordarme de Anquela y de la maravillosa gente que tengo allí y espero conservar siempre. Si bien no he podido ir estos años con mucha frecuencia, se os echa de menos, y no está de más agradeceros no solo el apoyo sino todos los buenos momentos que he pasado con vosotros. Quiero acordarme especialmente de Paula, Rodrigo, Patricia, Diego, Cristina, Esteban, Silvia... Gracias por estar allí y haberme escuchado cuando lo necesitaba y haber disfrutado tanto con vosotros. Pero tampoco olvidarme de mis tíos Ester, Rafa y Jose, así como de Herminia, Rosa, Juanjo, Javier... Nombraría a mucha más gente, a todos vosotros gracias por estar ahí.

No puedo saltarme mi primera etapa del doctorado y menos olvidarme de nombrar a los primeros compañeros que conocí. Gracias a Eduardo, Pablo, Elisa, Jorge... esos cafés los necesitaba para sobrevivir y no precisamente por la cafeína. Tengo que acordarme también de la gente maravillosa que he ido conociendo después. Gracias Daniel por tu impagable apoyo durante este final de etapa. También Alina, gracias por todo. Me quiero acordar también de mi compañero de despacho Álex y de Guillaume, gracias por estar ahí. Tampoco me olvido de Tejeda y por supuesto es imposible no acordarse de las dos mejores químicas de la facultad que no son otras que Isolda y Raquel. Es a las personas a las que no te esperas conocer a las que al final les coges más cariño.

Estos años han dado mucho de sí y he podido conocer a muchas personas que han marcado la diferencia. Quiero nombrar a Víctor (a ver cuando hacemos un viaje), Edgar, Pablo, Juan, Santi, Álex, David ... Para muchos de vosotros han sido unos años muy duros a muchos niveles, me ha encantado estar ahí para ayudaros pero más todavía os agradezco el apoyo recibido. Esta tesis es en parte vuestra.

Me acordaré siempre también de la gente que conocí durante la estancia en Madrid no se me olvidará nunca, fue una de las etapas más bonitas que he tenido. Quiero hacer también una breve mención a Joaquín mi profesor de teatro amateur en el Teatro de las esquinas y a mi profesor de piano Israel con vosotros las semanas se hacían infinitamente más soportables. También quiero acordarme de mi entrenador Fran y sus duros entrenamientos gracias por animarme con el deporte.

No está de más acordarse de todos y cada uno de los profesores que he tenido a lo largo del colegio, la academia de inglés (Cris no me he olvidado tampoco), el instituto y la universidad, con la mención especial de Juan mi profesor de física del colegio de San Antonio. Cada uno de vosotros habéis contribuído de manera imprescindible a que haya conseguido llegar al final de este sendero.

Estos años han sido los más duros a nivel intelectual pero sobre todo personal y sé que me habré dejado a muchísima gente importante en el tintero. A todos ellos gracias por estar ahí no me he olvidado.

Por último, quiero agradecer al Ministerio de Economía y Competitividad el haberme concedido un contrato FPI con referencia BES-2015-075328, asociada al proyecto MAT2014-53432-C5-1-R. El dinero no está siquiera entre mis primeras prioridades pero oye facilita mucho la vida.

Bibliography

[1] Serge Haroche. Nobel lecture: Controlling photons in a box and exploring the quantum to classical boundary. *Rev. Mod. Phys.*, 85:1083–1102, Jul 2013.

[2] T. Rocheleau, T. Ndukum, C. Macklin, J. B. Hertzberg, A. A. Clerk, and K. C. Schwab. Preparation and detection of a mechanical resonator near the ground state of motion. *Nature*, 463(7277):72–75, Jan 2010.

[3] Frank Arute, Kunal Arya, Ryan Babbush, Dave Bacon, Joseph C. Bardin, Rami Barends, Rupak Biswas, Sergio Boixo, Fernando G. S. L. Brandao, David A. Buell, Brian Burkett, Yu Chen, Zijun Chen, Ben Chiaro, Roberto Collins, William Courtney, Andrew Dunsworth, Edward Farhi, Brooks Foxen, Austin Fowler, Craig Gidney, Marissa Giustina, Rob Graff, Keith Guerin, Steve Habegger, Matthew P. Harrigan, Michael J. Hartmann, Alan Ho, Markus Hoffmann, Trent Huang, Travis S. Humble, Sergei V. Isakov, Evan Jeffrey, Zhang Jiang, Dvir Kafri, Kostyantyn Kechedzhi, Julian Kelly, Paul V. Klimov, Sergey Knysh, Alexander Korotkov, Fedor Kostritsa, David Landhuis, Mike Lindmark, Erik Lucero, Dmitry Lyakh, Salvatore Mandrà, Jarrod R. McClean, Matthew McEwen, Anthony Megrant, Xiao Mi, Kristel Michielsen, Masoud Mohseni, Josh Mutus, Ofer Naaman, Matthew Neeley, Charles Neill, Murphy Yuezhen Niu, Eric Ostby, Andre Petukhov, John C. Platt, Chris Quintana, Eleanor G. Rieffel, Pedram Roushan, Nicholas C. Rubin, Daniel Sank, Kevin J. Satzinger, Vadim Smelyanskiy, Kevin J. Sung, Matthew D. Trevithick, Amit Vainsencher, Benjamin Villalonga, Theodore White, Z. Jamie Yao, Ping Yeh, Adam Zalcman, Hartmut Neven, and John M. Martinis. Quantum supremacy using a programmable superconducting processor. *Nature*, 574(7779):505–510, Oct 2019.

[4] Salvatore Gambino, Marco Mazzeo, Armando Genco, Omar Di Stefano, Salvatore Savasta, Salvatore Patanè, Dario Ballarini, Federica Mangione, Giovanni Lerario, Daniele Sanvitto, and Giuseppe Gigli. Exploring light

matter interaction phenomena under ultrastrong coupling regime. *ACS Photonics*, 1(10):1042–1048, 2014.

[5] I. I. Rabi. On the process of space quantization. *Phys. Rev.*, 49:324–328, Feb 1936.

[6] Heinz-Peter Breuer and Francesco Petruccione. *The Theory of Open Quantum Systems*. Oxford University Press, 2003.

[7] Jens Jensen and Allan R. Mackintosh. *Rare Earth Magnetism - Structures and Excitations*. Clarendon Press - Oxford, 2 edition, June 1991.

[8] A. González-Tudela, C.-L. Hung, D. E. Chang, J. I. Cirac, and H. J. Kimble. Subwavelength vacuum lattices and atom–atom interactions in two-dimensional photonic crystals. *Nature Photonics*, 9(5):320–325, May 2015.

[9] Kun Huang, Avril Rhys, and Nevill Francis Mott. Theory of light absorption and non-radiative transitions in f-centres. *Proceedings of the Royal Society of London. Series A. Mathematical and Physical Sciences*, 204(1078):406–423, 1950.

[10] Anton Frisk Kockum, Adam Miranowicz, Simone De Liberato, Salvatore Savasta, and Franco Nori. Ultrastrong coupling between light and matter. *Nature Reviews Physics*, 1(1):19–40, 2019.

[11] Niels Borh. *Discussion with Einstein on epistemological problems in atomic physics, in Albert Einstein, Philosopher-scientist, edited by Paul Arthur Shilpp*. Harper, New York, 1949.

[12] I. I. Rabi. Space quantization in a gyrating magnetic field. *Phys. Rev.*, 51:652–654, Apr 1937.

[13] D. Braak. Integrability of the rabi model. *Phys. Rev. Lett.*, 107:100401, Aug 2011.

[14] E. M. Purcell, H. C. Torrey, and R. V. Pound. Resonance absorption by nuclear magnetic moments in a solid. *Phys. Rev.*, 69:37–38, Jan 1946.

[15] E. T. Jaynes and F. W. Cummings. Comparison of quantum and semiclassical radiation theories with application to the beam maser. *Proceedings of the IEEE*, 51(1):89–109, Jan 1963.

[16] S. Haroche. *In New Trends in Atomic Physics*. G. Grynberg and R. Stora (editors), Amsterdam: Elsevier, 2 edition, 1984.

[17] Christopher Gerry and Peter Knight. *Introductory Quantum Optics*. Cambridge University Press, 2004.

[18] P. Goy, J. M. Raimond, M. Gross, and S. Haroche. Observation of cavity-enhanced single-atom spontaneous emission. *Phys. Rev. Lett.*, 50:1903–1906, Jun 1983.

[19] J. H. Eberly, N. B. Narozhny, and J. J. Sanchez-Mondragon. Periodic spontaneous collapse and revival in a simple quantum model. *Phys. Rev. Lett.*, 44:1323–1326, May 1980.

[20] D. Meschede, H. Walther, and G. Müller. One-atom maser. *Phys. Rev. Lett.*, 54:551–554, Feb 1985.

[21] M. Brune, F. Schmidt-Kaler, A. Maali, J. Dreyer, E. Hagley, J. M. Raimond, and S. Haroche. Quantum rabi oscillation: A direct test of field quantization in a cavity. *Phys. Rev. Lett.*, 76:1800–1803, Mar 1996.

[22] D. M. Meekhof, C. Monroe, B. E. King, W. M. Itano, and D. J. Wineland. Generation of nonclassical motional states of a trapped atom. *Phys. Rev. Lett.*, 76:1796–1799, Mar 1996.

[23] P. Forn-Díaz, L. Lamata, E. Rico, J. Kono, and E. Solano. Ultrastrong coupling regimes of light-matter interaction. *Rev. Mod. Phys.*, 91:025005, Jun 2019.

[24] David Zueco. Light-matter interaction in the nonperturbative regime: a lecture. *Real Academia de Ciencias. Zaragoza.*, 74, 2019.

[25] Wolfgang P. Schleich. *Quantum Optics in Phase Space*. John Wiley & Sons, February 2001.

[26] R. H. Dicke. Coherence in spontaneous radiation processes. *Phys. Rev.*, 93:99–110, Jan 1954.

[27] Peter Kirton, Mor M. Roses, Jonathan Keeling, and Emanuele G. Dalla Torre. Introduction to the dicke model: From equilibrium to nonequilibrium, and vice versa. *Advanced Quantum Technologies*, 2(1-2):1800043, 2019.

[28] Michael Tavis and Frederick W. Cummings. Exact solution for an n-molecule—radiation-field hamiltonian. *Phys. Rev.*, 170:379–384, Jun 1968.

[29] Claude Cohen-Tannoudji, Jacques Dupont-Roc, and Gilbert Grynberg. *Photons and Atoms: Introduction to Quantum Electrodynamics*. John Wiley & Sons, March 1997.

[30] Marlan O. Scully and M. Suhail Zubairy. *Quantum Optics*. Cambridge University Press, September 1997.

[31] Crispin Gardiner and Peter Zoller. *Quantum Noise*. Springer-Verlag Berlin Heidelberg, 3 edition, 2004.

[32] Pierre Meystre and Murray Sargent. *Elements of Quantum Optics*. Springer-Verlag Berlin Heidelberg, 2007.

[33] Serge Haroche and Jean Michel Raimond. *Exploring the Quantum: Atoms, Cavities, and Photons*. Oxford Univ. Press, Oxford, 2006.

[34] Wolfgang Nolting and Anupuru Ramakanth. *Quantum Theory of Magnetism*. Springer-Verlag Berlin Heidelberg, 1 edition, 2009.

[35] Y. Kaluzny, P. Goy, M. Gross, J. M. Raimond, and S. Haroche. Observation of self-induced rabi oscillations in two-level atoms excited inside a resonant cavity: The ringing regime of superradiance. *Phys. Rev. Lett.*, 51:1175–1178, Sep 1983.

[36] R. J. Thompson, G. Rempe, and H. J. Kimble. Observation of normal-mode splitting for an atom in an optical cavity. *Phys. Rev. Lett.*, 68:1132–1135, Feb 1992.

[37] Peter Lodahl, Sahand Mahmoodian, and Søren Stobbe. Interfacing single photons and single quantum dots with photonic nanostructures. *Rev. Mod. Phys.*, 87:347–400, May 2015.

[38] Xiu Gu, Anton Frisk Kockum, Adam Miranowicz, Yu xi Liu, and Franco Nori. Microwave photonics with superconducting quantum circuits. *Physics Reports*, 718-719:1 – 102, 2017. Microwave photonics with superconducting quantum circuits.

[39] Gerhard Rempe, Herbert Walther, and Norbert Klein. Observation of quantum collapse and revival in a one-atom maser. *Phys. Rev. Lett.*, 58:353–356, Jan 1987.

[40] S. Ashhab and Franco Nori. Qubit-oscillator systems in the ultrastrong-coupling regime and their potential for preparing nonclassical states. *Phys. Rev. A*, 81:042311, Apr 2010.

[41] Andrew P. Hines, Christopher M. Dawson, Ross H. McKenzie, and G. J. Milburn. Entanglement and bifurcations in jahn-teller models. *Phys. Rev. A*, 70:022303, Aug 2004.

[42] Carlos Sánchez Muñoz, Franco Nori, and Simone De Liberato. Resolution of superluminal signalling in non-perturbative cavity quantum electrodynamics. *Nature Communications*, 9:1924, May 2018.

[43] Jared Lolli, Alexandre Baksic, David Nagy, Vladimir E. Manucharyan, and Cristiano Ciuti. Ancillary qubit spectroscopy of vacua in cavity and circuit quantum electrodynamics. *Phys. Rev. Lett.*, 114:183601, May 2015.

[44] Mauro Cirio, Kamanasish Debnath, Neill Lambert, and Franco Nori. Amplified optomechanical transduction of virtual radiation pressure. *Phys. Rev. Lett.*, 119:053601, Jul 2017.

[45] Justyna A. Ćwik, Peter Kirton, Simone De Liberato, and Jonathan Keeling. Excitonic spectral features in strongly coupled organic polaritons. *Phys. Rev. A*, 93:033840, Mar 2016.

[46] A. Ridolfo, S. Savasta, and M. J. Hartmann. Nonclassical radiation from thermal cavities in the ultrastrong coupling regime. *Phys. Rev. Lett.*, 110:163601, Apr 2013.

[47] Luigi Garziano, Alessandro Ridolfo, Simone De Liberato, and Salvatore Savasta. Cavity qed in the ultrastrong coupling regime: Photon bunching from the emission of individual dressed qubits. *ACS Photonics*, 4(9):2345–2351, 2017.

[48] Cristiano Ciuti, Gérald Bastard, and Iacopo Carusotto. Quantum vacuum properties of the intersubband cavity polariton field. *Phys. Rev. B*, 72:115303, Sep 2005.

[49] Aji A. Anappara, Simone De Liberato, Alessandro Tredicucci, Cristiano Ciuti, Giorgio Biasiol, Lucia Sorba, and Fabio Beltram. Signatures of the ultrastrong light-matter coupling regime. *Phys. Rev. B*, 79:201303, May 2009.

[50] T. Niemczyk, F. Deppe, H. Huebl, E. P. Menzel, F. Hocke, M. J. Schwarz, J. J. Garcia-Ripoll, D. Zueco, T. HÃ¼mmer, E. Solano, Marx A., and R. Gross. Circuit quantum electrodynamics in the ultrastrong-coupling regime. *Nature Physics*, 6(10):772–776, July 2019.

[51] David Zueco and Juanjo García-Ripoll. Ultrastrongly dissipative quantum rabi model. *Phys. Rev. A*, 99:013807, Jan 2019.

[52] Daniel Z. Rossatto, Celso J. Villas-Bôas, Mikel Sanz, and Enrique Solano. Spectral classification of coupling regimes in the quantum rabi model. *Phys. Rev. A*, 96:013849, Jul 2017.

[53] J. Casanova, G. Romero, I. Lizuain, J. J. GarcÃa-Ripoll, and E. Solano. Deep strong coupling regime of the jaynes-cummings model. *Phys. Rev. Lett.*, 105:263603, Dec 2010.

[54] Andreas Bayer, Marcel Pozimski, Simon Schambeck, Dieter Schuh, Rupert Huber, Dominique Bougeard, and Christoph Lange. Terahertz light matter interaction beyond unity coupling strength. *Nano Letters*, 17(10):6340–6344, 2017.

[55] A. Wallraff, D. I. Schuster, A. Blais, L. Frunzio, R.-. S. Huang, J. Majer, S. Kumar, S. M. Girvin, and R. J. Schoelkopf. Strong coupling of a single photon to a superconducting qubit using circuit quantum electrodynamics. *Nature*, 431(7005):162–167, Sep 2004.

[56] P. Forn-Díaz, J. Lisenfeld, D. Marcos, J. J. García-Ripoll, E. Solano, C. J. P. M. Harmans, and J. E. Mooij. Observation of the bloch-siegert shift in a qubit-oscillator system in the ultrastrong coupling regime. *Phys. Rev. Lett.*, 105:237001, Nov 2010.

[57] Fumiki Yoshihara, Tomoko Fuse, Sahel Ashhab, Kosuke Kakuyanagi, Shiro Saito, and Kouichi Semba. Superconducting qubit oscillator circuit beyond the ultrastrong-coupling regime. *Nature Physics*, 13, January 2017.

[58] Gülis Zengin, Martin Wersäll, Sara Nilsson, Tomasz J. Antosiewicz, Mikael Käll, and Timur Shegai. Realizing strong light-matter interactions between single-nanoparticle plasmons and molecular excitons at ambient conditions. *Phys. Rev. Lett.*, 114:157401, Apr 2015.

[59] Rohit Chikkaraddy, Bart de Nijs, Felix Benz, Steven J. Barrow, Oren A. Scherman, Edina Rosta, Angela Demetriadou, Peter Fox, Ortwin Hess, and Jeremy J. Baumberg. Single-molecule strong coupling at room temperature in plasmonic nanocavities. *Nature*, 535:127–130, Jun 2016.

[60] Gilad Haran and Lev Chuntonov. Artificial plasmonic molecules and their interaction with real molecules. *Chemical Reviews*, 118(11):5539–5580, 2018. PMID: 29781601.

[61] James A. Hutchison, Tal Schwartz, Cyriaque Genet, Eloïse Devaux, and Thomas W. Ebbesen. Modifying chemical landscapes by coupling to vacuum fields. *Angewandte Chemie International Edition*, 51(7):1592–1596, 2012.

[62] Johannes Feist and Francisco J. Garcia-Vidal. Extraordinary exciton conductance induced by strong coupling. *Phys. Rev. Lett.*, 114:196402, May 2015.

[63] Johannes Schachenmayer, Claudiu Genes, Edoardo Tignone, and Guido Pupillo. Cavity-enhanced transport of excitons. *Phys. Rev. Lett.*, 114:196403, May 2015.

[64] E. Orgiu, J. George, J. A. Hutchison, E. Devaux, J. F. Dayen, B. Doudin, F. Stellacci, C. Genet, J. Schachenmayer, C. Genes, G. Pupillo, P. Samorì, and T. W. Ebbesen. Conductivity in organic semiconductors hybridized with the vacuum field. *Nature Materials*, 14:1123 EP –, 09 2015.

[65] Sanli Faez, Pierre Türschmann, Harald R. Haakh, Stephan Götzinger, and Vahid Sandoghdar. Coherent interaction of light and single molecules in a dielectric nanoguide. *Phys. Rev. Lett.*, 113:213601, Nov 2014.

[66] Mark Jenkins, Thomas Hümmer, María José Martínez-Pérez, Juanjo García-Ripoll, David Zueco, and Fernando Luis. Coupling single-molecule magnets to quantum circuits. *New Journal of Physics*, 15(9):095007, sep 2013.

[67] Jasper Chan, T. P. Mayer Alegre, Amir H. Safavi-Naeini, Jeff T. Hill, Alex Krause, Simon Gröblacher, Markus Aspelmeyer, and Oskar Painter. Laser cooling of a nanomechanical oscillator into its quantum ground state. *Nature*, 478(7367):89–92, Oct 2011.

[68] Felix Benz, Mikolaj K. Schmidt, Alexander Dreismann, Rohit Chikkaraddy, Yao Zhang, Angela Demetriadou, Cloudy Carnegie, Hamid Ohadi, Bart de Nijs, Ruben Esteban, Javier Aizpurua, and Jeremy J. Baumberg. Single-molecule optomechanics in "picocavities". *Science*, 354(6313):726–729, 2016.

[69] H. Mabuchi and A. C. Doherty. Cavity quantum electrodynamics: Coherence in context. *Science*, 298(5597):1372–1377, 2002.

[70] Stéphane Kéna-Cohen, Stefan A. Maier, and Donal D. C. Bradley. Ultrastrongly coupled exciton polaritons in metal clad organic semiconductor microcavities. *Advanced Optical Materials*, 1(11):827–833, 2013.

[71] Hans Huebl, Christoph W. Zollitsch, Johannes Lotze, Fredrik Hocke, Moritz Greifenstein, Achim Marx, Rudolf Gross, and Sebastian T. B. Goennenwein. High cooperativity in coupled microwave resonator ferrimagnetic insulator hybrids. *Phys. Rev. Lett.*, 111:127003, Sep 2013.

[72] Yutaka Tabuchi, Seiichiro Ishino, Toyofumi Ishikawa, Rekishu Yamazaki, Koji Usami, and Yasunobu Nakamura. Hybridizing ferromagnetic

magnons and microwave photons in the quantum limit. *Phys. Rev. Lett.*, 113:083603, Aug 2014.

[73] A. Zrenner, E. Beham, S. Stufler, F. Findeis, M. Bichler, and G. Abstreiter. Coherent properties of a two-level system based on a quantum-dot photodiode. *Nature*, 418(6898):612–614, 2002.

[74] Kotni Santhosh, Ora Bitton, Lev Chuntonov, and Gilad Haran. Vacuum rabi splitting in a plasmonic cavity at the single quantum emitter limit. *Nature Communications*, 7, June 2016.

[75] F. Jelezko, T. Gaebel, I. Popa, A. Gruber, and J. Wrachtrup. Observation of coherent oscillations in a single electron spin. *Phys. Rev. Lett.*, 92:076401, Feb 2004.

[76] Volkhard May and Oliver Kühn. *Charge and Energy Transfer Dynamics in Molecular Systems*. Wiley-VCH Verlag GmbH & Co. KGaA, 3 edition, February 2011.

[77] T Holstein. Studies of polaron motion: Part i. the molecular-crystal model. *Annals of Physics*, 8(3):325 – 342, 1959.

[78] T. Holstein. Studies of polaron motion: Part ii. the small polaron. *Annals of Physics*, 8(3):343 – 389, 1959.

[79] F. C. Spano. Optical microcavities enhance the exciton coherence length and eliminate vibronic coupling in j-aggregates. *The Journal of Chemical Physics*, 142(18):184707, 2015.

[80] Brandes T. Phonons in electronic transport in nanoscale systems. *Lecture Notes Caltech NEMS Summer School*, 2007.

[81] Justyna A. Ćwik, Sahinur Reja, Peter B. Littlewood, and Jonathan Keeling. Polariton condensation with saturable molecules dressed by vibrational modes. *EPL (Europhysics Letters)*, 105(4):47009, feb 2014.

[82] Javier del Pino, Johannes Feist, and F. J. Garcia-Vidal. Signatures of vibrational strong coupling in raman scattering. *The Journal of Physical Chemistry C*, 119(52):29132–29137, 2015.

[83] Ning Wu, Johannes Feist, and Francisco J. Garcia-Vidal. When polarons meet polaritons: Exciton-vibration interactions in organic molecules strongly coupled to confined light fields. *Phys. Rev. B*, 94:195409, Nov 2016.

[84] Felipe Herrera and Frank C. Spano. Cavity-controlled chemistry in molecular ensembles. *Phys. Rev. Lett.*, 116:238301, Jun 2016.

[85] Felipe Herrera and Frank C. Spano. Absorption and photoluminescence in organic cavity qed. *Phys. Rev. A*, 95:053867, May 2017.

[86] M. Ahsan Zeb, Peter G. Kirton, and Jonathan Keeling. Exact states and spectra of vibrationally dressed polaritons. *ACS Photonics*, 5(1):249–257, 2018.

[87] Tomáš Neuman, Ruben Esteban, Geza Giedke, MikoÅ‚aj K. Schmidt, and Javier Aizpurua. Quantum description of surface-enhanced resonant raman scattering within a hybrid-optomechanical model. *Physical Review A*, 100(4), Oct 2019.

[88] Peter W. Atkins and Ronald S. Friedman. *Molecular Quantum Mechanics*. Oxford University Press, 5 edition, November 2010.

[89] Peter F. Bernath. *Spectra of Atoms and Molecules*. OUP USA, 2 edition, 2005.

[90] Ángel Rivas and Susana F. Huelga. Open quantum systems. *SpringerBriefs in Physics*, 2012.

[91] Howard J. Carmichael. *Statistical Methods in Quantum Optics*, volume 1. Springer-Verlag Berlin Heidelberg, 1 edition, 1978.

[92] G. Lindblad. On the generators of quantum dynamical semigroups. *Communications in Mathematical Physics*, 48(2):119–130, Jun 1976.

[93] Ling Hu, Yue-Chi Ma, Yuan Xu, Wei-Ting Wang, Yu-Wei Ma, Ke Liu, Hai-Yan Wang, Yi-Pu Song, Man-Hong Yung, and Lu-Yan Sun. Simulation of molecular spectroscopy with circuit quantum electrodynamics. *Science Bulletin*, 63(5):293 – 299, 2018.

[94] Frank C. Spano. The spectral signatures of frenkel polarons in h- and j-aggregates. *Accounts of Chemical Research*, 43(3):429–439, 2010. PMID: 20014774.

[95] Roel S. Sánchez-Carrera, M. Carmen Ruiz Delgado, Cristina Capel Ferrón, Reyes Malavé Osuna, Víctor Hernández, Juan T. López Navarrete, and Alán Aspuru-Guzik. Optical absorption and emission properties of end-capped oligothienoacenes: A joint theoretical and experimental study. *Organic Electronics*, 11(10):1701 – 1712, 2010.

[96] M. Zeb, Peter Kirton, and Jonathan Keeling. Exact quantum states of the holstein-tavis-cummings model. *arXiv*, Aug 2016.

[97] Claude Cohen-Tannoudji, Diu Bernard, and Frank Laloe. *Quantum Mechanics*, volume 1. WILEY-VCH, 2019.

[98] Michele Cini. *Topics and Methods in Condensed Matter Theory.* Springer-Verlag Berlin Heidelberg, 1 edition, 2007.

[99] A. A. Clerk, M. H. Devoret, S. M. Girvin, Florian Marquardt, and R. J. Schoelkopf. Introduction to quantum noise, measurement, and amplification. *Rev. Mod. Phys.*, 82:1155–1208, Apr 2010.

[100] S.-P. Yu, J. D. Hood, J. A. Muniz, M. J. Martin, Richard Norte, C.-L. Hung, SeÃ¡n M. Meenehan, Justin D. Cohen, Oskar Painter, and H. J. Kimble. Nanowire photonic crystal waveguides for single-atom trapping and strong light-matter interactions. *Applied Physics Letters*, 104(11):111103, 2014.

[101] M. Arcari, I. Söllner, A. Javadi, S. Lindskov Hansen, S. Mahmoodian, J. Liu, H. Thyrrestrup, E. H. Lee, J. D. Song, S. Stobbe, and P. Lodahl. Near-unity coupling efficiency of a quantum emitter to a photonic crystal waveguide. *Phys. Rev. Lett.*, 113:093603, Aug 2014.

[102] Vladimir P Bykov. Spontaneous emission from a medium with a band spectrum. *Soviet Journal of Quantum Electronics*, 4(7):861–871, jul 1975.

[103] Tao Shi, Ying-Hai Wu, A. González-Tudela, and J. I. Cirac. Bound states in boson impurity models. *Phys. Rev. X*, 6:021027, May 2016.

[104] T Shi, Y-H Wu, A González-Tudela, and J I Cirac. Effective many-body hamiltonians of qubit-photon bound states. *New Journal of Physics*, 20(10):105005, oct 2018.

[105] E. Sanchez-Burillo, D. Zueco, J. J. Garcia-Ripoll, and L. Martin-Moreno. Scattering in the ultrastrong regime: Nonlinear optics with one photon. *Phys. Rev. Lett.*, 113:263604, Dec 2014.

[106] E. Sánchez-Burillo, D. Zueco, L. Martín-Moreno, and J. J. García-Ripoll. Dynamical signatures of bound states in waveguide qed. *Phys. Rev. A*, 96:023831, Aug 2017.

[107] Landau Rubin H. *Quantum Mechanics II: A Second Course in Quantum Theory*, volume 2. WILEY-VCH, 2nd edition, July 2008.